Nevada Department of Transportation

Report No. 744-18-803

Proof-of-Concept Research of Roadside LiDAR Sensing Multimodal Traffic

May 2022

Disclaimer

This work was sponsored by the Nevada Department of Transportation. The contents of this report reflect the views of the authors, who are responsible for the facts and the accuracy of the data presented herein. The contents do not necessarily reflect the official views or policies of the State of Nevada at the time of publication. This report does not constitute a standard, specification, or regulation.

Technical Report Documentation Page

1. Report No.	2. Government Accession No.	3. Recipient's Catalog No.
744-18-803		

4. Title and Subtitle	5. Report Date
Proof-of-Concept Research on Roadside LiDAR Sensing Multimodal Traffic	May 30, 2022
	6. Performing Organization Code

7. Author(s)	8. Performing Organization Report No.
Hao Xu, Junxuan Zhao, Hongchao Liu, Zong Tian, Carlos Cardillo, Fraser Schilling	

9. Performing Organization Name and Address	10. Work Unit No. (TRAIS)
Department of Civil and Environmental Engineering & Nevada Center of Applied Research, University of Nevada, Reno Department of Civil, Environmental, and Construction Engineering, Texas Tech University Road Ecology Center, University of California, Davis	11. Contract or Grant No. P744-18-803

12. Sponsoring Agency Name and Address	13. Type of Report and Period Covered
Nevada Department of Transportation 1263 South Stewart Street; Carson City, Nevada	Final Report Feb 2019-Apr 2022
	14. Sponsoring Agency Code

15. Supplementary Notes

16. Abstract

Based on the project team's multiple years of research, deployment, and engineering application expertise, this project evaluated the accuracy, reliability, and efficiency of roadside LiDAR sensing and explored various traffic scenarios and applications of roadside LiDAR sensors. This project evaluated the accuracy, reliability, and efficiency of roadside LiDAR sensing and explored various traffic scenarios and applications of roadside LiDAR sensors. The project report provides examples, case studies, and evaluations of these applications.

17. Keywords	18. Distribution Statement

19. Security Classif. (of this report)	20. Security Classif. (of this page)	21. No. of Pages	22. Price
Unclassified	Unclassified		

Proof-of-Concept Research on Roadside LiDAR Sensing Multimodal Traffic

Hao Xu , University of Nevada, Reno
Junxuan Zhao, Texas Tech University
Hongchao Liu, Texas Tech University
Fraser Shilling, University of California, Davis
Carlos Cardillo, University of Nevada, Reno
Zong Tian, University of Nevada, Reno

Research Project P744-18-803
Nevada Department of Transportation

University of Nevada, Reno
TEXAS TECH UNIVERSITY
UCDAVIS UNIVERSITY OF CALIFORNIA

ABSTRACT

New traffic systems and applications require traffic flow information with more detail and higher accuracy—specifically, multimodal, all-traffic trajectories. Light detection and ranging (LiDAR) sensors are considered and turn out to be a promising high-quality traffic data solution for more and more scenarios. There are various LiDAR sensors for mapping, survey, and autonomous vehicles. With the consideration of device cost, performance, installation, and maintenance, the project mainly used 360-degree LiDAR sensors. Research and field testing of roadside LiDAR at UNR has demonstrated that roadside LiDAR is an effective solution for sensing the movements of all road users for both permanent deployment and short-term data collection. Based on the project team's multiple years of research, deployment, and engineering application expertise, this project evaluated the accuracy, reliability, and efficiency of roadside LiDAR sensing and explored various traffic scenarios and applications of roadside LiDAR sensors.

With more and more published research on roadside LiDAR processing algorithms and available software solutions, possible roadside LiDAR system or data users need to know the details of installation, maintenance, the influence of different weather conditions, and how they can use the all-traffic trajectory data to promote engineering tasks, data analysis, and evidence-based decisions. These are the project's goals, and study results related to these interest areas are summarized in this project report, including:

1) Roadside LiDAR hardware, software, installation guidance, occlusion impact, and influence of weather conditions;
2) The critical data processing algorithms developed in this project, performance evaluation of roadside LiDAR data, and a comparison between LiDAR all-traffic trajectory data and video-generated spatial trajectories by the latest video processing AI;
3) Various applications of roadside LiDAR sensing and LiDAR data, including offline data usage, a real-time traffic signal system, and the real-time broadcast of LiDAR trajectory data from the roadside systems to connected vehicles.

This project report provides examples, case studies, and evaluations of these applications. It needs to be noted that this project report only lists some of the applications rather than all. Readers' innovative thinking will lead roadside LiDAR sensing/data to extensive scenarios to benefit our communities' mobility, safety, and energy efficiency.

TABLE OF CONTENTS

LIST OF FIGURES

LIST OF TABLES

1. INTRODUCTION

Existing traffic data, such as flow rates, occupancy, average speed, and spot speed, have been widely used for traffic mobility and safety. Yet new traffic systems and applications require traffic flow information with more detail and higher accuracy—specifically, multimodal, all-traffic trajectories. All-traffic trajectory data from either traveler-equipped or roadside sensors is critical to various traffic research/engineering areas, including but not limited to:

- **Connected and autonomous vehicles (CAVs):** At present, independent onboard sensing systems do not provide enough information for safe operation in multimodal traffic. Autonomous vehicles need to obtain the locations and movements of all road users and obstacles in extended distances and need to "see" around corners.
- **Near-crash analysis:** Near-crash events provide essential data for proactive safety analysis and countermeasure recommendations, but this data is challenging to obtain. When all-traffic trajectory data is available, interactions of vehicles and vulnerable road users can be studied at multiple scales to identify traffic safety issues and recommend countermeasures before crashes happen.
- **Traffic performance evaluation/adaptive traffic signal control:** All-traffic trajectories provide comprehensive information to evaluate traffic performance. Trajectory data reports each road user's stop location, stop time, speed change, interaction with other road users, and conventional vehicle-traffic performance indices such as the number of stops, delay, travel time, and queue length. Using traditional traffic sensors, optimizing signals along a road is challenging because system details cannot be accurately observed. Real-time, all-traffic trajectory data can make the traffic system completely observable, thus revolutionizing adaptive traffic control and outperforming conventional systems.
- **Automatic pedestrian/wildlife-crossing warning signals:** An important application of real-time all-traffic trajectories is monitoring and predicting vehicle-pedestrian conflicts on urban roads or vehicle-wildlife collision risks on rural highways. Trajectory data tracks the continuous movement of each road user, so crossing detection and prediction can be accurate and reliable with real-time direction/speed/location for superior accuracy and reliability.

Trajectories can be collected by probe vehicles or connected vehicles, but this provides only sample vehicle trajectories due to low penetration rates. From the roadside traffic sensing perspective, existing Intelligent Transportation Systems (ITS) employ loop detectors, video detectors, radar, and Bluetooth sensors for traffic measurement, mainly macro traffic data such as traffic flow rates, spot speeds/average speeds, and occupancy. Although conventional video sensors measure only the average speeds of vehicles that cross their detection zones, new video processing methods combine two or more cameras to measure distance. However, the accuracy of video sensing can be significantly influenced by low-light conditions. Recent research demonstrated the possibility of tracking vehicles with radar. Current low-cost radar sensors have difficulty detecting and tracking pedestrians near vehicles, while high-resolution radar sensors are much more expensive than other traffic sensors, including LiDAR.

Given the limitations of existing traffic sensors, light detection and ranging (LiDAR) sensors attract more interest for roadside traffic monitoring and tracking. The project team has developed dedicated data processing algorithms for roadside LiDAR sensing systems. This project evaluated the accuracy, reliability, and efficiency of roadside LiDAR sensing and explored various traffic scenarios and applications of roadside LiDAR sensors.

A LiDAR instrument principally consists of a laser, a scanner, and a specialized GPS receiver. It creates 360-degree 3D point clouds representing the surrounding environment in real-time by rapidly spinning laser beams mounted in a compact housing. Advanced digital signal processing and waveform analysis provide high accuracy, extended distance sensing, and calibrated reflectivity data. The working principle of LiDAR is that when the laser beam emitted by LiDAR hits an object, the laser energy is reflected and received by the LiDAR receiver. The object can be located by combining the laser beam's direction and the time difference between the emitted and received laser beams. With a 360-degree horizontal FoV and a 40-degree vertical FoV, LiDAR provides each object's three-dimensional information in the point cloud.

LiDAR can scan objects in 3-dimensional (3D) space and report their locations accurately under different illumination conditions, which is a major advantage over video cameras [1]. In addition, the data collected by LiDAR sensors are point clouds (i.e., massive sets of points), which require lower processing computation than image/video data (i.e., pixel information) of cameras.

There are various LiDAR sensors for mapping, survey, and autonomous vehicles. Considering the cost, performance, installation, and maintenance, we used 360-degree LiDAR in this project and in most of our roadside LiDAR systems. Research and field testing of roadside LiDAR at UNR has demonstrated that roadside LiDAR is an effective solution for sensing the movements of all road users for both permanent deployment and short-term data collection.

LiDAR data processing and high-resolution trajectory extraction are the fundamental functions of roadside LiDAR sensing systems. Data background filtering, object clustering, object classification, and real-time object movement tracking are required to process LiDAR data. Due to sensor installation and data characteristics, methods for processing roadside LiDAR data differ from solutions for autonomous vehicles. A roadside sensing system can include a network of LiDAR sensors, and the spatial data can be easily integrated. For the same sensor type, the density of cloud points from roadside LiDAR is often lower than what onboard LiDAR processing algorithms require because of the extended detection distance needed by roadside sensing systems.

With more and more published research on roadside LiDAR processing algorithms and available software solutions, possible roadside LiDAR system or data users need to know the details of installation, maintenance, influence of different weather conditions, and how they can use the all-traffic trajectory data to promote engineering tasks, data analysis, and evidence-based decisions. These are the project's goals, and study results related to these interest areas are presented in this project report. Chapter 2 – Chapter 5 are about roadside LiDAR hardware, software, installation guidance, occlusion impact, and influence of weather conditions, which can be more beneficial for the readers performing or managing fieldwork. Chapter 6 – Chapter 7 present two critical data processing algorithms developed during this project, performance evaluation of roadside LiDAR data and a comparison between LiDAR all-traffic trajectory data and video-generated spatial

trajectories by the latest video processing AI. The two chapters can be a reading focus for the audiences interested in data processing and data quality. Chapter 8 – Chapter 14 introduce various applications of roadside LiDAR sensing and LiDAR data, including offline data usage, a real-time traffic signal system, and the real-time broadcast of LiDAR trajectory data from the roadside systems to connected vehicles. Therefore, these seven chapters provide examples, case studies, and evaluations of these applications. It needs to be noted that this project report only lists some of the applications rather than all. Readers' innovative thinking will lead roadside LiDAR sensing/data to extensive scenarios to benefit our communities' mobility, safety, and energy efficiency.

2. ROADSIDE LIDAR SYSTEM COMPONENTS

A roadside LiDAR traffic sensing system typically includes hardware components of LiDAR sensor(s), data processing unit, communication devices, data storage (if field data log is needed), power supply & power distribution unit, and equipment enclosure housing all devices except the LiDAR sensors. An example of components of a roadside LiDAR sensing system deployed at N Boulder Hwy and Coogan Dr, Henderson, NV, is presented in Figure 2-1.

Equipment	Quantity	Description
VLP-32c 32-Channel LiDAR	1	32-channel LiDAR, provide 360-degree LiDAR cloud points to cover the whole intersection and extend sensing distance along Boulder Hwy.
New Dell Rugged Latitude 5420 Laptop	1	8th Gen Intel® Core™ i7-8650U Processor (Quad Core, 8M Cache, 1.9GHz,15W, vPro); 32G DDR4 Memory; 256G solid state hard drive; work temperature range is –20°F to 145°F
External Hard Drive	3	WD 4TB Black My Passport Portable External Hard Drive
Network Switch	1	D-Link 5 Port Gigabit Unmanaged Metal Desktop Switch (DGS-105)
LTE Wireless Connection Device	1	For remote monitoring of the system status, hard drive usage and real-time system alert to the UNR team's email box.
Temperature Data Logger	1	
Electrical Enclosure	1	29*24*12 inch, Type 3R Enclosure, Steel, Weather flo with Fan

Figure 2-1. Hardware components of a roadside LiDAR sensing deployment

Determined by the sensing system functions, LiDAR sensors can be installed permanently on traffic signal or street light poles at intersections or midblock, semi-permanently on an ITS trailer for freeway or rural area deployment, short-term deployment for days, or short-term deployment for peak hours only, as shown in Figure 2-2.

Figure 2-2 Demonstration of different roadside LiDAR sensing deployment

For a permanent installation, two to four LiDAR sensors are suggested. Based on the project team's test, LiDAR sensors with 32 or more channels (laser beams) are preferred, which provide the required effective sensing range for most scenarios. 360-degree LiDAR sensors are often installed 3-4 meters above the ground, and directional LiDAR sensors are normally installed on the traffic signal arms at intersections. A recommended installation location for 360-degree LiDAR at a signalized intersection is on top of the pedestrian signal heads. A more comprehensive analysis of LiDAR installation's influence on sensing performance is introduced in Chapter 3. Sensors at opposing corners of the intersection can minimize occlusions caused by large vehicles. It is essential for safety-related functions of real-time traffic signal systems or connected-autonomous vehicle systems taking the roadside LiDAR input. A detailed analysis of the relationship between sensor installation and occlusion is documented in Chapter 4. The deployment of sensors at an intersection may need to be adjusted for its dimensions and existing underground conduits. For example, the pilot deployment at Texas Ave and Boulder Hwy, Henderson, NV, installed sensors at the northeast intersection corner and a median to avoid wiring distance longer than 100 meters, the maximum data transmission distance of ethernet cable without a signal repeater. Locations of LiDAR sensors and the traffic signal cabinet are shown in Figure 2-3.

Communication, software, and maintenance

A data logging software developed was also developed in this project and installed on the edge computer for receiving LiDAR data from the sensors and saving data to external hard drives. The software created a pcap data file for each sensor's half-hour LiDAR data. When running 24/7, 32-channel LiDAR sensors generate a large amount of data; each Veloydne vlp-32c sensor generates about 1T of data per week. The project team researched various data compression algorithms to compress raw LiDAR data. The implemented data compression function can reduce a LiDAR data file to 1/3-1/8 of the original size. A real-time sensing and tracking software, developed by UNR, was also installed on the edge computers that can receive and process two sensors' data in real-time (10 HZ of each LiDAR data frame frequency)

The project tested three communication solutions: fiber, high-speed microwave communication, and the 5G data connection. Only the fiber connection could provide reliable communication to send raw LiDAR cloud points from the roadside sensing system to a UNR data center. However, communication of raw LiDAR data through a city traffic fiber network may cause concern for some agencies for the possible influence on regular traffic data communication. The raw data communication is more challenging when there is a network of LiDAR sensors. Therefore, cloud-based or central processing of raw LiDAR data, the roadside unit sending raw LiDAR data to a remote server for data processing and then receiving the processing results, is not recommended for extended deployments of roadside LiDAR sensors.

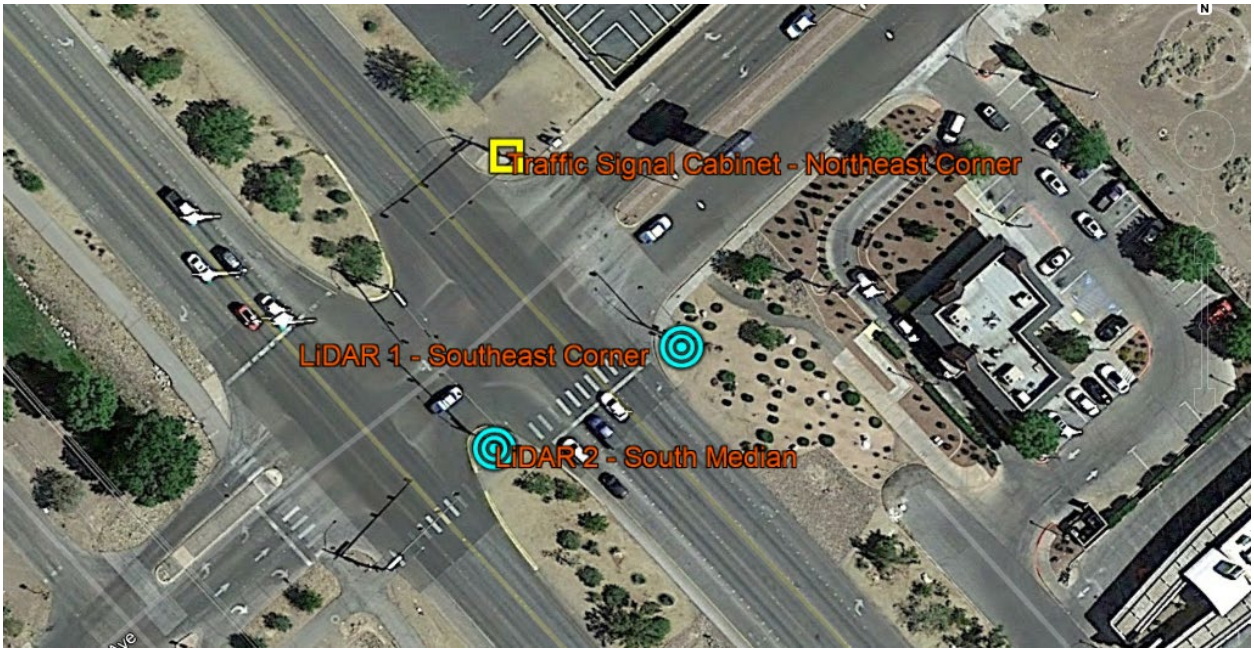

Figure 2-3 Locations of LiDAR sensors and traffic signal cabinet at S Boulder Hwy and Texas Ave

The high-speed microwave communication can provide enough bandwidth for LiDAR data communication but is often unstable or stopped when transferring the data 24/7. 5G data connection is expensive for real-time communication of raw LiDAR data, and communication was slowed sometime during our tests. However, all three communication solutions - fiber, microwave, and LTE/5G- were successfully used to monitor the edge system's health remotely. The project developed a software program on the edge computer that monitors the hardware and software health and sends system status or alert messages to the operators through an LTE/5G connection.

The maintenance effort includes monitoring the system's health through received system status messages and alerts. The LiDAR sensors also need to be cleaned; when the LiDAR glass surface is dirt, the LiDAR data quality and detection range can be reduced. The local weather and environment determine the cleaning frequency. UNR developed a software program to monitor LiDAR sensor data quality to warn operators when the sensor needs maintenance or cleaning.

The project team originally developed software programs for the Windows operation system, as agency engineers and technicians are more comfortable operating Windows configuration and

software. However, Windows automatic system updates often caused the edge computer to restart during multiple pilot deployments, even though the project team turned off its automatic update. A scheduled system update is needed when using Windows OS and software. Later, the project team switched to the Linux system and re-programmed the related software. The system was configured to automatically start the logging, processing, and system monitoring software programs when being turned on, without operation by technicians or engineers.

3. INSTALLATION HEIGHT AND TILT ANGLE

Currently, guidance for roadside LiDAR installation cannot be found in manufacturers' manuals. For agencies or other institutes to consider roadside LiDAR sensing deployment and systems, it is urgent to develop knowledge and guidance about selecting and installing LiDAR sensors on the infrastructure side for better traffic detection performance. As a part of this project, a study was performed to identify the roadside sensor installation's impact on the scanning range and quality. The project team first conducted a theoretical study to analyze the best installation strategy, including location, height, and tilt angle. Then three commonly used 360-degree LiDAR sensor models were tested in the field under different height and inclination settings (with/without considering occlusion) to examine the theoretical results. At last, installation recommendations of single and multiple LiDAR sensors at a selected road segment were provided in a case study.

Based on the mechanical structure and operational principle of LiDAR sensors, laser beams are rotated 360-degree along the sensor's central axis to form a series of conical surfaces for each scan. Each laser channel is fixed at a specific elevation angle relative to the sensor's central axis for a specific model. As an example in Figure 3-1, two laser beams generate two conical surfaces independently. Laser channels can be divided into two groups: the lasers with a positive elevation angle (a1) and the lasers with a negative angle (a2). The perpendicular direction of the sensor's central axis is zero-degree. In addition, the density of LiDAR point clouds is varied with the distance to the LiDAR sensor. An object near the LiDAR sensor generates intensive laser scan points and gets fine details of its surface shape; the same object only gets sparse scan points when it is far away from the sensor.

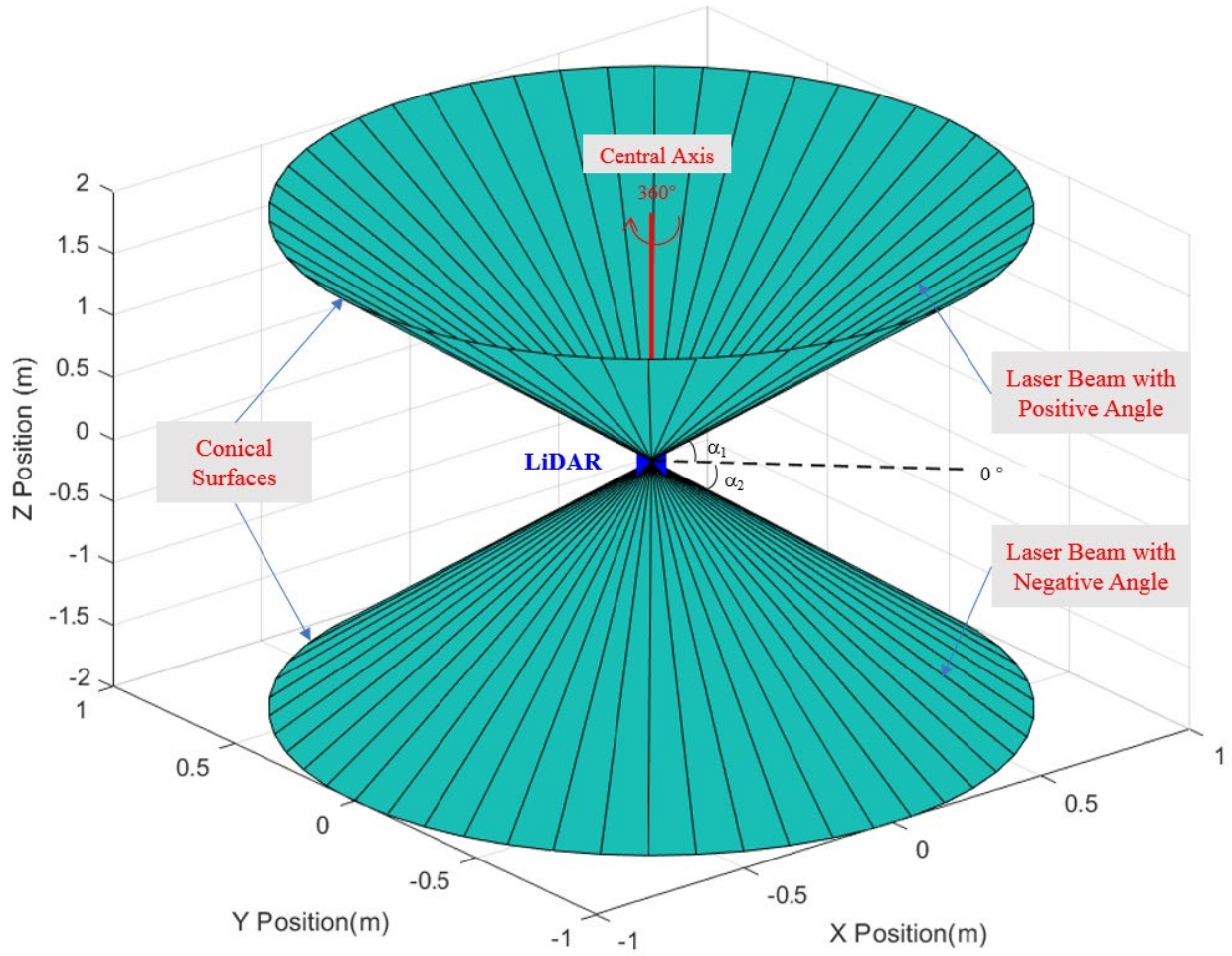

Figure 3-1. Laser beams of LiDAR sensor

LiDAR Built-in Features

LiDAR sensors' primary features and specifications include the number of channels, the vertical field of view (FOV), the vertical resolution of laser beams, the horizontal FOV, and the horizontal resolution of each laser beam. Their definitions are summarized as follows:

1) Channel: laser beam, a pair of laser emitter and receiver.
2) Vertical FOV: sensor's vertical sensing scope in degrees.
3) Vertical Resolution: vertical angle between adjacent laser beams in degrees.
4) Horizontal FOV: sensor's horizontal sensing scope in degrees; it is 360 degrees for 360-degree rotating LiDAR and can be 30-110 degrees for solid-state LiDAR.
5) Horizontal Resolution: horizontal angle in degrees between adjacent emission directions of the same laser channel; it can be converted to the number of scanning points generated by a laser beam during one rotation.

In general, the more laser channels, the more data points can be collected. The vertical FOV is determined by the number of channels and the vertical resolution of the laser beams. Table 3-1 lists the main features of three 360-degree LiDAR sensors from Velodyne company. Puck and

Puck Hi-Res LiDAR sensors have 16 laser channels, and the vertical angle between adjacent laser beams is fixed. The Ultra Puck LiDAR sensor has 32 laser beams, and the distribution of laser beams' vertical resolutions is non-linear..

Table 3-1. Specifications of three selected LiDAR sensors

Name	Channels	Vertical FOV	Vertical Resolution	Measurement Range	Rotation Frequency
Puck (VLP-16)	16	−15° to +15° (30°)	linear distribution (2°)	100m	5-20Hz
Puck Hi-Res	16	−10° to +10° (20°)	linear distribution (1.33°)	100m	5-20Hz
Ultra Puck (VLP-32C)	32	−25° to +15° (40°)	Non-linear distribution (0.33° for −4° to +1.33° FOV; Others are non-linear)	200m	5-20Hz

LiDAR Installation Position

The sensor installation plays a pivotal role in determining the LiDAR's sensing range. Depending on the sensing objective, LiDAR sensors can be temporarily installed on a tripod for short-term data collection or permanently mounted on roadside infrastructures for long-term data collection and real-time traffic sensing. The effective sensing range of a LiDAR sensor is determined by the installation location and position, vertical FOV, horizontal FOV, vertical resolution, horizontal resolution, and the maximum sensing distance of a laser beam (determined by the power of the laser and sensitivity of its receiver), and the minimum dimensions of sensing targets. The installation height and inclination are the two most influential factors when a sensor is selected.

The installation height refers to the vertical distance between the LiDAR sensor and the ground surface. Regarding the occlusion issue, LiDAR sensors installed at a higher position minimize the occlusion impact; however, there is an undetectable area under the LiDAR sensor (blind area) caused by the vertical FOV, and a higher installation position leads to an extended blind area under the sensor. Figure 3-2 illustrates a LiDAR sensor (N = 8 channels, θ vertical field of view, and fixed vertical resolution of laser beams) installed at the height of H above the ground. If the vertical angle of the lowest laser beam relative to the sensor's central axis is γi, then the farthest detection location of this laser beam is H × tan γi. The laser beams with positive angles can reach the maximum sensing distance claimed by the sensor manufacturer. In contrast, the detection range of the negative laser beams is H × (tan γj - tan γi), where the smallest and the largest vertical angle of negative laser beams are γi and γj, respectively. A target object within the sensor's detection range may not be detected when its heigh is lower than the lowest laser beam, as demonstrated by the first "undetectable" pedestrian in Figure 3-2. This pedestrian is actually in the blind area of the sensor. A LiDAR sensor may also fail to detect an object when the object is between two adjacent

laser beams without being hit by any laser channel, as the second undetectable pedestrian in Figure 3-2. This second failure scenario can be avoided when using a sensor with a high vertical resolution.

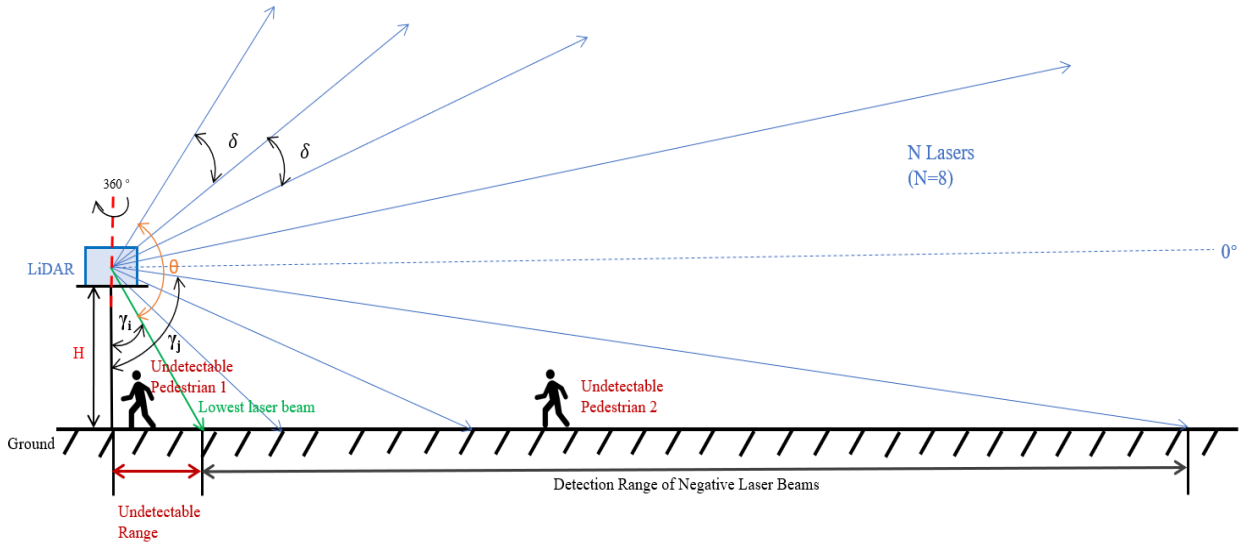

Figure 3-2. Example of two undetectable scenarios

A LiDAR sensor can be installed at any inclination angle. When it is placed on a horizontal plane, the sensor's central axis is perpendicular to the horizontal plane. Since all the laser beams are rotated along the sensor's central axis, the effective sensing distance is the same for different directions. As shown in Figure 3-3 (a), the angle of the laser beam (AB or AC) relative to the horizontal plane is equal to α during the 360° scan. If we place a LiDAR sensor on a slope, the sensor's central axis is vertical to the slope's surface. During the 360° scan, the same laser beam's scanning distance is different along with different sensor directions. The detection range reduces along the sensor's inclination direction. In Figure 3-3 (b), a LiDAR sensor is titled for b degree relative to the vertical plane, and the sensing range changes to α+β and α−β at 0° and 180° orientations, respectively.

The following is a theoretical derivation of the relationship between the laser beam's angle relative to the horizontal plane and the target object's direction for an inclined LiDAR sensor. In Figure 3-4, point A is the center of a LiDAR sensor. AX is the sensor's central axis, with a relative inclination angle of β to the vertical line AE (AE is perpendicular to the horizontal plane). A laser beam AB reaches AC after horizontally rotating θ degrees (assume the lengths of AB and AC are equal to R). The angle γ of the laser beam AB (or AC) relative to the AX is pre-defined by the LiDAR's specification.

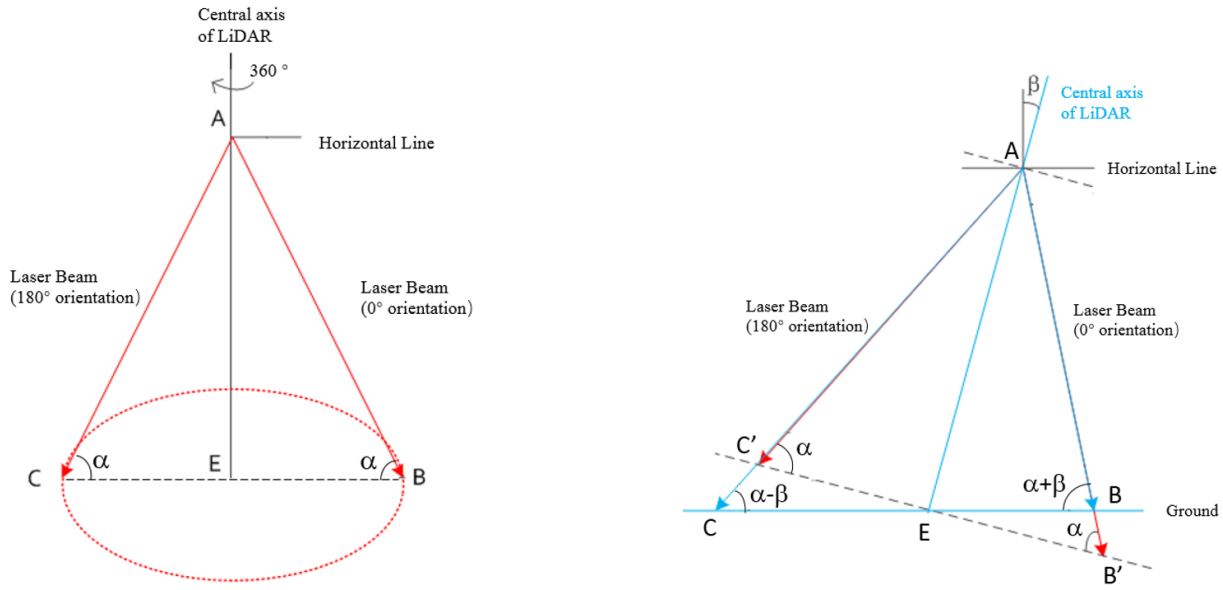

(a). Horizontal LiDAR. **(b).** Inclined LiDAR.

Figure 3-3. Geometric demonstration of laser beams with/without LiDAR inclination

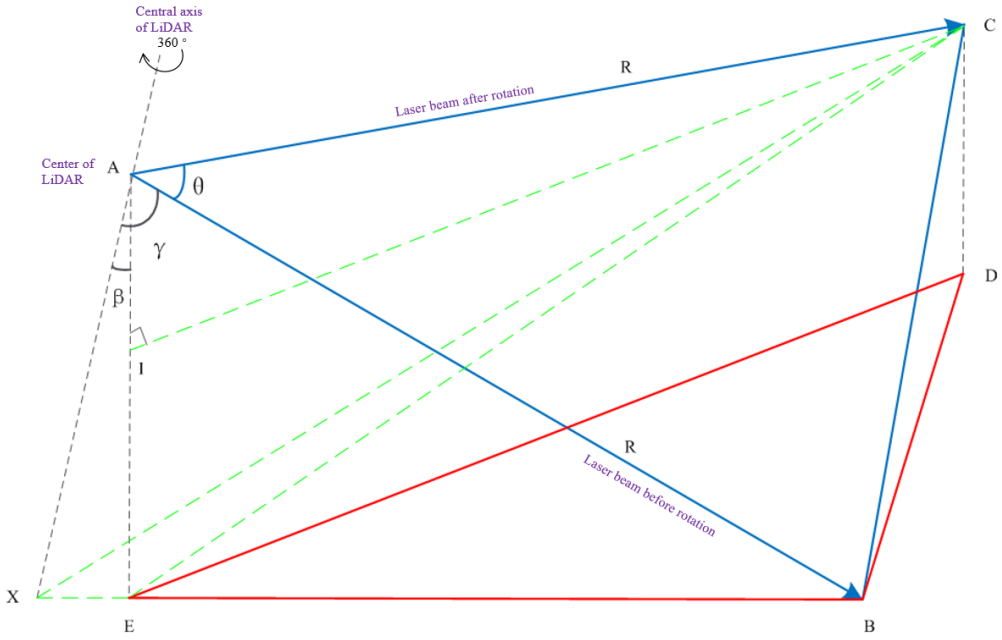

Figure 3-4. Geometric demonstration of rotating laser beams with inclined LiDAR sensor

Given: AB = AC = R (the length of laser beams)

$\angle XAE = \beta$ (LiDAR's inclination angle relative to the vertical line)

$\angle XAB = \angle XAC = \gamma$ (the angle of laser beams relative to the sensor's central axis)

$\angle BAC = \theta$ (laser beam's rotation angle)

Find: 1) $\angle ACI$ (the angle of the laser beam AC relative to the horizontal plane)

2) $\angle DEB$ (the angle formed by projecting rotation angle θ to the horizontal plane)

In order to solve the above problem, we added several auxiliary lines: reversely extend BE to the sensor's central axis at point X; project point C to the horizontal plane as point D; CI is perpendicular to AE; connect XC, EB, ED, BC, and BD. Note that ΔEBD is the projection of ΔABC on the horizontal plane. Based on the spatial geometry, the angle of the laser beam AB relative to the horizontal plane can be defined, which is:

$$\alpha = \angle \mathrm{ABE} = 90° - \angle \mathrm{EAB} = 90° - \left(\angle \mathrm{XAB} - \angle \mathrm{XAE}\right) = 90° - \gamma + \beta \quad \text{(Eq.3-1)}$$

Calculate ∠ACI

In Rt ΔAEB, $AE = Rsin\alpha, BE = Rcos\alpha$

In Rt ΔAEX, $XE = AEtan\beta$

In ΔXBC, $XC = XB = XE + BE$

In ΔABC, $BC = 2Rsin(\frac{\theta}{2})$

In ΔXBC, $\cos\left(\frac{\angle \mathrm{CXB}}{2}\right) = \frac{BC/2}{XC}$

In ΔXEC, $\cos\left(\angle \mathrm{CXB}\right) = \cos\left(\angle \mathrm{CXE}\right) = \frac{XC^2+XE^2-EC^2}{2XC \cdot XE}$

In ΔEAC, $\cos\left(\angle \mathrm{EAC}\right) = \frac{AE^2+AC^2-EC^2}{2AE \cdot AC}$

In Rt ΔAIC, $\angle \mathrm{ACI} = 90° - \angle \mathrm{EAC}$

Therefore, $\angle \mathrm{ACI} = 90° - \arccos\left(\cos(\gamma - \beta) - \tan\beta\left(2 - \frac{1-cos\theta}{\cos(\gamma-\beta)tan\beta + \sin(\gamma-\beta)}\right)\right)$ (Eq. 3-2)

Calculate ∠DEB

In Rt ΔAEX, $IE = AE - AI = AE - ACsin(\angle \mathrm{ACI})$

In rectangle ICDE, $CD = IE, DE = IC = ACcos(\angle \mathrm{ACI})$

In Rt ΔCDB, $DB^2 = BC^2 - CD^2$

In ΔDEB, $\cos\left(\angle \mathrm{DEB}\right) = \frac{DE^2+BE^2-DB^2}{2DE \cdot BE}$

Therefore, $\angle \mathrm{DEB} = \arccos\left(\frac{cos\theta - \cos(\gamma-\beta)\left(\cos(\gamma-\beta) - \tan\beta\left(2 - \frac{1-cos\theta}{\cos(\gamma-\beta)tan\beta + \sin(\gamma-\beta)}\right)\right)}{\sin(\gamma-\beta)\sqrt{1 - \left(\cos(\gamma-\beta) - \tan\beta\left(2 - \frac{1-cos\theta}{\cos(\gamma-\beta)tan\beta + \sin(\gamma-\beta)}\right)\right)^2}}\right)$ (Eq. 3-3)

The next is a backward derivation of the previous problem. If the projection angle ∠DEB on the horizontal plane is given, how many degrees does the laser AB need to rotate?

Given: ∠DEB (the angle formed by projecting rotation angle θ to the horizontal plane)

∠XAE = β (LiDAR's inclination angle)

∠XAB = ∠XAC = γ (the angle of laser beams relative to the sensor's central axis)

Find: 1) ∠BAC = θ (laser beam's rotation angle)

2) ∠ACI (the angle of the laser beam AC relative to the horizontal plane)

Calculate θ and ∠ACI

Define: $A = \sin(\gamma - \beta)$

$B = \cos(\gamma - \beta)$

$C = tan\beta$

$$D = \cos(\angle \mathrm{DEB})$$
$$E = BC + A$$
$$x = cos\theta$$

Then the Eq. 3 can be modified as $D = \frac{x - B\left(B - C\left(2 - \frac{1-X}{E}\right)\right)}{A\sqrt{1 - \left(B - C\left(2 - \frac{1-X}{E}\right)\right)^2}}$ (Eq. 3-4)

In Eq. 4, the values of the variable A, B, C, D, E are computable based on the given information. The only unknown variable is x. After mathematical simplification, Eq. 3-4 can be written as a quadratic equation of x in a standard form:

$$\left(1 + \frac{B^2C^2 + A^2C^2D^2}{E^2}\right)x^2 +$$
$$\frac{2C}{E}\left(B - B^3 + 2B^2C - \frac{B^2C}{E} - A^2BCD^2 + 2A^2C^2D^2 - \frac{A^2C^2D^2}{E}\right)x +$$
$$B^2(B^2 - 2) + 2BC\left(2 - \frac{1}{E}\right)(1 - B^2) + B^2C^2(2 - \frac{1}{E})^2 - A^2D^2(1 - B^2 - 4C^2) +$$
$$2A^2BCD^2\left(2 + \frac{1}{E}\right) - \frac{A^2C^2D^2}{E}\left(4 - \frac{1}{E}\right) = 0 \quad \text{(Eq. 3-5)}$$

Using the Quadratic Formula, the value of x can be obtained. Since x is equal to $cos\theta$, θ is known. In addition, if we substitute x for the $cos\theta$ in Eq. 3-2, $\angle$ACI can also be calculated. Figure 3-5 shows an example to demonstrate the application of the above derivation. When a LiDAR sensor is horizontally installed ($\beta = 0°$), the angle of a laser beam relative to the horizontal plane is 3° ($\alpha = 3°$), that is, $\gamma = 90° - \alpha + \beta = 87°$. No matter the direction of the laser ben's scan ($\angle \mathrm{DEB} = 0°{\sim}360°$), its angle relative to the horizontal plane is fixed: $\angle \mathrm{ACI} = \alpha = 3°$. However, if we tilt the LiDAR sensor to −1° ($\beta = -1°$), the $\angle$ACI is changed with different orientations. For example, when a target object is located at 0° ($\angle \mathrm{DEB} = 0°$) orientation relative to the LiDAR sensor, the angle of the same laser beam relative to the horizontal plane is changed from 3° to 2° ($\angle \mathrm{ACI} = 2°$); When the same target object is located at 180° ($\angle \mathrm{DEB} = 180°$) orientation, the angle is changed from 3° to 4° ($\angle \mathrm{ACI} = 4°$). Two intermittent points at 90° and 270° directions are due to the undefined Tangent function used in the calculation equations.

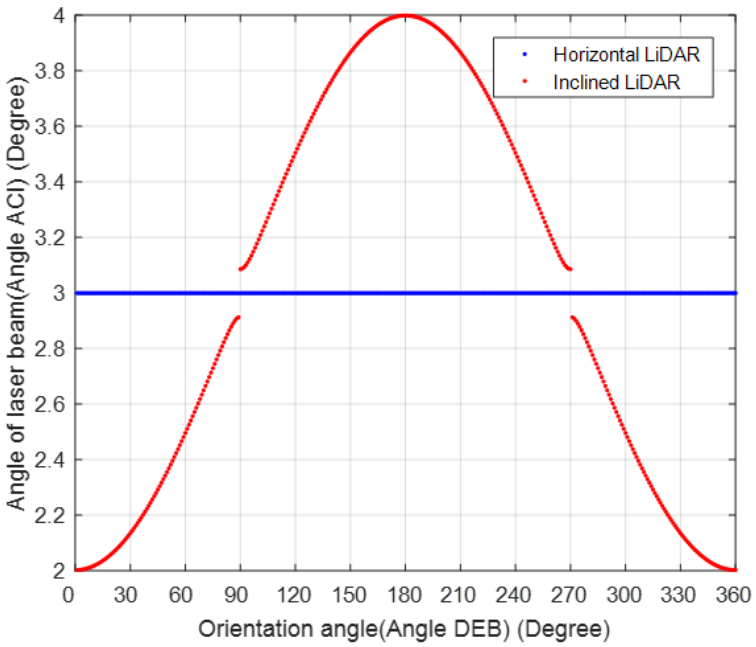

Figure 3-5. Angle variation with horizontal and inclined LiDAR sensor

Installation Height and Occlusion

Occlusion is a common challenge for over-road traffic sensors, including roadside LiDAR. LiDAR detection of a vehicle or a pedestrian can be occluded by other road users. The level of occlusion is affected by the LiDAR's built-in features and installation - the relative location and height of the target object and obstructions. Assuming that the numbers of valid laser beams shooting at the target object without and with occlusion are n_r and n_o, respectively. The detection loss percentage of the target object due to occlusion is calculated by Eq3-6.

$$Loss\ Percentage = \left(1 - \frac{n_o}{n_r}\right) \times 100\% \qquad \text{(Eq. 3-6)}$$

Figure 3-6 demonstrates an occlusion scenario of a roadside LiDAR sensor: a 1.5m height obstruction is at a 5.0m location, while a 1.0m height target object is moving within the sensor's detection range. Note that in the plot, the scales of the X and Y axes are different, so it seems that the angles between adjacent lasers are not the same. The resolution of the laser beams is fixed (2° for a Puck sensor). At the location A, the target object is fully blocked by the obstruction (loss percentage = 100%); At the location B, the target object is partially blocked by the obstruction (loss percentage = 50%); At the location C, even though the target object is located behind the obstruction, the detection of the target object is not affected by the obstruction since the valid laser beams are different (loss percentage = 0%).

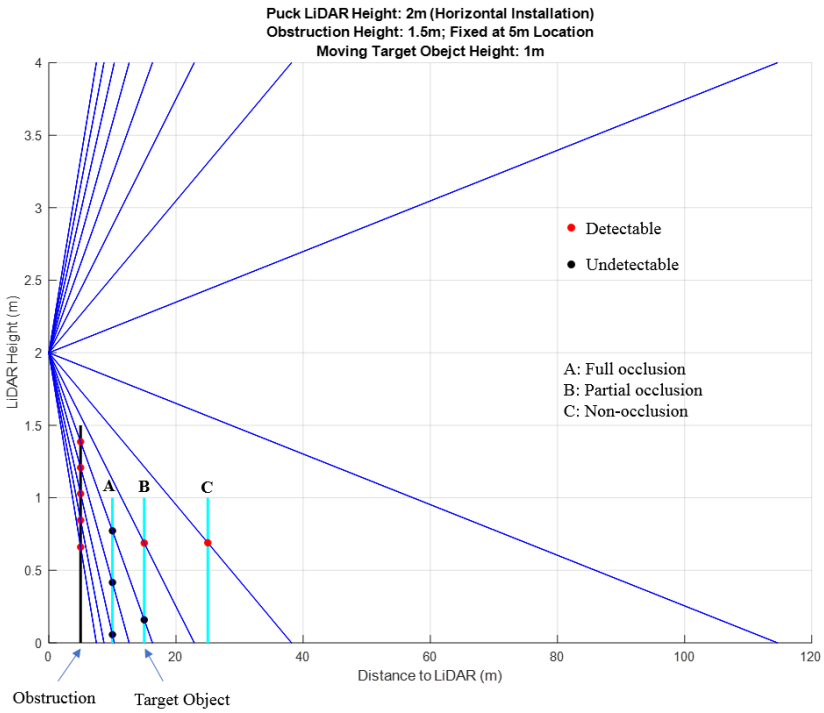

Figure 3-6. Demonstration of object detection with consideration of occlusion

Even though LiDAR manufacturers provide specifications on the measurement range of each model, it does not mean an object located at the farthest measurement distance can be correctly identified. For detecting and recognizing a road user correctly, at least two laser beams need to reach and be reflected at the target object. In our research, two criteria are used for assessing LiDAR detection performance: 1) how many valid laser beams can shoot at the target object; 2) the vertical height between two adjacent valid laser beams shooting at the target object.

Field Test

After the theoretical analysis has been presented, attention now can be directed to experimental studies, in which three types of commonly used LiDAR sensors (Puck, Puck Hi-Res, and Ultra Puck) were applied at installation sites (as shown in Figure 3-7) to examine the theoretical results. The sensors were mounted on a tripod for easy adjustment of the height and inclination angle. A scale rod, a protractor, and a distance ruler were used to measure the height and inclination as well as the horizontal distance to the LiDAR sensor. Whiteboards with different dimensions were used to represent objects of different sizes.

Figure 3-7. Installation position test in a parking lot

Different Heights & Same Moving Target

Case description: each LiDAR sensor was horizontally installed at the heights of 1.5m, 1.8m, and 2.0m above the flat ground, the height of a moving target object was 1.8m. Since the LiDAR senor did not have an inclination angle, the orientation of the objects which had the same distance to the LiDAR sensor was not an influential factor in the LiDAR detection range in this scenario. Table 3-2 lists the detection range of the three selected LiDAR sensors with different heights. For the same type of LiDAR sensors, it is clearly shown that different sensor heights would lead to different detection ranges.

Table 3-2. Detection Range of LiDAR Sensors (Horizontal Installation)

LiDAR	Height (m)	Detection Range (m)		
		≥ 1 laser	≥ 2 lasers	≥ 3 lasers
Puck	1.5	1.0-85.5	1.0-28.5	1.0-17.0
	1.8	1.0-100.0	1.0-34.0	1.0-20.5
	2.0	**1.0-100.0**	**1.0-38.0**	**1.5-22.5**
Puck Hi-Res	1.5	1.0-100.0	1.0-43.0	1.0-25.5
	1.8	1.0-100.0	1.0-51.5	1.0-30.5
	2.0	1.5-100.0	1.5-57.0	2.0-34.0
Ultra Puck	1.5	1.0-200.0	1.0-200.0	1.0-128.5
	1.8	1.0-200.0	1.0-200.0	1.0-154.5
	2.0	1.0-200.0	1.0-171.5	1.0-114.5

Note: The height of a target object is 1.8m.

The heatmaps in Figure 3-8 show the detection performance of a Puck sensor that was horizontally installed at a height of 2.0m. In the left plot, the color of each cell in the heatmap represents the valid number of laser beams (n) shooting at the target object. In the right plot, the color of each

cell in the heatmap indicates the vertical height (ΔY) between two adjacent valid laser beams shooting at the target object. As the distance between the target object and the sensor increases, the value of n decreases, and the ΔY increases because the scan planes of the LiDAR sensor are a series of conical surfaces.

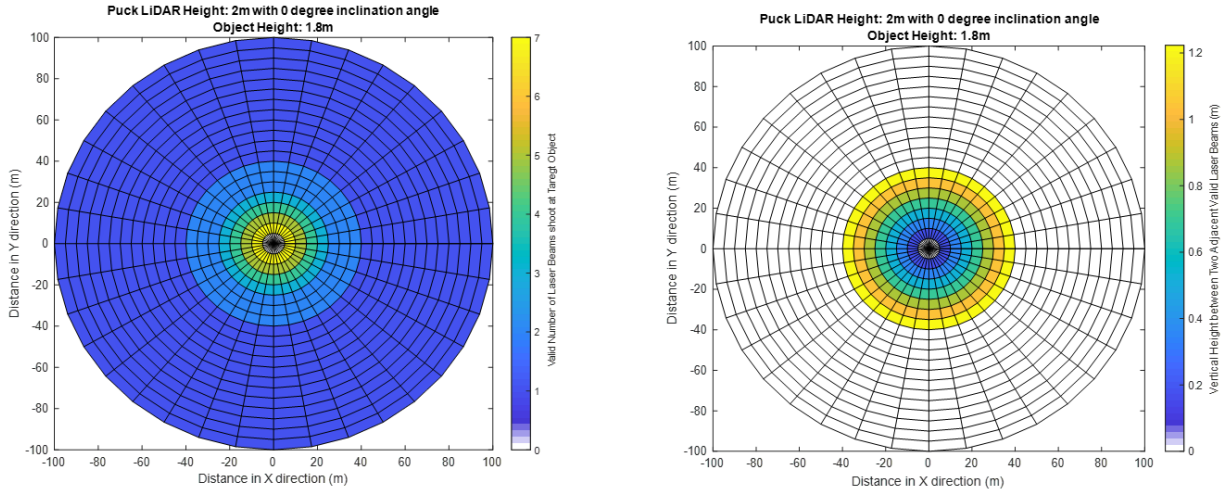

Figure 3-8. Heatmaps of Puck LiDAR sensor (horizontal installation)

Fixed Height & Changed Inclination

Case description: each LiDAR sensor was installed at a th 2.0m height and the sensor's inclination angle was −1° to + 2° with 1° resolution, the height of a moving target object was 1.8m. Since the LiDAR sensor was tilted, the objects located at different distances and orientations relative to the LiDAR sensor were scanned diversely. The heatmaps in Figure 3-9 and Figure 3-10 show the detection pattern changes of a Puck LiDAR sensor when the inclination angle was changed from −1° to + 2°. Figure 3-11 demonstrates the detection performance of Puck Hi-Res and Ultra Puck sensors with ±1° inclination. For an individual heatmap, the plot is symmetric about the X-axis; For a pair of heatmaps from the same LiDAR sensor with the same inclination angle but in opposite directions (e.g., ±1°), two corresponding heatmaps are centrosymmetric.

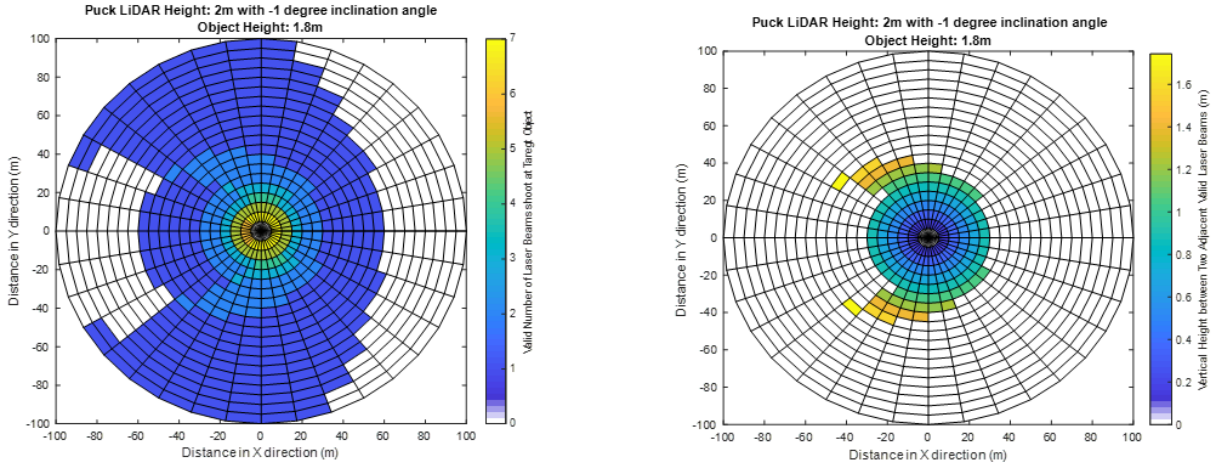

(a). Heatmaps of Puck LiDAR sensor with -1° inclination.

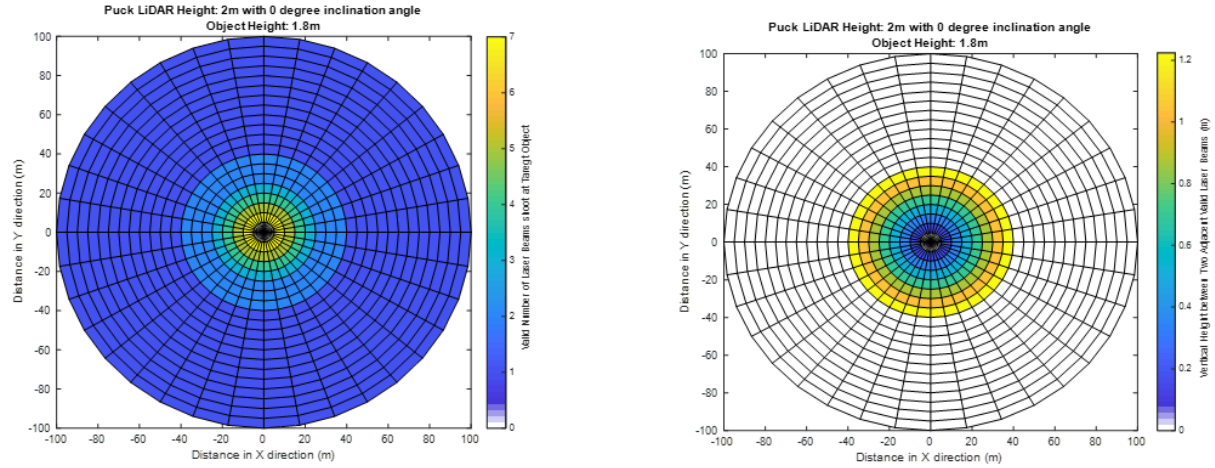

(b). Heatmaps of Puck LiDAR sensor with 0° inclination.

Figure 3-9. Heatmaps of Puck LiDAR sensor (inclined installation: -1° and 0°)

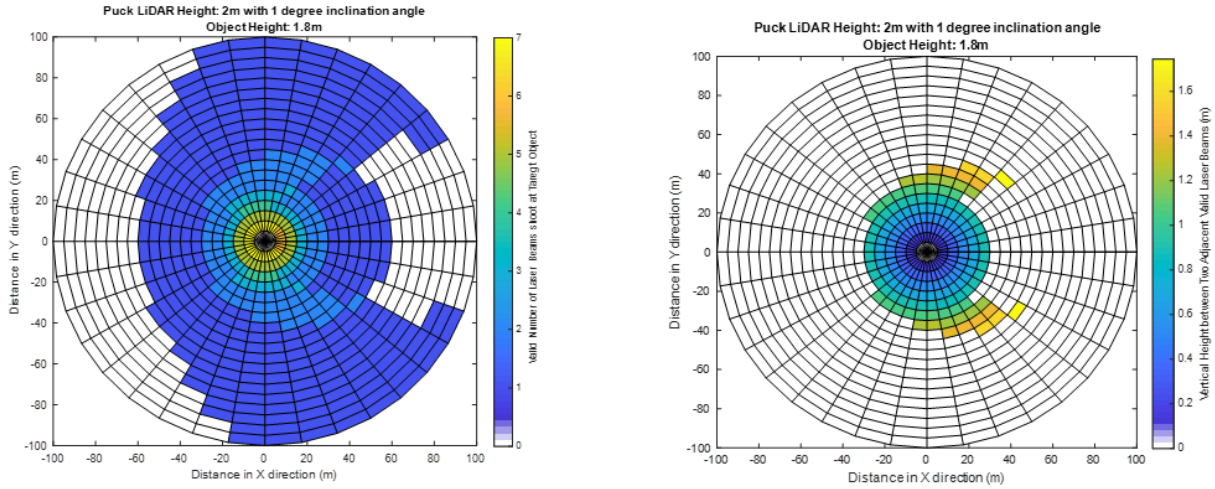

(c). Heatmaps of Puck LiDAR sensor with +1° inclination.

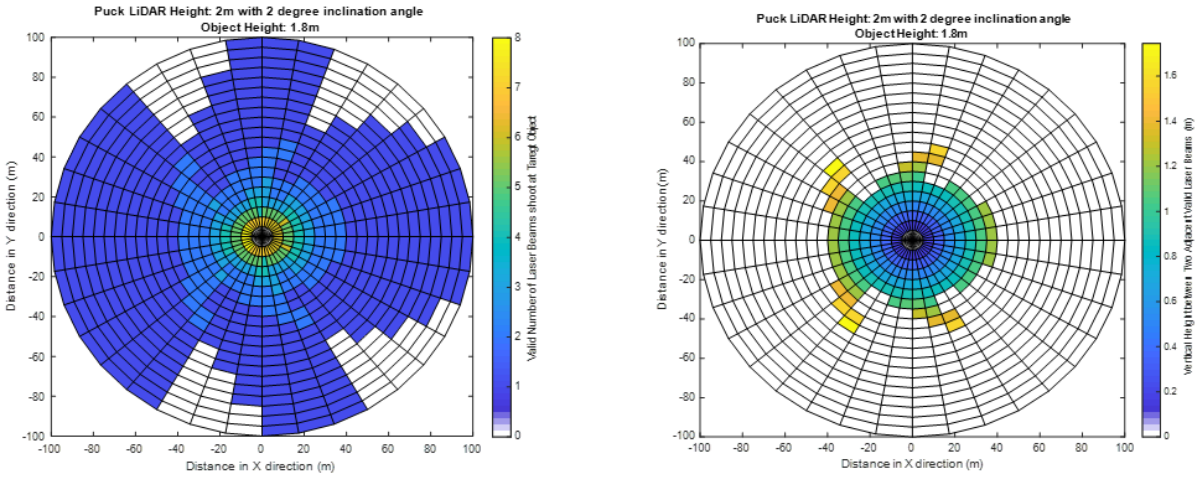

(d). Heatmaps of Puck LiDAR sensor with +2° inclination.

Figure 3-10. Heatmaps of Puck LiDAR sensor (inclined installation: +1º and +2º)

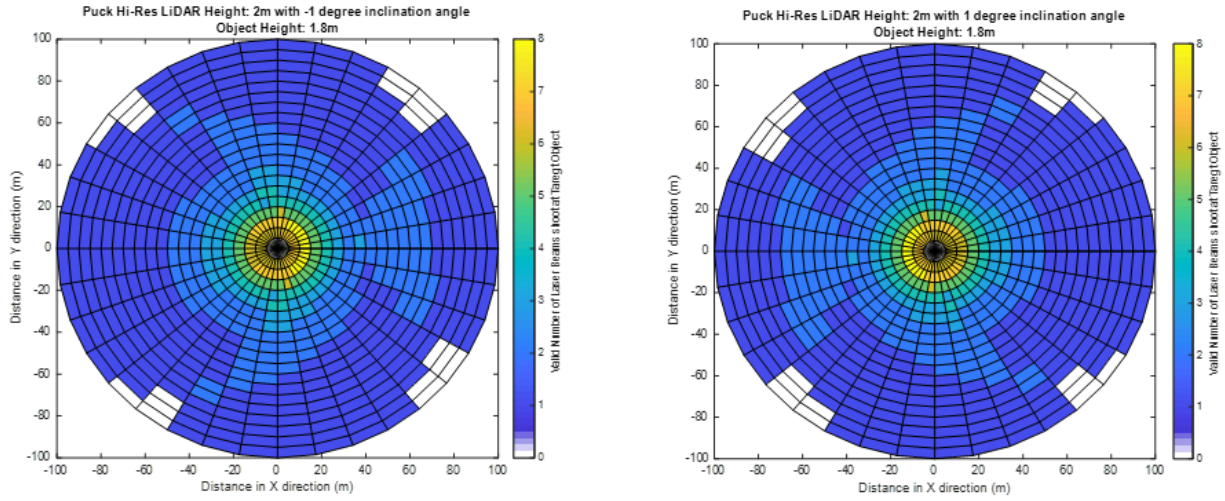

(a). Heatmaps of Puck Hi-Res LiDAR sensor with ±1° inclination.

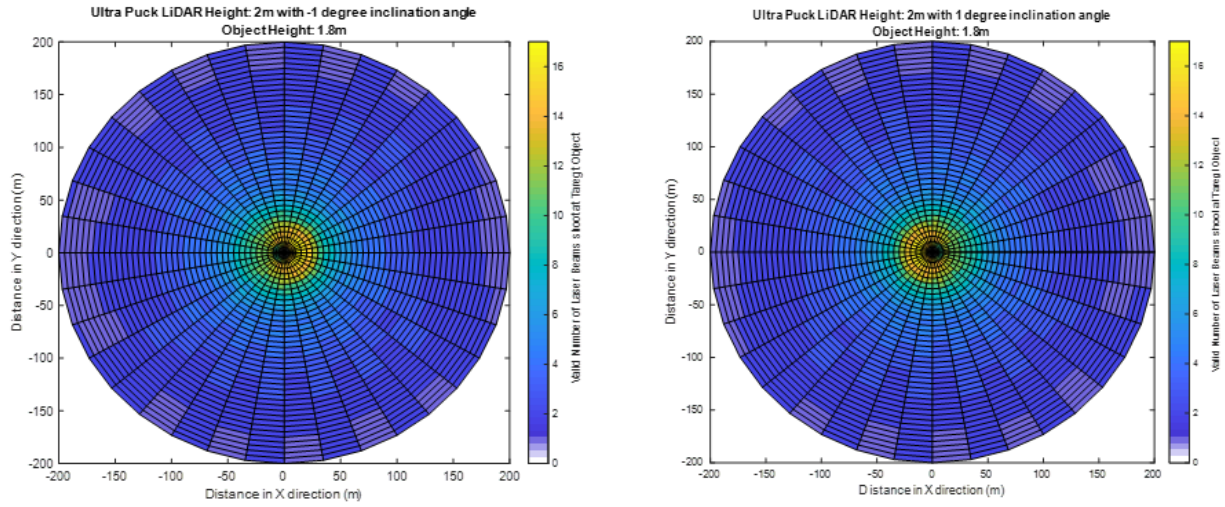

(b). Heatmaps of Ultra Puck LiDAR sensor with ±1° inclination.

Figure 3-11. Heatmaps of Puck Hi-Res and Ultra Puck LiDAR sensors (inclined installation)

Fixed Height & Vertical Installation

Case description: a LiDAR sensor was installed at a fixed height above the flat ground, and the sensor's inclination angle was 90° (i.e., vertical installation). In this case, the sensor's central axis was parallel to the horizontal plane. Thus, during the 360° scan, the downward 180° scan and the upward 180° scan were valid for detecting objects on the ground and in the air.

The project team conducted a field experiment in a warehouse to test this case: a Puck LiDAR sensor with a 90° vertical inclination angle was installed on a horizontal pole to scan the warehouse's ceiling (Figure 3-12). The height from the ceiling to the LiDAR sensor was about 5.13m, and the direction of the ceiling surface was perpendicular to the sensor's central axis. Under

this vertical deployment condition. Based on the theoretical derivation, the scan locations of the ceiling surface by a vertically installed Puck LiDAR senor at a fixed height are determined (as shown in Figure 3-13). To validate the calculation, the researchers randomly chose 16 locations along the X-axis (one specific location from each laser beam) and compared the widths along the Y-axis obtained from the calculation and the measurement. Table 3-3 lists the validation results and corresponding offsets. It showed that the average measurement accuracy of the field data was about 3.5cm and the relative offset was 1.6%. According to the user manual of Puck sensors (Velodyne, 2016), the measurement accuracy of this type of LiDAR sensor is about 3.0cm, which verified the result of the theoretical study. The measurement accuracy of the ceiling's height and the vertical deployment of the LiDAR sensor are the potential reasons for the offsets. Besides, we found that the laser beams with smaller vertical angles have better accuracy than those with larger vertical angles, and this issue may be caused by: 1) the LiDAR manufacturer does not provide information for angular correction; 2) at the same horizontal location/distance from the LiDAR sensor, laser beams with larger vertical angles travel a longer distance before shooting the surface than that propagated by laser beams with smaller angles; thus there is a higher probability of giving measurements with lower accuracy.

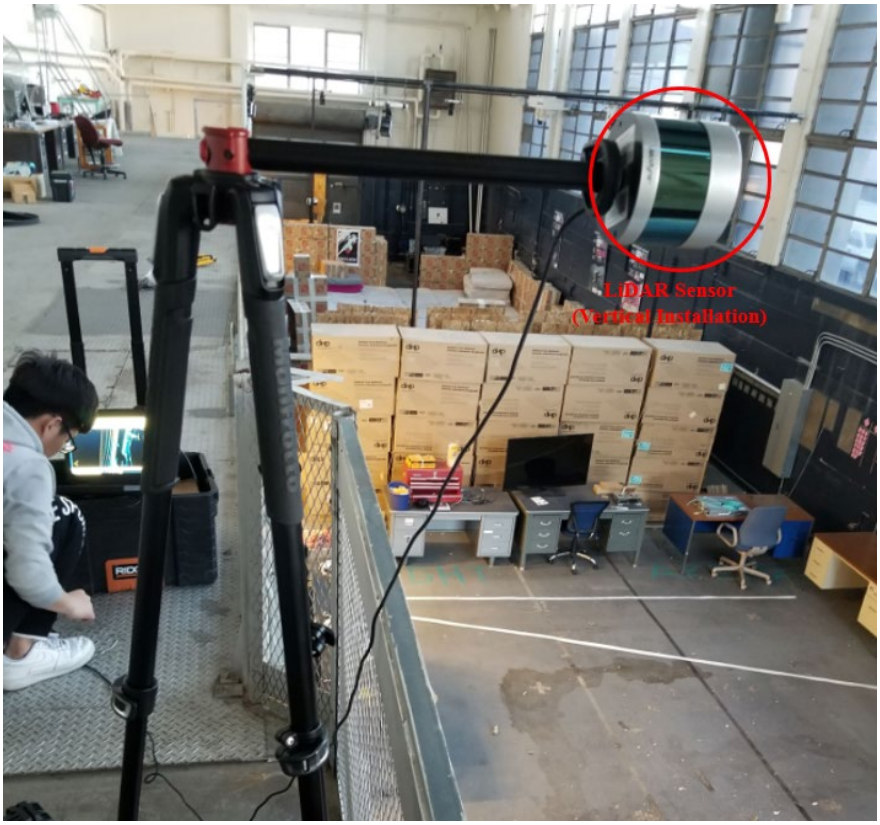

Figure 3-12. LiDAR installed for vertical scan

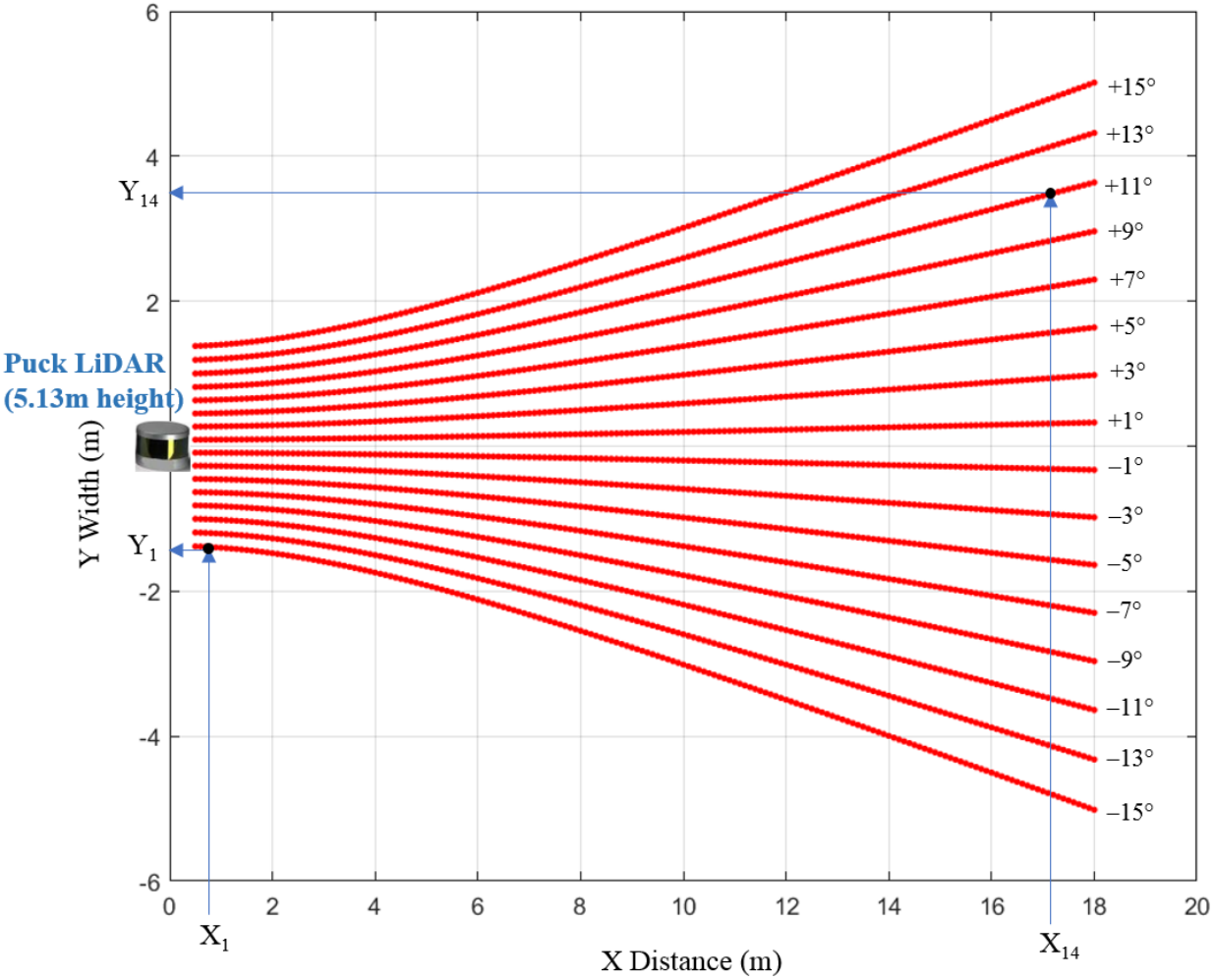

Figure 3-13. Calculated scan locations of the ceiling surface by a Puck LiDAR sensor (vertical installation)

Table 3-3. Validation for Scan Location Calculation

Laser Angle (degree)	Distance (m)	Calculated Width (m)	Measured Width (m)	Absolute Offset (m)	Relative Offset (%)
−15	0.767	−1.390	−1.357	0.033	2.374
−13	2.663	−1.335	−1.303	0.032	2.397
−11	3.137	−1.169	−1.147	0.022	1.882
−9	3.622	−0.995	−0.982	0.013	1.307
−7	4.468	−0.835	−0.828	0.007	0.838
−5	5.658	−0.668	−0.666	0.002	0.299
−3	6.370	−0.429	−0.428	0.001	0.233
−1	7.158	−0.154	−0.154	0.000	0.000
+1	9.595	0.190	0.192	0.002	1.053
+3	10.363	0.606	0.615	0.009	1.485
+5	11.365	1.091	1.109	0.018	1.650

+7	13.517	1.775	1.812	0.037	2.085
+9	14.661	2.460	2.516	0.056	2.276
+11	17.270	3.502	3.592	0.090	2.570
+13	17.656	4.245	4.356	0.111	2.615
+15	17.957	5.004	5.137	0.133	2.658
			Average	**0.035**	**1.608**

Occlusion Case

Case description: a LiDAR sensor was installed at the heights of 1.5m, 2.0m, and 2.5m above the flat ground. The heights of obstructions were set to 0.5m, 1.0m, 1.2m, and 1.5m. Two target objects of 1.0m and 1.5m in height were used as moving objects to test the level of occlusion due to the obstruction. In each case, the obstructions were set at fixed locations (5.0m, 10.0m, 15.0m, 20.0m, and 25.0m) from the LiDAR sensor.

Based on our previous research experience, correct object identification needs at least two laser beams shooting at the object. Table 3-4 summarizes the selected Puck sensor's valid detection range ($\geqslant$ 2 laser beams) in three representative cases. For example, a Puck LiDAR sensor was horizontally installed at a 2.0m location, a 1.0m height obstruction was at 10.0m from the sensor, and a 1.5m height target object was moving within 100.0m from the sensor. In Figure 3-14, the red lines represent the valid number of laser beams at each target object's location. The blue columns show the detection loss percentage of the target object. The two gray areas (3-22m, 29-38m) indicate the valid detection ranges where at least two laser beams can shoot at the target object.

Table 3-4. Detection Range of Puck LiDAR Sensor Considering Occlusion

h_{object} = 1.5m, h_{LiDAR} = 2.0m (horizontal)				
$h_{BlockObject}$ / $d_{BlockObject}$	Detection Range (≥ 2 lasers) (m)			
	0.5m	1.0m	1.2m	1.5m
5.0m	3-22, 29-38	3-22, 29-38	3-22, 29-38	3-4, 10-22, 29-38
10.0m	3-22, 29-38	**3-22, 29-38**	3-9, 29-38	3-9
15.0m	3-22, 29-38	3-14, 29-38	3-14, 29-38	3-14
20.0m	3-19, 29-38	3-19	3-19	3-19
25.0m	3-22, 29-38	3-22	3-22	3-22
h_{object} = 1.0m, h_{LiDAR} = 2.0m (horizontal)				
$h_{BlockObject}$ / $d_{BlockObject}$	Detection Range (≥ 2 lasers) (m)			
	0.5m	1.0m	1.2m	1.5m
5.0m	5-16, 20-22	7-17, 20-22	9-16, 20-22	20-22
10.0m	5-9, 12-16, 20-22	5-9, 20-22	5-9	5-9
15.0m	5-14, 20-22	5-14	5-14	5-14
20.0m	5-16	5-16	5-16	5-16
25.0m	5-16, 20-22	5-16, 20-22	5-16, 20-22	5-16, 20-22
h_{object} = 1.5m, h_{LiDAR} = 2.5m (horizontal)				
$h_{BlockObject}$ / $d_{BlockObject}$	Detection Range (≥ 2 lasers) (m)			
	0.5m	1.0m	1.2m	1.5m
5.0m	5-28	5-28	6-28	7-28

10.0m	5-28	5-9, 12-28	5-9,12-28	5-9, 20-28
15.0m	5-28	5-14, 20-28	5-14	5-14
20.0m	5-28	5-19	5-19	5-19
25.0m	5-24	5-24	5-24	5-24

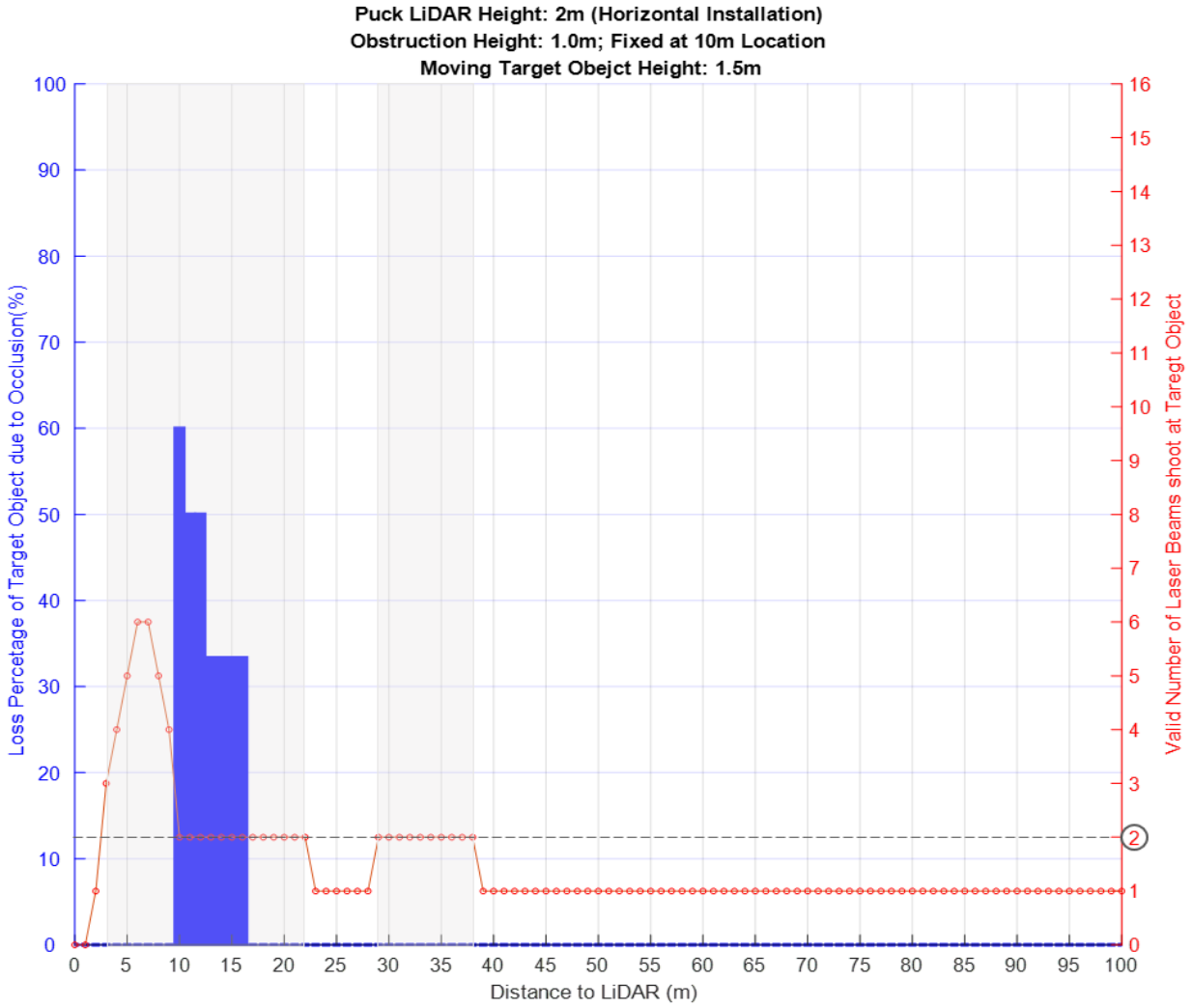

Figure 3-14. Demonstration of Puck sensor's detection performance considering occlusion

Summary

To apply LiDAR sensors for roadside detection of traffic and pedestrians, understanding how installation may affect LiDAR performance is critical. This research analyzed the built-in features of the selected models and conducted theoretical and experimental studies to explore and examine the installation methods for the best detection range and accuracy. After the theoretical analyses were made, four field test scenarios were conducted for examination, in which LiDAR sensors were 1) horizontally installed at different heights; 2) installed at a fixed height with different inclination angles; 3) vertically installed at a fixed height; and 4) horizontally installed at different heights with consideration of occlusion. The examination successfully validated the theoretical study. Besides, although Velodyne products were used in the investigation, this study provides general guidance on maximizing the performance by using the built-in features of LiDAR sensors.

4. OCCLUSION AND TRAFFIC FLOW

When over-road sensors are used for traffic detection, occlusion is an inevitable issue and hurts object detection. This project studied the relationship between traffic flow and vehicle occlusion rate. Firstly, with single and two LiDAR sensors installed at the roadside, simulated traffic data along urban freeways under conditions of different levels of services (LOS A to E) and truck percentages (5% to 30%) were analyzed to generate vehicle occlusion rates for each case, including percentages of fully detectable, partially detectable, (continuous) undetectable vehicles. Secondly, a case study using real LiDAR data collected from two experimental sites achieved 0.92% and 0.62% average offsets compared with the generated rates, verifying the simulation results' accuracy. The whole evaluation study provides expected vehicle occlusion rates from a roadside LiDAR system under different traffic conditions and gives guidance to traffic engineers or transportation agencies for planning and deploying sensors.

In this occlusion evaluation study, we divided all objects in each data frame into three categories based on their occlusion levels:

1) Fully detectable objects: the objects can be detected completely (No occlusion).
2) Partially detectable objects: the objects can be detected partially (Partial occlusion).
3) Undetectable objects: the objects cannot be detected (Full occlusion).

Figure 4-1demonstrates the above three occlusion scenarios: vehicle #1 is partially occluded by vehicle #3, vehicle #6 is fully occluded by vehicle #5, and other vehicles are not occluded at all. In other words, fully detectable vehicles are vehicles #2, #3, #4, #5, and #7; the partially detectable vehicle is vehicle #1, and the undetectable vehicle is vehicle #6.

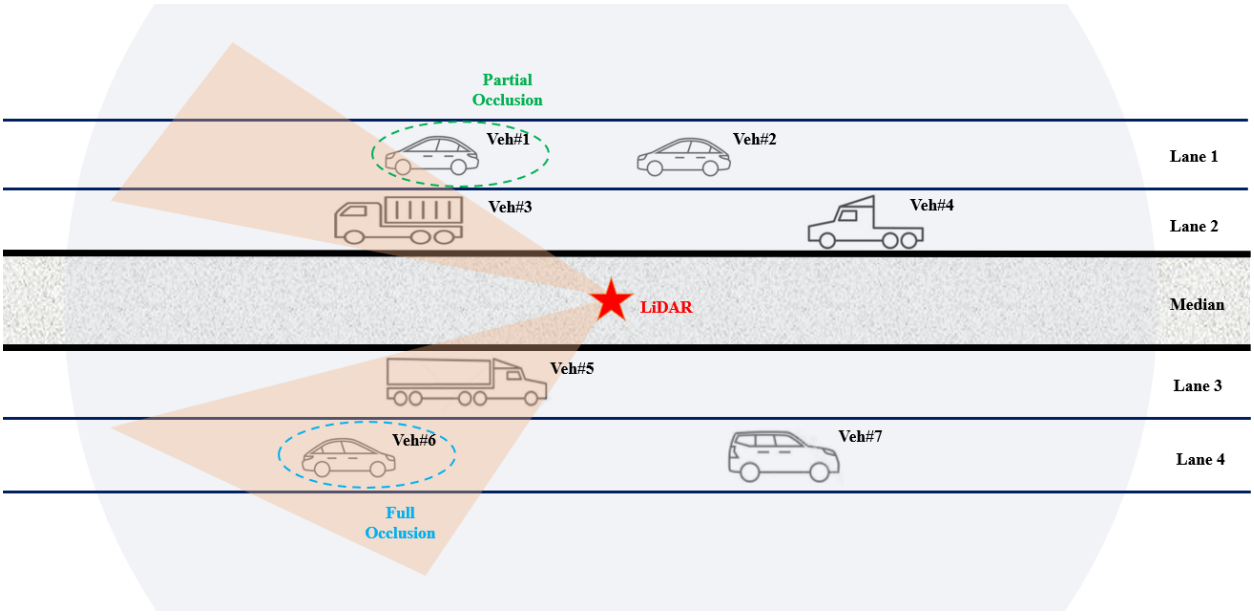

Figure 4-1. Traffic occlusion scenarios demonstration

This research used cuboids of different sizes to represent different types of vehicles. Considering a Cartesian coordinate system with a LiDAR sensor at the origin, the laser beams of the sensor can only scan three different planes among the six planes of a vehicle cuboid, that is, top/left/front planes for vehicles in the first quadrant, top/right/front planes for vehicles in the second quadrant, top/right/back planes for vehicles in the third quadrant, and top/left/back planes for vehicles in the fourth quadrant. In fact, the area of each plane from a vehicle should be equal to or less than the area of the corresponding plane from a designed cuboid. This means that theoretical calculations using cuboids may lead to the worst vehicle occlusion situation. In addition, the partial occlusion is not further distinguished based on the number of blocked laser beams. Therefore, it is acceptable to use a cuboid to represent the shape of a vehicle in simulation evaluation.

For a specific type of LiDAR sensor installed at the roadside, each laser beam's horizontal and vertical directions are known at a specific moment. This means that for a specific traffic scene at a certain moment, it is certain whether a laser beam can shoot at the surface of a vehicle. If so, the exact location of the reflection point can also be determined. During each 360° scan (one data frame), each detected vehicle's properties, the vehicle ID, and distance to the LiDAR sensor, are critical to determining the type of vehicle occlusion. To effectively save this information of each frame, this research proposed a 2D table/matrix structure H (defined by Equation 4-1) based on the configuration of the chosen sensor: each row of the table indicates each elevation angle/channel of the laser beams; each column of the table represents each azimuth interval of the laser beams during 0° to 360° scan; the contents of the table are the vehicle ID(s) with the corresponding 3D distance(s) (defined by Equation 4-2). In this way, the information of vehicles that are measured by the same laser beam at the same azimuth interval is recorded in the same cell of the 2D table.

$$H_{W\times L}=\begin{bmatrix} Q_{(1,1)} & Q_{(1,2)} & \cdots & Q_{(1,n)} & \cdots & Q_{(1,L)} \\ Q_{(2,1)} & Q_{(2,2)} & \cdots & Q_{(2,n)} & \cdots & Q_{(2,L)} \\ \vdots & \vdots & \vdots & \vdots & \vdots & \vdots \\ Q_{(m,1)} & Q_{(m,2)} & \cdots & Q_{(m,n)} & \cdots & Q_{(m,L)} \\ \vdots & \vdots & \vdots & \vdots & \vdots & \vdots \\ Q_{(W,1)} & Q_{(W,2)} & \cdots & Q_{(W,n)} & \cdots & Q_{(W,L)} \end{bmatrix} \quad \text{(Equation 4-1)}$$

$$Q_{(m,n)}=\begin{bmatrix} vehID(1) & distance\ (1) \\ vehID(2) & distance\ (2) \\ \vdots & \vdots \\ vehID(s) & distance\ (s) \end{bmatrix} (m=1,2,\dots W; n=1,2,\dots,L) \quad \text{(Equation 4-2)}$$

Where W is the total number of laser IDs and L is the total number of azimuth intervals within a 360° scan; Q(m,n) includes vehicle ID and distance information of s vehicles that are shot by the laser m at the azimuth angle n.

The number of data points collected from each vehicle during a 360° scan can be calculated– count the number of times (M) that each vehicle ID appears in the 2D table. Suppose there is more than one vehicle information saved in the same cell. The first vehicle occludes all other vehicles (vehicles are sorted by distance from near to far) since a specific laser beam at a specific azimuth cannot be used again after it shoots at the first vehicle. In this way, the number of times (N) that

each occluded vehicle ID appears in the 2D table can also be obtained. Comparing M and N, the vehicle occlusion level can be determined: full detection ($M > N = 0$), partial detection ($M > N > 0$), and non-detection ($M = N$). When two LiDAR sensors are used simultaneously, the detection of each vehicle from two sensors is independent. If a vehicle can be fully detected by at least one sensor, the vehicle is labeled as full detection; if any sensor cannot detect a vehicle, the vehicle is labeled as non-detection; for other detection combinations, the vehicle is labeled as partial detection. The whole process of the vehicle occlusion classification is shown in Figure. 4-2.

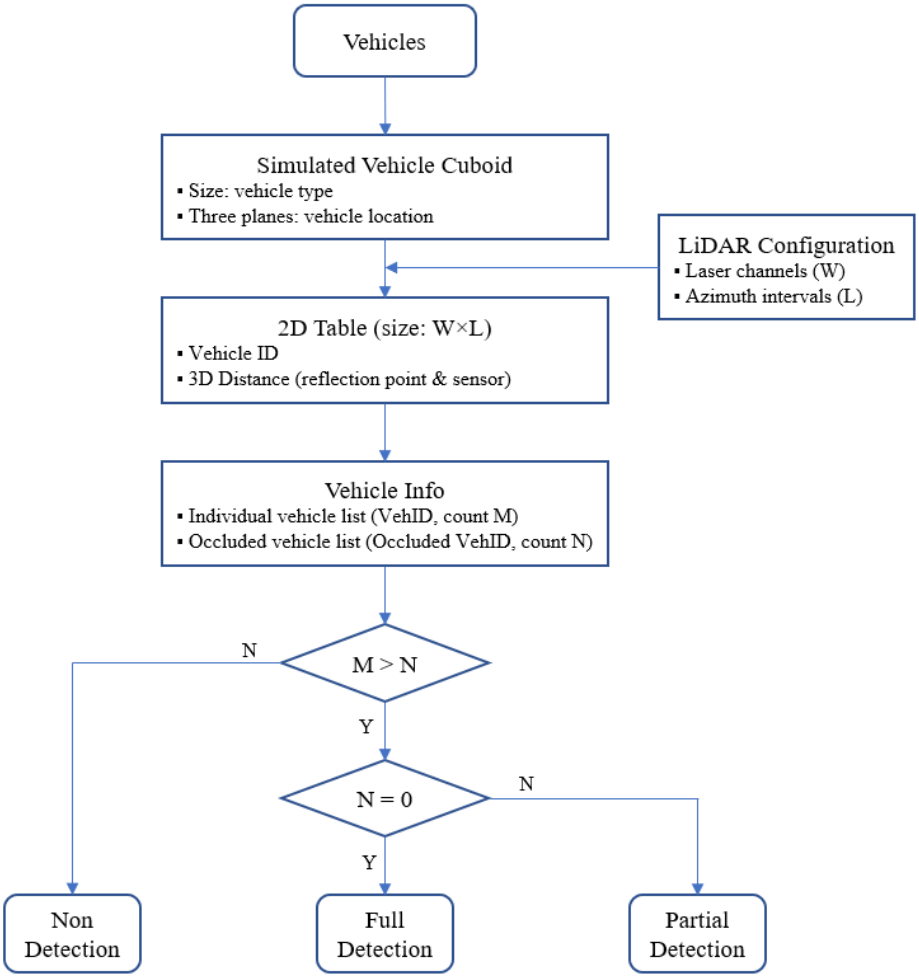

Figure 4-2 Flowchart of vehicle occlusion classification

This research aims to evaluate the impact of occlusion on vehicle detection using roadside LiDAR sensing systems. Due to field data collection and funding constraints, it is almost impossible for us to collect enough traffic flow data with a stable traffic density under various scenarios. Therefore, simulation is a good approach for vehicle occlusion analysis to generate traffic data at different LOS levels. Using the traffic simulation software PTV Vissim, the researchers simulated 30 traffic scenarios along an urban freeway segment to evaluate the impact of occlusion on vehicle detection (as shown in Figure 4-3). The details of the developed simulation environment are introduced as follows:

1) Urban freeway segment

   1000m length; 4 lanes (2 lanes in one direction) with 3.66m width; median with 17.6m width; right-side lateral clearance 2.5m; 2 ramps per mile.
2) FFS(free-flow speed) = 70mph.
3) PHF(peak hour factor) = 0.95; f_p(driver population adjustment factor) = 1.0; E_T(passenger-car equivalents) = 1.5 (type of terrain: level).
4) LiDAR sensor: Puck (VLP-16) and Ultra Puck (VLP-32C), 10Hz rotation frequency.

   Installation: LiDAR 1 is horizontally installed at the median (500m, 0m, 2.4m) location.
   LiDAR 2 is horizontally installed at the median (550m, 0m, 2.4m) location.
   (Zhao et al., 2020)
5) Region of Interest (ROI): [400m, 600m].
6) Level of Service (LOS): A, B, C, D, E.
7) Vehicle cuboid size: Passenger car (L = 4.5m, W = 1.8m, H = 1.6m).

   Truck (L = 16.2m, W = 2.6m, H = 2.6m).
   (Hancock and Wright, 2013)
8) Percentage of trucks: 5%, 10%, 15%, 20%, 25%, 30%.

Based on the settings above, the traffic volumes for five levels of services were calculated individually, considering different truck percentages (chosen the maximum density for each LOS). Then the classification and evaluation methods were applied to the generated simulation traffic data.

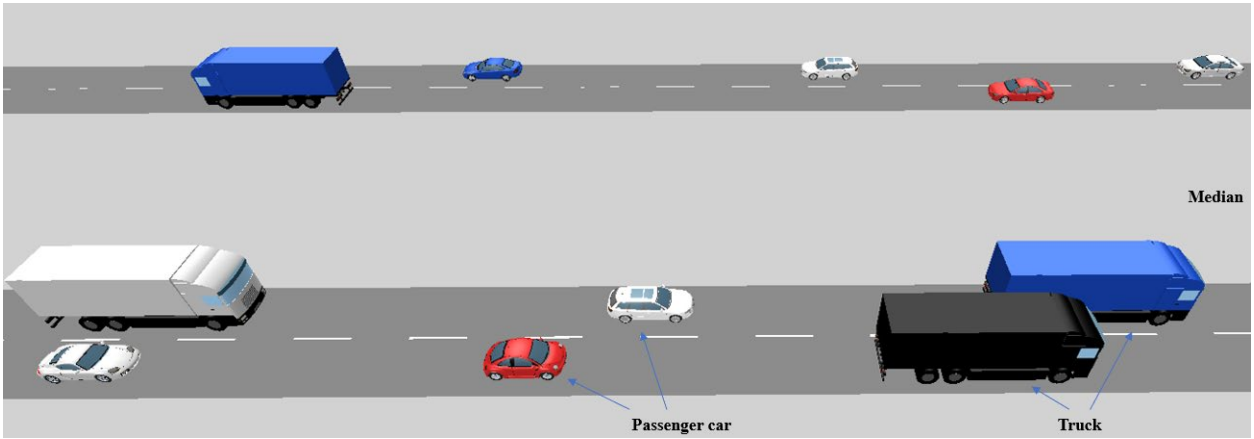

Figure 4-3 Simulation of traffic flow

This project research concluded vehicle occlusion evaluation results, including fully detectable rate, partially detectable rate, undetectable rate, percentage of undetectable vehicles (consecutive for at least 0.5 seconds), and percentage of undetectable vehicles (successive for at least 1 second) of two deployment scenarios - single LiDAR sensor case (use the LiDAR 1 only) and two LiDAR sensors case (use the LiDAR 1 and the LiDAR 2 together). Table 4-1 through Table 4-4 list the occlusion rates calculated for different LOS conditions and truck percentages using single and two Velodyne 16-laser and 32-laser LiDAR sensors.

Based on the tables, the findings are summarized as:

1) In general, for each LOS condition, with the increasing truck percentage, the fully detectable rate decreases, while the partially detectable rate, undetectable rate, percentage of undetectable vehicles (consecutive for at least 0.5 seconds) and percentage of undetectable vehicles (consecutive for at least 1.0 second) rise.

2) There is a significant increase in the undetectable rate from 25% truck to 30% truck.

3) Compared with using a single LiDAR sensor, the undetectable rate, percentage of undetectable vehicles (consecutive for at least 0.5 seconds), and percentage of undetectable vehicles (consecutive for at least 1 second) in the case of using two LiDAR sensors at the same time can be reduced.

4) In general, LiDAR sensors with more laser beams provide better detection performance in avoiding continuous full occlusion than LiDAR sensors with fewer laser beams.

Table 4-1 Vehicle occlusion results using a single 16-laser LiDAR sensor

LOS	Truck Percentage	Volume (veh/h)	Fully Detectable Rate	Partially Detectable Rate	Undetectable Rate	Percentage of undetectable vehicles (consecutive for at least 0.5 second)	Percentage of undetectable vehicles (consecutive for at least 1.0 second)
A	5%	2854	90.2340%	7.6813%	2.0846%	10.0561%	2.8031%
	10%	2783	89.2491%	8.3201%	2.4308%	10.9594%	4.1682%
	15%	2722	89.1081%	8.3496%	2.5424%	11.2785%	5.1800%
	20%	2660	88.3013%	8.8546%	2.8442%	11.8045%	5.7143%
	25%	2600	87.9856%	9.0315%	2.9829%	12.9231%	7.1923%
	30%	2542	86.6332%	9.0544%	4.3124%	13.4249%	7.9237%
B	5%	4673	84.9646%	11.8865%	3.1488%	17.0768%	3.9161%
	10%	4560	83.8670%	12.2553%	3.8777%	17.8289%	6.8202%
	15%	4454	83.2576%	12.6634%	4.0790%	17.9165%	8.4419%
	20%	4352	82.1930%	13.3498%	4.4573%	18.4972%	9.6048%
	25%	4257	81.7750%	13.6773%	4.5477%	18.6751%	10.6413%
	30%	4171	77.5417%	14.5251%	7.9332%	19.0053%	12.3472%
C	5%	6562	80.6021%	14.9750%	4.4229%	22.1355%	6.0500%
	10%	6406	79.3240%	15.8188%	4.8573%	22.4931%	8.5389%
	15%	6252	77.9545%	16.5377%	5.5078%	23.6404%	10.7806%
	20%	6106	77.1733%	17.0313%	5.7954%	24.1893%	12.6761%
	25%	5978	76.3101%	17.4143%	6.2756%	25.4600%	15.0719%
	30%	5847	69.5853%	19.0244%	11.3903%	25.7568%	18.0434%
D	5%	7970	77.2258%	17.7037%	5.0705%	25.8971%	7.0013%
	10%	7782	75.7754%	18.3890%	5.8356%	26.6255%	10.6399%
	15%	7600	74.5211%	19.0208%	6.4581%	27.5395%	13.0395%
	20%	7428	72.9538%	19.8421%	7.2041%	29.0522%	16.2224%
	25%	7262	72.0243%	20.3370%	7.6387%	29.0691%	17.6398%
	30%	7100	64.1991%	21.8813%	13.9196%	31.1268%	22.0704%
E	5%	8890	74.5929%	19.5995%	5.8076%	28.1440%	8.6952%
	10%	8666	73.3388%	20.2545%	6.4067%	28.7214%	11.5740%
	15%	8473	72.0165%	20.9403%	7.0432%	29.4229%	14.6111%
	20%	8287	70.4506%	21.5428%	8.0066%	31.0486%	18.1851%
	25%	8104	69.6553%	22.1009%	8.2437%	31.3302%	19.2127%
	30%	7922	61.0427%	23.6164%	15.3409%	34.5367%	25.0694%

Table 4-2 Vehicle occlusion results using two 16-laser LiDAR sensors

LOS	Truck Percentage	Volume (veh/h)	Fully Detectable Rate	Partially Detectable Rate	Undetectable Rate	Percentage of undetectable vehicles (consecutive for at least 0.5 second)	Percentage of undetectable vehicles (consecutive for at least 1.0 second)
A	5%	2854	95.7003%	3.8036%	0.4961%	2.3476%	0.5256%
	10%	2783	94.8648%	4.5066%	0.6285%	2.9824%	1.0780%
	15%	2722	94.5347%	4.7988%	0.6665%	3.0860%	1.3960%
	20%	2660	93.8358%	5.3936%	0.7706%	3.8346%	1.5414%
	25%	2600	93.5382%	5.6039%	0.8579%	4.7692%	1.8462%
	30%	2542	92.9160%	5.9853%	1.0987%	5.1078%	2.0129%
B	5%	4673	93.2719%	6.1330%	0.8951%	5.0387%	0.7062%
	10%	4560	92.1947%	6.8658%	0.9395%	5.2193%	1.6667%
	15%	4454	91.5231%	7.4732%	1.0037%	5.5231%	1.9533%
	20%	4352	90.5567%	8.3550%	1.0883%	5.8824%	2.6195%
	25%	4257	90.0098%	8.8388%	1.1514%	6.3425%	2.9833%
	30%	4171	87.3523%	10.4161%	2.2317%	7.0184%	3.5887%
C	5%	6562	90.9836%	8.1196%	0.8968%	4.9528%	1.3106%
	10%	6406	89.7662%	9.1458%	1.0880%	5.7602%	1.8889%
	15%	6252	88.5008%	10.1483%	1.3508%	7.3097%	2.6871%
	20%	6106	87.6801%	10.8663%	1.4536%	7.8939%	3.2263%
	25%	5978	86.6376%	11.7800%	1.5824%	8.4978%	3.5296%
	30%	5847	82.6985%	14.1012%	3.2003%	8.8592%	5.1650%
D	5%	7970	89.1568%	9.8213%	1.0219%	5.5332%	1.1794%
	10%	7782	87.6739%	10.9545%	1.3716%	7.3374%	2.3130%
	15%	7600	86.5257%	11.9085%	1.5658%	9.0000%	2.9079%
	20%	7428	85.0208%	13.1449%	1.8343%	9.9219%	3.9580%
	25%	7262	83.9357%	14.0246%	2.0396%	11.0851%	4.6268%
	30%	7100	79.4298%	16.6110%	3.9592%	11.5014%	6.3099%
E	5%	8890	87.6539%	11.1387%	1.2074%	6.4567%	1.5636%
	10%	8666	86.2246%	12.2690%	1.5063%	8.1814%	2.5040%
	15%	8473	85.0009%	13.2268%	1.7724%	9.7132%	3.3636%
	20%	8287	83.5545%	14.3888%	2.0567%	11.5482%	4.5010%
	25%	8104	82.4406%	15.3531%	2.2064%	11.8090%	5.1209%
	30%	7922	77.6677%	17.8311%	4.5012%	12.2696%	6.9679%

Table 4-3. Vehicle occlusion results using a single 32-laser LiDAR sensor

LOS	Truck Percentage	Volume (veh/h)	Fully Detectable Rate	Partially Detectable Rate	Undetectable Rate	Percentage of undetectable vehicles (consecutive for at least 0.5 second)	Percentage of undetectable vehicles (consecutive for at least 1.0 second)
A	5%	2854	89.5316%	8.9771%	1.4912%	7.0427%	2.2775%
	10%	2783	88.5885%	9.3940%	1.9001%	8.4082%	3.8088%
	15%	2722	88.5197%	9.5114%	2.0863%	8.7068%	4.8861%
	20%	2660	87.7750%	9.7820%	2.4430%	9.8872%	5.4887%
	25%	2600	87.4986%	9.8403%	2.6611%	10.8846%	6.7692%
	30%	2542	85.7182%	10.4074%	3.8744%	11.4020%	7.2303%
B	5%	4673	83.8559%	13.9614%	2.1827%	11.8339%	3.4453%
	10%	4560	82.9076%	14.0170%	3.0754%	13.8816%	6.2939%
	15%	4454	82.3527%	14.2976%	3.3497%	14.4140%	7.7458%
	20%	4352	81.3852%	14.7970%	3.8178%	15.1654%	9.1452%
	25%	4257	81.0161%	15.0181%	3.9658%	16.0677%	10.1715%
	30%	4171	76.1623%	16.8048%	7.0329%	16.5838%	11.5080%
C	5%	6562	79.2159%	17.6287%	3.1554%	15.9860%	5.1813%
	10%	6406	78.0488%	18.2016%	3.7496%	17.3431%	7.6335%
	15%	6252	76.7929%	18.7296%	4.4776%	18.6020%	10.0288%
	20%	6106	76.0818%	19.0420%	4.8762%	19.8493%	11.9718%
	25%	5978	75.3554%	19.2134%	5.4312%	22.1918%	14.2021%
	30%	5847	67.8779%	22.1398%	9.9823%	22.2336%	16.4529%
D	5%	7970	75.6025%	20.8043%	3.5932%	19.0715%	5.9849%
	10%	7782	74.3060%	21.2079%	4.4860%	20.8944%	9.4577%
	15%	7600	73.1946%	21.5865%	5.2188%	22.5789%	12.1316%

	20%	7428	71.7535%	22.2188%	6.0277%	24.7173%	15.0108%
	25%	7262	70.9492%	22.4540%	6.5967%	25.3649%	16.8273%
	30%	7100	62.2004%	25.7620%	12.0377%	26.3803%	19.8169%
E	5%	8890	72.8039%	23.0821%	4.1140%	21.4848%	7.3228%
	10%	8666	71.7242%	23.3928%	4.8830%	22.3402%	10.2123%
	15%	8473	70.5221%	23.8652%	5.6127%	24.1237%	13.4899%
	20%	8287	69.1038%	24.2299%	6.6663%	26.4511%	17.0629%
	25%	8104	68.4351%	24.5185%	7.0464%	27.4062%	18.0158%
	30%	7922	58.8528%	28.0341%	13.1131%	29.1972%	22.4565%

Table 4-4. Vehicle occlusion results using two 32-laser LiDAR sensors

LOS	Truck Percentage	Volume (veh/h)	Fully Detectable Rate	Partially Detectable Rate	Undetectable Rate	Percentage of undetectable vehicles (consecutive for at least 0.5 second)	Percentage of undetectable vehicles (consecutive for at least 1.0 second)
A	5%	2854	94.3861%	5.3669%	0.2470%	1.1563%	0.6657%
	10%	2783	93.3842%	6.1583%	0.4575%	2.4434%	1.2576%
	15%	2722	93.0182%	6.3947%	0.5871%	2.9023%	2.0206%
	20%	2660	92.1948%	7.0859%	0.7193%	3.7218%	2.5308%
	25%	2600	92.0119%	7.2536%	0.7346%	4.3077%	3.0077%
	30%	2542	91.5514%	7.4704%	0.9782%	4.8997%	3.3522%
B	5%	4673	90.7566%	8.9338%	0.3095%	1.6906%	1.0700%
	10%	4560	89.5792%	9.6839%	0.7369%	4.0570%	2.2588%
	15%	4454	88.8440%	10.2834%	0.8725%	4.8720%	2.6942%
	20%	4352	87.7951%	11.1322%	1.0727%	5.9513%	3.5156%
	25%	4257	87.2168%	11.5820%	1.2012%	6.2485%	4.0169%
	30%	4171	84.5781%	13.2562%	2.1658%	6.9628%	4.4764%
C	5%	6562	87.4133%	12.1138%	0.4729%	2.5907%	1.5087%
	10%	6406	86.0363%	13.0811%	0.8826%	4.5114%	2.7943%
	15%	6252	84.6542%	14.0982%	1.2476%	6.3980%	3.8388%
	20%	6106	83.5601%	14.9153%	1.5246%	7.8120%	4.7494%
	25%	5978	82.6719%	15.6899%	1.6381%	8.5647%	5.2359%
	30%	5847	78.0415%	18.7606%	3.1979%	9.0212%	5.4729%
D	5%	7970	84.5932%	14.8996%	0.5072%	2.6474%	1.5433%
	10%	7782	83.0910%	15.8850%	1.0240%	5.2043%	3.3410%
	15%	7600	81.7440%	16.7959%	1.4602%	7.6974%	4.6447%
	20%	7428	80.0604%	18.0710%	1.8686%	9.4507%	5.8966%
	25%	7262	78.9441%	18.8193%	2.2365%	10.9749%	6.7475%
	30%	7100	73.1284%	22.5443%	4.3273%	10.5211%	7.4085%
E	5%	8890	82.3654%	16.9942%	0.6404%	3.2508%	1.8560%
	10%	8666	81.0085%	17.8750%	1.1166%	5.5620%	3.3003%
	15%	8473	79.6263%	18.7946%	1.5791%	8.2733%	4.9569%
	20%	8287	77.8137%	20.0387%	2.1476%	10.8966%	6.6490%
	25%	8104	76.7619%	20.7926%	2.4455%	12.0064%	7.7493%
	30%	7922	70.3472%	24.8310%	4.8218%	12.1308%	8.4196%

Validation of Occlusion Results using Field Data

LiDAR data collected from two experimental sites were used to verify the occlusion results from the simulation study. Two 32-channel LiDAR sensors (VLP-32C, 10Hz) were installed at two urban freeway segments located at I-80 (39.51°N, −119.94°W, median) and US395& North McCarran Boulevard (39.55N, −119.79°W, southbound onramp) in Reno, Nevada, as shown in Figure 4-4. For site 1, the LiDAR data on August 15th, 2019 (7 am to 8 am) was used. For site 2, the data on August 28th, 2019 (7 am to 8 am) was used. Since the chosen one-hour period was during morning peak hours and the traffic density changed dynamically, we divided one-hour traffic volumes into 12 5-minute intervals. The traffic density can be obtained by using the

previously developed traffic volume calculation algorithm and manually counting the truck volumes, thus knowing the LOS level.

Figure 4-4 ITS trailer equipped with two LiDAR sensors

In summary, Table 4-5 and Table 4-6 show the details of partial occlusion results using field data at the two sites. By comparing the experimental results with the corresponding simulation results under the same LOS level and similar truck percentage conditions, the average offset of partially detectable rates for the two sites are 0.92% and 0.62%, respectively, which proves the accuracy of the simulation results.

Table 4-5. Validation of partial occlusion results from site 1

Time (mins)	0-5	5-10	10-15	15-20	20-25	25-30	30-35	35-40	40-45	45-50	50-55	55-60
Volume (veh/5mins)	225	212	223	251	273	255	240	264	234	244	223	206
Truck (veh/5mins)	34	18	32	40	38	56	50	30	34	36	26	48
Volume (veh/hr)	2700	2544	2676	3012	3276	3060	2880	3168	2808	2928	2676	2472
Truck (veh/hr)	408	216	384	480	456	672	600	360	408	432	312	576
Truck percentage (%)	**15.11**	**8.49**	**14.35**	**15.94**	**13.92**	**21.96**	**20.83**	**11.36**	**14.53**	**14.75**	**11.66**	**23.30**
Passenger-car equivalent flow rate (pc/hr/ln)	1019	931	1006	1141	1229	1192	1116	1175	1057	1103	994	968
Speed (mph)	70	70	70	70	70	70	70	70	70	70	70	70
Density (pc/mi/ln)	15	13	14	16	18	17	16	17	15	16	14	14

LOS Level	B	B	B	B	B	B	B	B	B	B	B	B
Partially detectable rate (experiment) (%)	14.24	10.28	14.30	14.36	15.31	15.41	16.45	13.95	14.95	15.56	12.74	15.64
Partially detectable rate (simulation) (%)	14.30	14.02	14.30	14.30	14.30	14.80	14.80	14.02	14.30	14.30	14.02	15.02
Absolute offset (%)	0.06	3.74	0.00	0.06	1.01	0.61	1.65	0.07	0.65	1.26	1.28	0.62
Average offset (%)	**0.92**											

Table 4-6. Validation of partial occlusion results from site 2

Time (mins)	0-5	5-10	10-15	15-20	20-25	25-30	30-35	35-40	40-45	45-50	50-55	55-60
Volume (veh/5mins)	526	598	612	677	625	573	493	531	565	514	497	563
Truck (veh/5mins)	22	30	34	26	30	16	20	18	20	20	20	24
Volume (veh/hr)	6312	7176	7344	8124	7500	6876	5916	6372	6780	6168	5964	6756
Truck (veh/hr)	264	360	408	312	360	192	240	216	240	240	240	288
Truck percentage (%)	**4.18**	**5.02**	**5.56**	**3.84**	**4.80**	**2.79**	**4.06**	**3.39**	**3.54**	**3.89**	**4.02**	**4.26**
Passenger-car equivalent flow rate (pc/hr/ln)	1696	1936	1986	2179	2021	1835	1588	1705	1816	1655	1601	1816
Speed (mph)	67	64	63	59	62	65	68	67	66	68	68	66
Density (pc/mi/ln)	25	30	32	37	33	28	23	25	28	24	23	28
LOS Level	C	D	D	E	D	D	C	C	D	C	C	D
Partially detectable rate (experiment) (%)	18.28	20.68	19.86	23.71	21.47	19.68	17.14	17.28	20.32	18.63	18.29	21.12
Partially detectable rate (simulation) (%)	17.63	20.80	20.80	23.08	20.80	20.80	17.63	17.63	20.80	17.63	17.63	20.80
Absolute offset (%)	0.65	0.12	0.94	0.63	0.67	1.12	0.49	0.35	0.48	1.00	0.66	0.32
Average offset (%)	**0.62**											

5. WEATHER CONDITIONS AND ROADSIDE LIDAR DATA

LiDAR sensing could be negatively affected by rain, snow, and wind conditions. Weather-caused impacts can lead to difficulties in data processing and accuracy. In this research, a methodology was developed to automatically identify whether LiDAR data are affected by rain, snow, and wind conditions. The automatic identification can be used to adaptively adjust data processing algorithms/parameters or search required weather-impacted LiDAR data in a LiDAR "data lake." First, the impacts of rain, snow, and wind were characterized using statistical measures. Detection distance offset (DDO) and detection distance offset for wind (DDOW) were calculated and investigated.

As shown in Figure 5-1, the three pictures are one-frame LiDAR point clouds captured from the Veloview (the imaging and analysis software for LiDAR data) in terms of various weather conditions. Figure 5-1(a) intuitively indicates that the ground surface and surrounding objects are quite clear with normal weather conditions; however, rain and snow conditions can lead to many noise points obstructing the ground surface points and surrounding objects, which would be a major impact on the accuracy of the data.

The patterns of rain and snow are similar, they interfere with LiDAR data collection due to raindrops or snowflakes that produce noise on the point clouds as a part of scanning and therefore lasers are blocked. In order to characterize the impact caused by rain and snow conditions, this research developed two methods: statistical analysis and DIFFSUM analysis to analyze the data under rainy and snowy conditions in the same way and then compare with the data under normal conditions to determine the impact of rain and snow on data accuracy.

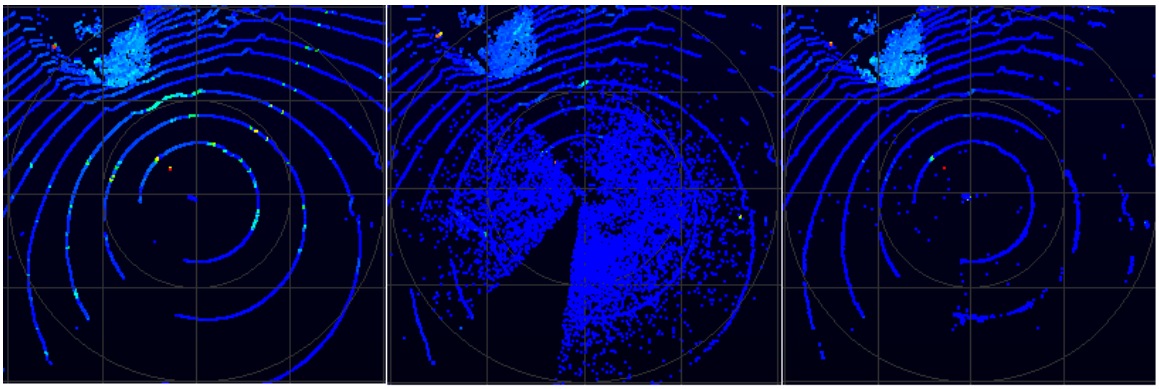

Figure 5-1. LiDAR Point Clouds under Different Weather Conditions

LiDAR measure distances to the object; that means for each measurement, a distance value is returned to each point. Distances are with respect to the sensor's origin. One sensor rotation can be referred to as a single frame; the horizontal azimuth resolution is about 0.2 degrees. The VLP-32 sensor used in this study has 32 laser beams and scanning 360 degrees. That means for one

frame, the sensor will return the distance value of 32 columns (laser beam) and 1800 rows (azimuth). For this study, since the LiDAR sensor rotates 360 degrees for one data frame to objects, different objects in different directions will have different values, according to the distances from the LiDAR and the objects.

Because of the impact of inclement weather, the quality of the data has deteriorated. In order to better address this impact, this study uses the detection distance to calculate the DDO under different frames. As shown in Figure 5-2, at frame *i*, the LiDAR scans the object and returns to distance *Di,* and at frame $_{i+1}$, the LiDAR scans the object and returns to distance D_{i+1}; the difference between D_{i+1} and D_i is the distance offset. This offset calculation method calculates the difference in the distance between a frame and the base frame in an azimuth angle. The DDO can be obtained as follows:

$$D_\delta = D_i - D_{base} \qquad \text{(Equation 5.1)}$$

where

D_δ is the DDO at the δ degree;

δ is the specific azimuth angle value;

D_i is the distance value at the *i* frame;

D_{base} is the distance value at the base frame.

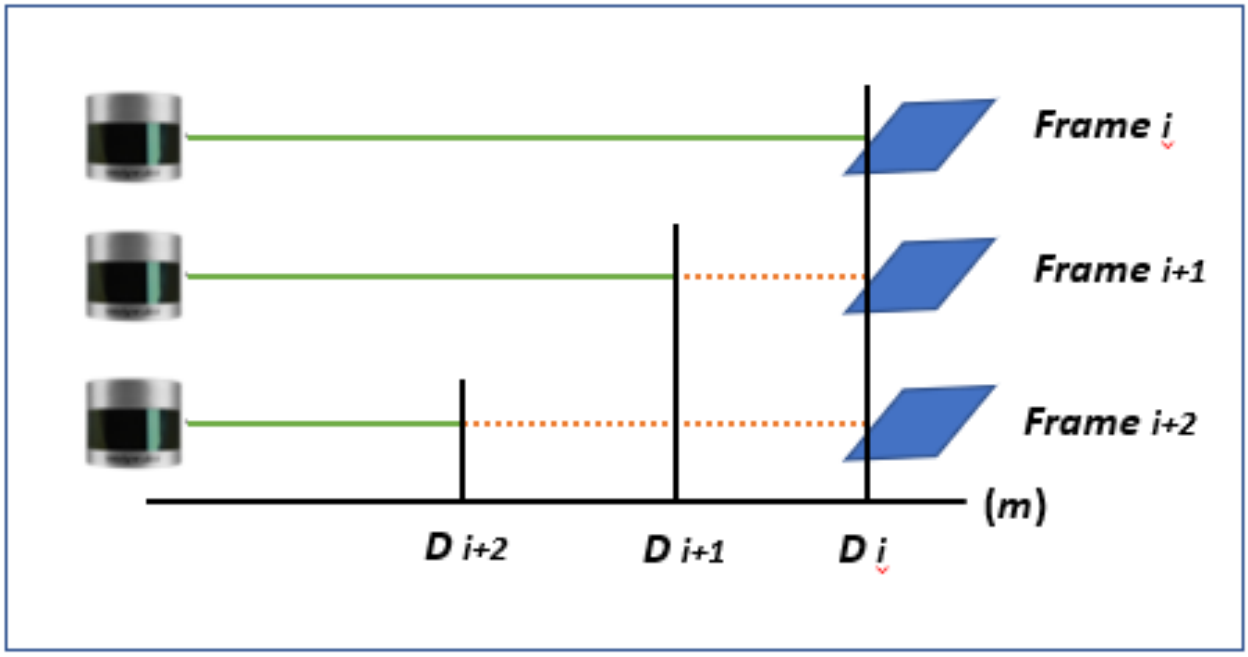

Figure 5-2. Distance Measurement Concept

This study started with percentile analysis and standard deviation to understand the difference of LiDAR data in different weathers. We calculated and compared the 25th, median (50th), and 75th percentile of data offset values for different weathers. The data offsets were differences between the LiDAR-to-point distances in a data frame and the LiDAR-to-point distances in the base frame, and the base frame is usually the first no traffic frame in a period. A one-minute (600 frames) LiDAR dataset for each of the weather conditions was used for the percentile calculation

Figure 5-3 demonstrates the normal weather condition's 25th percentile, median, and 75th percentile offset values at each azimuth angle (60 frames). There was basically no frame-by-frame offset under normal weather conditions.

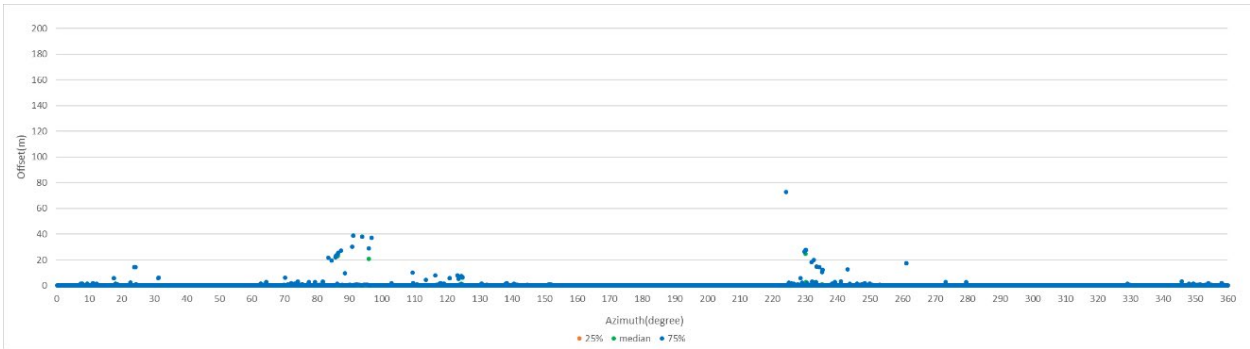

Figure 5-3 Offset Plot of Normal Condition

We also calculated the percentile offsets of continuous 600 frames for snow weather data and rain data. Examples of 25th percentile, median, and 75th percentile offset values are presented in Figure 5-4 and Figure 5-5. More and higher percentile offsets can be observed in the snow and rain data than percentile offsets in the normal weather data.

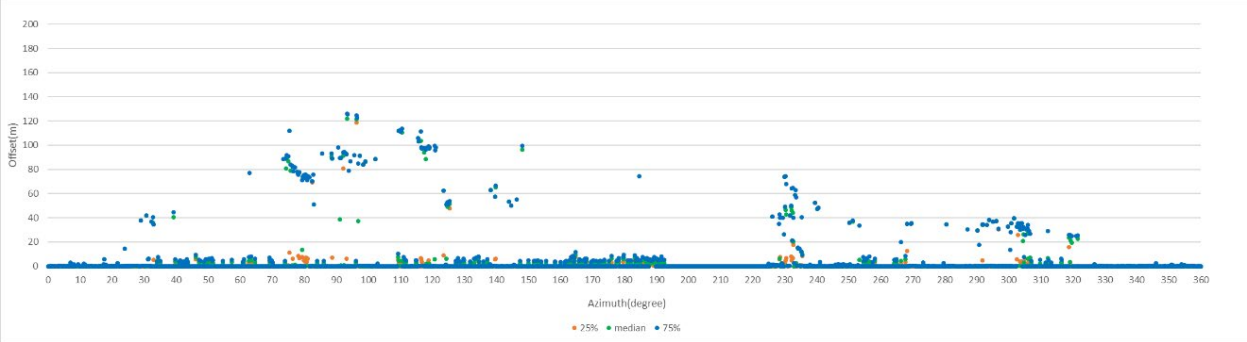

Figure 5-4 Offset Plot of Snowy Condition

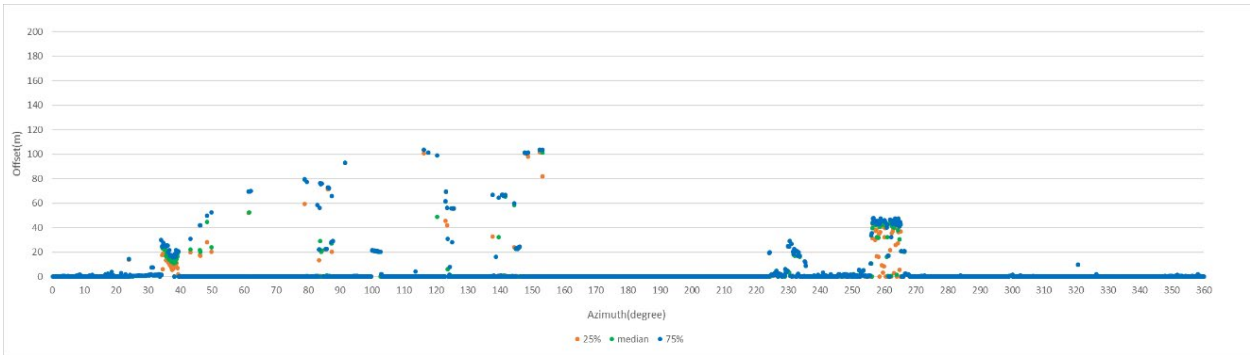

Figure 5-5 Offset Plot of Rainy Condition

Standard Deviation Analysis

Standard deviation measures the amount of variation or dispersion of a set of values. Same as percentile calculation, the standard deviation was calculated with 600 frames of LiDAR data. For each laser beam and each azimuth angle, the offset values of 600 frames were aggregated to calculate the offset standard deviation.

After calculating the sample standard deviations for normal, snowy, and rainy conditions at each azimuth, the results were plotted in Figure 5-6. For the normal weather condition, the standard deviations are slight at most azimuth values, indicating that the dispersion is weak and the offset is not apparent. For the snowy and rainy weather condition, the standard deviations are high at most azimuth angles, meaning that the dispersion is strong.

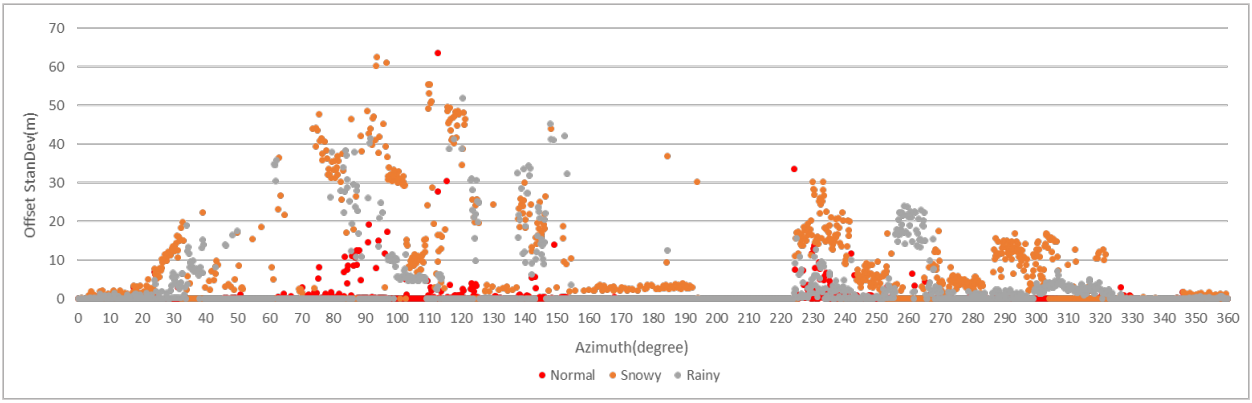

Figure 5-6 Offset Standard Deviation of Normal, Snowy, and Rainy Conditions

Observed through point cloud data, the fluctuations under snowy and rainy weather are obviously greater than in normal weather. However, the standard deviation analysis has 1800 values for 1800 azimuth angles, which is easier to be observed by the chart visualization but not for an automatic identification process. This study then converted those 1800 standard deviations into one index value with the DDO standard deviation. The results are shown in Figure 5-7.

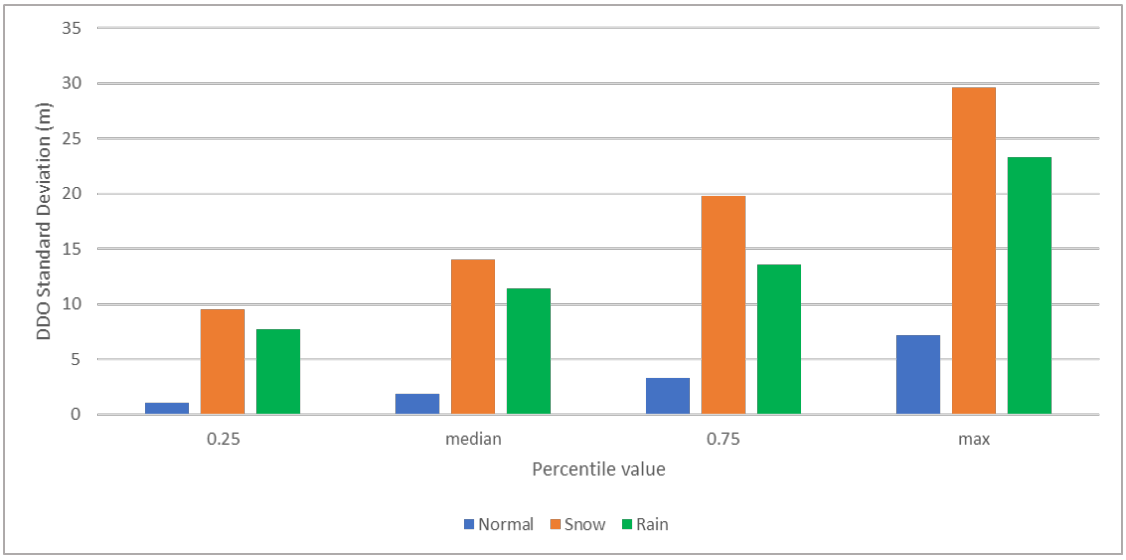

Figure 5-7 Percentile Values of Standard Deviation

DIFFSUM Analysis

According to the analysis results of the percentile offsets and the standard deviations, it can be concluded that the DDO distributions are different and can be used to classify normal, snow, and rainy weather LiDAR data.

To further verify this conclusion, this study developed a DIFFSUM method to calculate the sum of the DDO of all lasers at all azimuth. DIFFSUM is calculated by comparing the absolute cumulative residual of the compared frame and the base frame, serving as a measurement of the similarity between frames. The calculation equation is given as follows:

$$DIFFSUM = \sum_{i=1}^{n_i} \sum_{i=1}^{n_j} |DDO_{i,j}^{frame} - DDO_{i,j}^{base}| \quad \text{(Equation 5-2)}$$

where

$DDO_{i,j}^{frame}$ is the DDO matrix of the frames to be compared;

$DDO_{i,j}^{base}$ is the DDO value of the base frame.

Extract ten frames of DDO from normal, snowy, and rainy weather conditions for DIFFSUM calculation, and then compare the DIFFSUM results of these three weather conditions. In the demonstration of Figure 5-8, the DIFFSUM values in rainy and snowy conditions are significantly higher than values in normal weather conditions, so diffsum can be used as a data index to automatically report the weather condition based on LiDAR data.

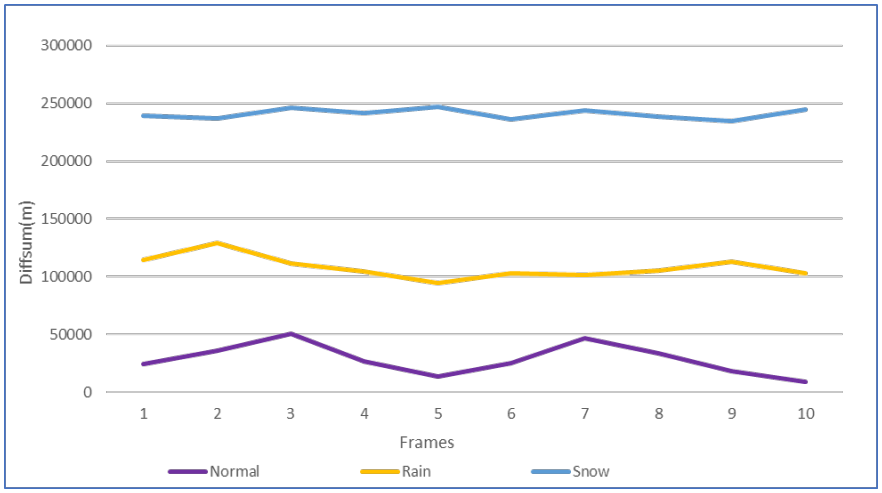

Figure 5-8 DIFFSUM Results of Normal, Snowy, and Rainy Conditions

Analysis of the influence of wind on sensor performance

Unlike snowy or rainy weather, the wind has a different impact on roadside LiDAR sensing. When wind shakes the roadside LiDAR, the vibration of laser beams causes offsets of distance measurements differently from the offsets caused by snow or rain droplets. Wind's impact on roadside LiDAR sensor data can be minor for light wind or when the sensor is mounted on the traffic signal poles. Still, it can be significant with trailer poles, other thin poles, or temporary installation.

The data used to analyze the offset standard deviation of windy and normal weather were collected at the intersection of Coogan Dr & Boulder Hwy, Henderson, NV, on June 14 and June 15, 2020; the selected comparison laser beam is ID1, the elevation angle of the laser ID1 is -1 degree, and the distance to the sensor is 21-96 meters for this intersection. Same analysis method as rain and snow, first, we extracted the continuous 600 frames of LiDAR data, and according to the corresponding to the azimuth angle, extract the distance value of the laser ID 1 in the data. Next, compare the distance of these 600 frames with the base frame to obtain the DDO value between each frame and the base frame at 1800 azimuth angles, then get the offset standard deviation value of all frames at each azimuth angle. Figure 5-9 shows the distribution of standard deviations at all azimuth angles for normal weather and windy weather.

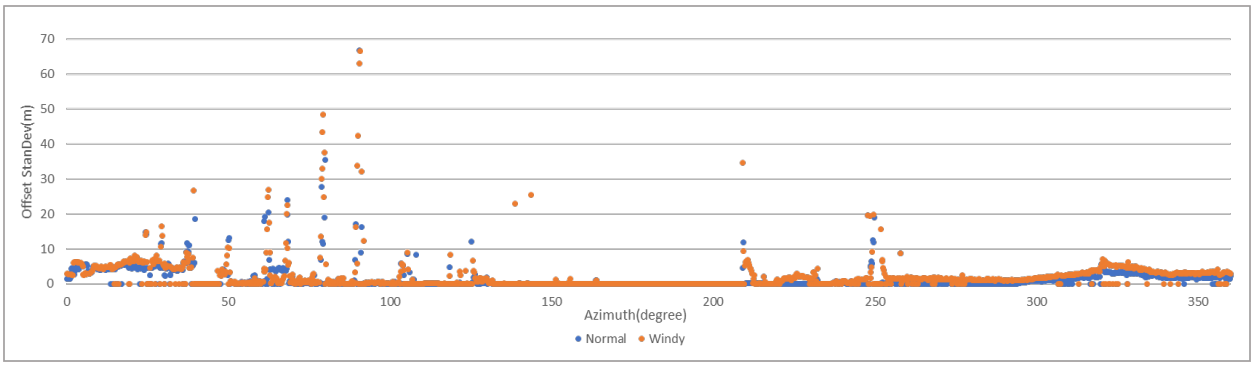

Figure 5-9. Offset Standard Deviation of Normal and Windy Conditions

The offset standard deviations of windy weather and normal weather are not evident in Figure 5-9, although researchers could see significant sensor shaking and point shifting when watching the continuous frames of wind weather LiDAr data. Further analysis found that wind shaking causes different distance measurement offsets on horizontal and vertical surfaces. Wind shaking mainly causes up-and-down vibration of laser beams, which can be considered the vertical angle of laser beams changing frame by frame. The vertical angle change causes major distance offsets when the reflection points are on a horizontal surface. However, this type of vibration does not generate major offsets when the reflection surface is vertical. Laser ID 1 in Figure 5-9 was a laser beam mainly scanning the surrounding objects rather than the road surface, so the offset standard deviation was similar to the deviation of normal weather. Table 5-1 and Figure 5-10 compared wind shaking's impact on distance measurements for horizontal and vertical surfaces.

Also, the offsets caused by wind shaking are positive and negative values around the mean value, almost the distance measurement of normal weather. Therefore, the aggregated offsets showed a similar trend as the trend of normal weather.

Table 5-1 Data Analysis of DDOW between Vertical Surface and Horizontal Surface under Windy Condition

	Min(m)	25th Percentile(m)	Median(m)	75th Percentile(m)	Max(m)	Mean(m)	Range(m)
Horizontal Surface	10.48	10.75	10.97	12.69	14.56	11.47	4.08
Vertical Surface	0.02	0.02	0.04	0.04	0.08	0.04	0.06

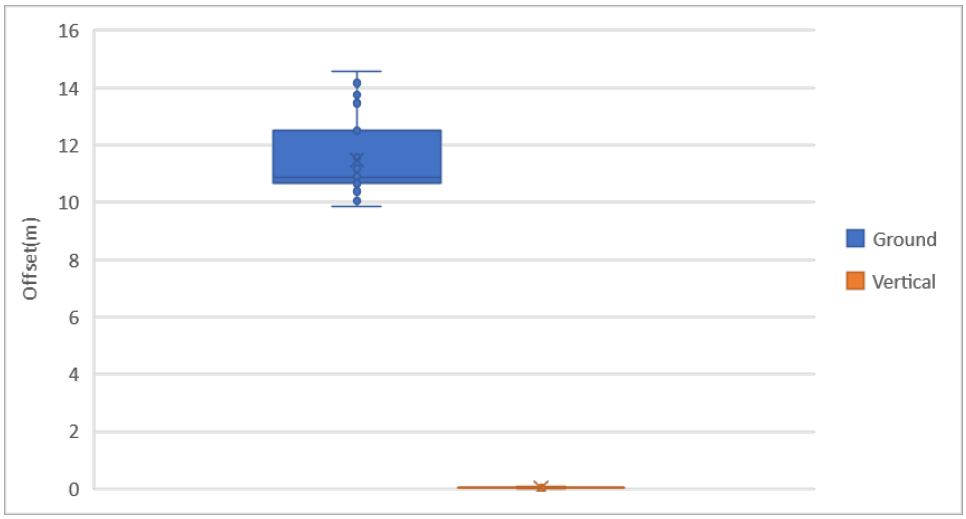

Figure 5-10 Box Chart of DDOW between Vertical Surface and Horizontal Surface under Windy Condition

As the DDO deviation values cannot effectively separate the LiDAR data in normal weather and windy conditions, a new calculation method was applied based on the wind-shaking characteristics to analyze the influence of wind on roadside LiDAR measurement. When calculating the DDOW, the maximum measurement distance of all frames of the same laser ID at the same azimuth angle minuses the minimum measurement distance, as shown in Equation 5-2.

$$Dw_{\delta} = D_{max} - D_{min} \qquad \text{(Equation 5-2)}$$

where

Dwδ is the DDOW at the δ degree;

δ is the specific azimuth value;

Dmax is the maximum distance value for all frames of the same laser ID at the same azimuth angle;

Dbase is the minimum distance value for all frames of the same laser ID at the same azimuth angle.

The validation analysis used the same data collected at Coogan Dr & Boulder Hwy intersection. Three sets of 600 frames of CSV data were selected from June 15, 2020, June 28, 2020, June 20, 2020, and June 14, 2020, for the normal weather condition, 20mph, 40mph, and 60mph wind speeds. The results are shown in Figure 5-11. Obvious DDOW differences exist for the normal weather and different wind speed conditions. This new calculation method allows accurate classification of normal weather and windy conditions.

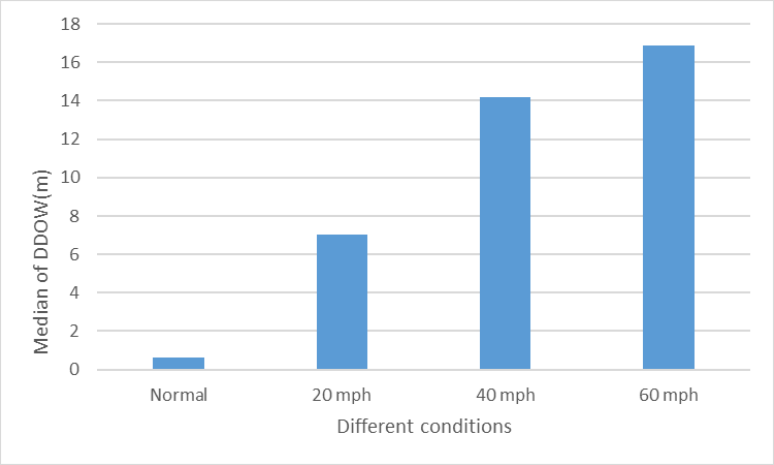

Figure 5-11 Median Value of DDOW for Normal and Three Wind Speed

According to the analysis, the sensor vibration caused by wind mainly impacts laser beams reaching horizontal surfaces but not vertical surfaces. Therefore, classification of wind LiDAR data and normal weather LiDAR data can use the distance measurement offsets of ground surfaces. As an example, we used two sets of sample data from windy and normal weather for comparison. The two sets of sample data are from June 14, 2020 (Windy), June 15, 2020 (Normal) at the Coogan Dr & Boulder Hwy intersection, with the same laser and same azimuth angles to the horizontal surface. Figure 5-12 shows the comparison results: under normal conditions, the distance offset of the horizontal surface was less than 1 meter, and in the windy condition, the distance offset of the horizontal surface was 9-15 meters.

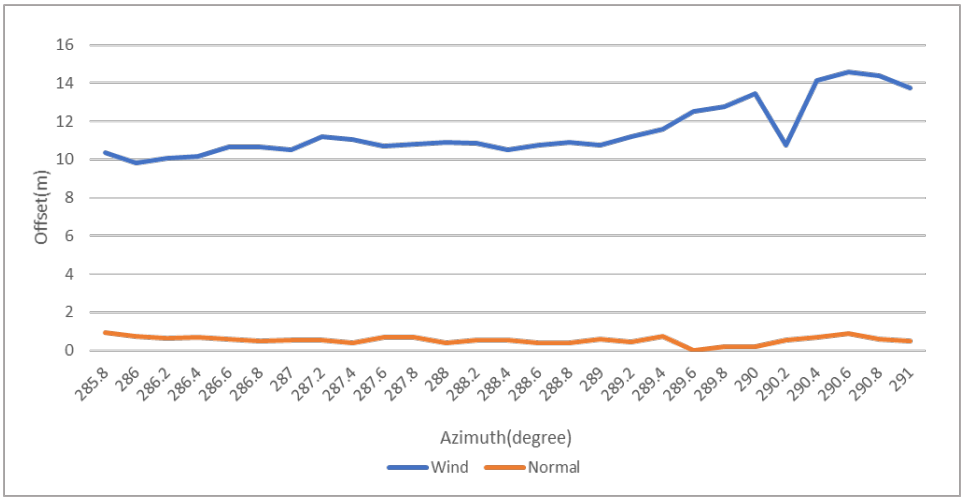

Figure 5-12 DDOW results between Normal and Windy Weather Conditions on Horizontal Surface

Based on all the analysis on characteristics of LiDAR data in different weather conditions, an automatic data monitoring program can be developed with the steps presented in Figure 5-13.

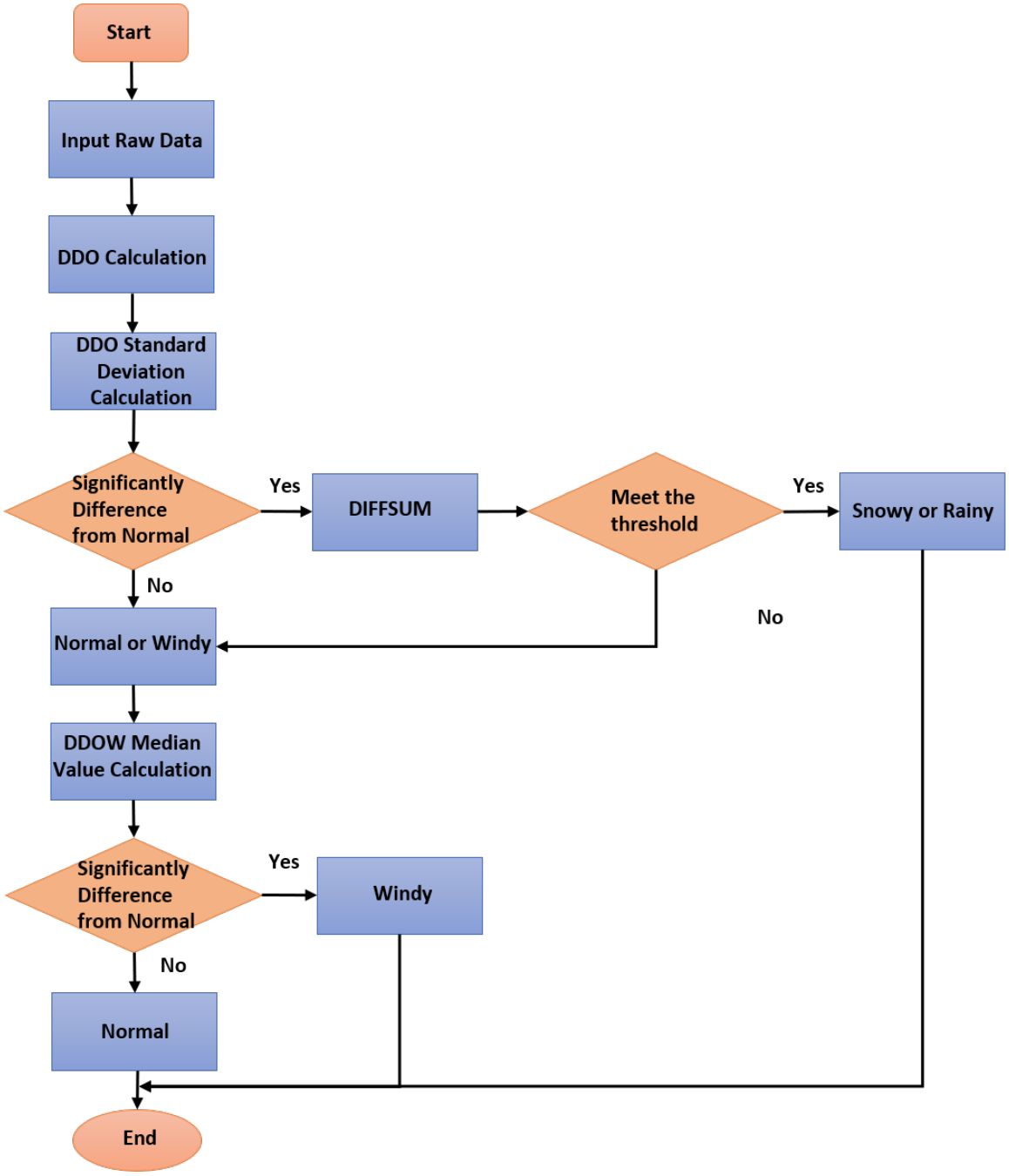

Figure 5-13 Flow Chart of Identification Method

6. IMPROVED LIDAR PROCESSING ALGORITHMS

6.1. Improved Background Filtering

In order to detect interesting target objects such as pedestrians and vehicles efficiently and effectively, the first step in roadside LiDAR data processing is to exclude background information because the background objects within the fixed roadside LiDAR sensor's detection range are almost unchanged. Since the number of data points collected from the target objects using roadside LiDAR sensors is limited compared with a large portion of unrelated backgrounds, it is necessary to filter the background points from the raw LiDAR data so that the processing speed and accuracy of analyzing the remaining small amount of target object points in the following steps.

UNR previously developed a 3D density statistic filtering method for roadside LiDAR data, and the main steps included frame aggregation, points density statistic, threshold learning, and real-time filtering. The 3D space was divided into continuous cubes, and the density threshold of background points in each cube was the key to making decisions about keeping or deleting raw LiDAR data. The computational expense and filtering accuracy of the whole filtering process heavily depended on the length of the cube: the smaller the cube length requires higher computational cost of searching and larger memory, with increased filtering accuracy. The project researchers also proposed a real-time Azimuth-Height background filtering method by comparing the heights between raw LiDAR data and background objects. Three aspects need to be improved are: 1) the height information of each data point cannot be obtained through parsing raw data directly, which means extra computational time is needed; 2) an ideal background frame without target objects is sought; 3) filtering dynamic background objects such as waving bushes is challenging.

This project developed an innovative real-time Azimuth-Channel-Distance background filtering method for roadside LiDAR sensing systems. Saving the 3D coordinate information of 3D point clouds into a 2D table based on azimuth angle (rows) and laser channel properties was the basis of increasing processing speed and reducing computer memory in this new background filtering method. A 2D background table recording the distance information of background objects was generated automatically without manually finding the no-traffic data frames. When parsing the original LiDAR files, distance comparison was executed between raw data points and the corresponding background object points which were shot by the same laser beam and located within the same azimuth interval. Finally, only target points were further parsed and saved in the dataset. In addition, the performance of filtering dynamic background objects was improved by integrating data frames over a period of time so that the small vibration of the dynamic background objects can be captured more precisely. A comprehensive case study showed the effectiveness and efficiency of filtering background objects and keeping target objects at the same time using two types of LiDAR data. The filtered roadside LiDAR data can be further analyzed to generate high-resolution, high-accuracy trajectories of all road users, valuable information for connected/autonomous vehicles, traffic signal design, driver and pedestrian behavior analysis, etc.

LiDAR Sensor

The LiDAR sensor uses an array of a certain number of infra-red lasers paired with infra-red detectors to measure distances to objects. The device is mounted securely within a compact,

weather-resistant housing. The array of laser/detector pairs spins rapidly within its fixed housing to scan the surrounding environment and provide a rich set of 3D point data in real time.

To determine the performance of a LiDAR sensor from a mechanical aspect, the number of channels, vertical field of view (VFOV), and vertical resolution of laser beams are the main factors considered for LiDAR selection. In general, the more laser channels with larger vertical FOV and smaller vertical resolution, the more data points can be collected. Users can customize the rotation frequency of LiDAR sensors: the lower rotation frequency (i.e., slower rotation speed) means more data points can be collected when using the same type of LiDAR. The manufacturers claim the measurement range of LiDAR sensors, but it does not mean all the objects within this range can be identified and tracked successfully. Due to the laser's beam divergence, a single laser firing often hits multiple objects producing multiple returns. The LiDAR sensor analyzes multiple returns and reports either the strongest, last, or both returns [2].

LiDAR Data

In general, LiDAR sensors output two types of packets: data packets and position packets (also called GPS packets). The data packet contains the 3D data measured by the LiDAR sensor as well as the calibrated reflectivity of the surface from which the light pulse was returned. The position packet is used to verify that the LiDAR sensor is receiving valid time updates from a GPS receiver.

One data frame is generated after the sensor completes a 360° scan and the collected point clouds are stored in a packet capture (pcap) file, whose size is determined by the time of data collection and the number and complexity of the surrounding objects. There are two steps for parsing pcap files to obtain raw LiDAR data: 1) obtain azimuth (α), elevation angle (ω), 3D distance (R) between the object and the LiDAR sensor, timestamp, and intensity information; 2) a computation is necessary to convert the spherical coordinates to Cartesian coordinates using the Equation 6-1 to Equation 6-3.

$$X = R \times \cos(\omega) \times \sin(\alpha) \quad \text{(Equation. 6-1)}$$

$$Y = R \times \cos(\omega) \times \cos(\alpha) \quad \text{(Equation. 6-2)}$$

$$Z = R \times \sin(\alpha) \quad \text{(Equation. 6-3)}$$

where $(\mathrm{R}, \omega, \alpha)$ represents the location of the data point in spherical coordinates; (X, Y, Z) represents the location of the data point in Cartesian coordinates.

In other words, the azimuth, elevation angle, and 3D distance properties of each point can be obtained directly from parsing the original LiDAR data file, while information such as 3D locations of each point in Cartesian coordinate systems needs further analysis. In this regard, it is not necessary to calculate and save Cartesian coordinates of all raw data since the data points from the background objects will be deleted after the background filtering process. Therefore, the proposed Azimuth-Channel-Distance background filtering method was developed to classify background and target (non-background) points based on the obtained direct information after parsing the file.

LiDAR data are point clouds. (X, Y, Z) in 3D Cartesian coordinate systems and $(\mathrm{R}, \omega, \alpha)$ in spherical coordinate systems can determine the same location of the data point, respectively. In

general, the 3D Cartesian coordinates of a LiDAR dataset are usually described by a 3D matrix (as shown in Figure 6-1(a)), which may require a large storage memory and a high computational cost for searching using an index table.

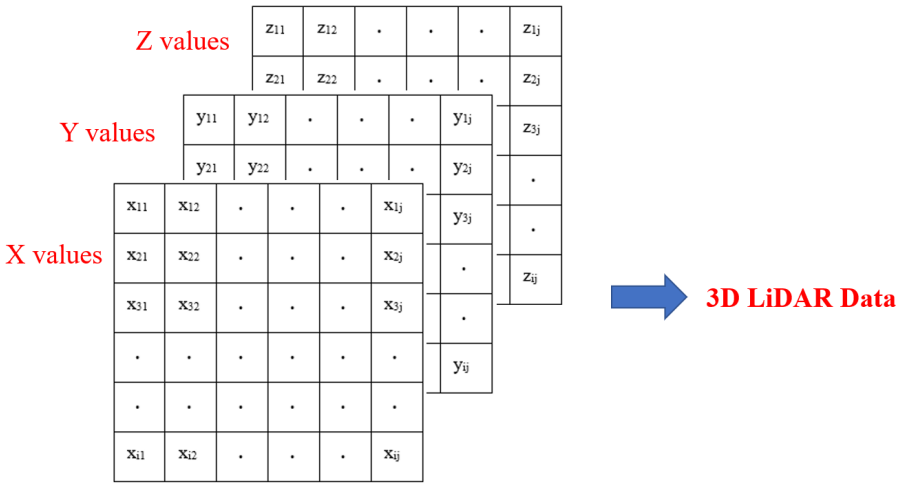

Figure 6-1 A 3D matrix representing LiDAR data

From another perspective of viewing LiDAR data, we proposed a new data structure to describe the locations of 3D point clouds using a 2D table/matrix based on the inherent properties of the LiDAR data: each row of the table represents each azimuth interval of the laser beams during 0° to 360° scan; each column of the table indicates each elevation angle/channel of the laser beams; the content of the table is the 3D distance (LiDAR sensor to an object surface) value of the data point (as shown in Figure 6-2). In this way, the distance values of the data points which were shot by the same laser beam at the same azimuth interval are recorded in the same location/element of the 2D table.

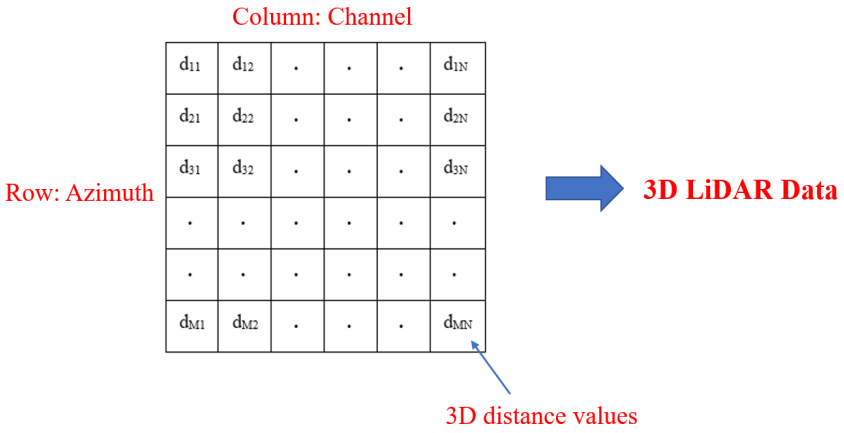

Figure 6-2 A 2D table representing LiDAR data

For a LiDAR sensor installed at the roadside, background objects within the sensor's detection range are almost unchanged. In this research, we only considered road users (e.g., vehicles and pedestrians) as target objects, and all the other objects are background objects. To be more specific, background objects can be classified into two categories: static background objects (e.g., buildings

and ground surfaces) and dynamic background objects (e.g., waving bushes and trees). The goal of background filtering for roadside LiDAR data is to exclude background objects to the maximum while ensuring the completeness of the target objects as much as possible at the same time.

Two main steps of the proposed background filtering algorithm are Background table generation and Real-time background filtering. In generating a background table, the initial background table recognizes the locations of static background objects and then updates the final background table by adding dynamic background information. The proposed background filtering process was performed using the obtained final background table while parsing the original LiDAR file, and only target data were saved. The flowchart of the whole process is demonstrated in Figure 6-3.

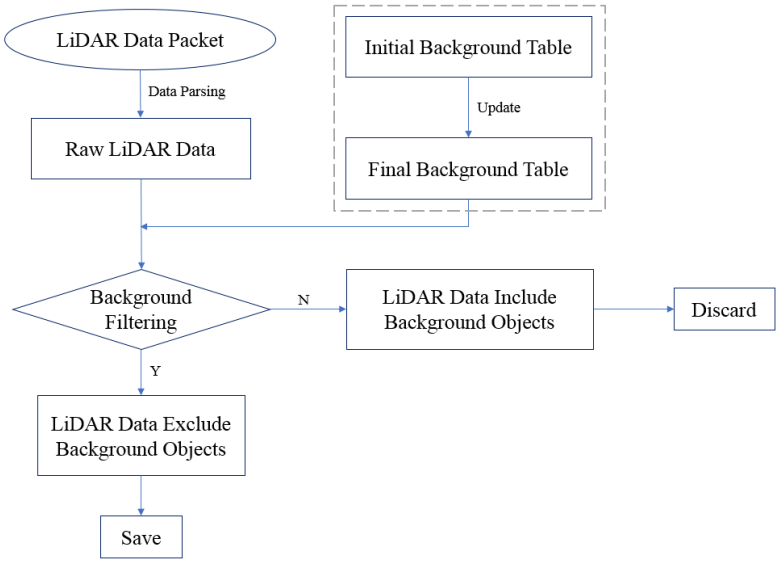

Figure 6-3 Flowchart of the improved background filtering method

Background Table Generation

For a specific LiDAR sensor, a 2D blank background table can be created based on the sensor's configuration and rotation frequency. The proposed initial background table was designed to record a distance threshold in each element to distinguish static background objects and other objects. It needs to be noted that the vertical angle between laser beams does not need to be the same. Different vertical angles between laser beams are common in new LiDAR sensors.

After parsing the LiDAR packet, the 3D distance value of each data point was saved in a 2D table based on the azimuth and channel information. However, even for a static object, the laser beams shot at the object during each rotation cannot be guaranteed to return, thus the number of data points collected in each 360-degree scan was not exactly the same in general. In order to find more accurate locations of the static background objects, we integrated continuous raw LiDAR data frames for analysis. The number of integrated data frames depended on the actual application case. For example, we can determine how many data frames are needed based on the cycle length of the traffic signal at the intersection. In this way, the distance values saved in the same element of the 2D table were from the objects which were located within the same azimuth interval and shot by the same laser beam. Figure 6-4 show the distribution of collected distance values of a building

(static background object) from two representative elements. The x-axis and y-axis in the plot represent frame number and distance value, respectively. In Figure 6-4(a), without any occlusion, the collected distance values of a building corner were varied within a very small interval (about 10cm). In Figure 6-4 (b), the building edge was blocked by passing or stopped vehicles, so the locations of the collected data points from the vehicles were closer to the LiDAR sensor compared with the building edge since the laser beams cannot penetrate the vehicles and continue to shoot at the building edge.

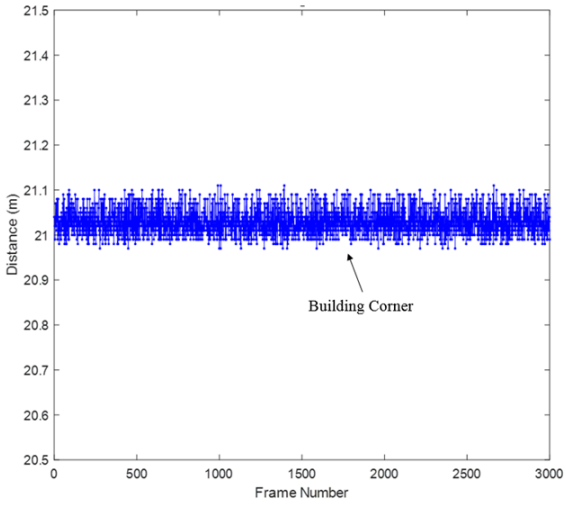

Fig. 4(a) Building corner.

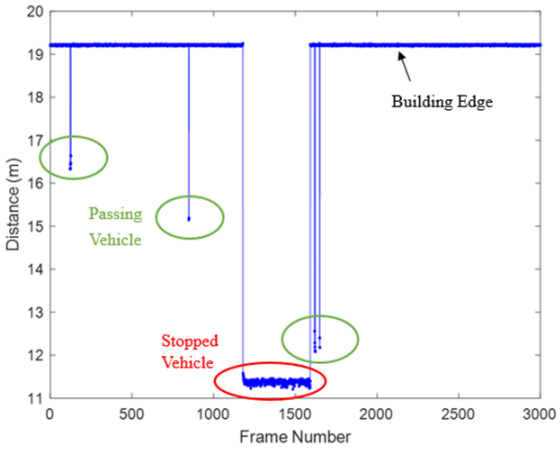

Fig. 4(b) Building edge with passing/stopped vehicles.

Figure 6-4 Examples of background distance measurement

To find the distance threshold in each table cell, firstly, we segmented all the data in each element based on the distance values and sorted the obtained groups from the minimal distance to the maximal distance. If the number of data points in the last group (i.e., the farthest one from the LiDAR sensor) is greater than a point threshold which was defined as a large percentage of the total number of data frames for integration, then this group of data points was considered to have been collected from static background objects. Secondly, the distance threshold was chosen as the minimal distance value of that group. The reasons for this judgment are: 1) the number of data points collected from static background objects during a certain period of time should be far greater than the number of points collected from target objects; 2) the location of the static background objects should be the farthest from the LiDAR sensor; 3) choosing the minimal distance of the selected group as the threshold can filter this group of data itself. Using this criterion, the minimal distance value of the qualified farthest group in each element was used to update the blank background table; thus, an initial background table was generated. For example, in Figure 6-4(b) case, the farthest group was made up of the building edge (2,587 data points were collected from 3,000 frames), and the distance threshold in the corresponding element was 19.18 meters from the LiDAR sensor.

Dynamic Background Identification

Using the obtained initial background table, static background objects can be excluded from the selected data frames of integration (the filtering criteria will be introduced in Section 3.3). The

remaining LiDAR data included target objects, dynamic background objects, and some noise points. The purpose of processing the remaining data is to find the location of dynamic background objects and update the initial background table by adding dynamic background knowledge. Due to the properties and motion patterns of dynamic background objects, the variation of measured distance of dynamic background objects is much larger than that of static background objects. Figures 6-5(a) and 6-5(b) show the measure distances of dense and sparse bushes from the LiDAR sensor, respectively. According to Figure 6-5(b), the largest distance difference from the same part of the low-density bushes can be up to nearly 0.4 meters, which was caused by heavy wind. Therefore, it is not accurate to use only one data frame to capture the location of dynamic background objects in practice.

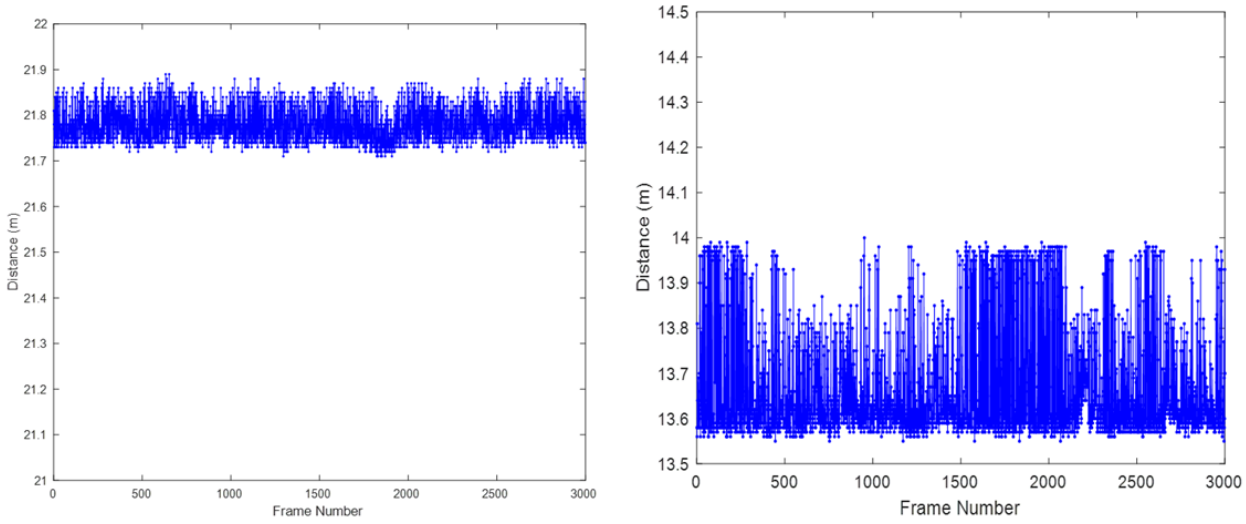

(a) High-density Bushes (b) Low-density Bushes

Figure 6-5 Demonstration of two different dynamic background measurements

To identify dynamic background objects completely and accurately, we applied a density-based clustering method, density-based spatial clustering of applications with noise (DBSCAN) [2], to the same set of aggregated LiDAR data frames (collected in a period of time) in which static background points have been excluded. One advantage of DBSCAN is this method does not need to predefine the number of clusters, which is especially useful for transportation application since it is almost impossible to predict the number of target objects. Target objects (e.g., pedestrians and vehicles) move in general, while dynamic background objects (e.g., bushes) are almost stationary, even though they may have some shaking movements. Based on the distribution of clustered data points in 3D space, three features were extracted from the obtained clusters to distinguish dynamic background objects and target objects using Extra Trees (Extremely Randomized Trees) classifiers. This classifier is an ensemble deep learning method based on Decision Trees [3] and considered as a variant of Random Forest [4]. Similar to Random Forest, they all build multiple trees and split nodes using subsets of features. But the Extra Trees method does not bootstrap observations and nodes are split randomly (not the best split), which lead to lower computational cost and variance of the model [5].

After classification, the minimal distance of each dynamic background object cluster was used to update the distance threshold in the corresponding element of the initial background table, thus a final background table including the distance information of both static and dynamic background objects was generated. In summary, the whole flowchart of developing background table is demonstrated in Figure 6-6.

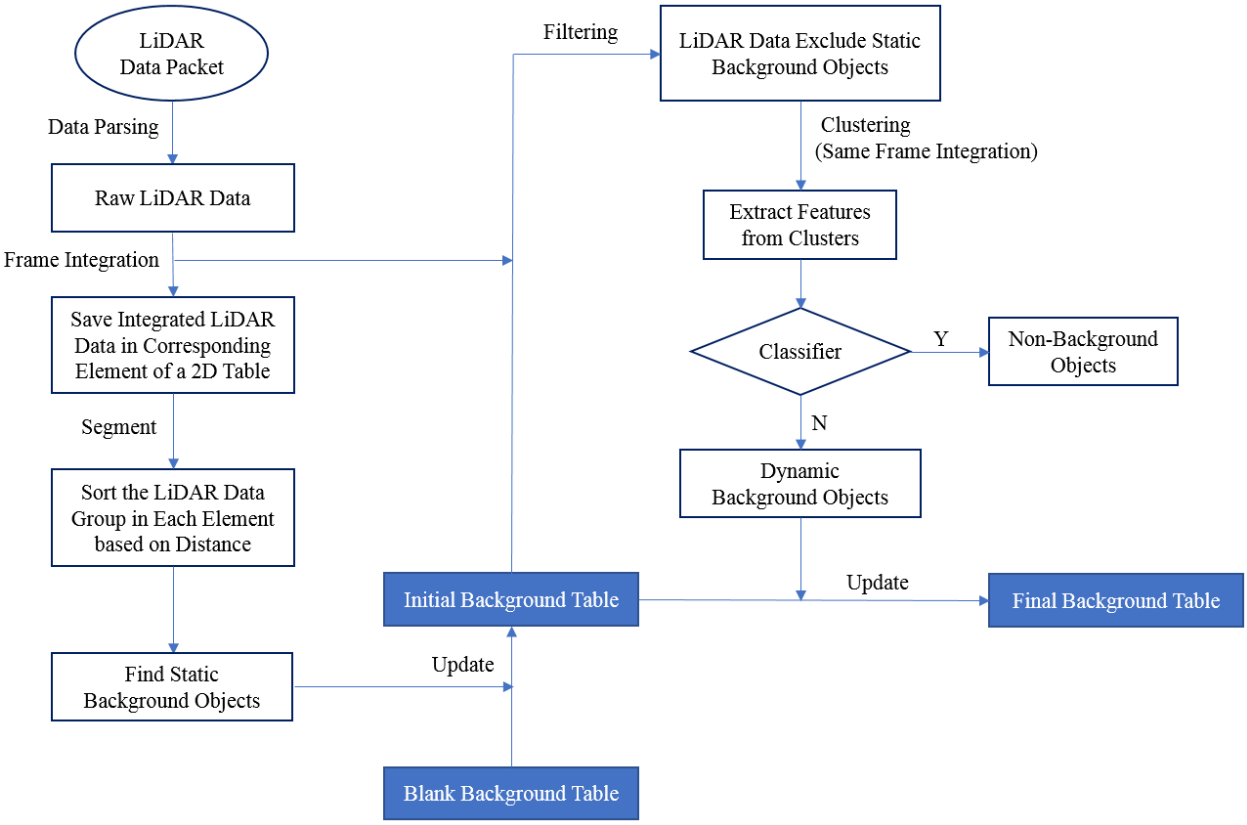

Figure 6-6 Flowchart of background table generation

Evaluation of Filtering Accuracy

In order to evaluate the performance of the proposed background filtering method, we chose some data frames in which vehicle and pedestrian target objects were located at different distances from the LiDAR sensor. Due to the mechanical characteristic and working principle of the LiDAR sensor, the density of point clouds is decreased as the distance from the LiDAR sensor increases. How many data points can be collected from the target object depends on several factors such as the distance between the sensor and the object, the size of the object, sensor's installation, occlusion, etc. Our goal is to filter the background points to the maximum and keep the same amount of target points at the same time. If the target points are excluded, they cannot be recovered, while a small amount of remaining background points (noise) can be further deleted in the following procedure. Table 6-1 lists the background filtering rate and target retention rate for target objects at different distances using the data collected by VLP-16 and VLP-32C LiDAR sensors. In general, most of the background points had been filtered successfully and the target points were

well maintained within the valid detection ranges. Besides, we found that it is challenging to filter the background objects and keep the target objects at the same time if they are located very close to each other.

Table 6-1. Filtering Results Evaluation for Target Objects at Different Distances

Location	Target object	Background points before/after	Background filtering rate	Target points before/after	Target retention rate
Site 1 (VLP-16)	Vehicle 1 8.5m	27614/69	99.75%	452/449	99.34%
	Vehicle 2 17.9m	26999/73	99.73%	166/160	96.39%
	Vehicle 3 45.7m	27352/63	99.77%	69/62	89.86%
	Pedestrian 1 6.4m	27558/51	99.81%	41/41	100.00%
	Pedestrian 2 15.7m	27001/60	99.78%	20/19	95.00%
	Pedestrian 3 25.6m	27235/65	99.76%	6/5	83.33%
Site 2 (VLP-32C)	Vehicle 1 7.5m	55190/134	99.76%	427/425	99.53%
	Vehicle 2 29.5m	56001/145	99.74%	161/158	98.14%
	Vehicle 3 75.5m	55581/138	99.75%	15/13	86.67%
	Pedestrian 1 4.2m	56568/155	99.73%	55/55	100.00%
	Pedestrian 2 14.8m	56005/146	99.74%	37/37	100.00%
	Pedestrian 3 35.3m	55894/131	99.77%	17/15	88.24%

Evaluation of Filtering Speed

Since the roadside LiDAR sensing system is designed to detect and track road users in real-time, fast processing speed is an important factor for deployment. To examine the speed of data parsing with the judgment of classifying background points and target points, the authors implemented the proposed algorithm in Matlab and recorded the computational time on a regular Dell desktop (Intel Core i7-4790 CPU (3.60 GHz) and 16 GB of RAM). It took only about 0.65 millisecond and 0.90 millisecond to process one single data frame collected by 16-channel and 32-channel LiDAR sensors in average. With the 10Hz rotation frequency (0.1 second/frame) of the sensors, such a background filtering speed lays a solid foundation for the following procedure like object clustering and tracking. In Wu's paper [9], with the same computer configuration, the processing speed of filtering 16-channel LiDAR data is about 100 millisecond per frame. Therefore, our new background filtering method using 16-channel LiDAR data has increased the computational speed by approximately 150 times, which makes it possible to use in practice. The main contributor for this fast computation is that the unrelated background points from the raw data do not need to be further analyzed after data parsing.

6.2. Improved Object Classification

Among traffic study and performance evaluation using offline trajectory data, one challenge is how to accurately classify all road users as far as possible. In general, large-sized road users (e.g., vehicles) are relatively easy to be identified than small-sized road users (e.g., pedestrians and cyclists) because the moving direction and appearance of small-sized road users are constantly changing. In addition, road users who are located near the sensor and are not occluded by other objects are more likely to be classified into correct category since the information collected by sensors is more comprehensive and reliable.

In terms of on-board sensing systems, the classification can be achieved by LiDAR-Vision or LiDAR standalone sensing systems. In the classic LiDAR-Vision on-board sensing systems, two sensors are working together in a centralized or a decentralized way. The centralized way means the sensor fusion process occurs at the feature level, that is, features extracted from LiDAR and video data are combined in a single vector for posterior classification using a single classifier [9]. The decentralized way means two classifiers are trained with LiDAR and video data individually, and then the final classification results are combined through a set of fusion methods [10]. For the standalone LiDAR on-board sensing systems, the major approach to classifying different types of road users is feature-based machine learning classification. Most of the features used in previous studies are related to the shape or dimension profile (e.g., length, height, symmetry) of different parts of the object [11,12], and popular classifiers include Support Vector Machine (SVM), Naïve Bayes (NB), K-nearest neighbor classification (KNN), Random Forest (RF), artificial neural network (ANN), etc.

In this project, a feature-based offline classification method combined with historical trajectory information was developed to classify vehicle, pedestrian, cyclist, and wheelchair using roadside LiDAR sensors (as shown in Figure 6-7). Taking into account the information provided by historical trajectories, the impact of occlusion on the classification accuracy can be reduced to some extent. Through extracting effective features and training four classifiers using field data, we found that the dimension characteristic, especially the 2D length feature, can greatly improve the classification accuracy if the entire trajectory is considered. The AdaBoost and RUSBoost methods were recommended for classifying imbalanced datasets.

vehicle **pedestrian** **cyclist** **wheelchair**

Figure 6-7. Examples of different road user clusters collected by 32-laser roadside LiDAR sensor

Feature Selection

For supervised classification tasks, feature selection is a critical step in training classifiers. Good features should be able to effectively distinguish different classes and can be easily obtained from datasets. LiDAR sensors are good at accurately capturing the surface shape of objects, therefore, we extracted seven features (five of them are related to dimensionality) from the point cloud of clusters for vehicle/pedestrian/cyclist/wheelchair classification.

- Feature 1 (3D distance): the average distance value of each cluster from LiDAR sensors.
- Feature 2 (Point count): the total number of data points in each cluster.
- Feature 3 (Direction): the direction of the clustered points' distribution. With the least-square linear regression method, a linear function can be generated to describe the main distribution direction of each cluster.
- Feature 4 (Height): The difference between the maximal and minimal height (Z value) of each cluster.
- Feature 5 (Height variance): the variance of the maximal height of each sliced cluster along the 2D length direction, as shown in Figure 6-12 (right).
- Feature 6 (2D length): the longer side of the bounding box (e.g., the minimum rectangle that covers all clustered points based on the minimal and maximal values projected on XY plane) of each cluster, as shown in Figure 6-12 (left).
- Feature 7 (2D area): the 2D area of the bounding box of each cluster.

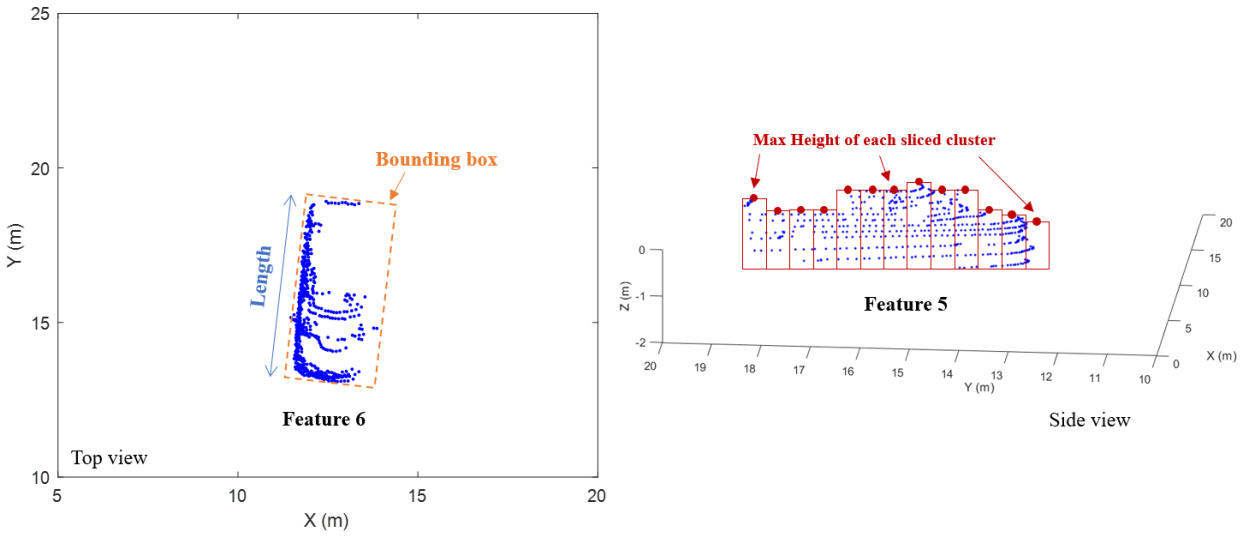

Figure 6-8. Features extracted from clusters

Classification Methods

In this study, four supervised classification methods were selected, namely artificial neural network (ANN), random forest (RF), adaptive boosting (AdaBoost), and random undersampling boosting (RUSBoost) for vehicle/pedestrian/cyclist/wheelchair classification. This section will briefly introduce those methods.

Artificial Neural Network (ANN)

ANN is a multilayer feedforward neural network composed of an input layer, a hidden layer, an output layer, and neurons in each layer. Input data are fed into the input layer. The activity of each hidden layer is determined by the inputs and the weights that connect the input layer and hidden layer. A similar process takes place between the hidden layer and the output layer, and the transmission from one neuron in one layer to another neuron in the next layer is independent. The output layer produces the estimated outcomes. The comparison information (error) between the target outputs and the estimated outputs is given back to the input layer as a guidance to adjust the weights in the next training round. Through each iteration, the neural network gradually learns the inner relationship between the input and the output by adjusting the weights for each neuron in each layer to reach the best accuracy. When the minimum error is reached, or the number of iterations is beyond a predefined range, the training process is terminated with fixed weights.

Random Forest (RF)

Random forest is an ensemble learning method for classification, regression, and other tasks that operates by constructing a multitude of decision trees at training time. For classification tasks, each individual decision tree in the random forest spits out a class prediction and the class with the most votes become the output of the random forest. Essentially, random forest enables a large number of weak or weakly-correlated classifiers to form a strong classifier, and generally outperforms decision trees, but its accuracy is lower than gradient boosted trees. In addition, the computational cost of running random forest on large datasets is low.

Adaptive Boosting (AdaBoost)

AdaBoost is an ensemble learning method which was initially created to increase the efficiency of binary classifiers. AdaBoost uses an iterative approach to learn from the mistakes of weak classifiers, increase weights for misclassified observations and reduce the weights for correctly classified observations, and turn weak classifiers into strong ones. In terms of AdaBoost for multiclass classification, instead of weighted classification error, weighted pseudo-loss is used as a measure of the classification accuracy from any learner in an ensemble. AdaBoost is fast, simple, and easy to implement and has the flexibility to be combined with other machine learning algorithms, but it is sensitive to noisy data and outliers.

Random Undersampling Boosting (RUSBoost)

Random undersampling boosting is especially effective at classifying imbalanced data, meaning some classes in the training data have much fewer members than others (Seiffert et al., 2013). The algorithm takes N observations in the class with the fewest observations in the training data, as the basic unit for sampling. Classes with more observations are under sampled by taking only N observations of every class. In other words, if there are K classes, for each weak learner in the ensemble, RUSBoost takes a subset of the data with N observations from each of the K classes.

The boosting procedure follows the procedure in AdaBoost for multiclass classification for reweighting and constructing the ensemble.

Classification considering historical trajectory information

This project proposed to update significant features according to the properties of continuous tracking trajectories. To be more specific, during the feature extraction step, the feature 6 (2D length) of each sample in both training set and testing set was updated to the maximum value of all detected lengths within the corresponding trajectory. Then the same training and testing process was applied.

Using the modified features as input, the recalls of four types of road users using the same classification methods are listed in Table 6-2, that shows that the recall rates of cyclist and wheelchair were all above 99% when using AdaBoost and RUSBoost classifiers, which was a huge improvement compared with the previous results in Table 3(a). This indicated the effectiveness of updating features by considering historical trajectory information to increase classification accuracy.

Table 6-2. Classification recall rates considering historical trajectory information

Trajectory Length	Classifier	Vehicle Recall	Pedestrian Recall	Cyclist Recall	Wheelchair Recall
Greater than 20 frames (2.0s)	ANN	99.79% (+0.24%)	97.89% (+0.38%)	44.56% (+20.98%)	74.96% (+1.27%)
	RF	100% (+0.14%)	99.85% (+1.85%)	94.82% (+54.66%)	98.02% (+16.83%)
	AdaBoost	100% (+0.24%)	99.96% (+2.56%)	100% (+52.33%)	99.86% (+17.68%)
	RUSBoost	100% (+0.21%)	100% (+8.44%)	99.74% (+33.68%)	99.43% (+17.11%)

Note: The value in the parentheses represents the increased recall value compared to Table 3(a).

In classifying four types of road users, distinguishing small-sized road users (e.g., wheelchair, pedestrian and cyclist) is the most challenging task. Due to the inherent characteristic of LiDAR sensors, as the distance between the object and the sensor increases, the density of point cloud drops sharply. In addition, the moving direction of road user relative to the scanning direction of laser beams also affects the detection quality: perpendicular movement can generally collect more data points from objects than parallel movement and more data points mean a fine description of objects. It is not difficult to find that the wheel part of the wheelchair cluster was not fully detected so that the main shape/dimension difference between the wheelchair and the cyclist/pedestrian is not obvious. Through checking the raw LiDAR stream, the entire movement routes of these two wheelchairs were not well covered in the detection range of the LiDAR sensor. This may be the main reason for the misclassification of these wheelchairs, especially at a far distance.

7. DATA QUALITY EVALUATION AND COMPARISON WITH VIDEO SENSING

This section compares the trajectory outputs from one LiDAR sensor and four cameras at the same intersection during the same time (Figure 7-1), in terms of general location accuracy, volume counting accuracy, detection range, and speed. Both the frequency of LiDAR-based and Vision-based trajectory data is 10 Hz. Trajectories were demonstrated in Figure 7-2 Since the studied size of the intersection is too large that the camera cannot cover the separate right-turn lanes, the right-turn vehicles are not considered in this study.

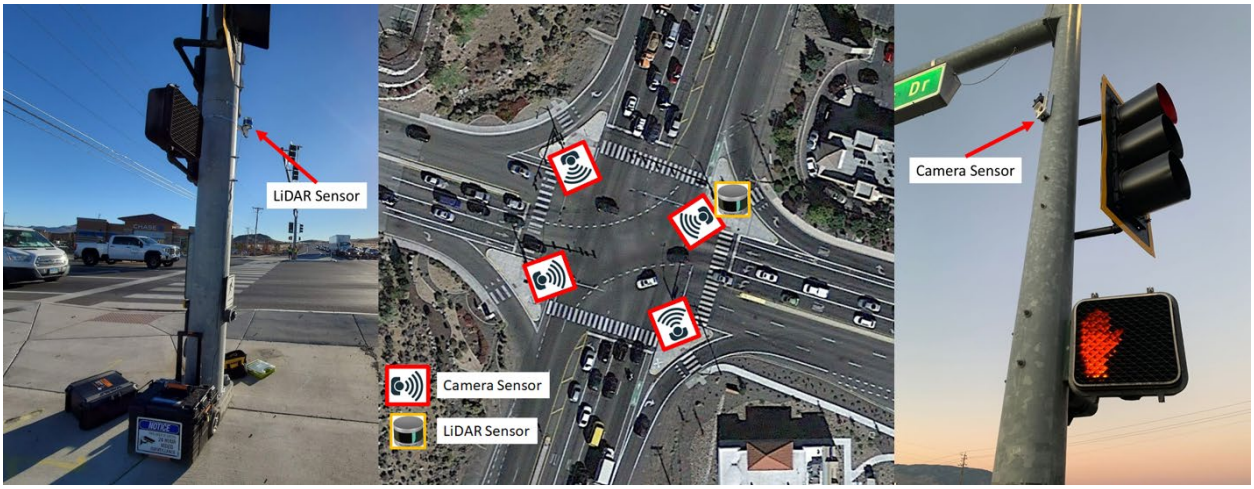

Figure 7-1 LiDAR and camera sensors installed at the same intersection (Pyramid Way and Los Altos Road, Sparks, NV)

Figure 7-2 shows two 30-min data from 12:00 am to 12:30 pm on December 23 (left) and from 4:00 am to 4:30 am on December 24th (right), the pink points represent Lidar output, the green points represent camera output. Based on the general observation, both LiDAR and camera trajectories fit the lane well. The detection range of vision-based trajectory is shorter than the detection range of LiDAR in both daytime and nighttime conditions. The specific analysis of the detection range is evaluated and discussed later in this article.

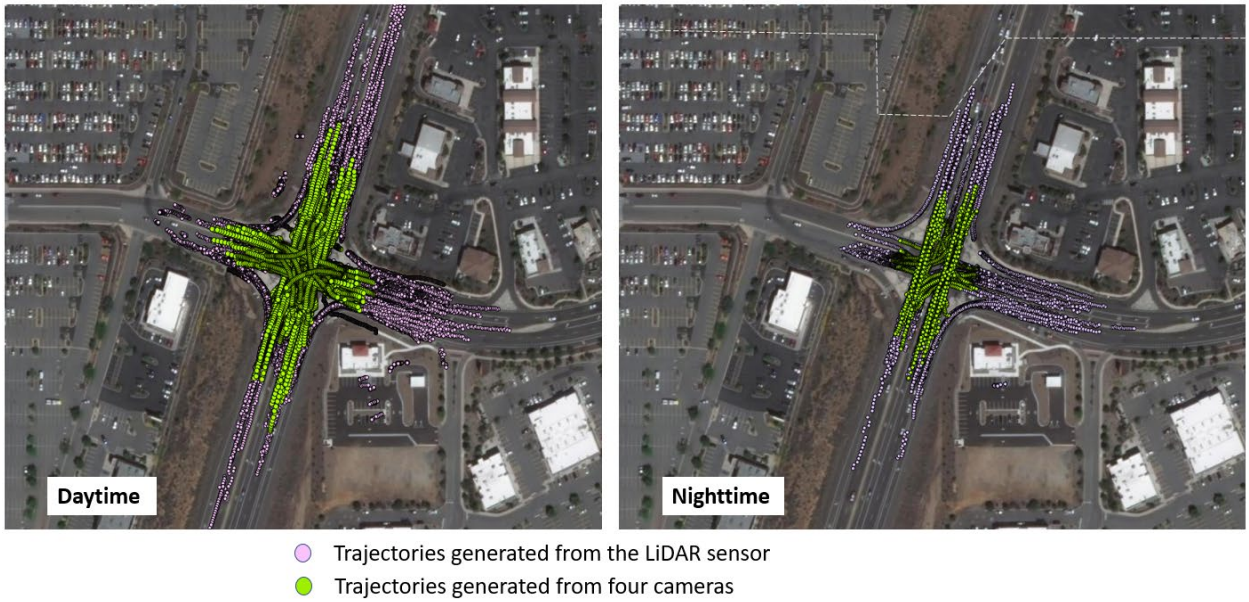

Figure 7-2 Daytime (left) and nighttime (Right) trajectory overview

Vehicle Volume Count Accuracy

Although the volume counts are not automatically generated, they can be gathered by counting the different object IDs in each lane. Some detection zones are set up in the ArcGIS software, which is shown in Figure 7-3. The number of different objects in each detection zone can be counted by ArcGIS built-in function automatically so that the volume of each movement can be obtained. Two volume counts are compared with the ground truth volume data, which is manually counted by our team.

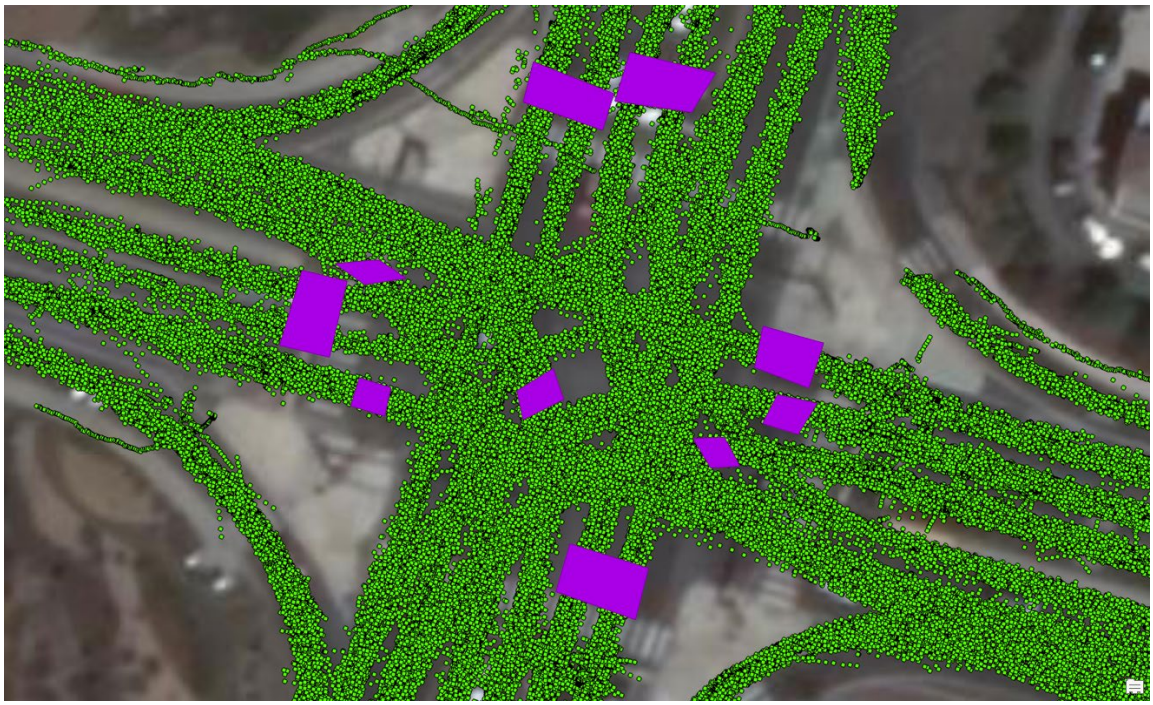

Figure 7-3 Detection zones for counting the volume

The results of volume count accuracy are shown in Figure 7-4 and Figure 7-5. each column stands for the percentage of accuracy the sensor achieved in the northbound through (NBT), northbound left turn (NBL), southbound through (SBT), southbound left turn (SBL), eastbound through (EBT), eastbound left turn (EBL), westbound through (WBT) and westbound left turn (WBL), respectively. For the daytime peak time (12:00 pm to 12:30 pm) on December 24th, both vision-based and LiDAR-based output perform well, achieving an accuracy rate of more than 96% for all movements. For most movements, LiDAR performs slightly better than computer vision, but in Eastbound left turn, Northbound through, and Northbound Left turn, cameras show better accuracy.

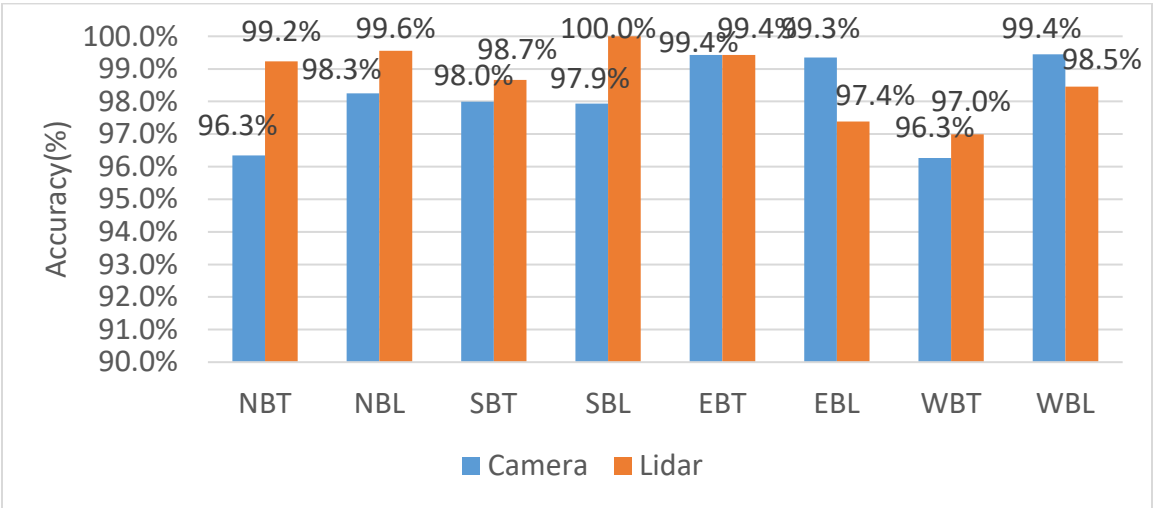

Figure 7-4 Volume Count Accuracy for Daytime Volume (Dec 24th 12:00pm - 12:30pm)

For the nighttime (3:00 am to 3:30 am) on December 24th, by comparing with manually counted volume, it shows that lidar reaches 100% accuracy for all movements. Cameras also reached 100% for all movements except southbound through. For southbound through, the accuracy is only 81.5%, which only captured 22 out of the 27 vehicles.

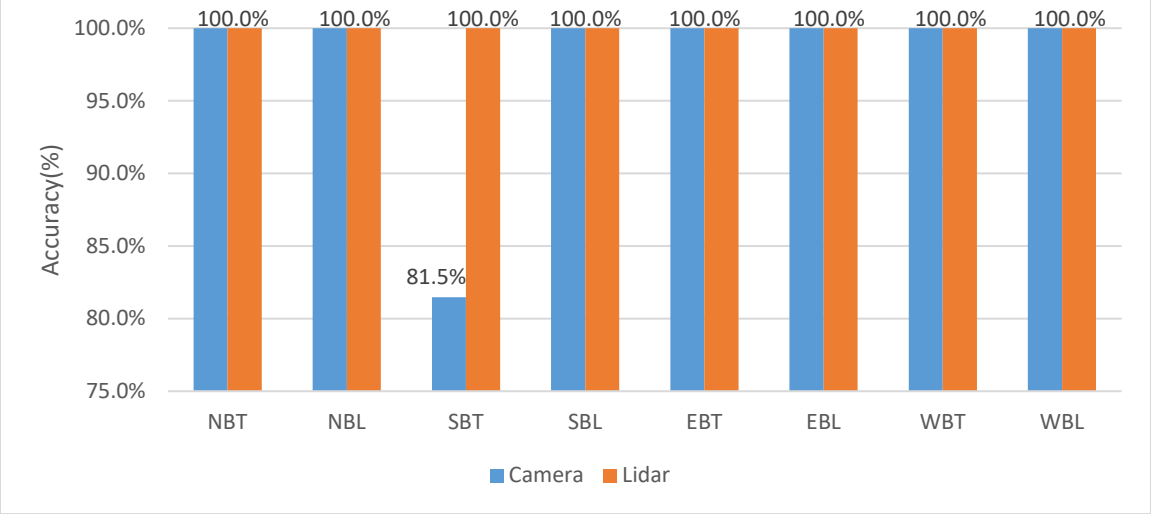

Figure 7-5 Volume count accuracy for nighttime (Dec 24th 3am - 3:30am)

Detection Range

To evaluate the detection range of two different sensors, 4 detection zones for each bound were set. Each zone is 50 ft long, the front edge of the first zone is the stop bar. The detection range can be evaluated by comparing the percentage difference of vehicles detected in different zones.

Figure 7-6 below shows the detection rate of LiDAR for different bounds over different distances to the stop bar. Lidar successfully detects all vehicles at a distance of 0 to 50ft to the stop bar. With the distance increase, the detection n rates of these two bounds farther from the lidar installation position (northeast side of the intersection), northbound and eastbound, dropped more significantly. The detection rate of eastbound dropped to 53% from 50ft to 100ft to the stop bar and further dropped to 11% when the detection range was between 100ft and 150ft to the stop bar. Detection range of northbound dropped from 88% of 50-100 ft to 14% of 100-150ft to stop bar. When the detection range is 150 to 200ft to the stop bar, both detection rates of the northbound and eastbound drop to 2%, southbound and westbound still perform well, which is 84% and 96%, respectively.

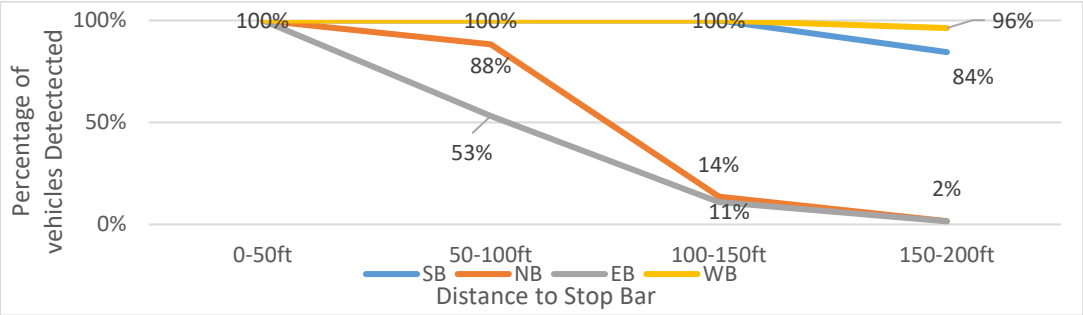

Figure 7-6 Lidar vehicle detection rate for each bound (12/23/2020 12:00 pm to 12:30 pm)

As shown in Figure 7-7, Lidar performed similarly during the night as the day: two bounds closer to lidar installation location (northeast side of the intersection) show better performance, the westbound keeps detection rate of 100% in four zones, southbound maintains detection rate of 100% in the first three zones (0 to 150 ft) and decreases to 79% in the fourth zone (150 to 200 ft). The performance of northbound and eastbound is slightly better than that in the daytime. The detection rate of eastbound is 100% in 0 to 150 ft to stop bar, but it is 0% in the area of 150 to 200 ft to stop bar. North bound's detection rate dropped from 100% to 42% at 100-150 ft to stop bar and kept dropping to 17% at 150-200 ft to stop bar.

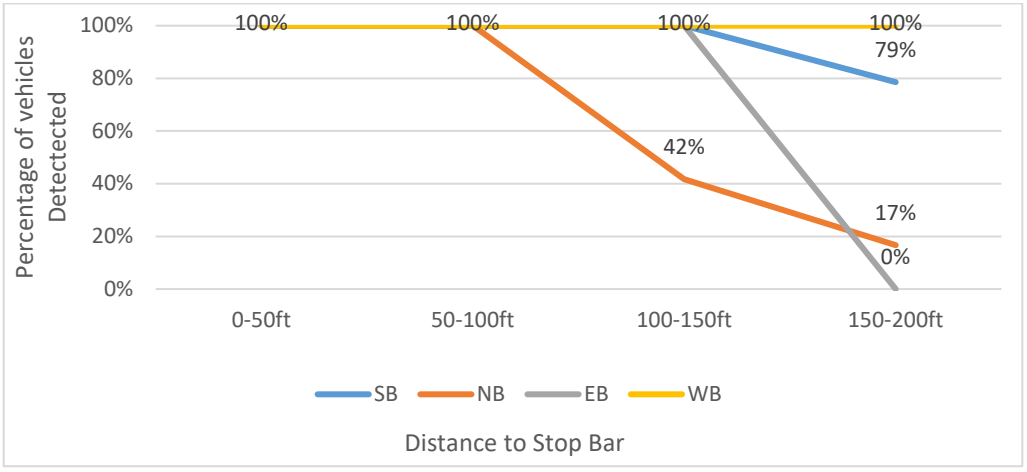

Figure 7-7 Lidar vehicle detection rate for each bound (12/24/2020 3:00 am to 3:30 am)

The performance of vision-based trajectory is worse than LiDAR. Figure 7-8 shows the detection rate of cameras from 12/23/2020 12:00 pm to 12:30 pm. even in the area of 0 to 50ft to the stop bar, some vehicles cannot be detected, which means that a significant portion of vehicles can only be detected after they have entered the intersection. The detection rate of four bounds sharply when the distance to the stop bar is greater than 50 ft. Very few vehicles can be detected over 100 ft to the stop bar.

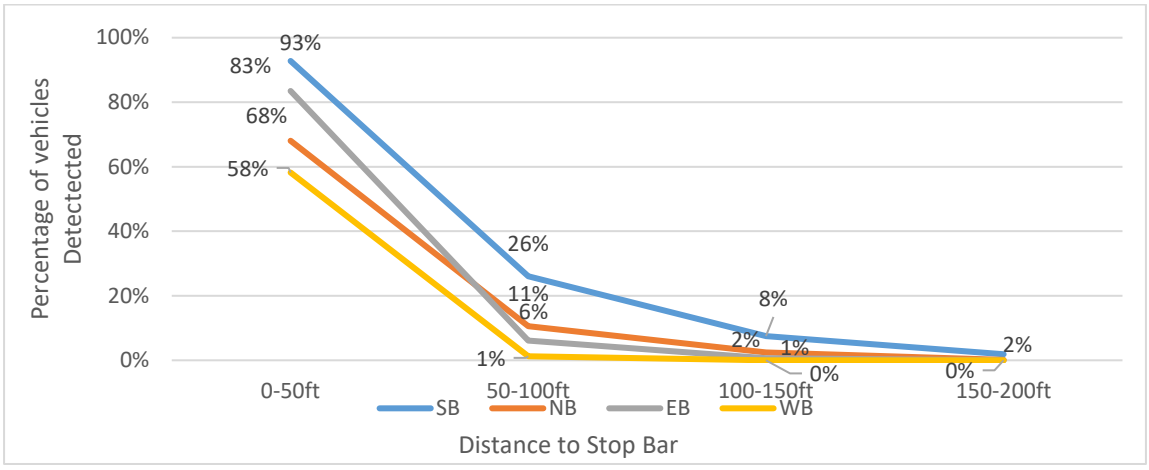

Figure 7-8 Camera vehicle detection rate for each bound (12/23/2020 12:00 pm to 12:30 pm)

The performance of the vision-based detection rate at night is worse than that in the daytime (Figure 7-9). For westbound, only 20% of the vehicles (1 vehicle out of 5)can be detected before reaching the stop bar. The detection rates of both eastbound and westbound above are 0 when the detection range is 50ft or longer to the stop bar, and that of northbound and eastbound is only 8% and 7%, respectively.

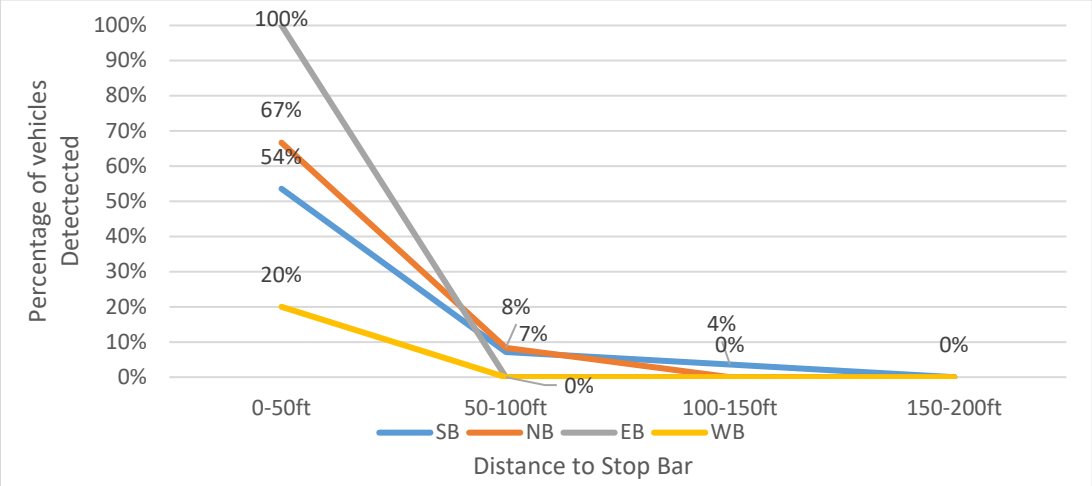

Figure 7-9 Cameras Detection Range for each Bound (12/24/2020 3:00 am to 3:30 am)

Pedestrian Detection

Pedestrian detection plays a very important role in the traffic safety analysis. In this study, 4-hour daytime and 4-hour nighttime data are selected to compare the performance of two sensors in pedestrian detection. Figure 10 shows the pedestrian crossing trajectories from 12/23/2020 12:00 PM to 4:00 PM. After comparing with the manually counted value, both LiDAR and computer-vision captured all the pedestrian activities. LiDAR can capture the pedestrian before they enter the intersection, but for the camera, the trajectory length of pedestrians is much shorter. Some pedestrians can only be captured after walking on the crosswalk, as shown in Figure 7-10.

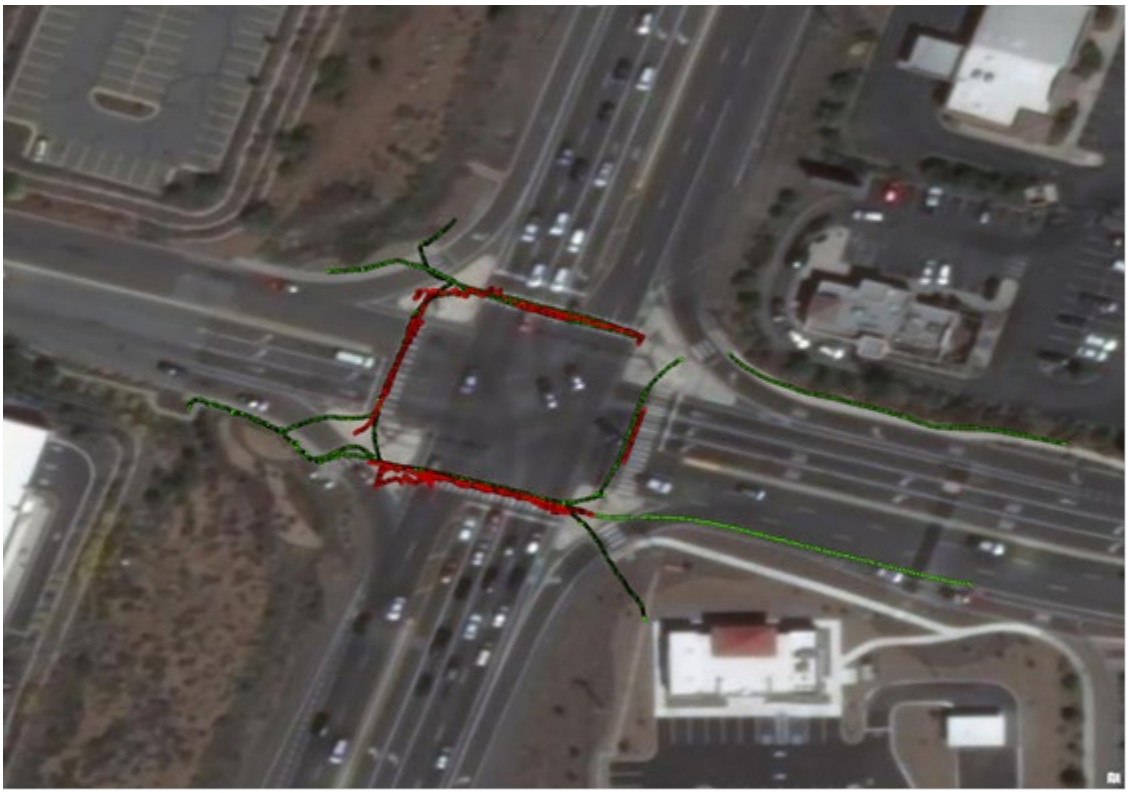

Figure 7-10. Pedestrian crossing trajectories captured by Lidar(green) and Camera (Red)

For the nighttime from 12/24/2020 12:00AM to 4:00 AM, there are 4 pedestrian crossing happened, the LiDAR captured all of them, but none of them was captured by camera.

Speed

Since the trajectory data is the location point of the road users every 0.1 seconds, the speed information can be calculated by calculating the distance difference over time difference. Figure 13 shows trajectories of one southbound left-turn vehicle captured from both LiDAR and Video. Based on the trajectory data, the speed of the sample vehicle in each frame is calculated, which is shown in Figure 14. Since the offset of the location information can significantly affect the result of calculated speed, the speed is smoothed by MA (Moving Average) method in order to get closer to the real value. The raw speed and smoothed speed information are shown in Figure 7-11 and Figure 7-12.

Figure 7-11 Same Vehicle trajectories captured by LiDAR (left) and computer vision (right)

From the raw data, it can be seen that the magnitude of speeds calculated by the two sensors is similar. LiDAR has greater fluctuation, but its trajectory length is much longer than that of computer vision. It can be seen from the figure that LiDAR can capture the whole procedure of the vehicle, from decelerating towards the intersection, stopping at the intersection, and finally accelerating out of the intersection, which is important for intersection-level analysis.

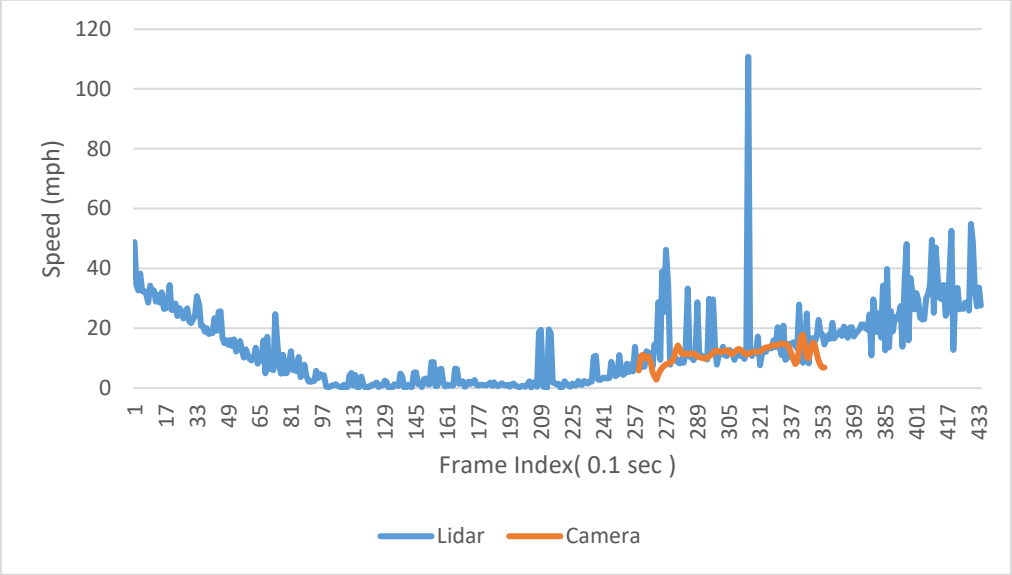

Figure 7-12 Speed of the sample vehicle calculated based on trajectory location.

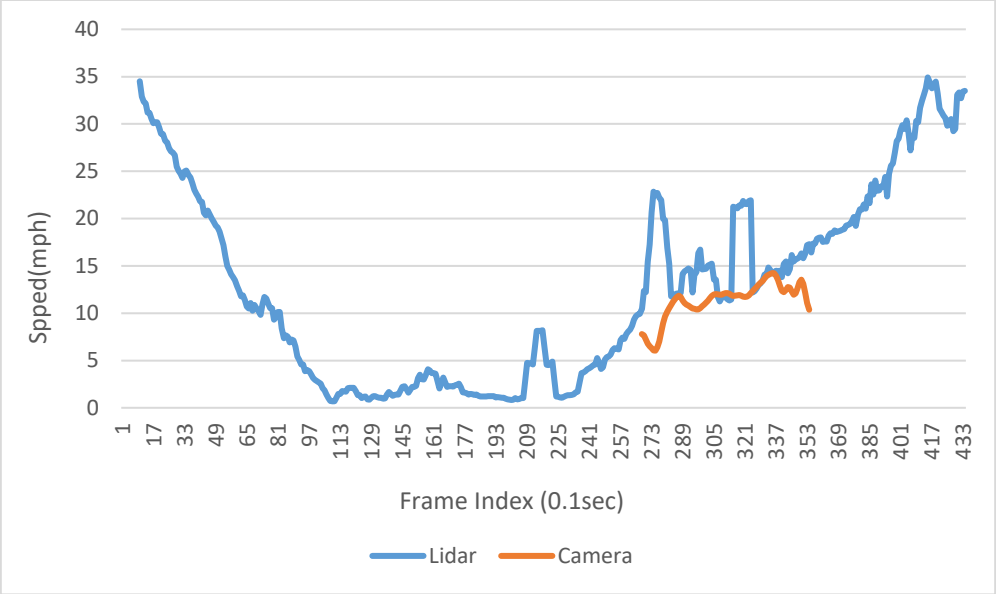

Figure 7-13 Smoothed speed of the sample vehicle

For pedestrian detection, since the size of the pedestrian is much smaller than that of vehicles, the point that Lidar reflects from the pedestrian will also be significantly reduced, which reduces the potential distance offset caused by the fluctuation of the reference point chosen on the object, thus the pedestrian speed detection of LiDAR is more accurate than vehicle speed detection. As shown in Figure 7-14, Lidar shows very good speed detection of pedestrians, on the contrary, the camera does not perform well in speed detection of pedestrians, the detected pedestrian speed is significantly higher than the normal walking speed of pedestrians (around 3-4 mph). In addition, due to the short detection range of the camera, the camera can only capture the data of pedestrians walking on the crosswalk. As shown in Figure 7-15, the camera cannot cover the pedestrians entering the island or how long the pedestrians waiting to cross.

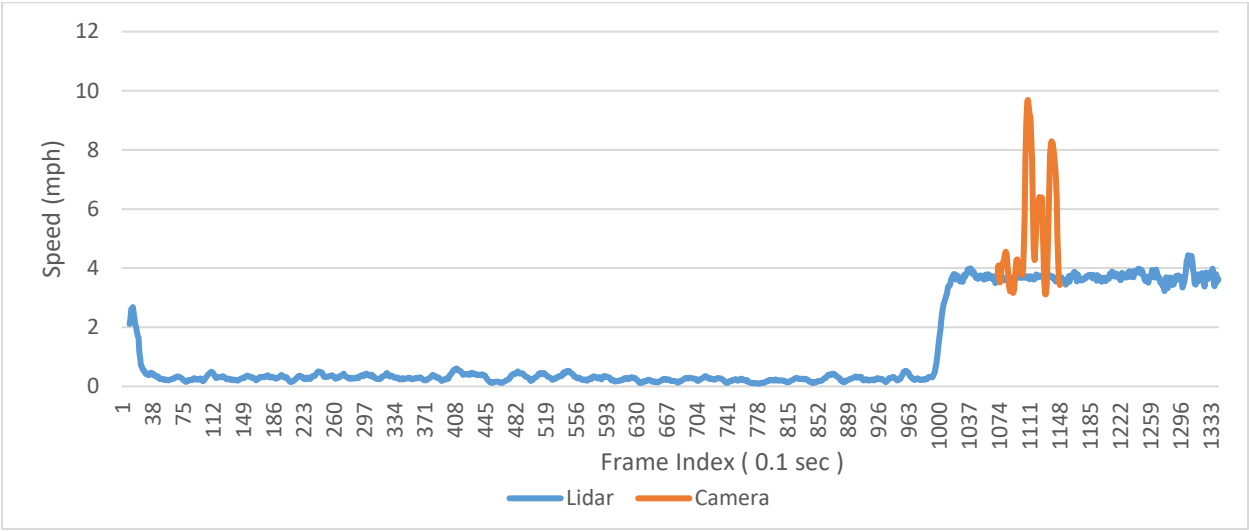

Figure 7-14 Sample pedestrian speed

Figure 7-15 Sample pedestrian trajectories captured by LiDAR (left) and Camera (Right)

Although from a data comparison point of view, the LiDAR-based trajectory appears to be more dominant, data quality is not the only criterion when considering which data source to choose. Factors such as data storage, installation and maintenance accessibility are all need to be considered. Combined with the data quality analysis above and other factors, Table 7-1 provides a general recommendation for other researchers to refer to when choosing which type to use. Cells with one black dot mean that this type of data source shows good performance in such assessment.

Table 7-1 Reference table for LiDAR-based and Vision-based trajectory data

	LiDAR-based	Vision-based	Comments
Device Cost		●	Cameras are currently much cheaper than LiDAR
Installation and maintenance accessibility	●	●	Installation takes about 30 minutes
Data storage	●		Video needs much more storage space for same time period than LiDAR since for one intersection at least 4 cameras are needed
Detection Range	●		Lidar shows longer detection range
Daytime Vehicle Volume	●	●	Both sensors show good daytime vehicle counting capability
Nighttime Vehicle Volume	●		Cameras may miss some vehicles at night
Daytime Pedestrian Volume	●	●	Both sensors show good daytime pedestrian counting performance
Nighttime Pedestrian Volume	●		The camera barely recognizes pedestrians at night
Vehicle Speed	●	●	Both sensors generate decent vehicle speed information
Pedestrian Speed	●		LiDAR shows brilliant speed detection for relatively small objects such as pedestrians/bicyclist

8. TRAFFIC PERFORMANCE MEASUREMENT WITH LIDAR DATA

UNR performed a trajectory-based traffic study at Pyramid Way and Calle De La Plata. LiDAR data collection covered 24-hour traffic information on Saturday, August 29, Sunday, August 20, Tuesday, September 1, and Wednesday, September 2, 2020. The study findings are summarized as the following:

Vehicle traffic volumes – highest traffic volumes were observed with northbound through movement, northbound left-turn movement, southbound through movement, and eastbound right-turn movement. The four movements' daily traffic volumes were 4,558, 4,277, 4,527, and 4,128 on Wednesday, September 2, the highest of the four data collection days. Peak hour volumes of the four movements were about 400 vehicles/hour. Daily volumes of other movements were less than 1,000.

Speed study – The overspeeding problem was evident with the northbound through traffic along Pyramid Way. With the speed limit of 55 MPH, 20.4% (3,573 out of 17,488 vehicles during the data collection period) northbound through vehicles crossed the intersection at speeds of 60-70 MPH, and 1.7% (328 out of 17,488) northbound through vehicles were at speeds higher than 70 MPH. Overspeeding of the southbound traffic was minor, with 0.8% (124 out of 17,307) southbound through vehicles were at speeds higher than 60 MPH.

Much more southbound-through vehicles were slowed or stopped by the traffic signal than the northbound through traffic. A high volume of northbound left-turn traffic frequently called the northbound left-turn green signal and turned the southbound through signal to red.

Pedestrian and bike volumes – pedestrian and bike volumes at this intersection were not high. Daily total volumes at the north crosswalk (crossing Pyramid Way), west crosswalk (crossing Calle De La Plata), and the connected sidewalks had less than 20 pedestrian and bike counts on each. The maximum daily total pedestrians and bikes at the crosswalks were about 30. However, jaywalks crossing Calle De La Plata were observed especially on the east of the intersection by reviewing traffic trajectories.

Near-crash – the UNR researchers query trajectories with the criteria of crossing each other's trajectories in less than 3 seconds to identify possible conflict events. No near-crash was found in the four-day data.

Other situations – many activities were observed at the northeast corner and the southeast corner. The traffic accessing the two corner areas was mainly through unpaved at Calle De La Plata. test

Data Collection

UNR deployed portable roadside LiDAR equipment at the northeast corner of the intersection, as shown in Figure 8-1, from 8/28/2020 Friday 6:00 PM through 9/3/2020 Thursday 9:00 AM. LiDAR data of multimodal traffic were collected during the period except for 8/31/2020 Monday when a power cable misfunctioned. The collected LiDAR data was processed to generate information of multimodal traffic volumes, speeds, and conflicts of traffic flow.

Figure 8-1. Deployed portable LiDAR sensing equipment at the intersection

With the collected LiDAR data, UNR generated geo-located trajectories of all road users for each half-hour period. Traffic data analysis zones were created for each lane, movement, and crosswalk in GIS to perform volume and speed analysis. An example of half-hour trajectories and analysis zones is shown in Figure 8-2.

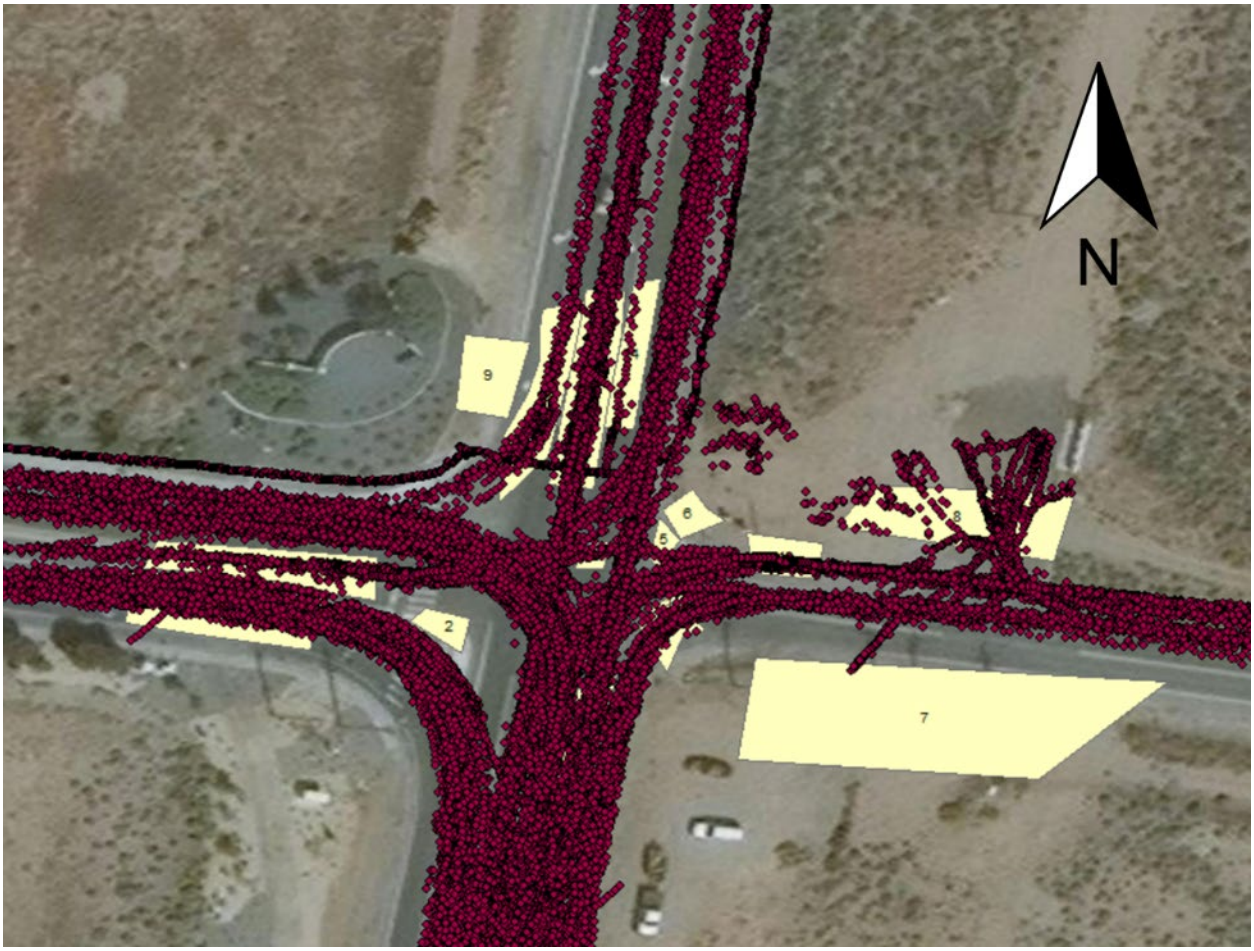

Figure 8-2 Sample of half-hour geo-located trajectories and traffic study zones from LiDAR data collection

Vehicle Volumes

Vehicle volumes of each movement and every half hour were extracted from trajectories. AM and PM peak hour volumes of all movements are shown in Figure 8-3 and Figure 8-4. Daily traffic volumes of all movements on Wednesday, September 3, maximum of the four data collection days, were summarized and presented in Figure 8-5. Figure 8-6 demonstrates 15-minute vehicle volumes extracted from LiDAR trajectory data.

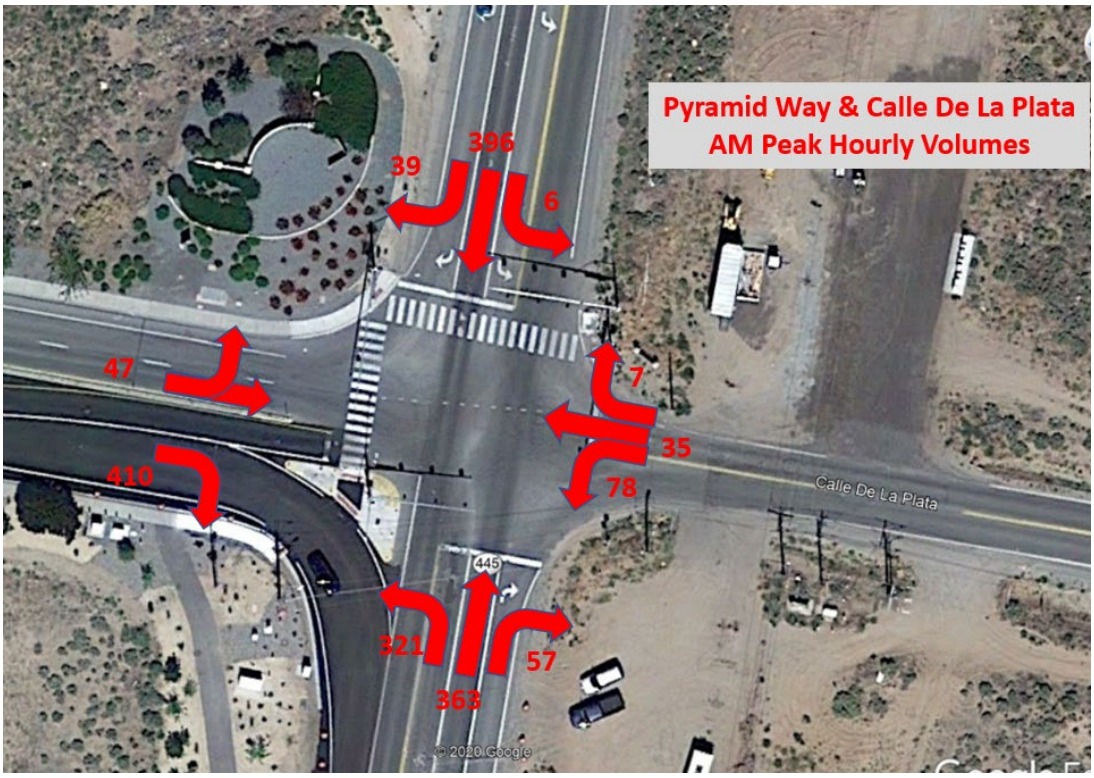

Figure 8-3 AM peak hourly volumes of all movements

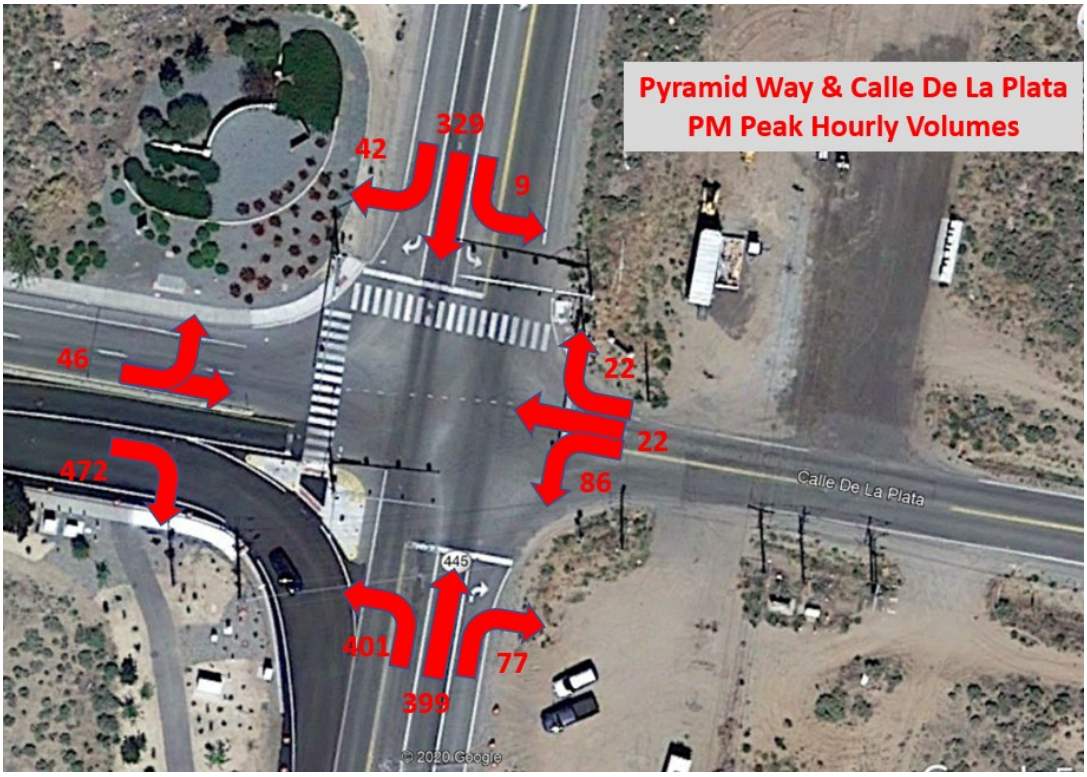

Figure 8-4 PM peak hourly volumes of all movements

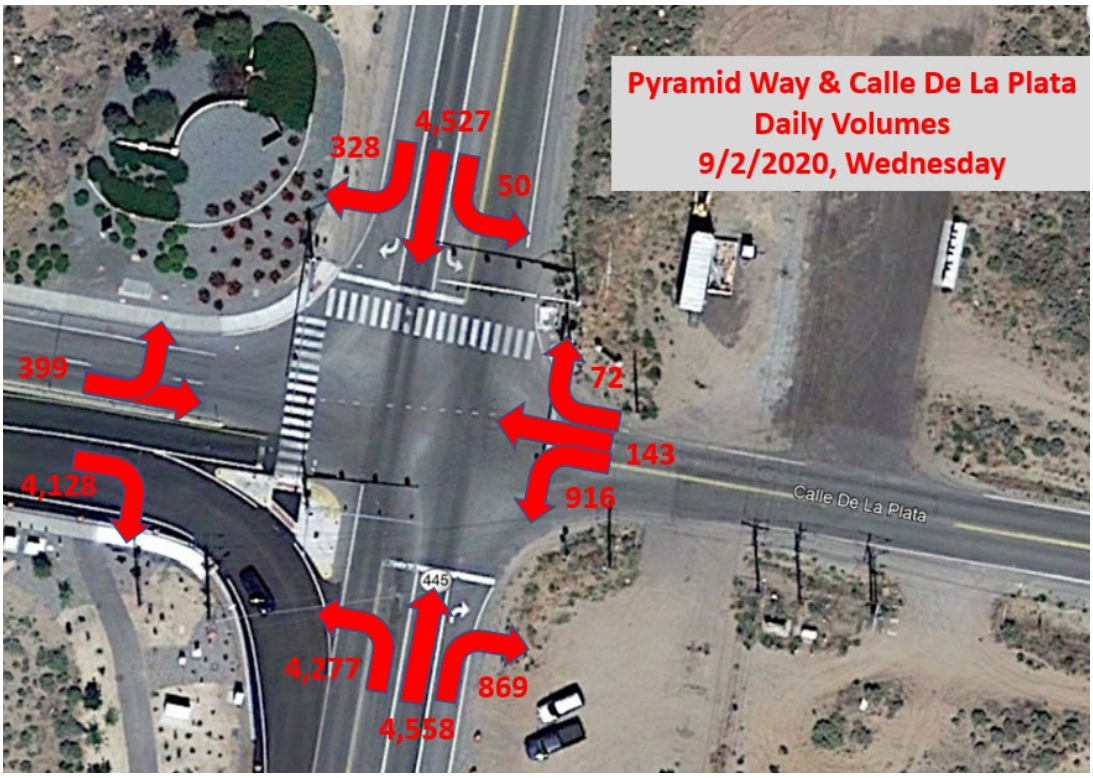

Figure 8-5 Daily traffic volumes of all movements

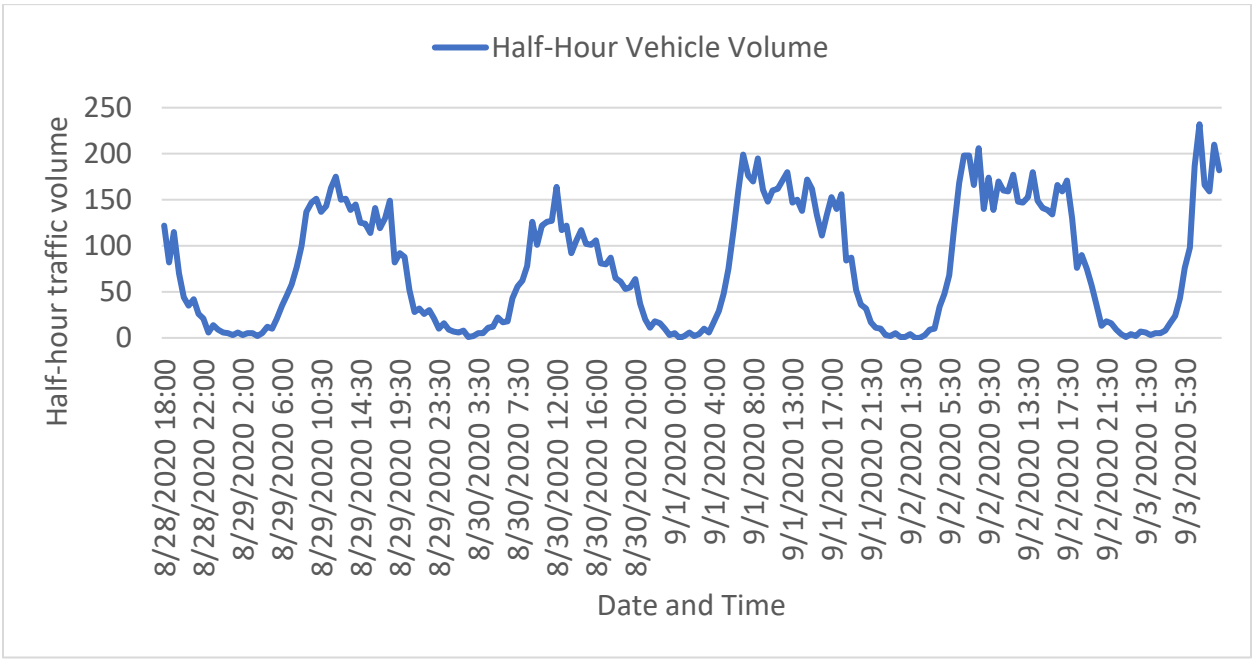

Figure 8-6 Southbound through-lane half-hour traffic volume change

Vehicle Speeds

Vehicle speeds of each vehicle for each movement were extracted from LiDAR data. The half-hour speed distributions (15th percentile, mean, 85th percentile, and 95th percentile) were presented for northbound in Figure 8-7. The over-speeding problem was obvious with the northbound through traffic along Pyramid Way. During the daytime, 85th percentile speeds were 55-65 MPH; during nights, 85th percentile speeds were about 65 MPH and higher; between midnights and early morning, 85th percentile speeds were above 70 MPH, and the highest speeds were around 80 MPH. Overspeeding with the southbound through traffic was only observed between midnights and early morning; 85th percentile speeds during those periods were 65 MPH or lower. Therefore, the overspeeding problem with the southbound traffic was not as serious as with the northbound traffic. The exclusive eastbound right-turn lane, its curbed island and its connected southbound auxiliary lane may have helped drivers to reduce speeds. For drivers, the southbound through lane (south of the intersection) feels narrower with the auxiliary lane than the northbound through lane that is adjacent to its shoulder, demonstration in Figure 8-8.

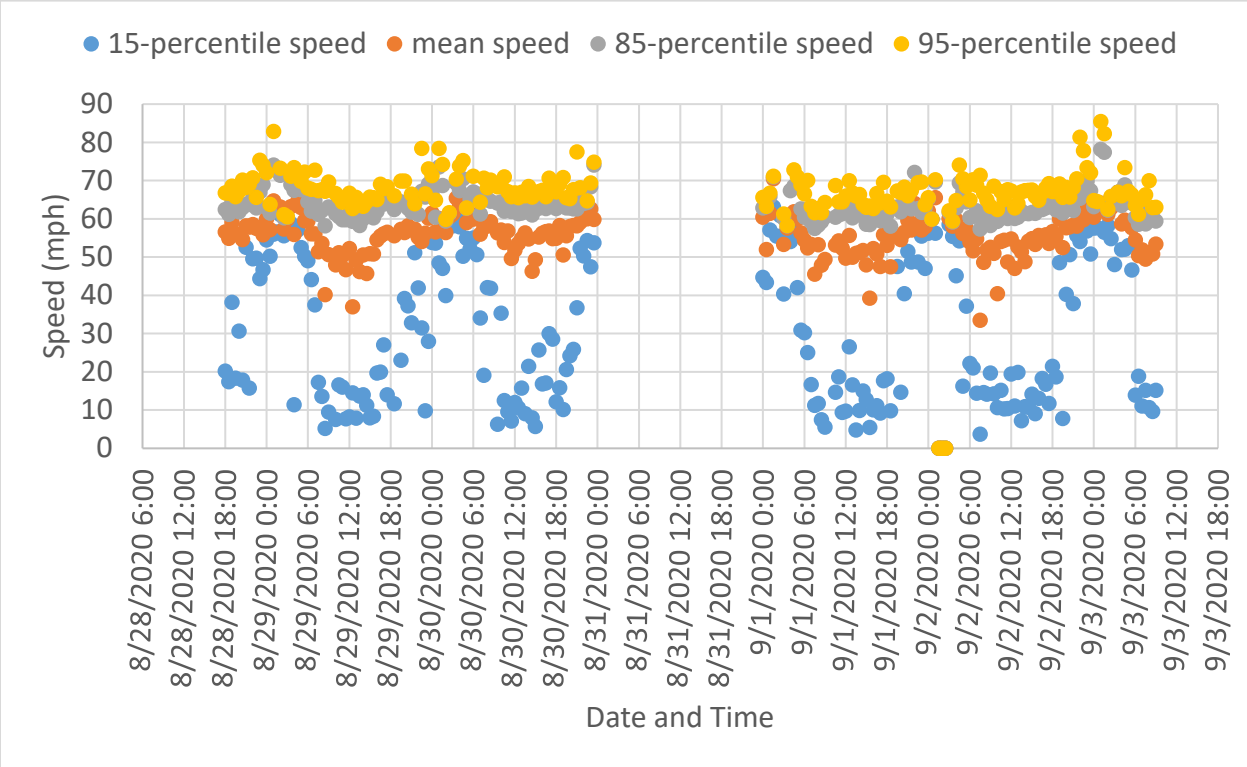

Figure 8-7 Northbound through traffic speed study

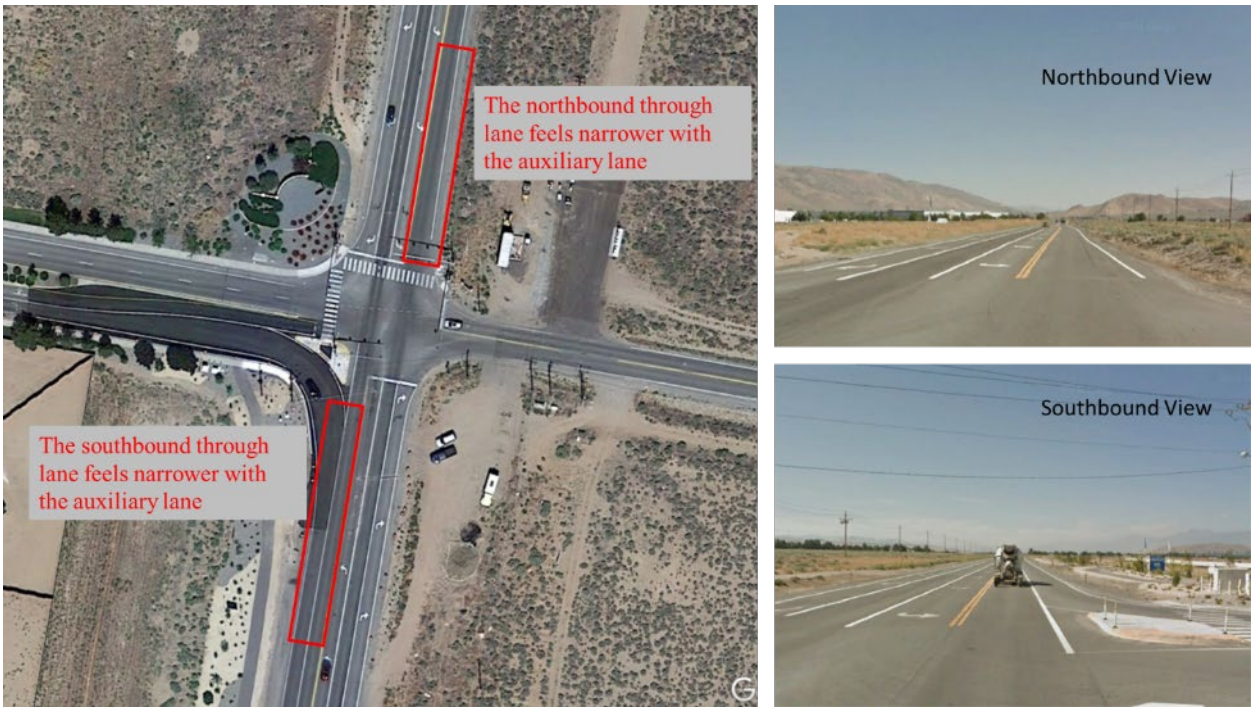

Figure 8-8 Comparison of northbound and southbound geometric elements that may have helped to reduce the southbound traffic speeds

Vehicle volumes in different speed ranges of northbound through are presented in Figure 8-9. Average speeds lower than 40 MPH usually mean vehicles slowed or stopped at the intersection because of traffic signal control. It is obvious that much more southbound through vehicles were slowed/stopped by the traffic signal than the northbound through traffic. The high volume of northbound left-turn traffic frequently called northbound left-turn green signal that turned southbound through signal to red and slowed the southbound traffic.

Pedestrian and Bike Volumes

There were low pedestrian activities at the intersection during the data collection period. The pedestrian (including bikes) volumes at the two sidewalks and two crosswalks were extracted from LiDAR data. The sidewalks and crosswalks are presented in Figure 8-10 with daily pedestrian-bike volumes. The half-hour pedestrian volumes of the sidewalks and crosswalks were presented in Figure 8-11 through Figure 8-14. Besides pedestrian activities along the sidewalks and crosswalks, multiple jaywalks (crossing roads not at crosswalks) were identified by reviewing LiDAR trajectories, especially on the east of the intersection. Jaywalk samples were demonstrated in Figure 8-15 and Figure 8-16.

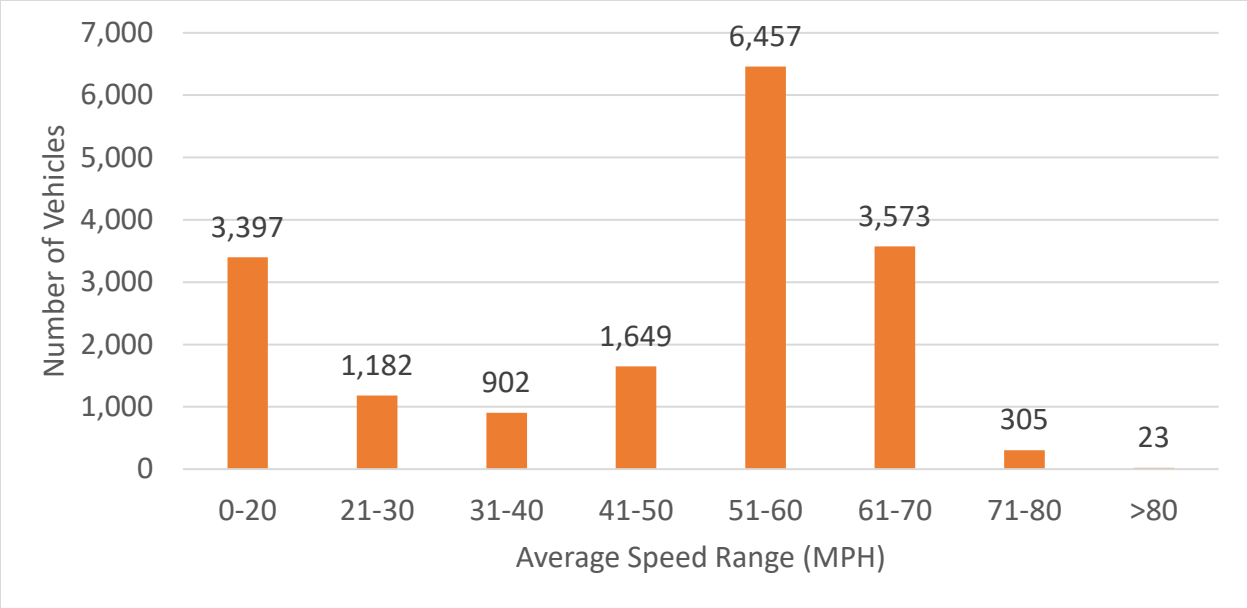

Figure 8-9 Number of vhicles in different average speed ranges – all northbound through vehicles

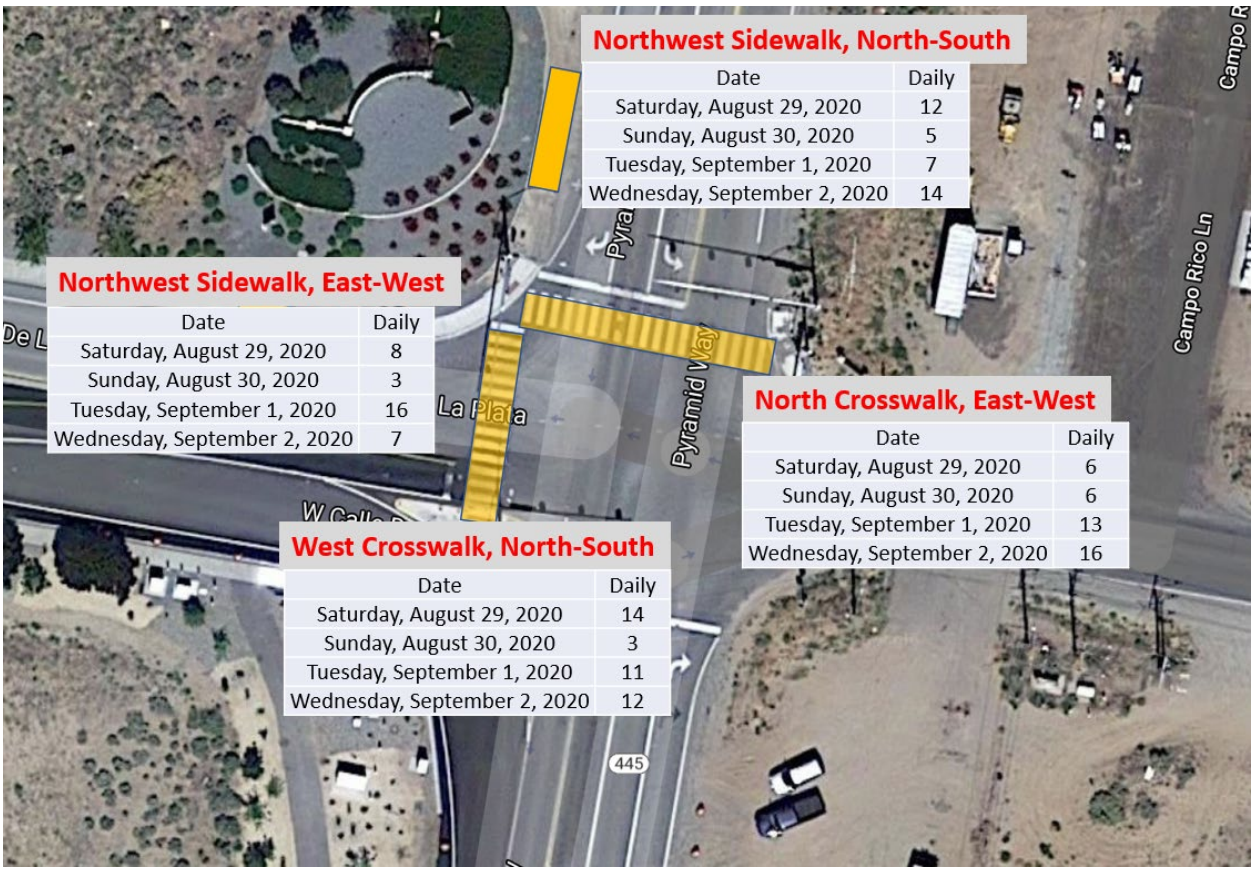

Figure 8-10 Pedestrian volume counting zones and their daily volumes

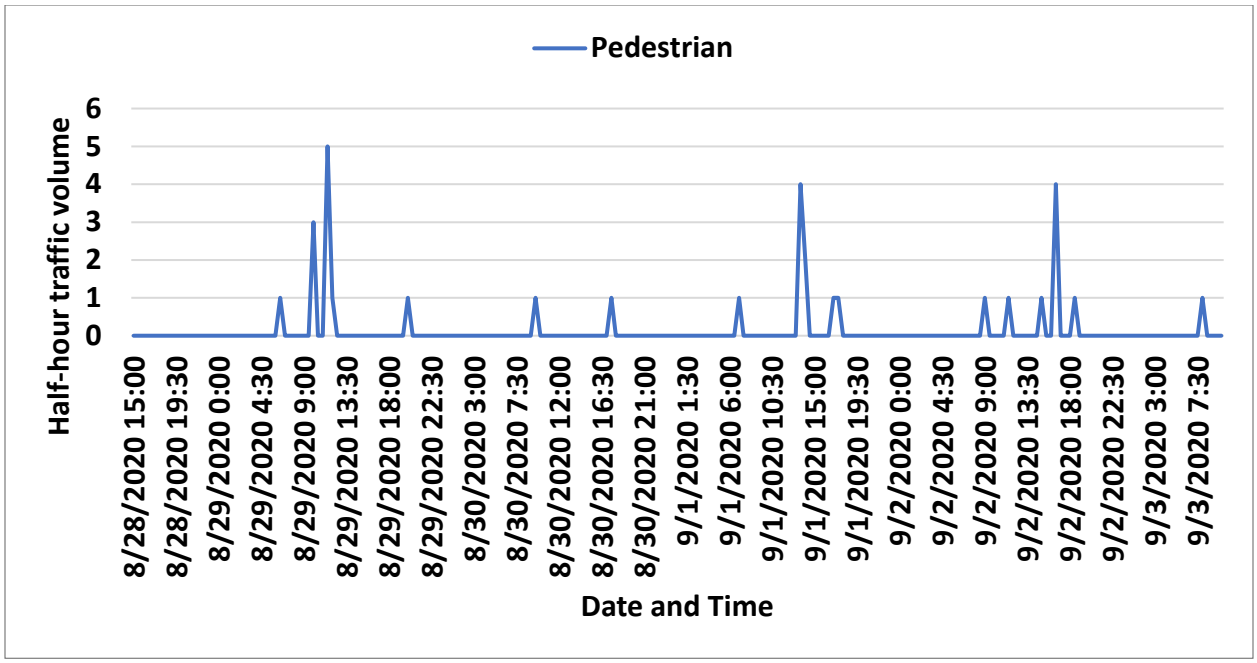

Figure 8-11 Half-hour pedestrian and bike volumes at the west crosswalk, north-south

Northwest sidewalk

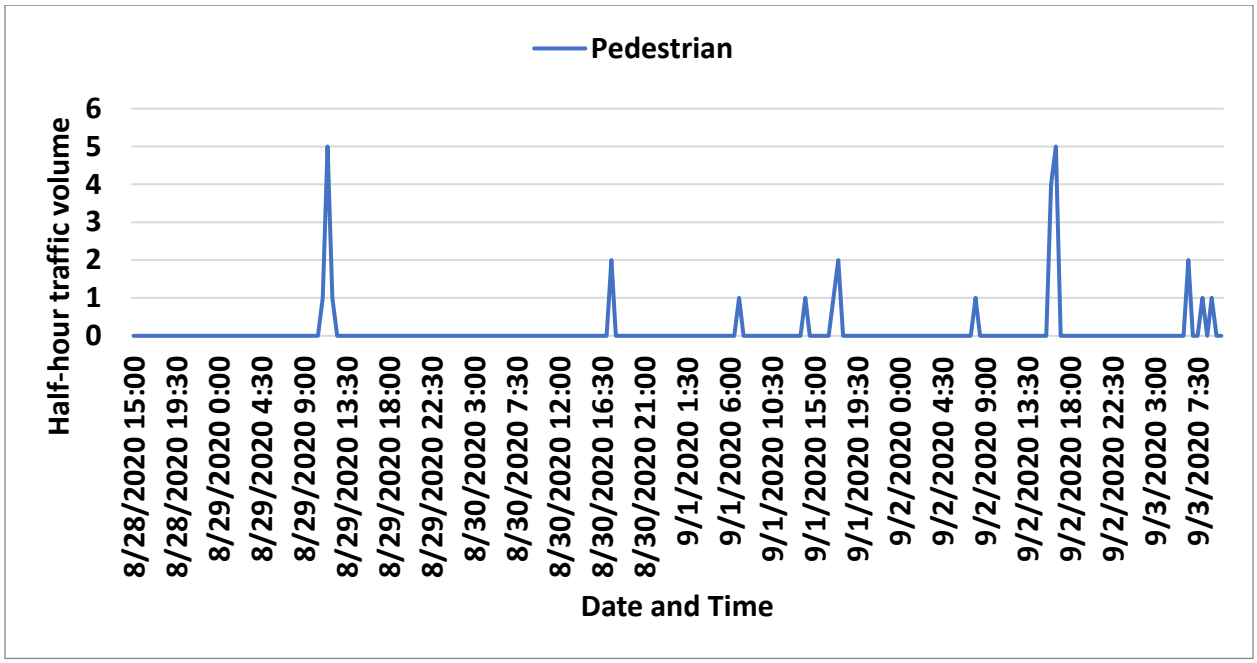

Figure 8-12 Half-hour pedestrian and bike volumes at the northwest sidewalk, north-south

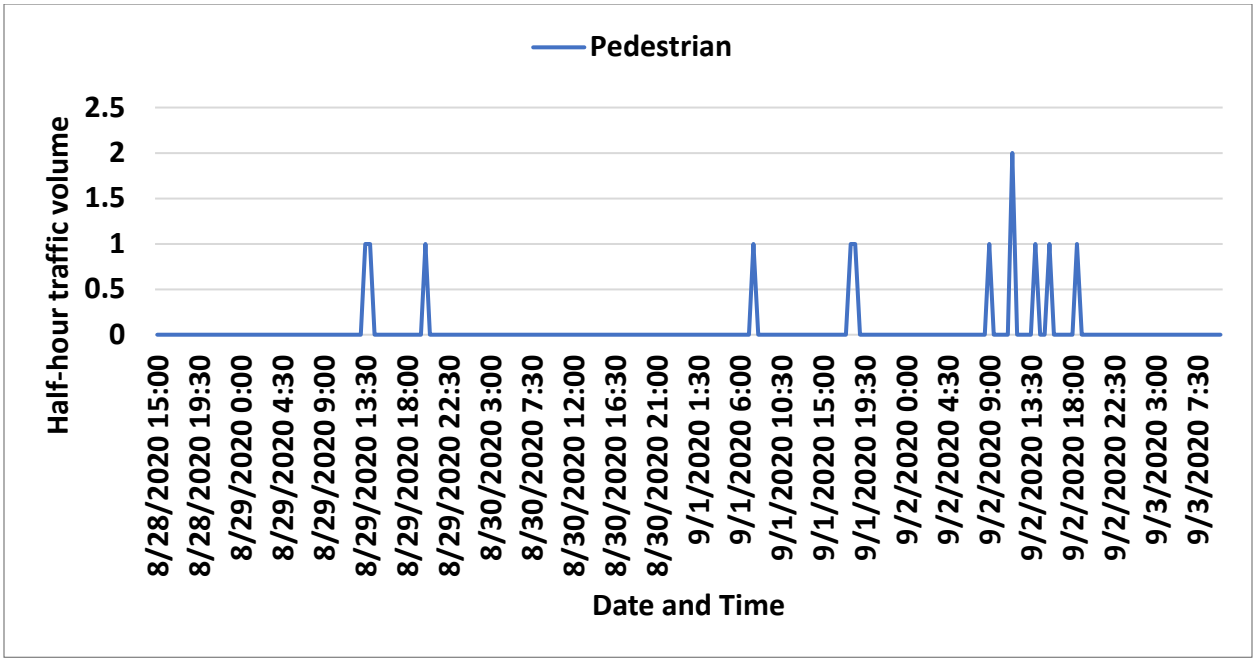

Figure 8-13 Half-hour pedestrian and bike volumes at the north crosswalk, east-west

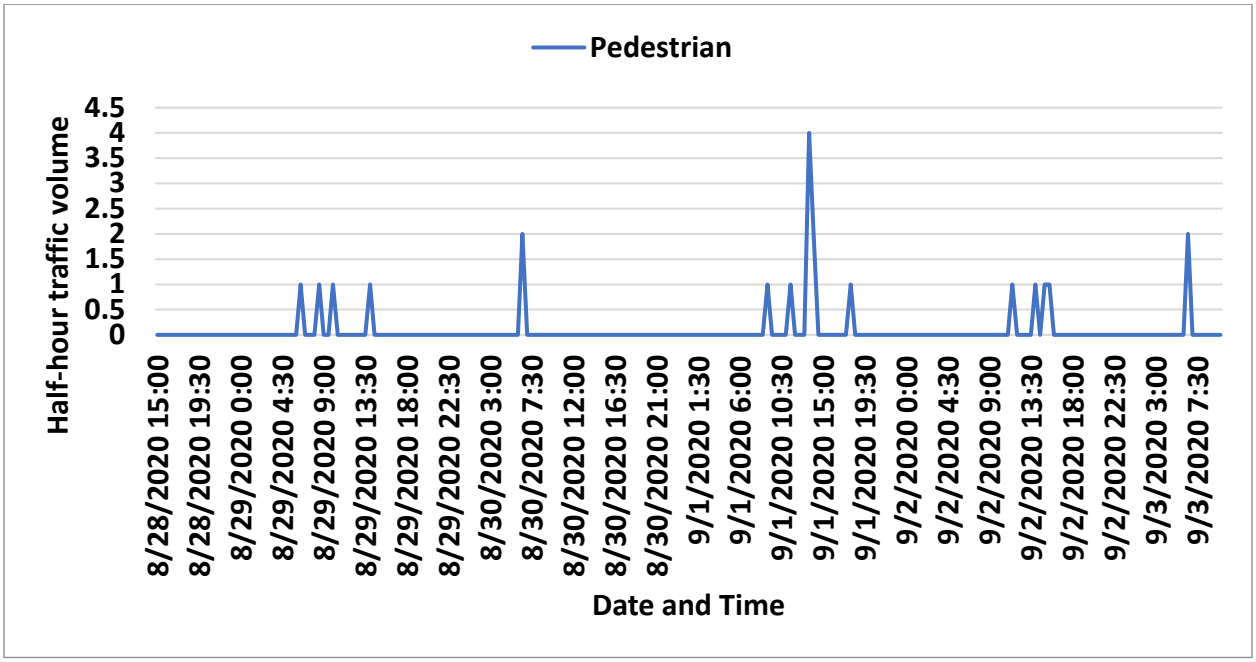

Figure 8-14 Half-hour pedestrian and bike volumes at the northwest corner, east-west

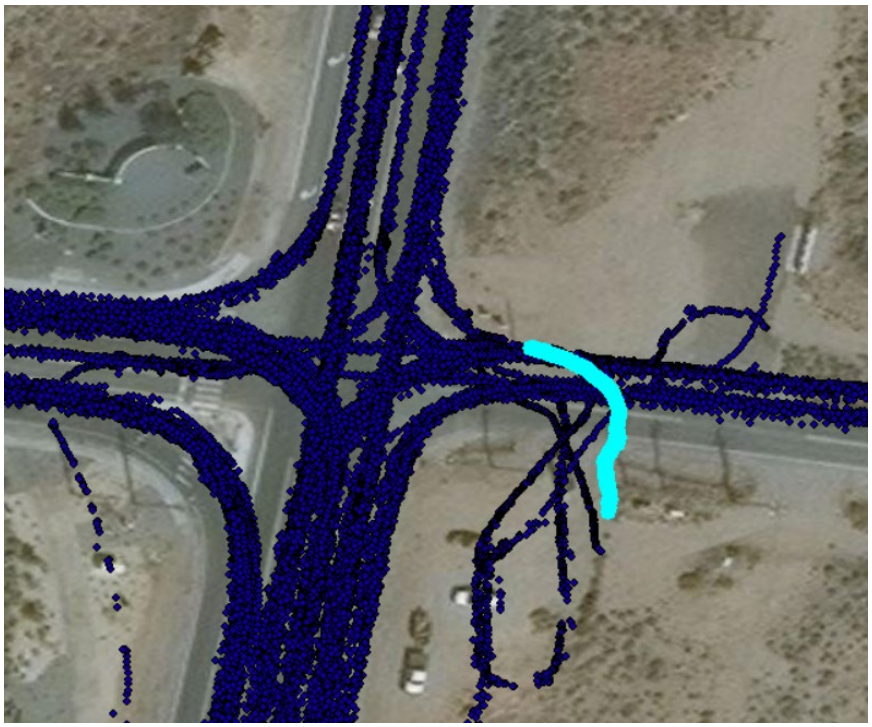

Figure 8-15 Pedestrians crossing Calle De La Plata at 08/29/2020 12:00-12:30PM (east of the intersection)(light blue means pedestrian crossing trajectories)

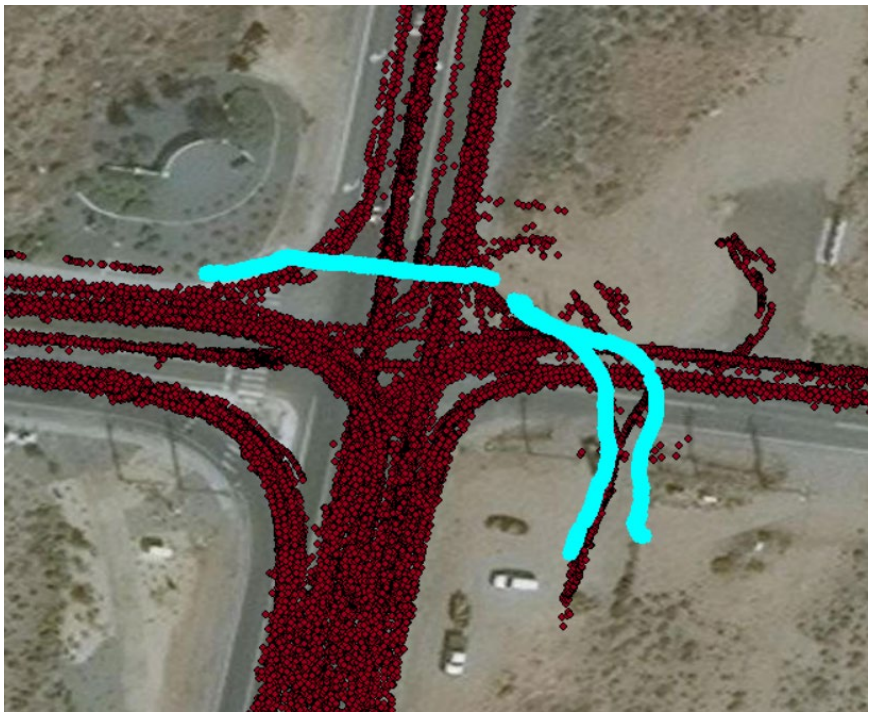

Figure 8-16 Pedestrians crossing Calle De La Plata at 08/29/2020 2:00-2:30 PM (east of the intersection)(light blue means pedestrian crossing trajectories)

Near Crash Identification

Identifying conflicts between road users, especially pedestrians/bikes and vehicles, is important for proactive traffic safety analysis and improvement. Traffic safety issues can be identified before any crash happens if traffic conflict data is available. The roadside LiDAR sensing system and generated all-traffic trajectories allows automatic traffic conflict identification by filtering events with criteria of distance, speed difference, and direction difference between road users. Further conflict analysis can be performed by applying various near-crash analysis methods documented in research papers, as summarized in Table 8-1.

Table 8-1 Summary of Traffic Conflict/Near-Crash Indicators

Indicators*	Authors	Description
Temporal Proximal based indicators		
Time-to-Collision (TTC)	Hayward (Hayward, 1971)	The time that remains until a collision between two vehicles would have occurred if the collision course and speed difference are maintained. (Hydén, 1996)
Time Exposed Time-to-Collision (TET)	Minderhoud and Bovy (Minderhoud and Bovy, 2001)	The duration of exposition to safety-critical time-to-collision values over specified time duration.
Time Integrated Time-to-Collision (TIT)	Minderhoud and Bovy (Minderhoud and Bovy, 2001)	Integral of the TTC-profile during the time it is below the threshold.
Post-Encroachment Time (PET)	Allen et al. (Allen et al., 1978)	The difference between the time when the lead vehicle last occupied a position and the time when the following vehicle first reached the same position.
Time Difference to the Point of Intersection (TDPI)	Wu et al. (Wu et al., 2018)	The time difference between one vehicle and one pedestrian reaching the same point in their trajectories.
Time Headway (H)	Michael et al. (Michael et al., 2000)	The time that passes between two vehicles' reaching the same location
Distance based proximal indicators		
Distance between stop position and pedestrian (DSPP)	Wu et al. (Wu et al., 2018)	The distance between one vehicle and one pedestrian when the vehicle firstly stopped before reaching the pedestrian
Potential Index for Collision with Urgent Deceleration (PICUD)	Iida et al. (Iida et al., 2001)	The distance between the two vehicles considered when they completely stop.
Proportion of Stopping Distance (PSD)	Allen et al. (Allen et al., 1978)	The ratio between the remaining distance to the potential point of collision and the minimum acceptable stopping distance

Difference of Space distance and Stopping Distance (DSS)	Okamura et al. (Okamura et al., 2011)	The difference between the space and the stopping distances.
Deceleration based indicators		
Deceleration Rate to Avoid a Crash (DRAC)	Almqvist et al. (Almqvist et al., 1991)	Differential speed between a following vehicle and the leading vehicle divided by their closing time
Crash Potential Index (CPI)	Cunto and Saccomanno (Cunto and Saccomanno, 2007)	The probability that a given vehicle exceeds its maximum available deceleration rate during a given time interval
Criticality Index Function (CIF)	Chan (Chan, 2006)	Multiplication of vehicle speed with the required deceleration

Most of those indicators were originally developed for vehicle-vehicle near-crash identification, especially for rear-end crashes. Some of those indicators can be used or can be modified for vehicle-pedestrian near-crash identification. The principal criterion for selecting the indicators is that the indicators could be calculated with the available trajectory data. Another consideration is that the selected indicators should catch all the safety-critical events at different scenarios with less "false" reports.

With geo-located trajectories (longitude and latitude), traffic conflict filtering and visualization can be easily achieved in GIS environments, such as ArcGIS software. There is no existing guidance to determine the thresholds of object distance, speed difference, and direction difference for traffic conflict identification.

UNR analyzed all collected data to identify whether there were any near-crashes. Near-crashes defined in this study were that two road users crossed the same spatial location within 3 seconds, and they were moving in different directions. The data search only identified one candidate near-crash event, as shown in Figure 31. After further-review trajectories in GIS, it was a left-turn after the opposing through traffic, although the time difference at the crossing point was less than 3 seconds. It was not a near-crash event. To conclude, **no near-crash was found in the collected data.**

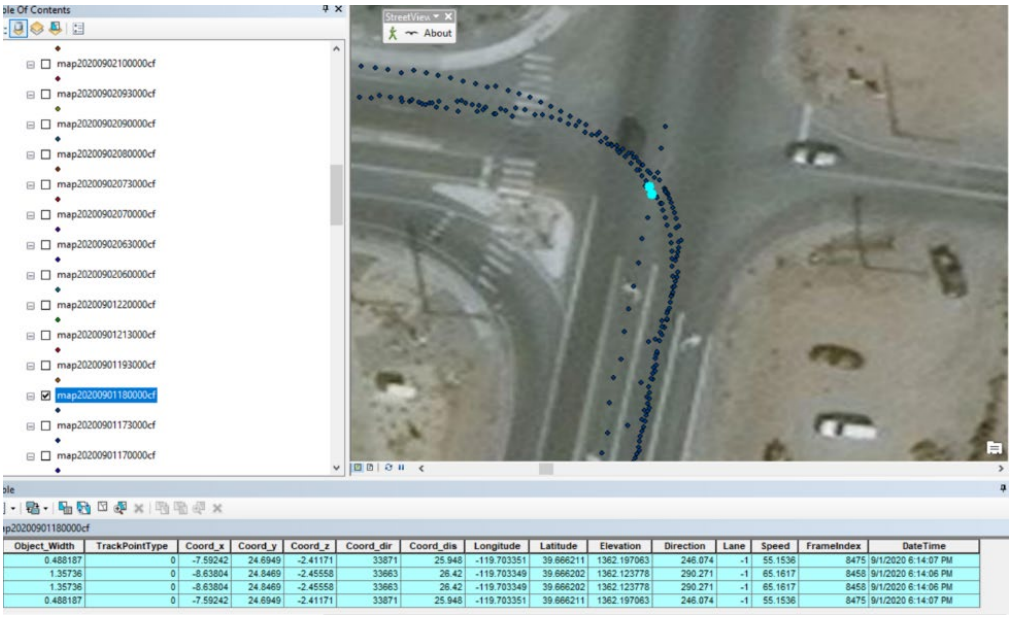

Object_Width	TrackPointType	Coord_x	Coord_y	Coord_z	Coord_dir	Coord_dis	Longitude	Latitude	Elevation	Direction	Lane	Speed	FrameIndex	DateTime
0.488187	0	-7.59242	24.6949	-2.41171	33871	25.948	-119.703351	39.666211	1362.197063	246.074	-1	55.1536	8475	9/1/2020 6:14:07 PM
1.35736	0	-8.63804	24.8469	-2.45558	33863	26.42	-119.703349	39.666202	1362.123778	290.271	-1	65.1617	8458	9/1/2020 6:14:06 PM
1.35736	0	-8.63804	24.8469	-2.45558	33863	26.42	-119.703349	39.666202	1362.123778	290.271	-1	65.1617	8458	9/1/2020 6:14:06 PM
0.488187	0	-7.59242	24.6949	-2.41171	33871	25.948	-119.703351	39.666211	1362.197063	246.074	-1	55.1536	8475	9/1/2020 6:14:07 PM

Figure 8-17 The suspected near-crash event that was confirmed as not near-crash in GIS

To demonstrate a near-crash event, the UNR team applied 30ft distance, 10mph speed difference, and 45-degree direction difference for the preliminary filtering. However, the extracted "conflicts" included conflict events, with one example shown in Figure 8-18 and Figure 8-19, but also included noises and events that were not conflicts. Extra effort is needed to investigate the filtering results to further identify optimized criteria for extracting conflict events from the available trajectory data.

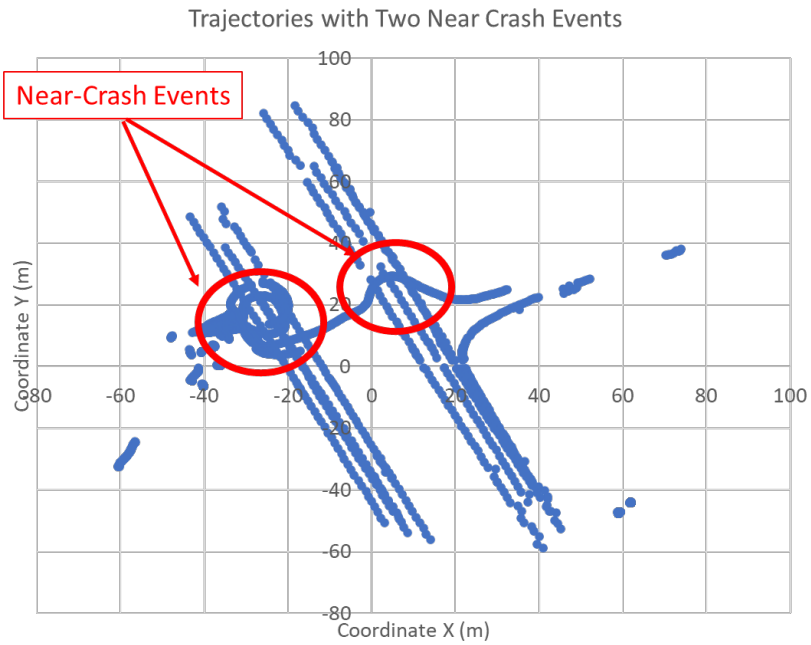

Figure 8-18 Example of conflict events identified from LiDAR data at N Boulder Hwy and Coogan Dr – LiDAR trajectories

Figure 8-19 Example of conflict events identified from LiDAR data at N Boulder Hwy and Coogan Dr – video screenshot

Other Situations

When reviewing the data, it was found that a high volume of activities at the northeast corner and the southeast corner, which caused much accessing-traffic on Calle De La Platte, east of the intersection, as shown in Figure 8-17. There were mailboxes at the northeast corner and car sales at the southeast corner of the intersection, which attracted those traffic and pedestrian jaywalks. The traffic accessing the two corner areas was mainly through unpaved at Calle De La Plata.

Figure 8-20 Sample of activities at the northeast corner and southeast corner at the intersection, 08/28/2020 7:00 PM

9. AUTOMATIC RECTANGULAR RAPID FLASHING BEACON (RRFB) WITH LIDAR SENSING

Site Introduction

Green Valley Pkwy at Amargosa Trail is a pedestrian crosswalk with RRFB pedestrian signals, as shown in Figure 9-1 and Figure 9-2 for the aerial map and street view.

The intersection properties are listed in follows:

- Two through lanes in each direction of Green Valley Pkwy; a northbound right-turn lane and a northbound left-turn lane on the north of the crosswalk; a southbound left-turn lane on the south of the crosswalk
- Raised median that is about 13-ft wide at the crosswalk, measured in Google Earth Pro
- 35 MPH speed limit with Green Valley Pkwy
- The closest AADT count station showed 35,000 AADT on Green Valley Pkwy in 2019 (NDOT TRINA database)
- Streetlights along Green Valley Pkwy

Figure 9-1 Aerial map of Green Valley Pkwy and Amargosa Trail

Figure 9-2 Street view of Green Valley Parkway (facing north)

- Separated sidewalks along with both directions of Green Valley Pkwy
- Northbound and southbound bike lanes along Green Valley Pkwy
- West of Green Valley Pkwy is a residential area; Paseo Verde Library, Country Fresh Farmers Market, Henderson Pavilion and a residential area are to the east of Green Valley Pkwy
- Bicycles and pedestrians crossing Green Valley Pkwy; some bicyclists rode along Green Valley Pkwy and crossed the road through the crosswalk median gap but did not use the crosswalk.
- Power supply available at the traffic poles on the north and south of the pedestrian crosswalk. Each pole is about 90 ft away from the crosswalk
- 20 crashes in 2011 through 2017, including five B and C-injury crashes, and 15 property-damage-only crashes (250-ft searching radius along Green Valley Pkwy)

Hardware

Table 9-1 lists the roadside LiDAR sensing equipment installed at Green Valley Pkwy and Amargosa Trail.

Table 9-1 Equipment List for Green Valley Pkwy and Amargosa Trail

Equipment	Quantity	Description
VLP-32c 32-Channel LiDAR	2	32-channel LiDAR, provides 360-degree LiDAR cloud points to cover the whole

		intersection and extend sensing distance along Boulder Hwy.
New Dell Rugged Latitude 5420 Laptop	1	8th Gen Intel® Core™ i7-8650U Processor (Quad Core, 8M Cache, 1.9GHz,15W, vPro); 32G DDR4 Memory; 256G solid-state hard drive; work temperature range is –20°F to 145°F
External Hard Drive	3	WD 4TB Black My Passport Portable External Hard Drive
Network Switch	1	D-Link 5 Port Gigabit Unmanaged Metal Desktop Switch (DGS-105)
LTE Wireless Connection Device	1	For remote monitoring of the system status, hard drive usage, and real-time system alert to the UNR team's email box.
Radio Communication for Remote RRFB Control	1	Tapco radio controller to remotely control the Tapco RRFB
Temperature Data Logger	1	For reading the enclosure inside temperature
Electrical Enclosure	1	29*24*12-inch, Type 3R Enclosure, Steel, Weather flow with Fan

LiDAR system and automatic RRFB installation

On June 19, 2019, two VLP-32c LiDAR sensors were installed at this site, one on the north traffic light pole and the other on the south pole. An electrical enclosure (LiDAR cabinet) was installed on the south traffic pole to house the edge computation laptop, external hard drives for data log, a network switch, an LTE modem for wireless communication to the system, and a TAPCO radio transmitter allowing the edge computer to turn on RRFB flashing remotely. The sensors and cabinet were about 9 ft above the ground. Locations of LiDAR sensors and the LiDAR cabinet are

shown in Figure 9-3, and pictures of installed equipment are presented in Figure 9-4. The sample LiDAR cloud points from the two sensors are presented in Figure 9-5. Only LiDAR data collection was operated in the first few months, for data to calibrate automatic RRFB and lab test.

Figure 9-3 Locations of LiDAR sensors and LiDAR processing cabinet at Green Valley Pkwy and Amargosa Trail

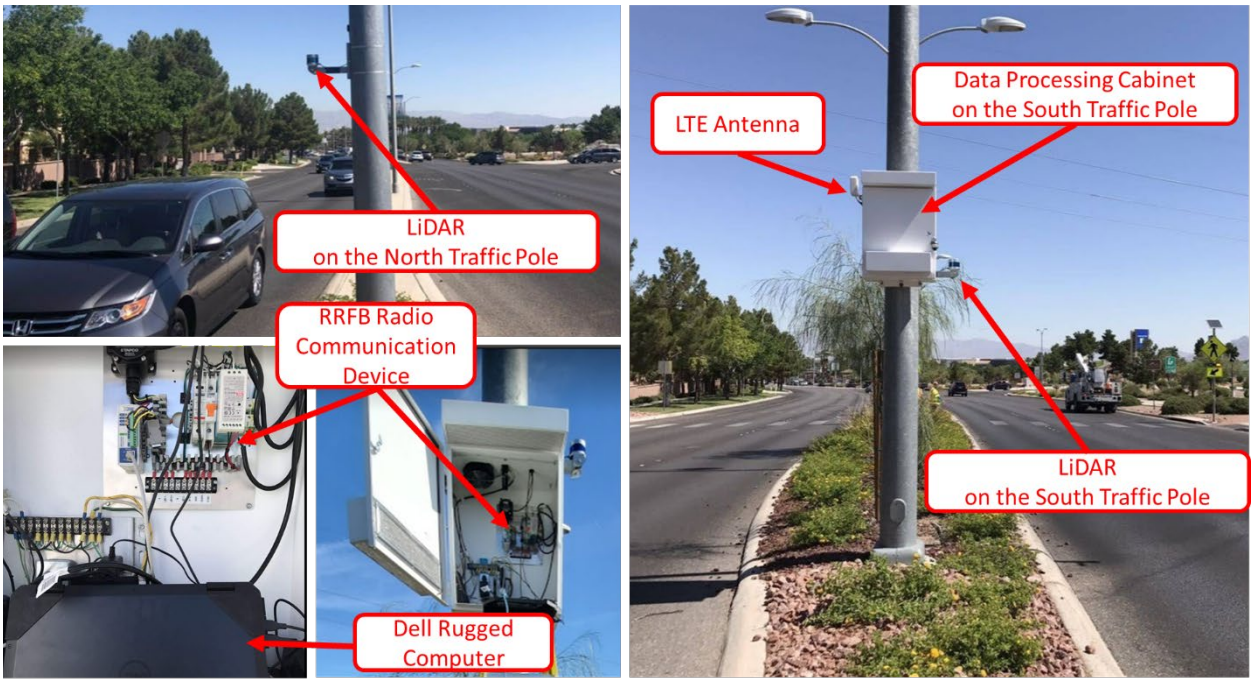

Figure 9-4 Pictures of the LiDAR sensors and the processing cabinet at Green Valley Pkwy and Amargosa Trail

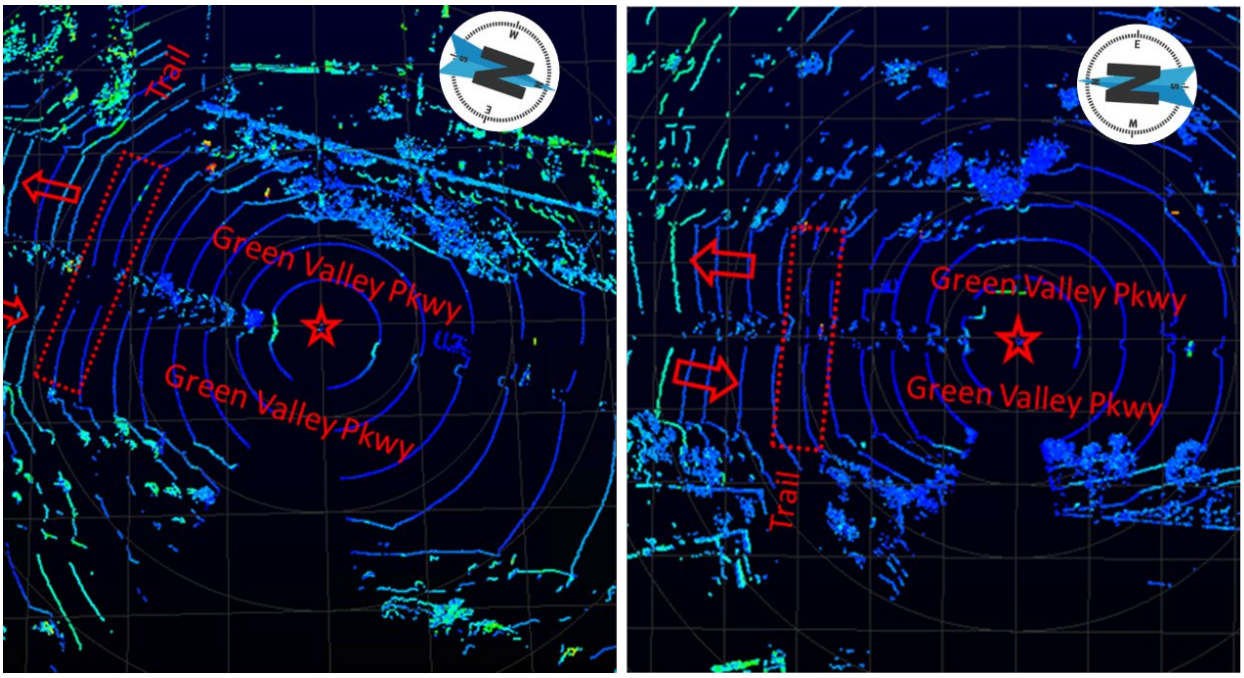

LiDAR data from the north sensor LiDAR data from the south sensor

Figure 9-5 Sample LiDAR cloud points from the LiDAR sensors at Green Valley Pkwy and Amargosa Trail

After the original system installation, it was found that the former RRFB radio signal receivers (at the RRFB poles) needed to be upgraded to receive the control signal from the LiDAR cabinet. Thus, new radio receivers were installed at the RRFB signals on July 1, 2019. The south LiDAR sensor was originally attached to the LiDAR device cabinet's bottom side, which caused significant occlusion and impacted the detection of southbound vehicle traffic. Therefore, the south LiDAR sensor was re-installed to the LiDAR cabinet top on August 26, 2019. Trees between installed LiDAR sensors and the crosswalk occluded LiDAR detection of pedestrians at the median, so the Henderson traffic team removed the trees. All these installation improvements significantly enhanced the sensing quality of the LiDAR system and are valuable experiences for future roadside LiDAR installation.

Communication, software, and maintenance

Remote connection to the LiDAR sensing system was through LTE wireless. The 10G LTE monthly data allowed UNR staff's daily system status check. The LTE connection allowed downloading new versions of LiDAR processing software to the edge computer and the software to send alert emails when system exception was detected. The UNR LiDAR logging software was installed on the edge computer. Another installed software package was for real-time crossing detection and automatic RRFB control. The detection and RRFB control software logged each crossing event and related the RRFB-triggering event.

The maintenance effort included a daily remote check of the system (started in February 2020) and replacement of external hard drives when they were full. During the Covid-19 virus pandemic lockdown, the Henderson traffic team exchanged hard drives and shipped them to UNR.

Problems and solutions

Windows 10 automatic system updates caused the edge computer restart and stopped the data logging software as at the other sites. Scheduled system updates are suggested for continuous maintenance and new deployment, especially in the early months of the deployment. The project team originally checked system status every week and sometimes found days of data missing because of the system restart. UNR allocated a dedicated staff to check the system status every day and added the system exception alert function to the software, which minimized data missing. Later in this project, the data compression function extended required hard drive exchange frequency to every three months.

The cat-5e ethernet cable between the north LiDAR sensor to the LiDAR cabinet experienced an issue of data transmission package loss, so for a LiDAR data frame, part of cloud points could be missing. The issue was caused by the long connection distance and cable crosstalk. The distance between the two traffic poles is about 180-ft. When cable wiring went through the poles and underground conduits and kept extra lengths of cable on each side of the connection, the total cat-5e cable length was about 250-ft. It did not reach the 300-ft limit of cat-5e but was long enough to be sensitive to crosstalk influence. The extra length of cable on each connection end was later cut off to shorten the total cable length, which solved the communication package loss issue.

When logging two LiDAR sensors' data to the same external hard drive, data transmission package loss also happened, which could be related to the hard drive's continuous read and write speeds. Therefore, each sensor's data was then logged to an individual hard drive.

This project implemented the first LiDAR automatic RRFB at Green Valley Pkwy and Amargosa Trail. LiDAR sensors continuously scan the crosswalk environment, and the roadside sensing system automatically triggers RRFB flashing if any crossing event is detected. The LiDAR automatic RRFB in this project was designed as a safety backup system of the conventional RRFB. Physical RRFB buttons are available for crossing pedestrians/bicyclists to trigger RRFB flashing. If any pedestrian/bicyclist does not press the RRFB button, the LiDAR system automatically turns on RRFB before the pedestrian steps into vehicle lanes. This first LiDAR automatic RRFB was implemented to address the low percentage of pedestrians pressing RRFB buttons at this crosswalk. The project team conducted a field study at the crosswalk on 9/15/2019 5:00 am through 9/17/2019 10:00 pm to identify percentages of pedestrians and bicycles not using the RRFB button. Among 194 crossings, 35.56% of pedestrians and bicyclists did not press RRFB buttons before crossing, as listed in Table 9-2. Notably, more than half of the bicyclists did not use RRFB buttons before crossing. More bicycles (71.70%) did not use the button from west to east than pedestrians (28.30%). The reason could be that the west RRFB button location is not convenient for bike riders to reach. From east to west, percentages of bicycles (58.85%) and pedestrians (46.15%) who did not use the RRFB button were closer.

For traffic engineers, a common consideration with RRFBs is the influence on vehicle traffic mobility, especially the reduced road capacity caused by unused RRFB flashing time. Most

pedestrians/bikes can cross a road in a shorter time than the predetermined RRFB flashing period. However, RRFB signals keep flashing until the configured flashing time (30 seconds for the Amargosa Trail crosswalk) is over. The flashing without pedestrians/bicyclists often confuses drivers and slows down traffic. The automatic RRFB implemented in this project can actively send out a "turn off" message for stopping RRFB flashing when crossings are completed and there are no other approaching pedestrians. However, the RRFBs at this crosswalk does not take any "turn off" control, so automatic "turn off" did not function at this crosswalk. It can be applied to other RRFBs or other pedestrian crossing signal systems if those systems take the "turn off" control.

Table 9-2 RRFB Button Usage at the Crosswalk of Green Valley Pkwy and Amargosa Trail

	Pedestrian Crossings (percent in total crossing events)	**Bicycle Crossings (percent in total crossing events)**	**Sum (percent in total crossing events)**
Pressing Button	79 (40.72%)	46 (23.71%)	125 (64.44%)
Not Pressing Button	21 (10.82%)	48 (24.74%)	69 (35.56%)
Total	100 (51.54%)	94 (48.45%)	194

Data flow and control logic

The roadside LiDAR sensing system detects, classifies, and tracks movement of each road user. It then determines whether an “on” message needs to be sent to RRFB for flashing based on pedestrians/bicyclists’ locations and movement directions. Figure 9-6 shows the system flow chart. The maximum sensing distance of VLP-32c LiDAR is a 200-meter radius, so the LiDAR system can detect jaywalks in an extended range (shorter than 200-meter radius for pedestrian detection). However, the system was configured to trigger RRFB flashing only when a crossing is at the crosswalk. This configuration avoids drivers being confused by the crosswalk RRFB flashing when jaywalking happens at an upstream or downstream location. Figure 9-7 demonstrated the defined zones where the roadside LiDAR system responds to crossing events for automatic RRFB flashing. The pedestrian crossing detection logic was developed based on the generated trajectories from LiDAR data. The direct and straightforward logic for crossing detection is determined by whether a pedestrian in the detection zone moves towards the other side of the road, based on LiDAR trajectory data.

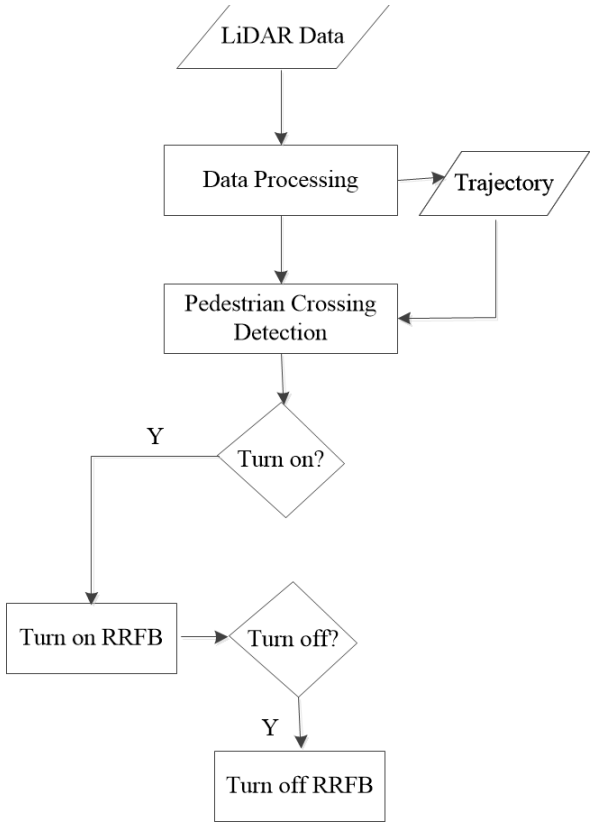

Figure 9-6 Flow chart of LiDAR automatic RRFB control logic

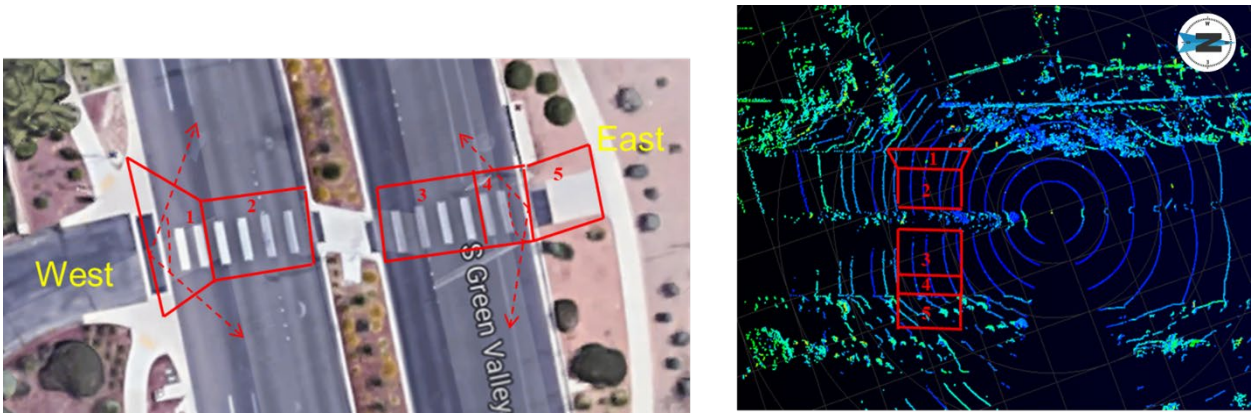

Figure 9-7 Configured crossing event zones for triggering RRFB flashing, on Google Aerial Map and LiDAR cloud points

Performance evaluation - Lab evaluation

Before operating the automatic RRFB at the crosswalk, the project team first evaluated the control logic performance in a UNR lab with logged LiDAR data and trajectories. The lab test simulated crossing events with historical LiDAR data and trajectories and then reviewed the control logic's responses. Accuracy of detection and RRFB control was evaluated by comparing the triggering

event to manually identified crossing events for the same historical data. Manual identification of crossing events was performed through the LiDAR data visualization software Veloview and conducted by two UNR staff for quality control. We utilized the data collected from 6/19/2019 10:00 am to 7/2/2019 8:30 am for the lab evaluation. There were 845 crossing events in the 13-day data. The following control exceptions were reviewed and logged:

False turn-on – there was no crossing event, but the system sent "on" signal

Missed turn-on – there was crossing events, but the system did not respond with "on" signal

False turn-off – a crossing event was not completed, but the system sent "off" signal (it can be evaluated in the lab test with historical data, but the automatic "off" function was not implemented in the field implementation)

Missed turn-off – a crossing event was completed and there were no other crossing requirements, but the system did not respond with "off" signal (it can be evaluated in the lab test with historical data, but the automatic "off" function was not implemented in the field implementation)

Among the control exceptions, false turn-off is most dangerous because it turned off RRFB flashing when pedestrians/bikes are still on the road. The lab evaluation results are presented in Table 9-3 that shows no false turn-off and less than 1% for each of the other three exception types. Looking into those exceptional cases, they were all caused by special events, as described in "3.5 Special events". The control logic correctly responded to all crossing events that used the crosswalk.

Table 9-3. Off-line test based on four types of errors (845 crossing events)

Error type	False turn-on	Missed turn-on	False turn-off	Missed turn-off
Number of errors (percentage)	5 (0.59%)	7 (0.83%)	0	8 (0.95%)

Here are examples of special events causing exceptions.

1) False turn-on example, Figure 9-8: a bicycle came from Amargosa Trail and showed a crossing intent but turned into the bicycle lanes in Zone 1. An “on” RRFB message was sent out as a false “turn on” case.

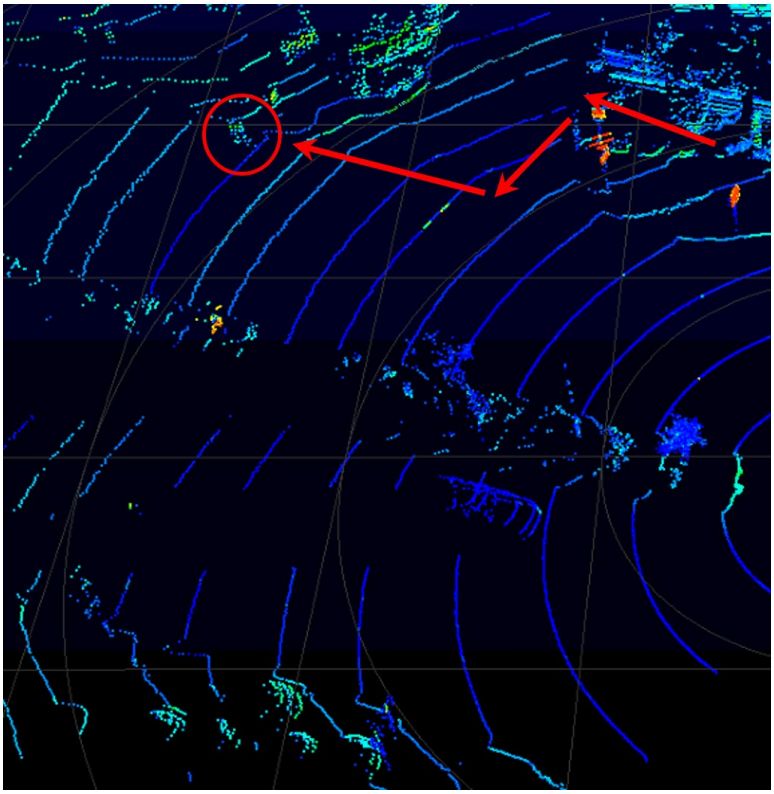

Figure 9-8 Illumination of a false turn-on event example

2) Missed turn-on example, Figure 9-9: a pedestrian walked along the median and then crossed the median. The automatic control did not respond to this crossing event.

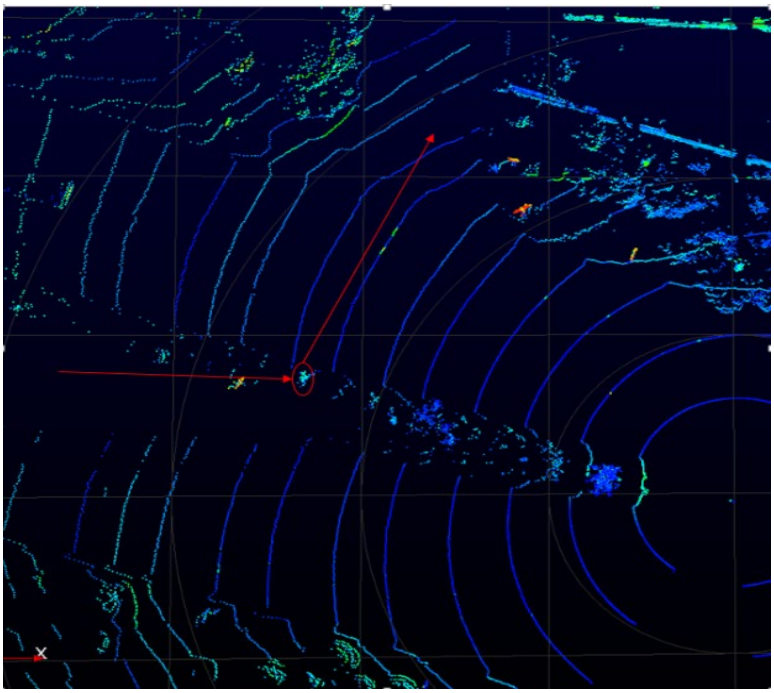

Figure 9-9 Illumination of a missed turn-on event example

3) Missed turn-off example, Figure 9-10: a pedestrian crossing was not along the crosswalk. The automatic RRFB control did not detect a completed crossing event at the other end of the crosswalk, so it did not send an "off" RRFB message.

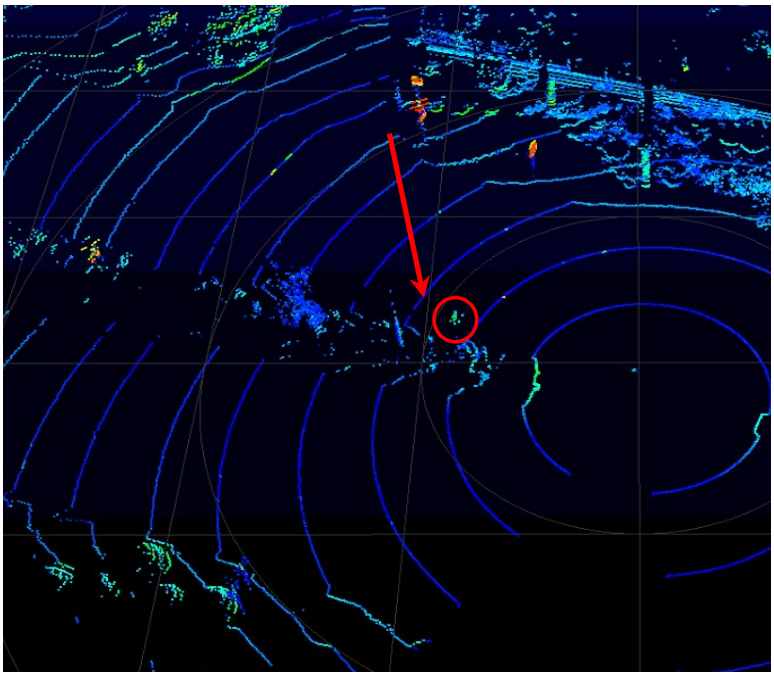

Figure 9-10 Illumination of a missed turn-off event example

Field test

After the lab evaluation proved the control logic performance and further system calibration based on the lab evaluation results, the LiDAR automatic RRFB was implemented at the crosswalk and turned on with UNR staff at the site to monitor the system operation and conduct field performance evaluation. Crossing events and RRFB flashing signals were recorded with a video camera three days from early morning to late night. Device locations are shown in Figure 9-11. The field evaluation validated whether all crossing events through the crosswalk were successfully detected, whether automatic RRFB responded to each crossing, and whether there was any false RRFB flashing when there was no actual crossing pedestrians or bikes.

The field test was performed from 9/15/2019 5:00 am to 9/17/2019 10:00 pm. With 194 crossing events during the field test, the system had only one missed turn-on exception: a bicyclist in a northbound vehicle lane crossed the median rather than from any end of the crosswalk. The system provided 99.5% control accuracy for responding to crossing events. After the field validation, the LiDAR automatic RRFB has been operating since February 18, 2020.

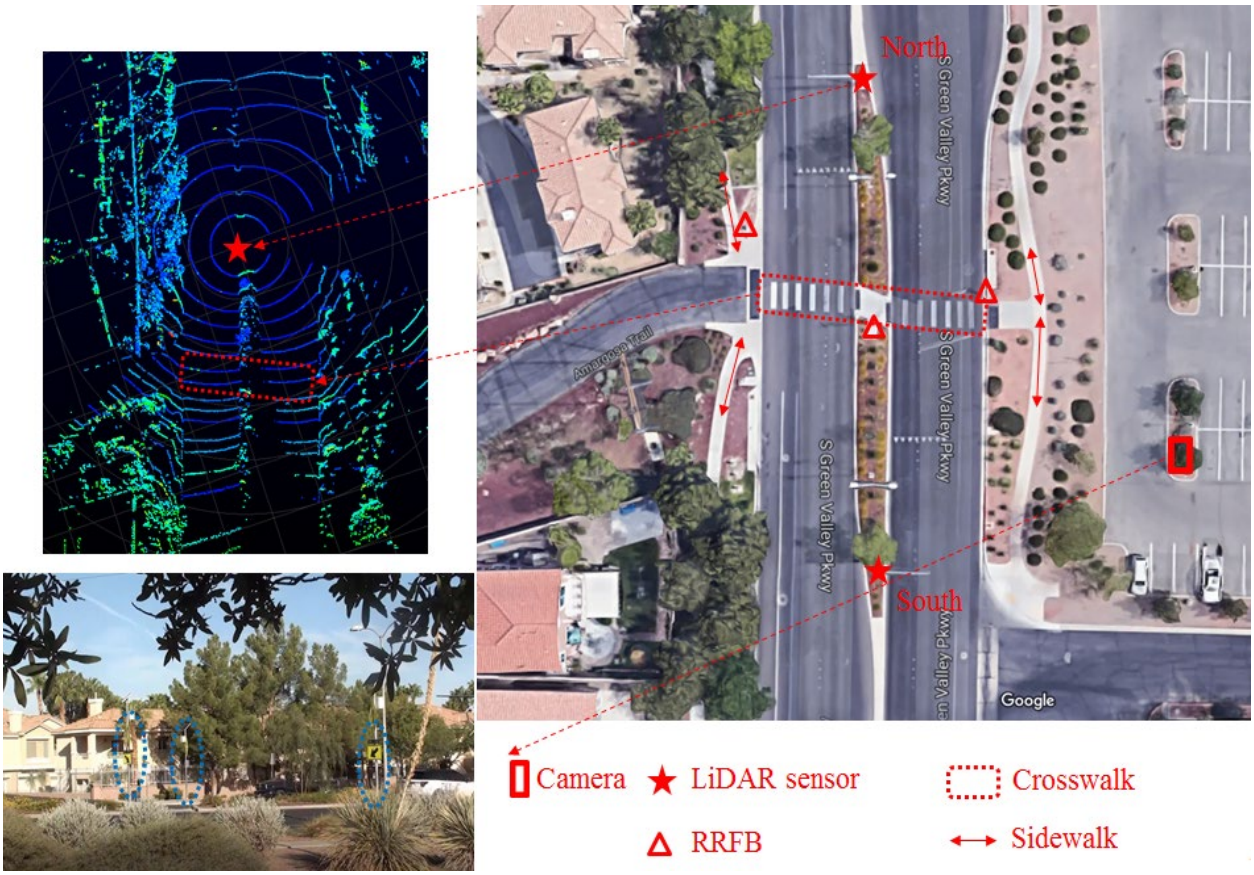

Figure 9-11 System layout during the field test

The implemented automatic RRFB control did not use prediction algorithms to control RRFB, although the UNR team developed and published several pedestrian trajectory prediction algorithms in journal papers [7]. Even the best of today's trajectory prediction algorithms could still cause multiple false turn-ons every day at this site, which could confuse drivers and may cause drivers to gradually ignore the RRFB warning signal. The LiDAR automatic RRFB system at this crosswalk, as a back-up of the physical RRFB buttons, turn on the flashing signal only when pedestrians/bikes entered the roadway area (curb to curb including vehicle lanes, bike lanes and shoulders). Among all crossings without pressing the button, RRFB automatically flashed when pedestrians or bicyclists entered roadway 3.5 ft from the curb based on the field evaluation, as shown in Figure 9-12.

Figure 9-12 Locations where RRFB automatically start flashing if buttons are not used

Crossing event log

During the 24/7 running of the automatic RRFB system, crossing events were logged to include time, crossing location, and triggering events. Each crossing event may include multiple pedestrians or bikes in a group. Figure 9-13 presents daily crossing events from 2/10/2020 to 5/3/2020, which are also frequencies of RRFB activation - manual and automatic. Due to system maintenance, the automatic RRFB system stopped on a few days. On average, the number of daily crossings at this crosswalk is about 133. An important note is that after the Nevada Governor Steve Sisolak ordered the closure of non-essential businesses in the state on March 17, 2020, there were more crossing events at the crosswalk.

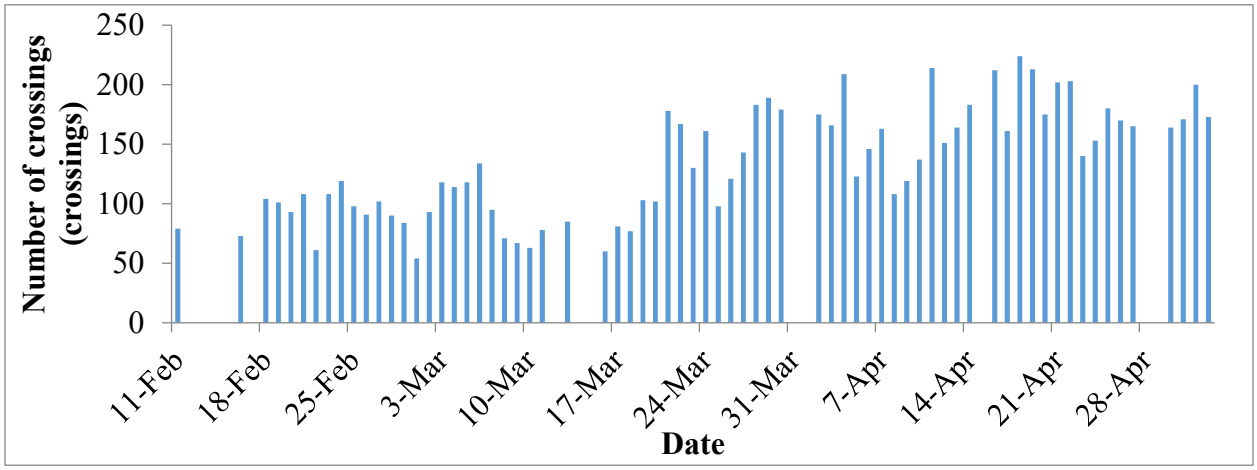

Figure 9-13 Daily distribution of crossing events at Green Valley Pkwy and Amargosa Trail

10. ROUNDABOUT CAPACITY CALIBRATION WITH LIDAR DATA

There have been many proposed methods for computing capacity at roundabouts either by regression models or analytic models, but the industry of traffic engineering utilizes the Highway Capacity Manual (HCM) as a guide to measuring capacity and other performance measures such as level of service (LOS), delay, queue, and volume-to-capacity ratio. For roundabouts, HCM employs a combination of regression and analytic models to derive a relationship between conflicting traffic flow and capacity of entry flow. For roundabouts, the conflicting traffic flow is the circulating flow, and the capacity of the entry is at the entry lanes of the roundabout leg. The entry capacity decreases as the conflicting circular flow increases. The analytic model that the HCM employs is based on the gap acceptance theory.

Gap acceptance theory has been a useful model to explain the two-way stopped controlled intersections where a minor stream vehicle needs to decide which gap or headway is large enough to enter into the major stream traffic. For the case of roundabouts, the minor stream refers to the entry lane(s) which is yield controlled, and the major stream refers to the circulatory lane(s). The minor stream driver is referred to as the decision vehicle. The headway with which the decision driver is willing to 'accept' and enter the major stream flow is a function of many factors such as the driver's experience, environmental factors, geometric design, speed, traffic volume, and more. The tendency for the decision driver to either reject or accept a headway is captured by measuring the critical headway. The critical headway is the minimum time headway between two successive major stream vehicles for which the minor stream decision vehicle can make a maneuver to enter the major stream (2). Critical headway is one of the gap acceptance parameters used. The second gap acceptance parameter is follow-up headway, which is the time headway between the departure of one minor stream vehicle and the departure of the subsequent minor stream vehicle into the major stream utilizing the same gap under the condition of continuous queueing (2). The HCM determines these gap acceptance parameters based on field data across the United States to derive a capacity equation that is a function of the conflicting flow.

Critical headway cannot be measured directly because each driver is different, so the individual critical headway will vary from driver to driver. Further analysis of rejected headway and accepted headway from field data must be conducted. A rejected headway is the major stream headway between two successive vehicles for which a minor stream decision vehicle decides not to enter the major steam. Conversely, an accepted headway is a major stream headway between two successive vehicles for which a minor stream decision vehicle decides to enter the major stream. Therefore, many data points of rejected and accepted headways need to be collected, and further analysis is conducted to extract the critical headway. Many methods have been developed to determine the critical headway such as Raff's Method, Maximum Likelihood Method, Probability Equilibrium Method, Median Method, and many more. The Raff's Method and Maximum Likelihood Method are the two most common in the literature. In this study, Raff's Method is employed due to its' ease of computation. The second gap acceptance parameter is the follow-up headway, which is calculated by taking the average of the field measured follow-up headways.

Once the two gap acceptance parameters are determined, they can be used to calibrate the HCM 2016 capacity equation. As a result of observed variability between states and cities in gap acceptance parameter results, HCM has provided a method for calibrating the capacity equation

for more accurate measurement of capacity at certain states, cities, and even specific roundabouts and roundabout legs. For example, Nevada has their own capacity equation developed by Ahiamadi et al (2).

Many research or government studies of gap acceptance are performed mainly by video data and extraction of data manually or through software. Some of the challenges of these studies are the use of multiple cameras to capture the areas of interest, typically two. The benefits that LiDAR has over video is that LiDAR is much less computationally demanding, its' 360-degree detection range makes it easier to outfit at an intersection as opposed to placing several cameras, and LiDAR is not limited by lighting condition. Because of this, LiDAR can sense a wider detection range for greater periods and is not limited to the vehicle's immediate surrounding environment as video sensors may be (3). Where video sensing provides high-resolution imaging, LiDAR provides high accuracy cloud points that can be used to track trajectories of all road-users such as volume, location, speed, direction, headways, and even road user size (3).

The purpose of this study is to propose an automatic method to extract headway information from roadside LiDAR trajectory data which is processed through Python Scripts and ArcGIS software. From this trajectory data, the speed and timestamps are used to determine the critical headway for stopped vehicles and entry capacity at roundabouts. Previous studies have yet to develop such automatic methods for headway extraction and analysis. Many use the method of manual extraction via video, or software to assist in generating the desired headway information. Further, headway data extracted from high-resolution traffic trajectory data has not been done using LiDAR or other sensing devices. The implication of such a methodology are that headway analysis can be completed automatically upon completion of data collection which allows for faster turnover times for analysis. Further, using the high-resolution traffic trajectories, altogether more detailed analysis at the behavior-level of the road user can be provided to gain greater insight into the operational and safety performances on the road.

Roadside LiDAR Trajectory Headway Extraction

With the georeferenced trajectory of all road users obtained in the data preprocessing stage, the volume, speed, and headways can be automatically extracted for specified detection zones for further analysis. First, each 30-minute geolocated trajectory data is converted to GIS feature classes. Then in ArcGIS, the detection zones are drawn for the entry lanes and conflicting circulatory lanes using the draw command and converting the drawings into feature classes; a schematic is shown in Figure 10-1. The points shown in Figure 10-1 illustrate the trajectory of the road user, in this case vehicles, every 0.1-seconds. Next, an ArcGIS plugin of python scripts created by the authors is run to determine the volume, direction, size, and speed of each road user within each detection zone. From the output obtained by the python script, the desired input for headway extraction are outlined in Figure 10-1 and detailed as follows:

- Conflict Zone: The area for which the vehicle trajectories cross or come into conflict.
- Entry Vehicle Stop (E_{stop}): Timestamp for which the entry vehicle begins stopping.
- Entry Vehicle Enters (E_{enter}): Timestamp for which the entry vehicle accepts the headway and enters the roundabout.

- Entry Average Speed (V_{avg}): Average speed of entry vehicle trajectory points in the detection zone.
- Circle Vehicle Enters Conflict Zone ($C_{conflict}$): Timestamp for which the circulating vehicle arrives at the conflict zone.

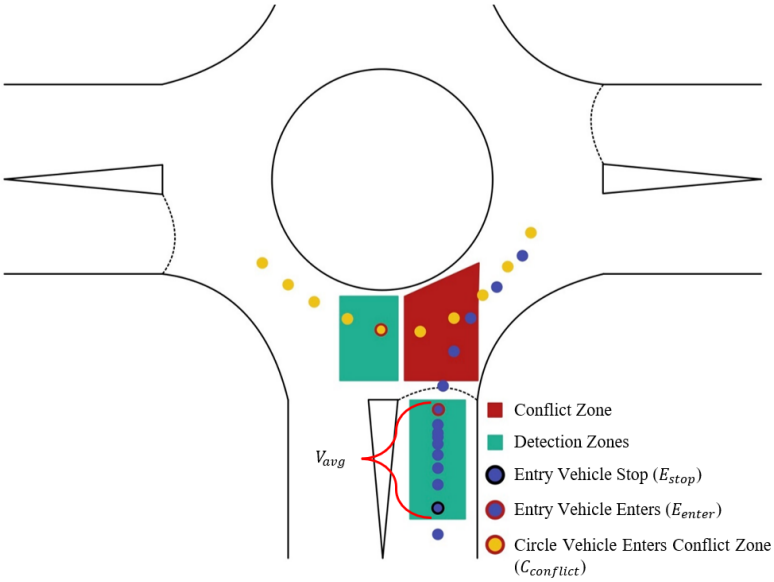

Figure 10-1 Vehicle Trajectories and ArcGIS Detection Zones

The data inputs outlined in Figure 10-1 are used to determine the following:

- Rejected lag: the time difference between an entry vehicle arriving at the yield line and a circulating vehicle arriving at the conflict zone for which the entry vehicles rejects.
- Accepted lag: the time difference between an entry vehicle arriving at the yield line and a circulating vehicle arriving at the conflict zone for which the entry vehicles accepts (does enter).
- Rejected Headway: the time difference between two following vehicles measured from the front bumper of the leading vehicle to the front bumper of the following vehicle for which a corresponding entry vehicle rejects.
- Accepted Headway: the time difference between two following vehicles measured from the front bumper of the leading vehicle to the front bumper of the following vehicle for which a corresponding entry vehicle accepts.
- Follow-up Headway: The time headway between queued entry vehicles utilizing the same headway in the conflicting circulatory flow.

For a rejected lag, the time difference between when an entry vehicle comes to a stop and the next circulatory vehicle enters the conflict zone is recored as the rejected lag if the entry vehicle does not enter the roundabout before the cirulatory vehicle enter the conflict zone. While this value is not used in this study, it may be used for further analysis in subsequent studies. Furthermore, it is essential to differentiate between rejected lags and rejected headways because the rejected

headways are major stream headways that are observed by the minor stream decision vehicle whereas rejected lags are not.

For a rejected headway, when an entry vehicle remains in the detection zones while two or more vehicles in the circulatory lane pass the conflict zone, the corresponding circulatory headways are extracted and set a rejected headways. Alternatively, when the timestamp for which the entry vehicle enters is in between two circulatory conflict entry timestamps, the entry vehicle entered the circulatory stream and the corresponding circulatory headway is recorded as an accepted headway.

The follow-up headway is determined by measuring the headway of queued entry vehicles that enters the same circulating headway when the leading vehicle comes to a stop. Once the maximum frame index for the entering vehicle is recorded, the headway of the following queued vehicles is recorded. The maximum threshold defined is 5-seconds to ensure that only vehicles in the queue are recorded. Similar to the average speed threshold, this threshold value was visually inspected checking the Veloview cloud points for validation. The measurement is stopped once a new circulatory vehicle enters the conflict zone or the entry headway exceeds 5-seconds.

HCM 2016 Capacity Equation Calibration

The method for calibrating the HCM 2016 capacity equations is outlined. Equations (2) – (4) outline the HCM calibration equations based on the inputs of critical headway, follow-up headway, and conflicting flow.

$$C = Ae^{(-Bv_c)}$$

(Equation 10-2)

$$A = \frac{3600}{t_f}$$

(Equation 10-3)

$$B = \frac{t_c - (\frac{t_f}{2})}{3{,}600}$$

(Equation 10-4)

Where;

$C = lane\ capacity, passenger\ cars\ (pc)/hr$

$v_c = conflicting\ flow, pc/hr$

$t_c = critical\ headway, seconds$

$$t_f = follow - up\ Headway, seconds$$

Evaluation with field Collected Data

The evaluation of the proposed method is outlined. First, the case study summarizes the site and data collection details. Then, the results and analysis go over the output from the method proposed such as rejected headway, accepted headway, critical headway, follow-up headway, and the capacity equation.

The case study for his report will be outlined. The study was conducted in Reno, Nevada, United States. The study roundabout is located in the South Reno residential area at the intersection of State Route (SR) 341 and Veterans Pkwy. Figure 10-2 on the left shows the roundabout and indicates the LiDAR sensor location, and Figure 10-2 on the right illustrates the georeferenced LiDAR trajectory results. For this study, only the south leg is considered. The south leg consists of two entry lanes that are yield controlled with the left – or inner – lane being a designated left-turn lane and the right – or outer – lane being a designated left-through-right lane. There is one corresponding conflicting – or circulatory – lane that is a designated through-left lane. Each entry lane will be considered separately for this study, with critical headway, follow-up headway, and capacity equations being determined for each. The vehicle trajectory data was collected at this roundabout using a single LiDAR sensor. LiDAR data collection took place on Sunday, June 7th, 2020 from 9:30 AM – 9:00 PM with 4:30 PM – 5:00 PM and 6:00 PM – 6:30 PM being omitted because of rain causing error in the headway extraction results. The traffic at this intersection is homogeneous and there were only 11 pedestrians for the full day on the south leg crosswalk. Therefore, heavy vehicle traffic and pedestrian factors are not considered.

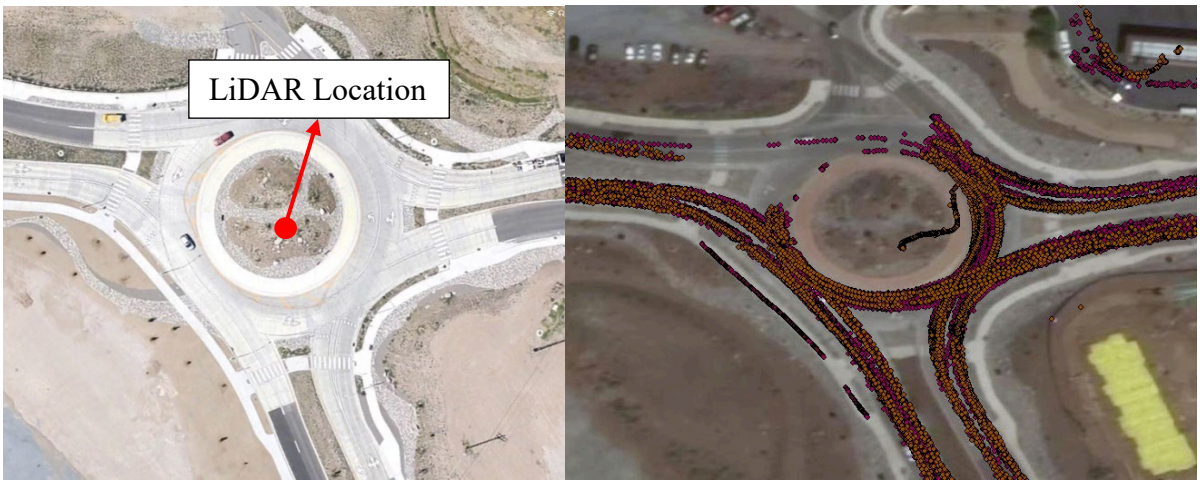

Figure 10-2 (left) Study Roundabout and LiDAR Locations and (right) Georeferenced LiDAR trajectory Results

Figure 10-3 illustrates sample trajectories and their corresponding detection zones. For the entry trajectories the detection zone tracks the first and last point within the detection zones, which is tracking the front left car of the vehicle. For the circle trajectory, the detection zone tracks the last point within the detection zones, which is the rear corner closest to the detection zone. The corner that is being tracked is consistent throughout each vehicle trajectory, which means the true headways are being measured.

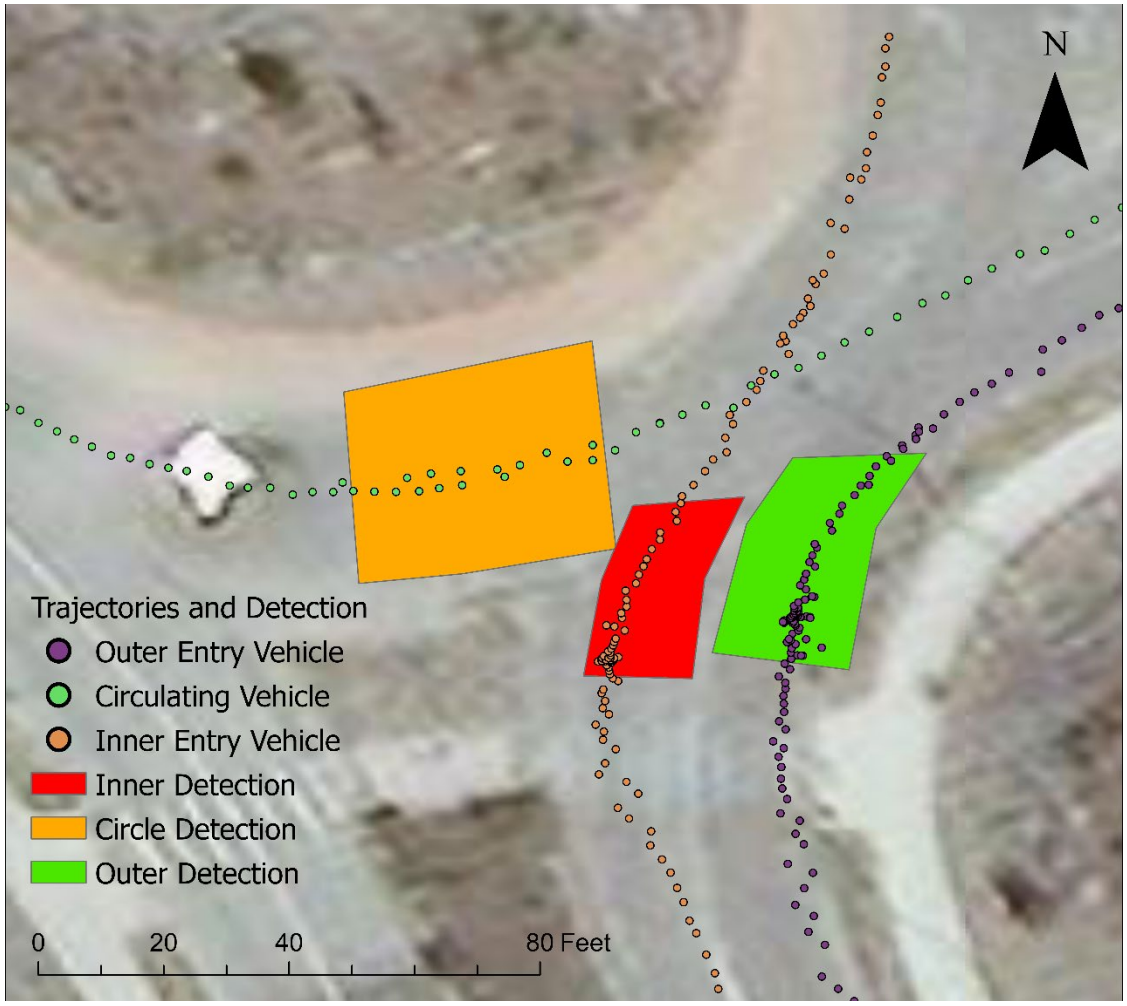

Figure 10-3 Case Study Sample Trajectories and Detection Zones

Results and Analysis

The results and analysis of the data extraction are outlined. The rejected, accepted, and follow-up headways were recorded for the full data collection period. Table 10-1 and

Table 10-2 Comparison of the Total Number of Headways from Code and Actual for the Outer Lane shows the number of headways extracted versus the actual number for the inner lane and outer lane, respectively. With higher traffic volumes determined for the outer entry lane, it is expected to see a greater number of headways for the outer lane. The reason for the difference between the code output and the actual is due to various errors outlined as such:

- Follow-up headways recorded that were outside the queue
- Vehicles that were in the queue and accepted the same headway that was not recorded
- Entry vehicles stopping before reaching the detection zone
- A trailer being counted as a vehicle
- Occlusion of a vehicle by another larger vehicle
- The vehicle made a stop, but was not recorded
- The vehicle did not make a full stop, but was recorded
- Change in 30-minute spreadsheet file
- Priority reversal

Table 10-1 Comparison of the Total Number of Headways from Code and Actual for the Inner Lane

Headway Type	Number of Headways		Percent Difference
	Code	Actual	
Rejected Headways	267	282	5%
Accepted Headways	43	46	7%
Follow-up Headways	43	45	5%

Table 10-2 Comparison of the Total Number of Headways from Code and Actual for the Outer Lane

Headway Type	Number of Headways Extracted		Percent Difference
	Code	Actual	
Rejected Headways	606	619	2%
Accepted Headways	123	122	1%
Follow-up Headways	251	236	6%

Gap Acceptance Parameters

The results for the gap acceptance parameters for each entry lane are outlined. The first gap acceptance parameter is the critical headway. There have been many proposed methods for determining this value. The method that this study is using is Raff's Method because of its ease of computation for this case study. Figure 10-4 and Figure 10-5 illustrate Raff's Method plots for the inner lane and outer lane, respectively. The follow-up headway is determined by taking the average of all the follow-up headways. The critical headways and follow-up headways for both the inner and outer lanes are tabulated in Table 10-3. The acceptable range of accepted headways used was 3 – 10 seconds as 10 seconds adequately captures real headways that are observed by the driver. Longer headways were not considered because they could not be reasonably observed by the driver. The lower thresholds ensure that no errors show up. It was observed that accepted headways lower than 3 seconds is due to detection zone issues of vehicles not following the usual travel lane path.

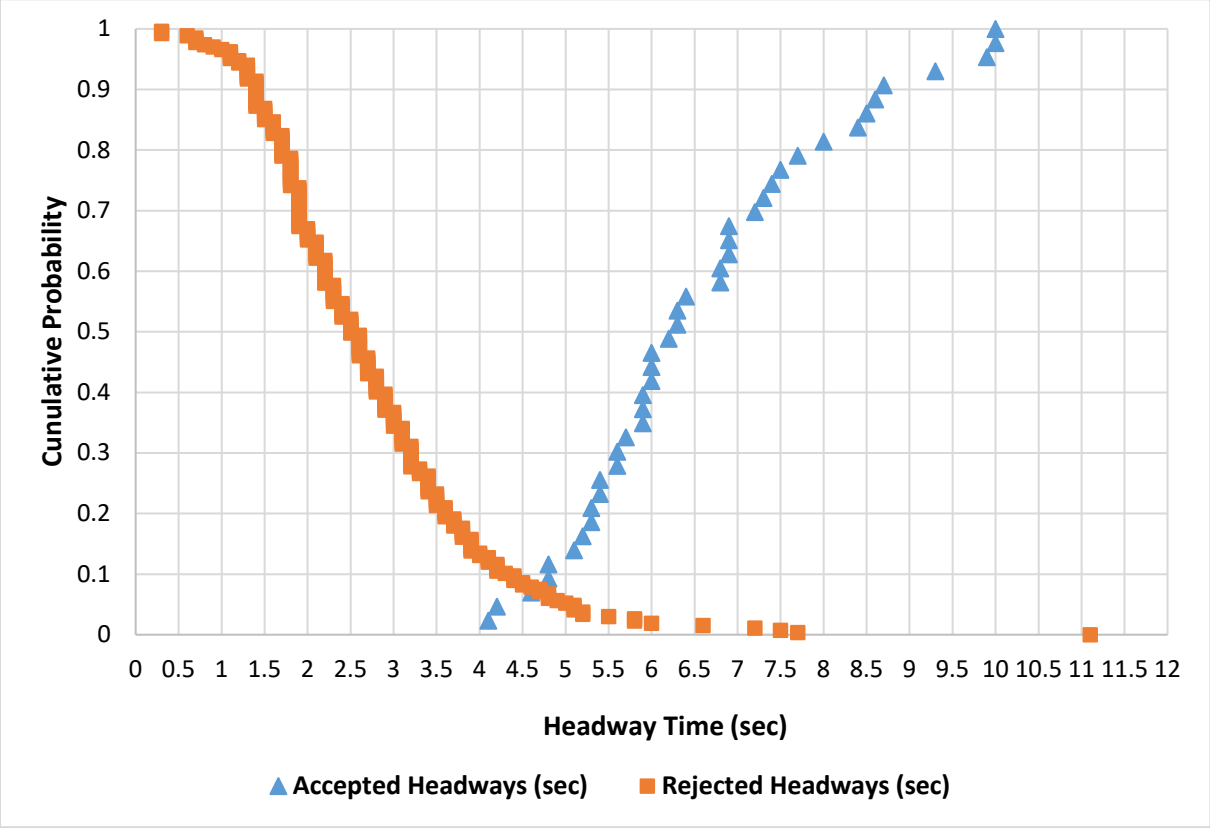

Figure 10-4 Raff's Method Cumulative Distribution Plot for the Inner Lane

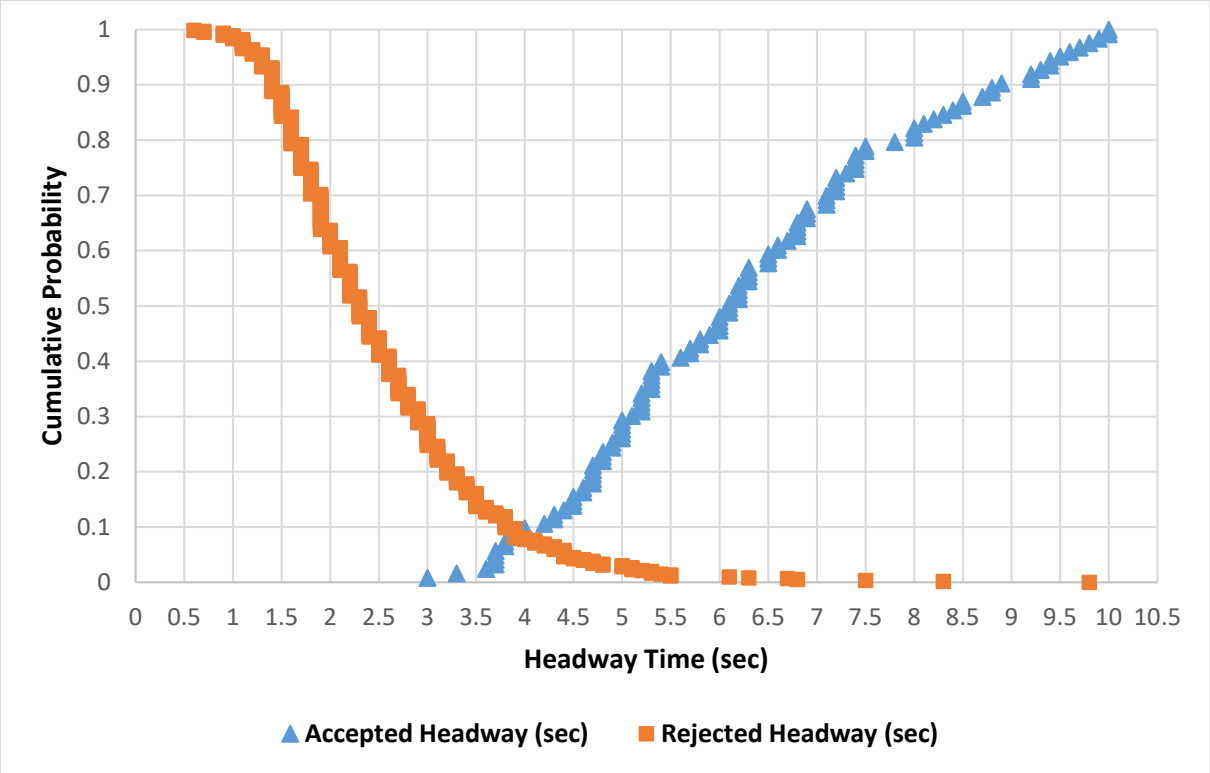

Figure 10-5 Raff's Method Cumulative Distribution Plot for the Outer Lane

Table 10-3 Critical Headway and Follow-up Headway

Headway	Inner Lane (sec)	Outer Lane (sec)	Percent Difference
Critical Headways (sec)	4.7	4.0	16%
Follow-up Headways (sec)	2.7	2.6	4%

HCM Calibration

The HCM calibration is conducted for both entry lanes based on the gap parameter results and is compared to the HCM 2016 and Nevada calibrations. Equation 5 is the capacity equation for the HCM 2016, Equation 6 is the capacity equation derived for the State of Nevada, Equation 7 is the capacity equation for the study inner lane, and Equation 8 is the capacity equation for the study outer lane.

$$C = 1{,}420e^{(-0.91\times10^{-3})v_c} \quad (5)$$

$$C = 1{,}230e^{(-0.67\times10^{-3})v_c} \quad (6)$$

$$C = 1{,}333e^{(-0.93\times10^{-3})v_c} \quad (7)$$

$$C = 1{,}385e^{(-0.74\times10^{-3})v_c} \quad (8)$$

Figure 10-6 graphically represent the difference between each capacity equation. The capacity is plotted for a variety of conflicting vehicle volumes ranging from 0 to 2500 vehicle per hour, with corresponding capacities ranging from 1400 vehicle per hour down to below 200 vehicles per hour. In comparing each of the curves. The study inner and outer lane capacity results are consistent with the capacities from the HCM 2016 and Nevada capacity results. The outer lane capacity is consistently larger than the inner lane capacity. Furthermore, the outer lane capacity has the highest capacity for most of the conflicting vehicle volume range; whereas, the inner lane capacity has the lowest capacity for most of the conflicting vehicle volume range.

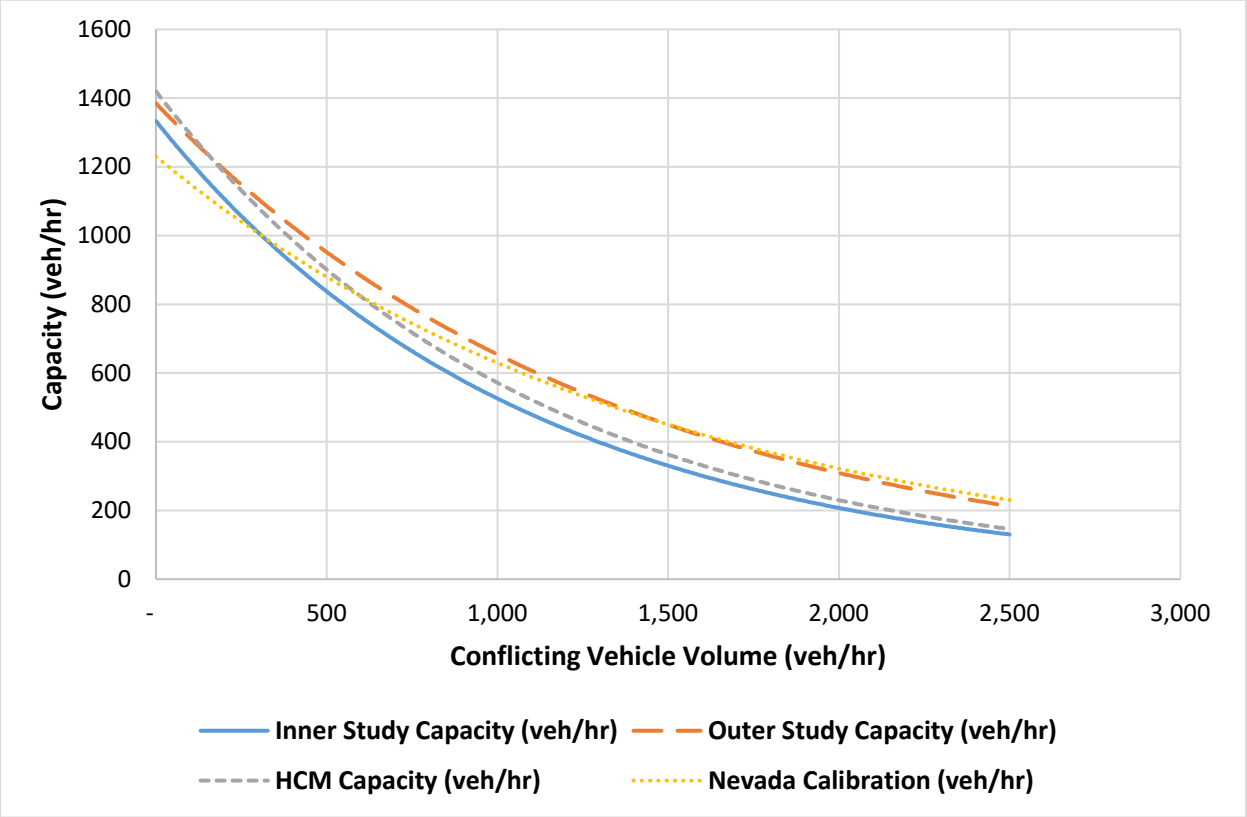

Figure 10-6 Capacity Equation Curves from the Study, HCM, and Nevada Calibrations

11. AUTOMATIC VEHICLE-PEDESTRIAN YIELD RATE ANALYSIS WITH LIDAR

In the case uncontrolled crosswalks, pedestrian-vehicle interactions (PVIs) can be defined by when a pedestrian has to slow down or stop at the curb because a vehicle is approaching, or when a vehicle decelerates, stops, or accelerated because of a pedestrian's intent to cross or during crossing. Two behaviors can be studied in such events, the behavior of the pedestrian, and the behavior of the vehicle. The most common measure of pedestrian behavior at uncontrolled crosswalks is gap time (Amado et al. 2020). In this context, the gap time is the vehicle time headway that a pedestrian is willing to cross within. In other words, gap time i s a measure of the assertiveness and comfort level of the pedestrian when navigating the crosswalk; however, it can also be used to measure the risk to the pedestrian. Gap acceptance theory is a common method to measure gap time, which looks at both gaps that pedestrians accept and reject and derives a critical gap for which most of the pedestrians are willing to accept.

Trajectory data extracted from sensors such as LiDAR and camera has birthed a new research area for SSM since it can track road users through time and space at a high frequency. Trajectory data can be used to measure SSM such as time to collision (TTC), post-encroachment time (PET), and deceleration rate to avoid collision (DRAC). TTC is the time to collision when two road users continue their trajectory at the same angle and speed without any kind of evasive behavior (Kizawi and Borsos, 2021). PET is the difference between times when one road user enters a conflict point until another road user arrives to the same conflict point (Kizawi and Borsos, 2021). The lower TTC and PET is, the closer to a collision the two road users were (Kizawi and Borsos, 2021). DRAC is a measure of the vehicle's own movement which is hard deceleration rates that the vehicle must perform to avoid a collision (Jiang et al. 2021).

However, this study focuses on the behavior of the vehicle at uncontrolled crosswalks which is commonly measured in yield rate. The yield rate is defined as the proportion of vehicles that yield to pedestrians over all PVIs (Fu et al. 2018). This can be more accurately measured in yield compliance, which is the proportion of vehicles that yield to pedestrians over the vehicles that are physically able to yield to crossing pedestrians (Fu et al. 2018). Yield compliance essentially considers the stopping sight distance (SSD) of the vehicle, which is the perception, reaction, and braking distance most drivers are expected to stop within for a given speed. In the current literature, yield rates from PVIs are commonly extracted manually in the field or through video for the purposes of modeling and microsimulations. Therefore, high accuracy movement (trajectory) data is not considered, which captures behavior-level information at high granularity. Furthermore, there are no previous methods for automating such yield analyses leading to extensive labor hours for data extraction.

The purpose of this study is to propose an automatic method for extracting PVIs and determining yield rate and compliance from roadside LiDAR trajectory data. From this trajectory data, the speed and timestamps are used to determine the crossing conflicts and yield or no yield events. Previous studies have yet to develop such automatic methods, especially from high-resolution traffic trajectory data. The implication of such a methodology is that yield analysis can be completed automatically upon completion of data collection which allows for faster turnover times for analysis and countermeasure selection. Further, using the high-resolution traffic trajectories,

altogether more detailed analysis at the behavior level of the road user can be provided to gain greater insight on the operational and safety performances at the uncontrolled crosswalk.

Yield rate is a measure of analyzing PVIs at uncontrolled pedestrian crossings, particularly driver behavior. Yielding is a critical component to measuring accessibility of and safety for pedestrians and striving to improve such measures will make streets more equitable. Most studies collect the yield data through field observations, video recordings and manual extraction, or a combination of the two (Sun et al., Ottomanelli et al., Chen et al., Lu et al., Feliciani et al.). In addition to video recordings, Schroeder et al. used a laser speed gun to collect vehicle speeds and used the data to determine when PVIs occurred. Some studies use driver simulations to measure VPIs for a variety of pedestrian crossing scenarios. The major limitations to field data collection methods are that it can limit the data collection time periods to day time periods. Most studies collected data during peak hours (Sun et al., Chen et al., Lu et al., Schroeder et al.). Ottomanelli et al. sought to collect data during non-peak hours to model regular conditions. Fitzpatrick and Park collected 48 hours of video recordings during daytime and nighttime periods to compare the difference in yield rates for crosswalks equipped with flashing pedestrian signals. However, to reduce the amount of manual extraction, staged pedestrians were used. A staged pedestrians is a volunteer who acts as a pedestrian and crosses at crosswalks to simulate real world PVIs. Most other studies used real PVIs without the use of staged pedestrians.

Cameras are most commonly used to generate trajectory data; however, the use of LiDAR sensors have become increasingly more common. Both sensors deal with the same issues of detecting, tracking, and classifying road users while also combating issues of occlusion of road users by vehicle, buildings, and other objects. Much of the applications surrounding roadside trajectory data is in behavioral analyses and surrogate safety measures (SSM) given the high frequency of road user detection. Fu et al. used vision-based trajectories from two cameras to extract PVIs and yield rates/compliance. Fu et al. used similar methods to investigate secondary PVIs at unsignalized intersection (Fu et al. 2019). Secondary PVIs are interactions between vehicles exiting the intersection and conflicting with crossing pedestrians, which are shown in the study to be more severe (Fu et al. 2019). Muppa et al. also analyzed PVIs at unsignalized interactions with vision-based trajectories, but used the surrogate safety measure of TTC to see if there is a difference in value when the vehicle passes first and when the pedestrian passes first. Golakiyaa et al. measured PVI at uncontrolled mid-block crosswalks using the SSM of time difference to collision (TDTC) in an attempt to classify levels of aggressive behavior exhibited by vehicles and pedestrians.

Trajectory-based PVI analyses have also been performed using LiDAR-based trajectories. Lv et al. proposed an automated method for identifying pedestrian vehicle conflict events using speed-distance profiles (SDP) to break up the conflicts into different risk levels. Wu et al. also used road user trajectories extracted from LiDAR sensors to calculate a variety of SSM such as post encroachment time (PET), the proportion of the stopping distance (PSD), and crash potential index (CPI). These SSMs have also been applied to vehicle-to-vehicle interactions. Xie et al. utilized vision-based trajectories to identify rear-end conflicts at two intersections with 70-hours of total video recordings. Jiang et al. also studied vehicle-to-vehicle conflicts from vision-based trajectories to measure SSM such as PET, TTC, and DRAC for rear-end, lane changes, and fixed

object conflicts on highways. Other interaction analyses can be done between vehicles and bicyclists, E-Bikes, and even wild animals.

Roadside LiDAR Trajectory Yield Input Data

With the georeferenced trajectory of all road users obtained in the data preprocessing stage, the desired yield parameters, such as vehicle speed and time to enter crosswalk, can be extracted for each trajectory in each specified detection zones. First, the geolocated trajectory data is converted to GIS feature classes every 30 minutes. Then in ArcGIS, the detection zones are drawn for the trajectory conflict points of interest, a schematic is shown in Figure 10-1. Next, an ArcGIS plugin of python scripts created by the authors is run to extract each pedestrian crossing event and each important yield parameters corresponding to the PVI. These parameters include time stamp for which the vehicle and pedestrian enters the crosswalk and corresponnding vehicle speeds.

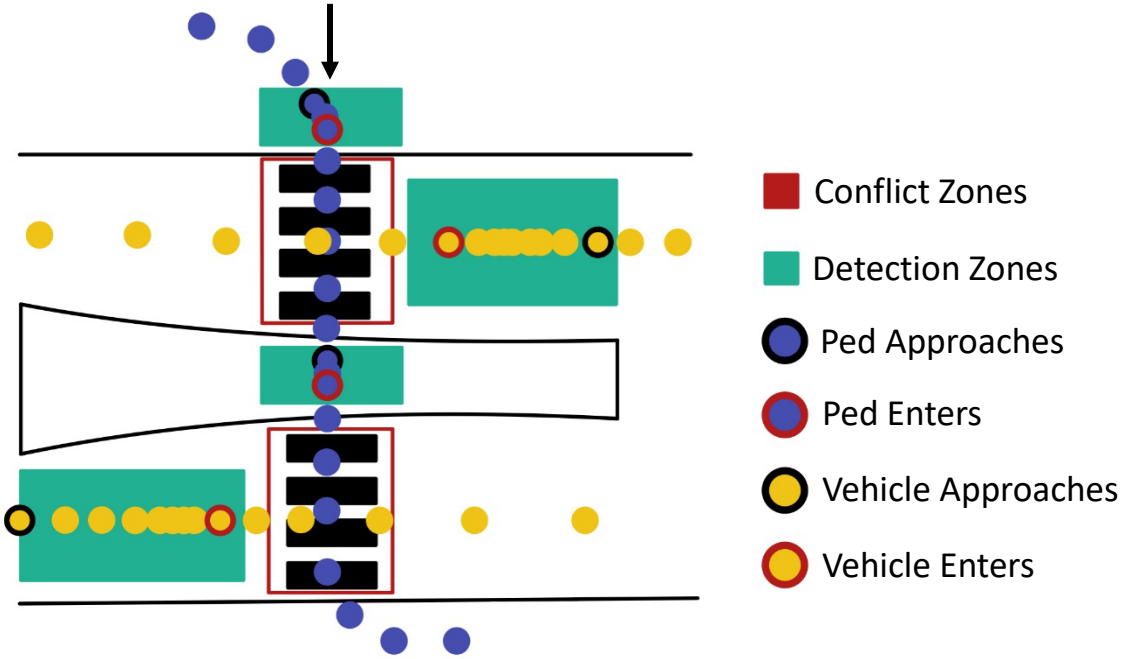

Figure 11-1 Vehicle and Pedestrian Trajectories and Detection Zones

Once the PVIs at the uncontrolled crosswalk are extracted through the Python Script, it is important to extract the yield information to know whether the vehicles yielded for pedestrians. Originally, the method was to measure the last trajectory point to leave the specifeied detection zone, which is the time stamp just before the vehicle or pedestrian enters the crosswalk. If the vehicle entered the croswalk before the pedestrian, then that was marked as a no yield case. If the pedestrian entered the crosswalk before the vehicle, then that was marked as a yield case. This timestamp between vehicles and pedestrians entering a crosswalk is also measured in the time difference to conflict (TDTC), which is the timestamp difference between the vehicle entering the crosswalk and the pedestrian entering the crosswalk. A positive value are yield cases while negative values are no yield cases.

However, there are several other considerations to be made to increase accuracy. First, only those crossing intances for which vehicles and pedestrians interact should be used. Next, the vehicle speed must be considered, which is important for ensuring vehicle actually yielded to pedestrians. Lastly, this method does not consider the stopping sight distance for which a driver needs to preceive, react, and brake for a pedestrian crossing. Therefore, the data needs to be filtered to only include interactions between vehicles and pedestrians, and to only include vehicles that are physically able to yield. Once this is performed, every real vehicle-pedestrian yield interaction is collected with the following yield paramters:

1. Time difference to conflict (TDTC)
2. Vehicle speed

Threshold-Based Method for Extracting Vehicle-Pedestrian Yield Data

The first proposed methodology is to extrtact the yeild cases using theshold values. The first threshold value is the vehicle-pedestrian interaction threshold, which is defined by the crossing time for pedestrian through the crosswalk. If the TDTC is less than the pedestrian crossing time, this is considered an intereaction. Otherwise, the data is filtered out as a non-interaction case. Next, is the vehicle speed threshold. This is perhaps not as intuitive to gather because it varies based on the site. Also, it is not clear whether it is important to only consider full stops, or also floating vehicles. In this study, both are considered, which means a higher vehicle speed threshold value is used. The vehicle speed threshold value can be gleaned by looking at the raw LiDAR data, or by looking at the PVIs through a speed vs. TDTC plot. When there is sufficient data, the speed vs. TDTC plot shows clusters of data that could help identify possible speed thresholds. The final threshold has to do with stopping sight distance (SSD). In other words, it is important to exclude cases for which vehicles are unable to yeild for pedestrians. This is performed by calculating the SSD and converting it to stopping sight time. Then, this value is compared to the time difference between the “vehicle enters” and “ped approaches. If the time difference is less than the stopping sight time, then the vehicle was able to yield, otherwise, the vehicle could not yield. Figure 11-2 is a flow chart illustrating the thershold-based method for extracting vehicle-pedestrian yield data.

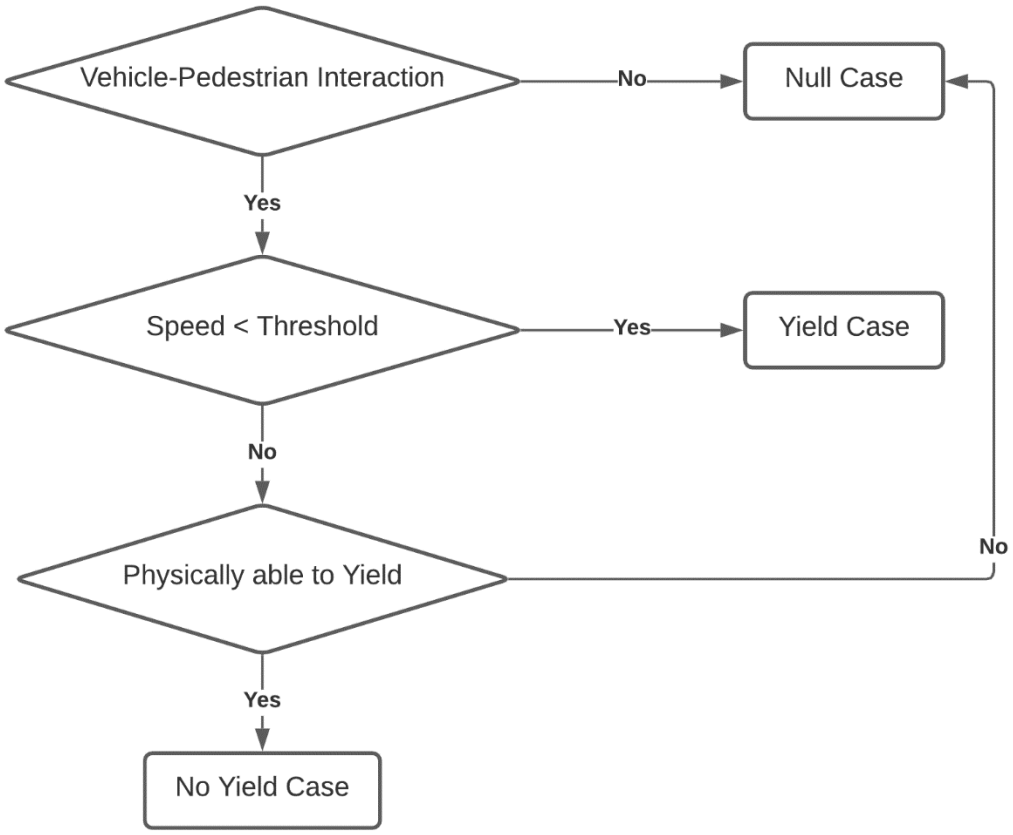

Figure 11-2 Threshold-Based Method for Extracting Vehicle-Pedestrian Yield Data

Statistical Method for Extracting Vehicle-Pedestrian Yield Data

The statistical method used for the yield extraction is discussed. This method seeks to fill gaps in understanding the variables that go into determining yield cases. Since such variables are continuous and PVI behaviors vary, it is perhaps more insightful to look into probabilities of yield cases to better understand these behaviors. First, the PVI data is filtered to only include true interactions and consider the SSD. With the data filtered, a statistical model is derived to extract vehicle-pedestrian yield data. The statistical method used in this paper is a logistic regression because the response variable is binary – yield versus no yield. The main covariates that are tested include the vehicle's speed and the TDTC. The general form of a logistic regression is written as such:

Linear model: $$y = b_0 + b_1 x \quad (1)$$

Logistic model: $$p = \frac{1}{1-e^{-(b_0+b_1 x)}} \overset{yields}{\Longleftrightarrow} \log\left(\frac{p}{1-p}\right) = b_0 + b_1 x \quad (2)$$

Where $y =$ Response, $b_0 =$ y-intercept, $b_1 =$ Slope, and $p =$ Probability of response

The first step is to generate real yield and no yield cases from the filtered PVI data. This is performed by going through each data point (interaction) and verifying whether it is a yield or no yield case by looking at the raw cloud point data. Once a sizeable sample has been manually compiled, the new dataset can be used to calibrate the model. Six models were tested in this paper, consisting combinaitons are covariates vehicle speed, TDTC, and the binary of who entered the crosswalk first. For the best models, the logistic regression "S" curve is generated to see the continuous probability of yield or no yield

CASE STUDY

The evaluation of the threshold-based method and statistical method for extracting vehicle-pedestrian yield data is detailed. First, the case study summarizes the site details and data collection date and time. Then, the threshold-based method case study results are outlined. Finally, the statistical method is detailed.

The case study for his report will be outlined. The study was conducted in Henderson, Nevada, United States at an uncontrolled mid-block crosswalk at Green Valley Pkwy and Amargosa Trail. The crossing is equipped with a rectangular rapid flashing beacon (RRFB) activated by a push-button pressed by the pedestrians to alert drivers of their intent to cross. Figure 10-2 on shows the mid-block crosswalk and indicates the LiDAR sensor location. For this study, only the westbound pedestrian crossings and corresponding northbound vehicle movements are considered. There are two northbound lanes which are analyzed together. The all-road users cloud point data was collected at this crosswalk using a LiDAR sensor for the purposes of generating the trajectories of

all road users. LiDAR data collection took place from 6/23/2019 8:00 AM to 6/29/2019 11:00 PM. The vehicle traffic at this intersection is mostly passenger vehicles and the crosswalk is used by pedestrians and bicyclists.

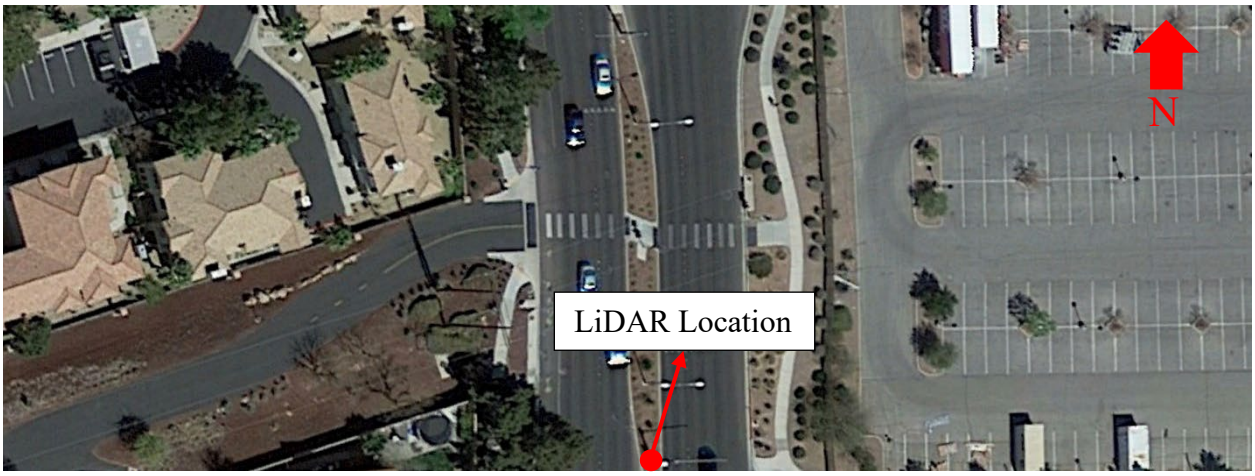

Figure 11-3 Study Mid-Block Crosswalk and LiDAR Location

Results and Analysis

The results and analysis of the yield data extraction are outlined. The PVI and corresponding vehicle speeds and timestamps are extracted for the full data collection period. There was a total of 866 PVIs recorded, which is also the same as the total number of pedestrians/bicycles crossing westbound.

Threshold-Based Method for Extracting Vehicle-Pedestrian Yield Data

The results for the threshold-based method is outlined. For this method, three threshold values need to be determined as follows:

- PVIs
- Vehicle speed
- Stopping sight distance

To help understand these thresholds, we will take a look at the speed vs TDTC plot shown in Figure 10-4. To help understand how to read the speed-TDTC plot, it is good to break the data into quadrants as such:

I. Non-interaction cases where the vehicles speeds are uninterrupted by the pedestrian → high TDTC, high vehicle speed
II. Non-interaction cases where the vehicles speeds are interrupted, hence there are fewer data points → high TDTC, low vehicle speed
III. Interactions where the vehicles speeds are interrupted, hence making up a cluster of yield cases → low TDTC, low vehicle speed

IV. Interaction cases where the vehicle enters the crosswalk before the pedestrian and does not slow down, hance making a cluster of no yield cases → high TDTC, high vehicle speed

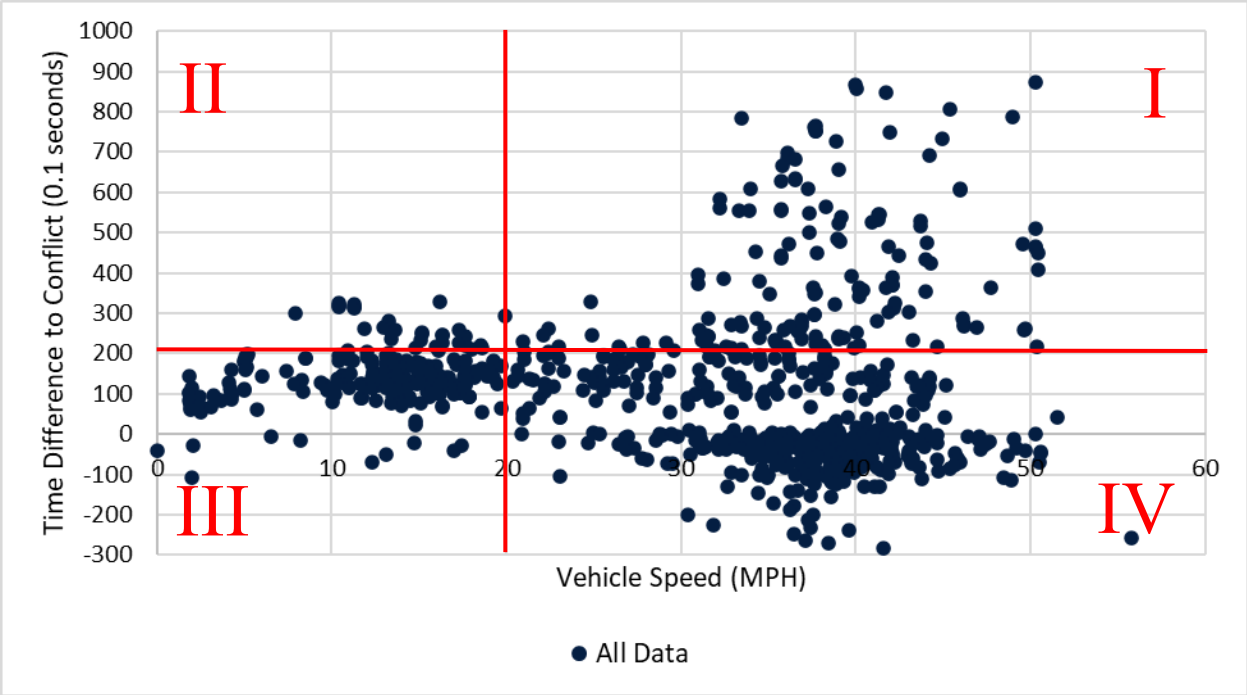

Figure 11-4 Speed vs TDTC plot

For the PVI threshold, the crossing time is used, which is based on the crosswalk length and a pedestrian speed of 3 feet per second. The value for this site is 20 seconds, so any TDTC that is greater than 20 seconds is filtered out as a non-interaction case A total of 309 points are filtered out non-interaction cases, which makes up 36% of the original data. Next, the vehicle speed threshold is determined. Given the speed limit of Green Valley Pkwy is 35 miles per hour (MPH), the threshold must be lower than the speed limit, but still large enough to capture the cluster shown in Figure 10-4. Based on manual observations, a vehicle speed threshold of 20 MPH was chosen. Finally, the SSD is considered, which is based on each individual vehicle speed and compared to the "vehicle enters" and "ped approaches" difference. SSD filtering will take points away from quadrant IV, which is the no yield quadrant. A total of 133 points were removed from the stopping sight distance filtering, leaving a total of 412 points. Figure 10-5 shows the filtered data and designates the yeild points and no yeild points. As shown in Table 11-1, there was 190 yield cases and 222 no yield cases for a yield compliance of 46%.

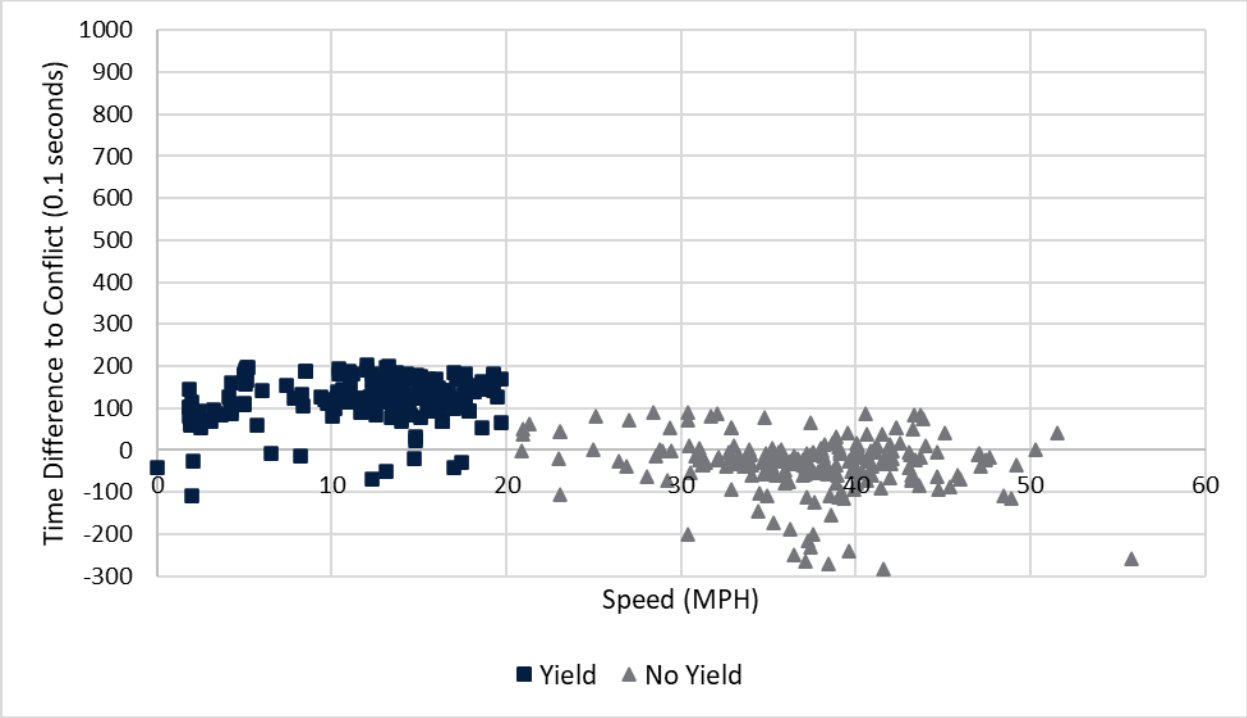

Figure 11-5 Filtered Speed vs TDTC plot

Table 11-1 Yield counts and yield compliance

Yield Cases	No Yield Cases	Yield Compliance
190	222	46%

Statistical Method for Extracting Vehicle-Pedestrian Yield Data

The process for determining the best logistic regression for the statistical method is discussed. The first step is to filter the non-interactions and based on the SSD, which leaves us with the same 412 data points. Then, a sample of real yield and no yield data is manually extracted from the raw LiDAR cloud points. 35 yields and 43 no yield for a total of 78 data points were manually extracted for the purposes of testing logistic regression models. The following models with corresponding variables are tested:

1. Vehicle speed
2. TDTC
3. Vehicle speed and TDTC
4. TDTC and pedestrian enters crosswalk first binary applied to the slope and intercept
5. Vehicle Speed and pedestrian enters crosswalk first binary applied to the slope and intercept

6. Vehicle Speed and TDTC with pedestrian enters crosswalk first binary applied to the slope and intercept

Each of the logistic regression model equations are outlined in Table 11-2 along with the Akaike information criterion (AIC). AIC is a mathematical method for evaluating how well a model fits the data. The lower AIC is, the better the model fits to the data. AIC typically is used to compare models. In the case of the models and corresponding AIC outlined in Table 11-2, it appears that vehicle speed is the best parameter for determining yield cases since each model that has vehicle speed as one of its' parameters has a lower AIC. Figure 11-6 and Figure 11-7 illustrate the logistic regression curve for Model 5 and 6, respectively. From the curves, it can be gleaned that there is very low uncertainty in the probability of vehicles yielding to pedestrians. Not only does this validate the yield data, but it also emphasizes the importance of vehicle speed in determining yield rates.

Table 11-2 Logistic Regression Model Results

ID	Logistic Regression Models	AIC
1	$\log\left(\frac{P}{1-P}\right) = 8.40275 - 0.36194V$	25.443
2	$\log\left(\frac{P}{1-P}\right) = -1.049140 + 0.027741T$	56.053
3	$\log\left(\frac{P}{1-P}\right) = 6.838362 + 0.007509T - 0.305876V$	26.58
4	$\log\left(\frac{P}{1-P}\right) = -2.605406 - 0.006273T - 8.209077d + 0.182603Td$	42.567
5	$\log\left(\frac{P}{1-P}\right) = 4.210 - 20.96V + 45.84d - 20.62Vd$	20.536
6	$\log\left(\frac{P}{1-P}\right) = 4.27011 - 0.25015V - 0.01886T - 6.85780d + 0.14556Td$	25.128

* Where $P = probability, V = vehicle\ speed, T = TDTC, d = ped\ enter\ first\ binary$

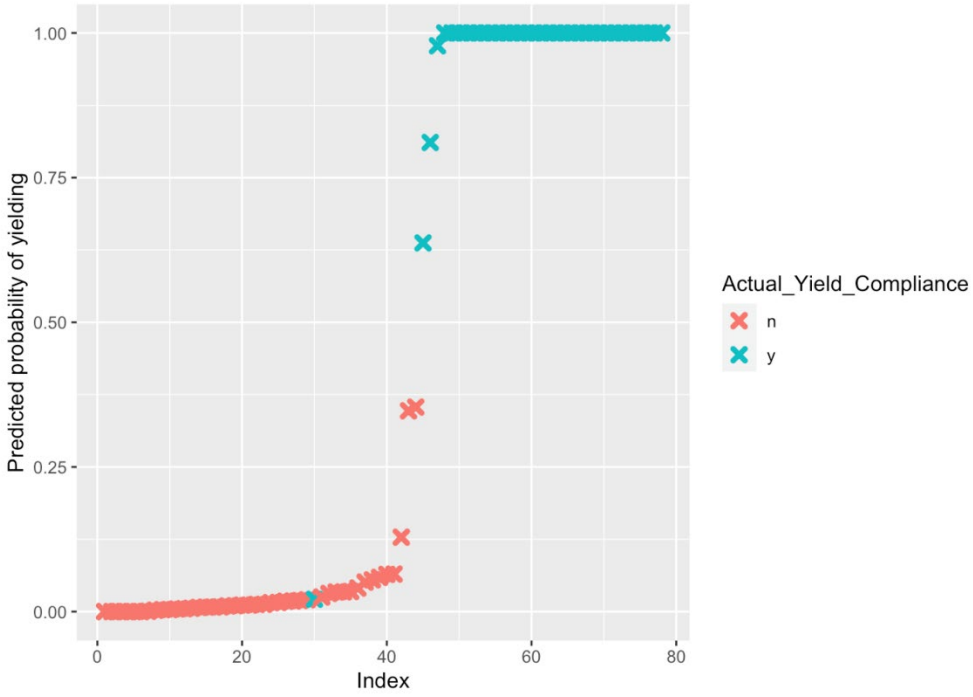

Figure 11-6 Logistic Regression Curve for Model 5

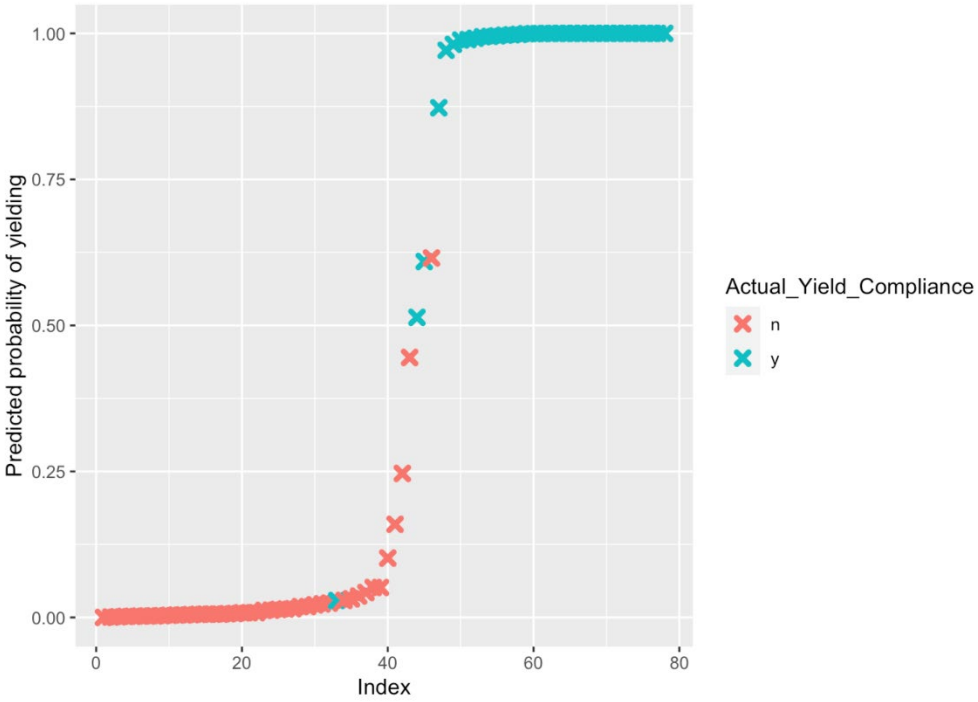

Figure 11-7 Logistic Regression Curve for Model 6

12. ANALYSIS OF WILDLIFE CROSSING EVENTS IMPACTING TRAFFIC WITH LIDAR

Wildlife-vehicle crash (WVC) is a global issue. With the continuous increase of the number of WVCs in many countries in recent years [61], it has begun to receive more attention. WVCs do not just cause safety problems for wildlife and drivers but also cause serious economic losses. According to National Highway Traffic Safety Administration (NHTSA), in 2015, a total of 278,000 WVCs were recorded. The loss caused by this kind of crash is about 8.4 billion per year [62].

Several previous studies have been conducted about investigating the factors influencing the frequency and severity of WVCs. Hothorn [63] demonstrated that the WVCS tend to occur at night, at twilight, and in some specific parts of the year, which is related to animal life cycles. WVCs also tend to occur at some particular sections of the road than the other parts [64]. These road sections are named hot spots, which only account for a small part of the entire road network where WVCs may occur [65]. Improper geometric design may also cause the occurrence of WVCs due to insufficient sight distance [66].

Although there have been a number of research on the factors that may affect or cause WVCs, most of them are studied based on past WVC records. Since the occurrence of WVCs is random and accidental, these records cannot fully explain the impact of WVCs and potential wildlife-vehicle near-crashes on driving vehicles. When wildlife crosses the road, even if there is no crash, it will still affect the normal driving of vehicles, causing potential delay problems and energy consumption issues. New methods related to real-time wildlife crossing detection and analysis are urgently needed. Cameras are the commonly used technology to capture wildlife crossing [67] [68] [69] [70][71]. But it shows weak performance during poor-light conditions [72]. Thermal cameras can overcome this shortage by capturing objects based on the temperature, which shows good performance even in completely dark conditions [73]. According to Christiansen [74], thermal cameras show a wildlife detection accuracy of 93.5% in the range of 3-5 meters and 77% in the range of 10-20 meters. The thermal camera cannot successfully detect wildlife if the distance is greater than 20 meters. Besides, the thermal camera's lateral detection angle is limited. There are also some studies using high-frequency radio-tracking (VHF) and GPS-based-tracking technologies [75] [76], which can track the wildlife accurately, and there is no limit for detection range, but it is only applied to the animals equipped with this device. Viani [77] developed a radar-based wildlife road-crossing early alert system that can successfully detect wildlife within 16 meters to the radar with a short reaction time (about 1 second). Like thermal cameras, the field of view of radar is also limited. Among these methods, advanced cameras and Light Detection and Ranging (LiDAR) sensor can capture objects within 100 meters with 360° field of view at any light conditions. Several algorithms have been conducted to classify wildlife and detect wildlife crossing using 3D roadside LiDAR [78].

This study introduces a new 3D-roadside-LiDAR-based conflict analyzing technology. It automatically captures all the wild horse and vehicle moving trajectories, distinguish wild horse road crossing events and determine the corresponding crossing area, wild horses' crossing trajectory, and crossing time information, then check every vehicle by comparing the time of the vehicle passing the crossing area with the crossing time of the wild horse to determine whether the vehicle is yielding to the wild horse or not, finally generating yield rate for each crossing event.

Methodology

After objects are classified and tracked, the trajectory data for wild horses could be extracted from the dataset. Crossing events can be determined by checking if the wild horse's trajectory intersects with the road zone. Once a crossing event is detected, as Figure 12-1 shows, the place within 30ft from the edge of the road is defined as a "waiting zone." Where the wild horse trajectory intersects with the road is defined as the horse's crossing zone. The algorithm will automatically record the time when the wild horse arrives in the waiting zone, when it starts to cross, and when it ends crossing. The time the wild horse arrives in the waiting room is the first time frame the wild horse was detected in the waiting room. The start-crossing time is the last time frame the wild horse was detected in the waiting room. The end-crossing time is the start-crossing time plus the crossing time of the wild horse computed by the tracking algorithm.

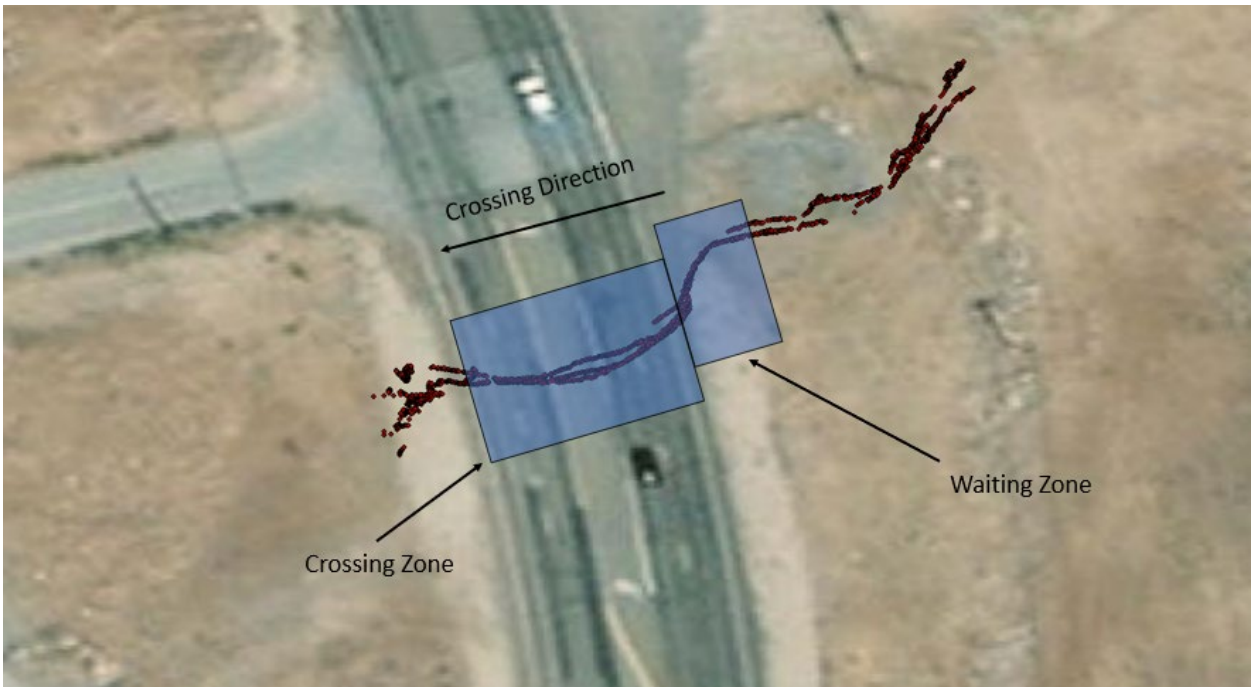

Figure 12-1 Crossing zone and waiting zone for crossing event

Based on the crossing zone obtained from the previous step, each vehicle is analyzed separately to checked whether this vehicle is relevant to any crossing events. For each crossing zone, the vehicle can either: pass through the zone before the wild horse crossing, pass through the zone during the wild horse crossing, or pass through the zone after the wild horse finish crossing.

$$
\begin{aligned}
&Vi < H_{min} \\
&Vi \in [H_{min}\ ,\ H_{min}] \\
&Vi \in [H_{max}\ ,\ H_{max} + C_j] \\
&Vi < [H_{max} + C_j, T_j\ ] \\
&Vi > T_j
\end{aligned}
\qquad (1)
$$

Equation 1 illustrates the five temporal relationships between a vehicle i and the crossing event j. Vi is the time frame for vehicle i to pass through the crossing zone. H_{minj} is the first time frame for the wild horse of crossing event j arrives at the waiting zone. H_{maxj} is the maximum time frame of the wild horse of crossing event j leaving waiting room, which is also the time frame for the wild horse to start crossing. C_j is the crossing time for the crossing event j. T_j is the time the queue caused by the crossing event has been cleared.

If the time for vehicle i to pass through the crossing zone is earlier than the time wild horse j arrives in the waiting zone, which means the vehicle i is not relevant to the crossing event j. If the vehicle i pass through the crossing zone after the wild horse j arrives in the waiting zone before the wild horse start to cross, the vehicle i will be defined as "non-yield" to the wild horse j. The vehicle is defined as "non-yield" if the vehicle passes through the crossing zone during the wild horse crossing. For the vehicle leaving the crossing zone after the wild horse finishing crossing, if the vehicle is earlier than T_j, it will be defined as "yield to the wild horse j"; otherwise, it is not related to the wild horse j. The schematic diagram is shown in Figure 12-2. This algorithm will keep cycling until all vehicles are checked for each crossing event.

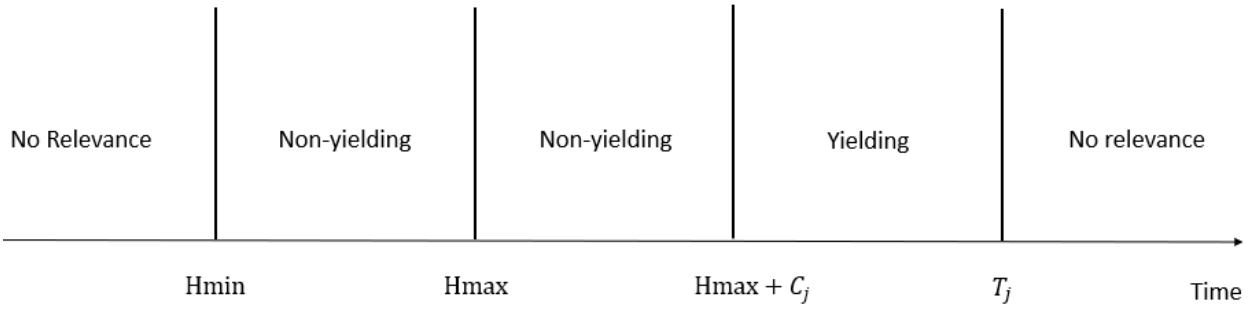

Figure 12-2 Five-phase diagram about how to determine if a vehicle i is yield to wild horse j

Case Study

The pilot site was selected at the USA Pkwy & Pittsburgh Ave intersection in Sparks, Nevada, USA. The historical data and field observation shows that there exist wild horses activities. The team of the University of Nevada, Reno, deployed the LiDAR sensor at the east side of the intersection on a trailer. The LiDAR is powered by four solar panels and a wind turbine, which is shown in Figure 12-3 (a). Extra energy will be stored in a battery which is used when there is no sunshine or wind. The installation location and the geometric information of the site are shown in Figure 12-3 (b)below. A pond is located east of the intersection, attracting the surrounding wild horses to drink water there.

Figure 12-3 Trailer for data collection(left) and Top view of the site and the location of the LiDAR (Right)

The main road of this intersection is a two-way-two-lane rural road with a speed limit of 45 MPH. The minor road leads towards an industrial factory. After the LiDAR data processing, the volume for the site is generated. Since the volume for the minor road is not significant, the minor road is not considered in this study. Figure 12-4 shows the one-week volume of the main road from Saturday, 11/17/2019 0:00 to Friday, 12/13/2019 24:00.

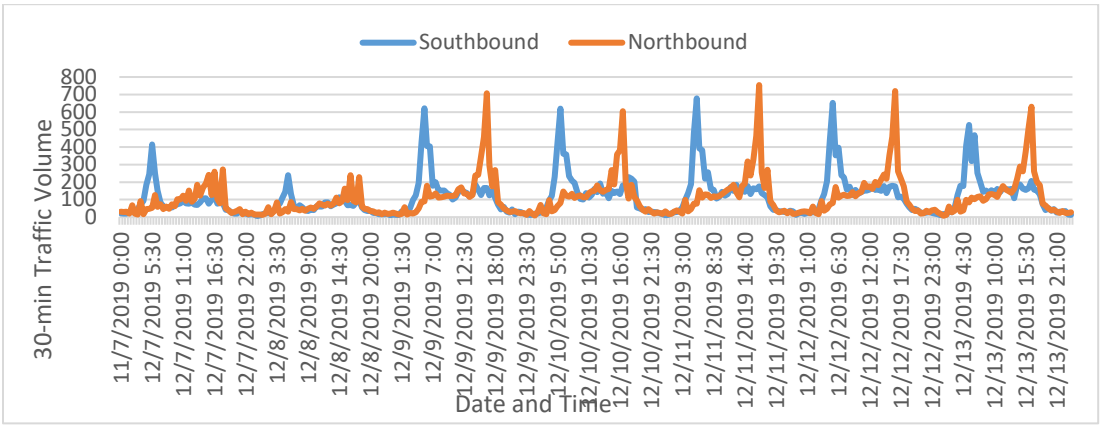

Figure 12-4 30-min Volume for each bound

Wild horse crossing events detection

Through the horse crossing detection algorithm, the horse crossing events were extracted. There were 14 crossing events detected at this site from November 17th to December 18th. Table 12-1 shows the general information of the crossing event, including the date and time, the number of horses in one crossing event, and the total crossing time. The date and time are the time the first horse starts crossing. The crossing time is the time difference between the first horse start crossing and the last horse finish crossing. Figure 12-5 shows the crossing time for each crossing event over

different numbers of horses for each crossing event. It shows that as the number of horses crossing at the same time increases, the average crossing time increases as well.

Table 12-1 Wild horse crossing events captured from LiDAR

Crossing Event Date and Time	Number of horses crossing	Crossing time (sec)
11/18/19 1:32 PM	4	36.3
11/18/19 1:48 PM	3	24.1
11/18/19 3:11 PM	4	28.6
11/18/19 3:13 PM	5	46.8
11/23/19 2:58 PM	5	45.5
11/23/19 3:08 PM	1	24.3
11/23/19 3:20 PM	1	20
11/24/19 1:36 PM	5	33.8
11/24/19 5:29 PM	5	24.9
11/25/19 4:57 PM	9	64.3
11/25/19 12:51 PM	5	79.7
12/17/19 3:04 PM	9	31.3
12/18/19 10:01 AM	3	26.6
12/18/19 1:09 PM	5	50.5

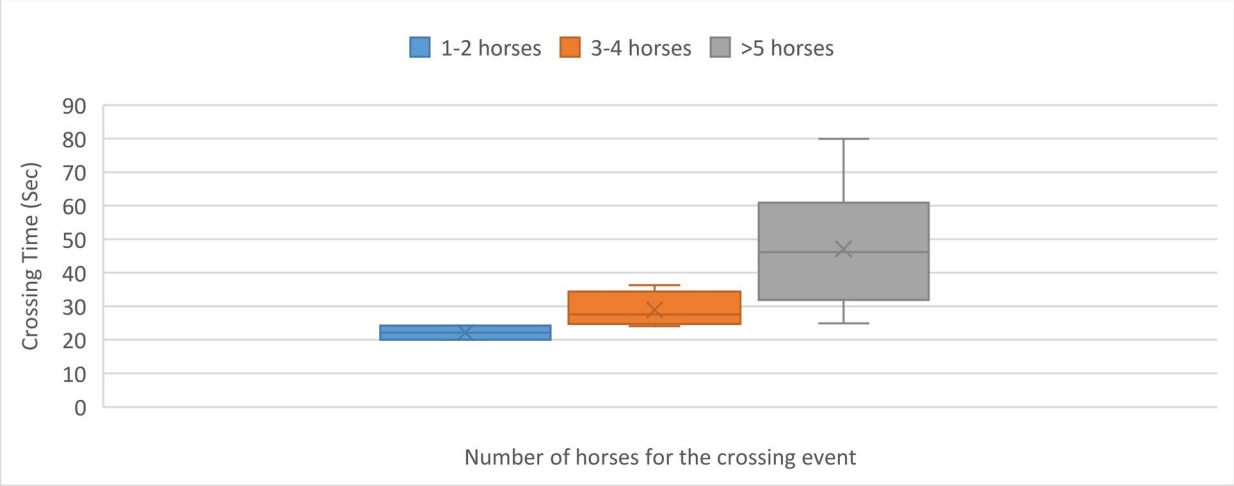

Figure 12-5 Crossing time over number of horses for each crossing event

Yield analysis

Figure 12-6 shows an output example of crossing event at 3:11 PM, 11/18/2019. Each point represents one vehicle, the x coordinate is the time frame it passes through the crossing zone (Vi), the horizontal coordinate is the average speed of the vehicle. This scatter plot meets the expectation that the average speed of vehicle yield to the wild horse are significantly lower than the vehicles which didn't yield to the wild horse.

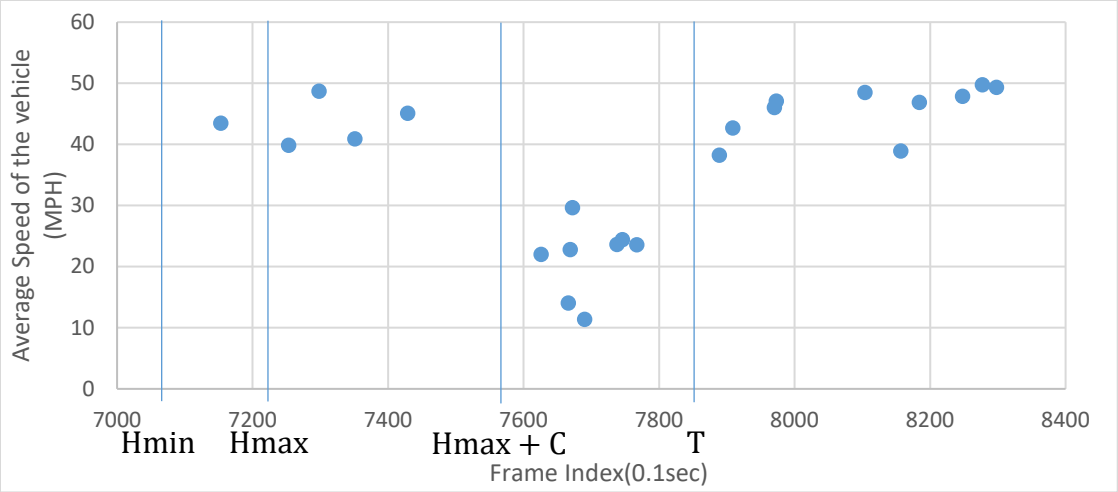

Figure 12-6 Example Crossing event (11/18/2019 3:11PM)

Table 3 shows all detected wild horse crossing events and their associated yielding and non-yielding vehicles and gives the yield rate for each event. The results show that almost all wild horse crossing events (13 out of 14) impact the passing vehicles. The result of yield rates reflects that it is ubiquitous for vehicles to choose not to yield to wild horses, which shows certain safety hazards on this road. Non-yielding vehicles may arouse the wild horse's unexpected reaction due to the distance being too close, thereby increasing the possibility of traffic accidents happens.

Table 12-2 Yield rate for each crossing event

Crossing Event Date and Time	Number of yielding vehicles	Number of no-yielding vehicles	Yield rate
11/18/19 1:32 PM	6	0	100.00%
11/18/19 1:48 PM	7	8	46.67%
11/18/19 3:11 PM	8	5	61.54%
11/18/19 3:13 PM	9	1	90.00%
11/23/19 2:58 PM	8	13	38.10%
11/23/19 3:08 PM	0	0	NA
11/23/19 3:20 PM	0	7	0.00%
11/24/19 1:36 PM	2	0	100.00%
11/24/19 5:29 PM	0	3	0.00%
11/25/19 12:51 PM	7	2	77.78%
11/25/19 4:57 PM	17	8	68.00%
12/17/19 3:04 PM	5	1	83.33%
12/18/19 10:01 AM	4	0	100.00%
12/18/19 1:09 PM	2	3	40.00%

13. AUTOMATIC COUNT TRIP GENERATION WITH LIDAR

Transportation planning based on historical data and methods have major limitations. Trip data can be useful to increase transportation safety of the specific sites and the process and programming purposes. One of the challenges in this regard is data collecting to gain accurate analysis of land used development. The previous methods of data gathering such as human observational data counting and automatic methods like pneumatic tubes and video camera suffers some limitations affect the accuracy of trip analysis which cause over mitigating or set some wrong rules and regulations. LiDAR sensing is yet to be further explored in trip generation, especially for the purpose of business development. This study is an initial attempt to: 1) perform a LiDAR-based trip generation data gathering for a business location, and 2) analyze the resulting data based on the GIS software to develop a systematic business plan for the case study and beyond.

In the recent years urban areas more and more need to control the conditions of multimodal trips to keep the cities livable and sustainable. Transportation planning plays a pivot role in this matter to set regulations and address some methods to mitigate the impact of automobiles in urban areas.

Thus, travel impact analysis is needed to choose the mitigation compatible with the level of impacts. Consequently, trip data for land use development and analysis the multimodal trip is essential and recently many researchers have been studying different aspects of this subject. For instance, trip data pattern was used for bike-sharing system users(2), to avoid the crowds and offer travelers more individualized travel plans(3), impact analyses for affordable housing development(4), in urban development area such as site design, scaling or scoping development, traffic consequences, system development charges, impact fees, emissions estimates, and even regional travel demand modeling(5).

Trip data also can help other organizations, especially those related to government, to increase transportation safety of the area and the process that leads to decisions on transportation policies and programs purposes (6). One of the most important function in creating a transport impact assessment (TIA) for a site, chosen to be developed, is to estimate the probable number of trips in that site. Trips that are created at a site refers as a trip generation (7)(8) and the goal of trip generation is to forecast the number of trips generated by and attracted to each zone in a research area based on their purpose. The number/frequency of trips is calculated by linking person, zone, and transportation network parameters to the number/frequency of journeys. Trip generation estimate is considered to be the most essential input for a TIA as it provides the data about the transport impact in a new site and what is needed to control those impacts(9). Vehicle trip generation has been used in traffic mitigation, which is estimation of system development or impact cost (providing improvements in network capacity and demand) and transportation utility cost (accommodating cost of operation and maintenance).

Trip generation can also be used to evaluate the safety of the nonmotorized modes of travel areas (10). However, lack of information may lead planning and design to wrong mitigation which has unintentional outcomes for the site(8). Multimodal trip counts data is the process of collecting the necessary information regarding the trips made by any transport mode in a site, i.e., (non)motorized, and is the best possible way to manage the probable impacts that can occur in that site.

This data can be collected manually, e.g., observing a site by an individual who counts the entering and exiting or by questionnaire survey (11). Schneider et al.(12) for their study of trip generation and smart growth, used door counts-and-intercept surveys. Each survey includes 10 questions regarding the mode, time of day, destination, and origin. Kristina M. Currans et al.(4) was counting the number of people and motorized vehicle manually at 26 sites through the visual observation and individuals who were temporary workers and trained by members of research team. Reid Ewing et al. gathered their data through counts and survey by using urban planning students. Forty-eight students from PSU at a one-day cost of almost $12,000 and twenty-four students from University of Utah with the cost of almost $6000. Also, automatically data collecting are prevalent among researcher, e.g. using installed video camera in the desired location in order to collect the pedestrians and vehicles trip data(13), pneumatic tubes which are made of stretched hallow rubber tubes across a section of road to collect vehicles count data. The tube is connected to a traffic counter on one end and plugged on the other to avoid air leakage as a vehicle passes through, pneumatic tubes(14), and etc. (9). The process of counting the number of people entering and exiting a site to estimate the related demand of a new development, estimates the “new trips”, and provides an estimation of total impact that helps for a better assessment of the future travels at the new site (15).

From various methods to collect multimodal trip generation data, namely manual/automatic vehicle/person counts (16), intercept survey (17)(18)(19), household travel survey (20)(21)(22), and workplace/school travel survey (23)(24)(25), each has some disadvantages. For instance, the major limitations in manual counts are the capture rate, the biased perception of the surveyors, and the cost-effectivity of the process itself, especially for long-term periods. On the other hand, automatic methods such as pneumatic tubes are not cost-effective for short-term periods, and several automatic counters might be required to complement information acquired from other methods. Video cameras are limited by the light conditions. All in all, most methods suffer from inability of obtaining; trajectory-level data, and accurate detection and tracking of pedestrians and vehicles(9).One of the major issues in trip generation assessments in the United States is that majority of agencies use the Institute of Transportation Engineering (ITE) guideline as a reference to provide the required estimation for land use development (11)(26). However, such guidelines have been shown not to be compatible by empirical data through several studies.

In the recent studies (1, 21-26) LiDAR is one of the trending methods in the field of transportation is Light Detection and Ranging (LiDAR) sensors which can include connected vehicles, traffic data collection, and auto-driving. Compare to the past methods LiDAR can cover a much wider detection range, has a finer resolution, and it can scan a 360º horizontal range and is able to detect the direction of arrival as well as the number of vehicles accurately (1)(27). Therefore, this method can detect information about the precise position of objects without being impaired by the light condition. By gathering real-time accurate position data for all road users, the LiDAR sensors can produce high-resolution traffic data (HRMTD) (28).The output of LiDAR can be divided in 5 categories: motorcycle, passenger, car, pickup or van, single unit truck or bus tractor-trailer (29). This method is very time saving to check the type of travelers coming and exiting and using a site and can be used for further analysis in transportation planning. The LiDAR sensors can be installed temporarily for short-time data collecting or permanently on roadside structure for long-term.

In this study, an enhanced data collecting method for trip generation was used to analyze the number of pedestrians, bicycles and public transits and vehicles that are generated for a specific location, i.e., CITIGAS gas station/store in Reno (**Error! Reference source not found.**3-1). For data extracting information from the raw LiDAR data, GIS software was used and data visualization for this method can be found in this paper. The rest of this paper is organized as follows: in the next section LiDAR device that used for data collecting is introduced. Then the data processing from raw data and GIS data analyzing method has been described. Subsequently we discussed the results obtained from GIS trajectories for each zone related to the case study in this research for 24 hours data that gathered by LiDAR. Finally, we conclude the results of this study and its benefits from the business owner point of view and propose suggestion for the future research.

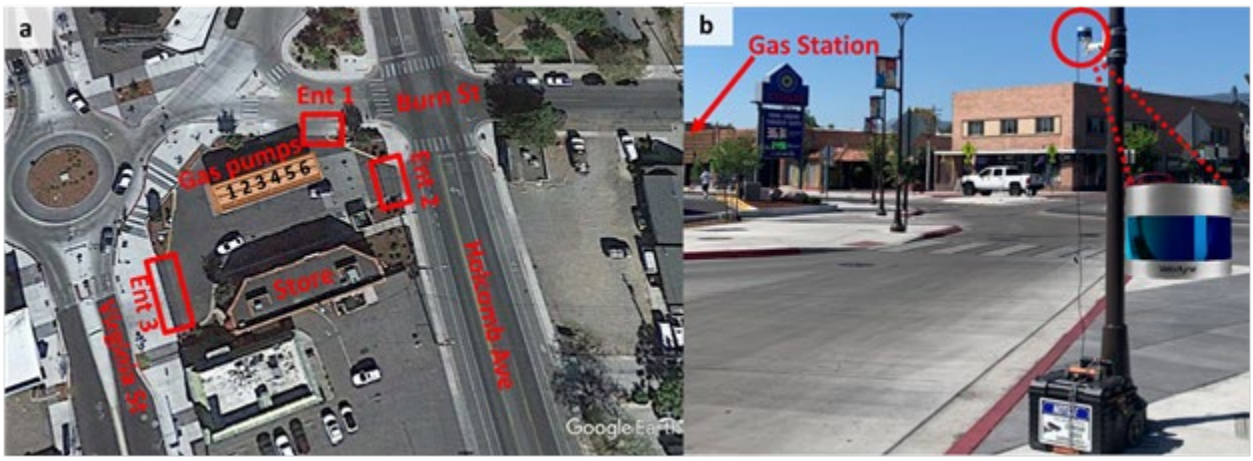

Figure 13-1. The location of the studied gas station/store (a), and the utilized LiDAR equipment installed in the northern part of the gas station/store (b)

The LiDAR sensor was set up on a roadside in the northern part of the gas station/store where the maximum signal can be received from all three accesses (Figure 13-1. b). The approximate height of the equipment was about 9 feet above the ground that is an optimized value based on our previous studies(29). The gas station was divided into six zones, each of which having one gas pump to monitor each pump separately. The number of entrances and exits from each access was separately monitored and counted for pedestrians and vehicles to distinguish the contribution of each into the business. At first raw data which was obtained for 24 hours data from 12:00 am 6/5/2021 until 23:00 pm 6/5/2021, processed and transformed to 3D space based on their coordinates XYZ. The data include XYZ position of points in each object, distance to LiDAR, tracking ID, frame number (timestamp), lane ID, velocity, and direction(33). Using ARC GIS desktop and Arc GIS Pro for define zone at each entrances and gas pumps and store building to find out the object clustering based on the DBSCAN method(29).Then by using GNN method we can track each type of object which are pedestrians or vehicles using the site.

After the processing LiDAR data is finished, trajectory data is ready for using in the ARC GIS Desktop, based on the location that we want to study. We defined some zones in GIS for the entrances, gas pumps, store building at the site. Based on the trajectories in the zones in GIS, directional information was obtained for each type of object to find the entering and exiting

vehicles and pedestrians. Then, for finding the angles of direction for entering and exiting, raw data of LiDAR was watched by VeloView software based on the XYZ of each object that has unique object ID we can track the specific object and find its location. In the next step, the total number of pedestrians and vehicles counted based on half hour data and classification of object that captured by LiDAR until they leave the detection zones.

RESULTS AND DISCUSSION

After data analysis was done by GIS for 24 hours data and visualized in line chart for each three entrances for pedestrians and vehicles. For evaluating the accuracy of this data analysis, four different half hour data was picked to count the manual data and compared to GIS trajectories data analytics. The accuracy level reached to 95% for vehicles and 93% for pedestrians that verified our proposed method. Line chart of 24 hours data for Ent 1. Located at Burn St. is shown in Figure 13-2.

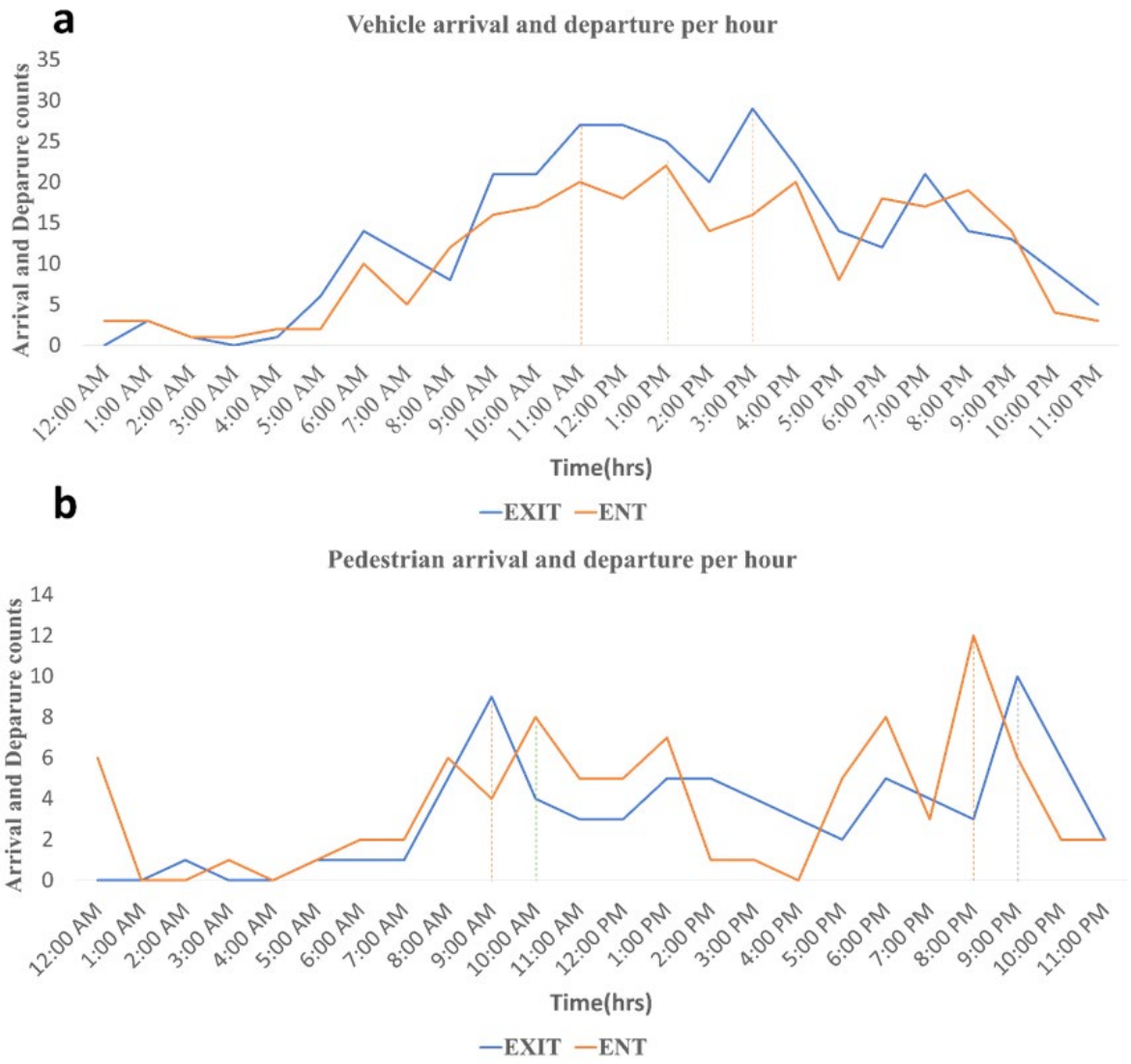

Figure 13-2. Twenty-four hours data visualization for Ent1 (a) for vehicles (b) for pedestrians

The results are presented within four temporal courses (each half an hour) when the maximum number of entering and exiting trips is counted (i.e., peak hours). It was expected to observe an overall balance between entering and exiting trips into the site within 24 hours and that is what the results indicate. However, this balance does not necessarily exist within different peak hours and for different accesses (Figures 13-3 – 13-5). For instance, the results indicate that the accesses from Holcomb Avenue and Virginia Street are more regularly used as an entrance access, while that from Burn Street is more regularly used as an exit access for both pedestrians and vehicles. Assuming that this result will be validated with a longer course of data acquisition (>> 24 hours), a beneficial business strategy is to set up more advertising signs and banners in the entrance accesses (i.e., Holcomb Ave and Virginia St).

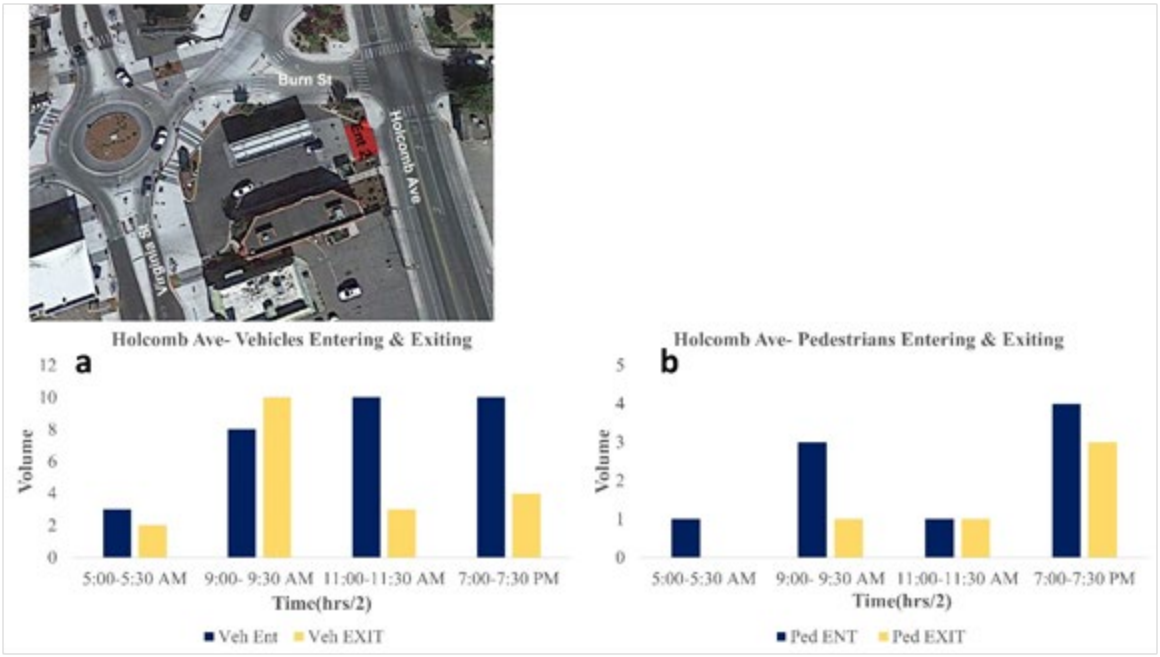

Figure 13-3. The entering and exiting trips at the Holcomb Ave drive way

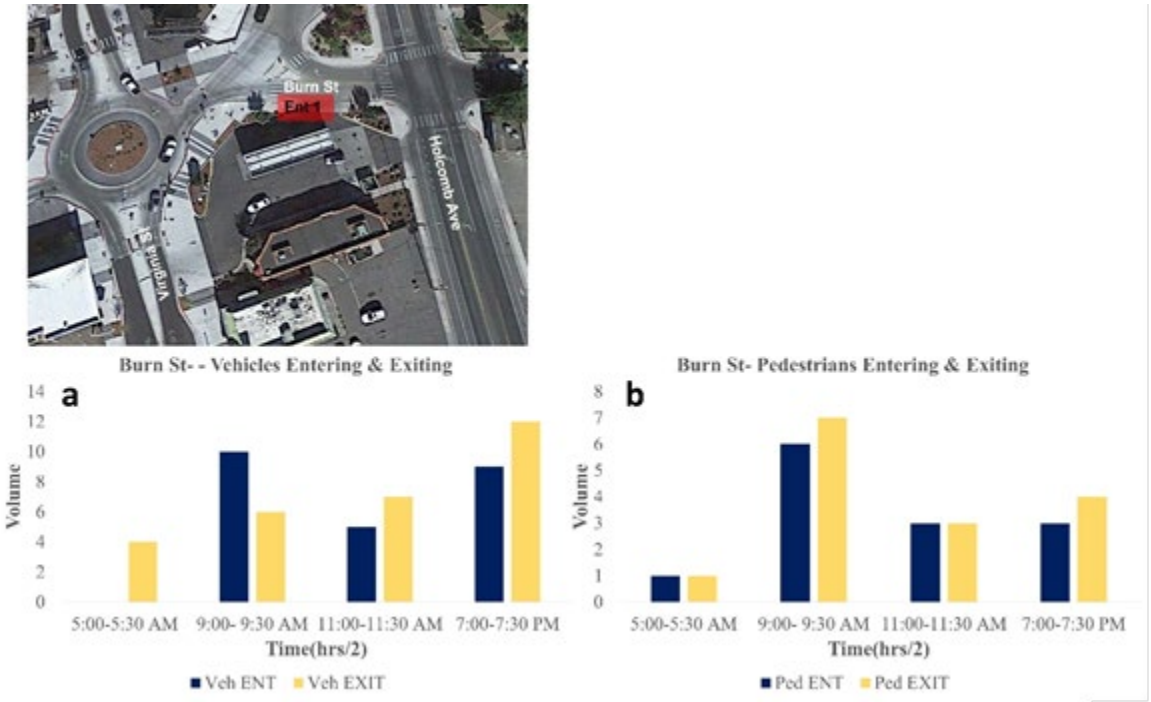

Figure 13-4. The entering and exiting trips at the Burn St drive way

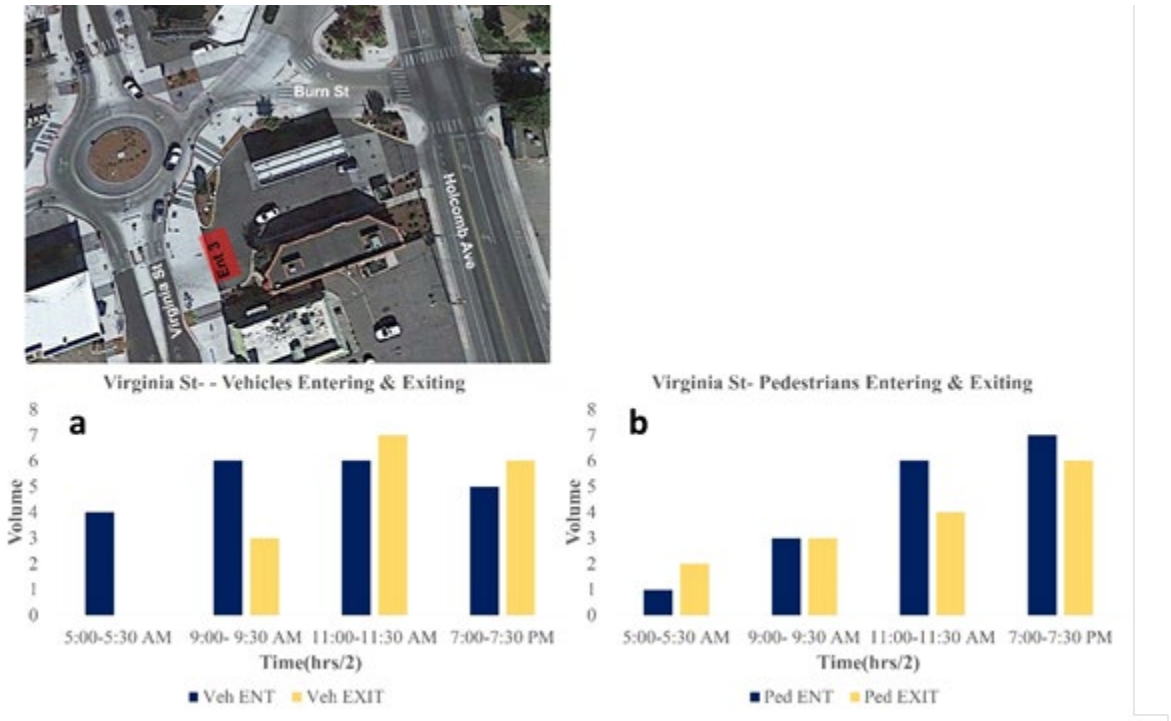

Figure 13-5. The entering and exiting trips at the Virginia St drive way

Also, in case there is a traffic loading in the business site, the exiting access (i.e., Burn Street in this case) could be widened to unload the traffic. A lasting trip of a pedestrian is an indicator of the contribution of the store into the business, while that of a vehicle could be an indicator of the contribution of the store and/or the gas station into the business. This suggests allocating more store related advertising signs to Holcomb Avenue, where the number of the entering trips by pedestrians is always more than the existing ones within the peak hours, except for 11-11:30 am when those numbers are equal. With an average of ~ 8 vehicles per half an hour, the access from Holcomb Avenue attracts more gas customers within the peak hours, 13-6. This is also evident from Figure 13-7. a, where pump 6, which is the closest one to Holcomb Avenue, is shown to have the maximum usage averaged over all four peak hours. This can be justified by the lower density of gas stations in Holcomb Avenue.

Figure 13-6 Gas pumps at the studied gas station

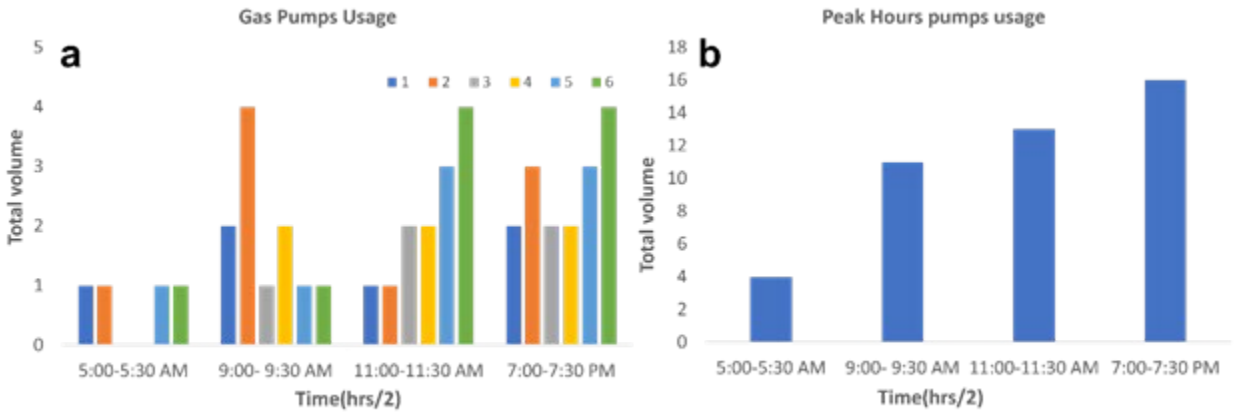

Figure 13-7. The Gas Pump's Usage for Six pumps(a), The Peak Hour Pump Usage(b)

Figure 13-8 indicates only ~ 30 % of pedestrians and ~ 25 % of vehicles entered the business site for the purpose of using the store. In general, this suggests that the gas station has the major contribution in trip attraction for the business assuming that vehicles do not solely pass through the gas station.

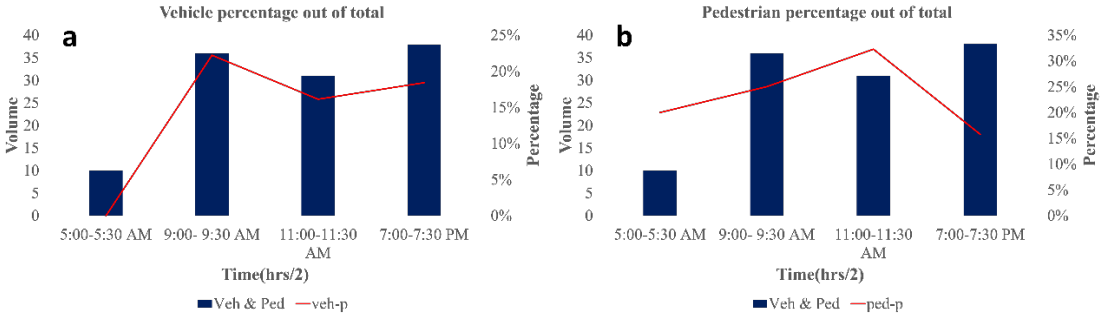

Figure 13-8. The percentage of Vehicles out of Total Number of Travelers in the Gas station(a) The percentage of Pedestrians out of Total Number of Travelers in the Gas station(b)

In average, the gas station/store has the greatest number of customers (pedestrians and vehicles) and maximum gas pump usage at 7-7:30 pm, for which a higher concentration of supplies and staffs is suggested. 9-9:30 am and 11-11:30 am are closely the next contributors. The trip trajectories of pedestrians and vehicles within these three time periods are for the gas station/store and its neighborhood. There is a great potential of attracting more vehicles (blue trajectories) and pedestrians (yellow trajectories) from Burn and Virginia Streets, respectively, within the peak hours.

Figure 13-9. GIS Trajectory for Pedestrians and Vehicles Based on LiDAR Data

14. CONNECTED AND AUTONOMOUS VEHICLES

While LiDAR sensors make it possible to locate vehicles and pedestrians accurately, they would contribute to CV systems in the mixed traffic environment - connected and non-connected. At the same time, a CV communication platform is needed to transfer high-resolution data from roadside LiDAR on mobile devices. Aiming to answer this question, the University of Nevada, Reno has been developing a new generation connected-vehicle system enhanced by roadside LiDAR sensors. As a parallel component of the systematic development, this work is to develop a communication framework that serves the connected-vehicle applications with the roadside LiDAR sensor data. A roadside system named DSRC-Bluetooth communication and mobile application with LiDAR sensor (DBCMA-LS) was designed to stream LiDAR data, package and transfer DSRC basic-safety messages (BSM) via dedicated short-range communications (DSRC). On the other hand, an onboard system was developed to receive, decode the DSRC messages, transfer decoded information through Bluetooth and visualize the LiDAR data in a smart phone application. In this proposed CV communication network, the overall performance of DSRC-Bluetooth communication was analyzed according to packet delay and packet-dropping probability. The analysis provided suggestions for the design of V2X data packets communicated through the complex DSRC-Bluetooth multi-hop environments.

System structure

The DBCMA-LS aims to feed roadside LiDAR data to the connected-vehicle applications. The target system consists of two parts: the DBCMA-LS RSU framework and the DBCMA-LS OBU framework, as shown in Figure 1. Primary functions of DBCMA-LS include:

1) collecting data from different sources such as connected traffic participants, traffic signals, and roadside LiDAR sensors,
2) formatting data into the standard basic safety messages (BSM) and signal phase and timing messages (SPaT) (*9*),
3) transfer data from RSU to OBU via DSRC network and from OBU to mobile devices via Bluetooth network,
4) dividing encoded BSM or SPaT into sub-packets to achieve efficient transmission between onboard DSRC devices and mobile devices through Bluetooth communication,
5) regrouping and unpacking BSM or SPaT sub-packets in the mobile application,
6) visualizing the real-time status of other traffic participants and providing a safety alerting service on mobile devices.

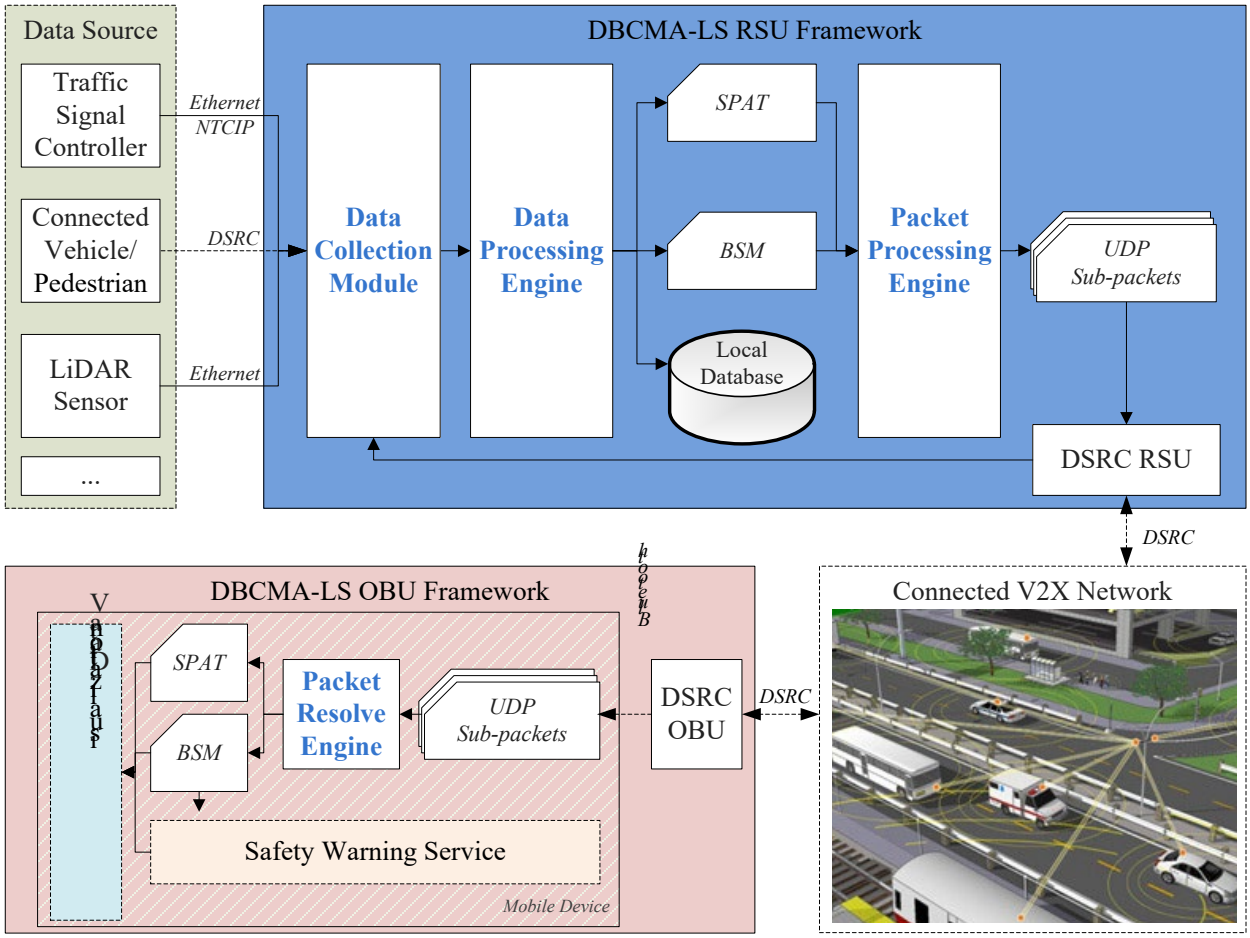

Figure 14-1. DBCMA-LS system structure

DBCMA-LS RSU framework

The RSU framework is DBCMA-LS's core component. It is linked to a commercially available DSRC roadside unit (RSU) that broadcasts and receives DSRC packets through the V2X communication network. Within the framework, the data collection module, data processing engine, and packet processing engine were implemented in the Next Unit of Computing (NUC) computer (10) (Figure 2). The NUC computer with the DBCMA-LS RSU framework can be deployed into the traffic cabinet at an intersection, linked with a traffic signal controller, LiDAR sensors, and DSRC devices via Ethernet cables.

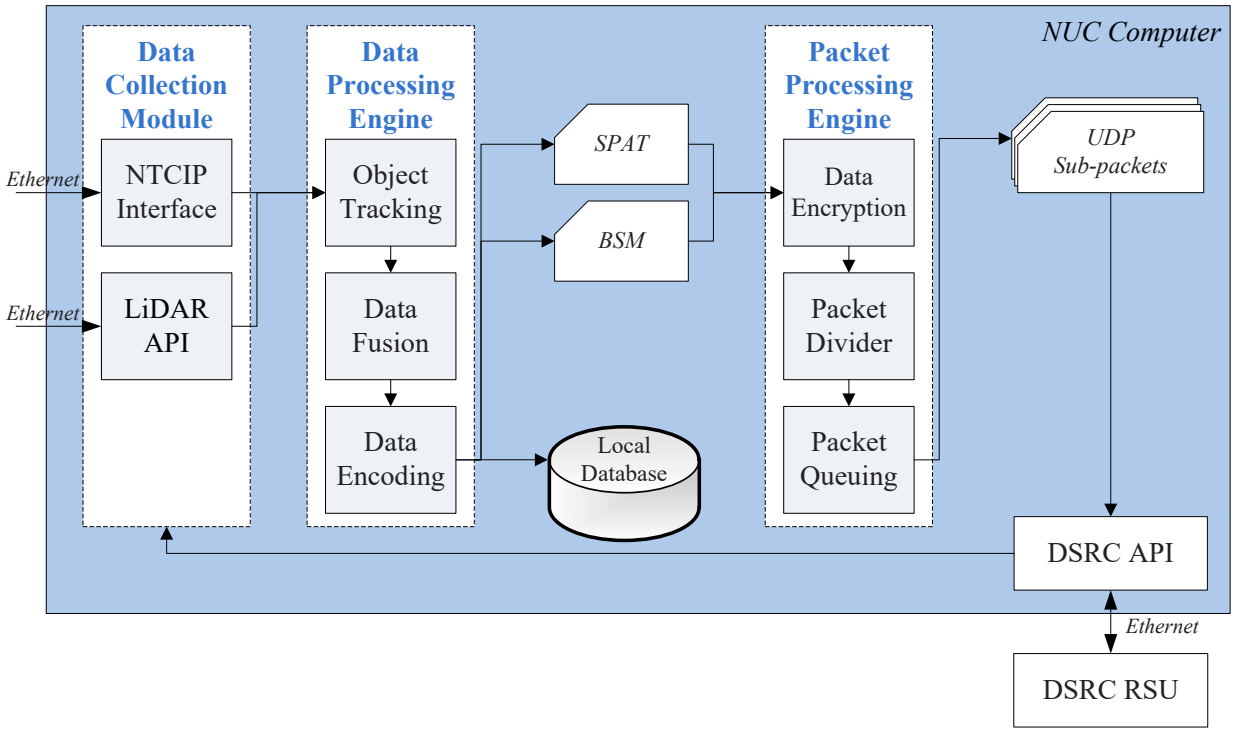

Figure 14-2. Modules in the DBCMA-LS RSU framework

Data collection module

A data collection module with several standard application-programming interfaces (APIs) was developed to extract data from different data sources. It reads traffic signal timing data from the traffic signal controller via Ethernet connection based on the National Transportation Communications for ITS Protocol (NTCIP). The data collection module streams High-resolution LiDAR data from the roadside sensors via Ethernet based on a custom API. The module also gathers connected-vehicle data from the DSRC network.

Data processing engine

Once data from different sources are received, the data are processed by a data processing engine, and then converted to standard BSM or SPaT messages. The real-time traffic signal timing data is encoded to SPaT messages. The high-resolution LiDAR point data is first pre-processed in the object-tracking module with the steps of background filtering, object clustering, object recognition, and object tracking. In the next step, information of traffic participants extracted from LiDAR sensor data or received from the DSRC network (information from connected vehicles) is merged in the data fusion module. Finally, the combined information of all traffic participants is encoded as BSM messages. It needs to be noted that a local database in the NUC computer is used to archive historical data for debugging and research purposes.

Packet processing engine

Compared to the traditional traffic sensors, 360-degree LiDAR sensors can detect and track traffic participants such as vehicles, bicycles, and pedestrians in a large area with a high frequency and

accuracy. The comprehensive traffic data from LiDAR need to be broadcast in real time; the information broadcasting can be challenging especially when a large number of participants are detected. As previously described, the encrypted SPaT and BSM messages are to be transferred via DSRC/Bluetooth communication by the user datagram protocol (UDP). A UDP packet needs to go through at least two hops to reach the destination: one hop in the DSRC network and the other hop in the Bluetooth connection. It is known that the bandwidth decreases and packet loss rate increases in a multi-hop environment, so data packets need to be processed in the packet-processing engine to ensure the communication performance of the system. Especially for the Bluetooth network, data packets are divided into smaller sub-packets to meet the bandwidth of the Bluetooth connection. A model is developed to adaptively determine the best broadcasting frequency for sub-packets, which will be discussed in Section 3.

2.3. DBCMA-LS OBU framework

In a connected vehicle, the DSRC OBU device receives the real-time SPaT and BSM messages; then the OBU device forwards the messages to a mobile device (smart phone or tablet) via the Bluetooth connection (Figure 14-3). The OBU is installed in a vehicle or held by a pedestrian, the Bluetooth communication distance between the OBU and the mobile device is in a short range. A packet resolving engine implemented in the mobile app regroups the sub-packets, decrypts the data and decodes it to real-time status of traffic participants and traffic signal. The mobile app finally visualizes the received information.

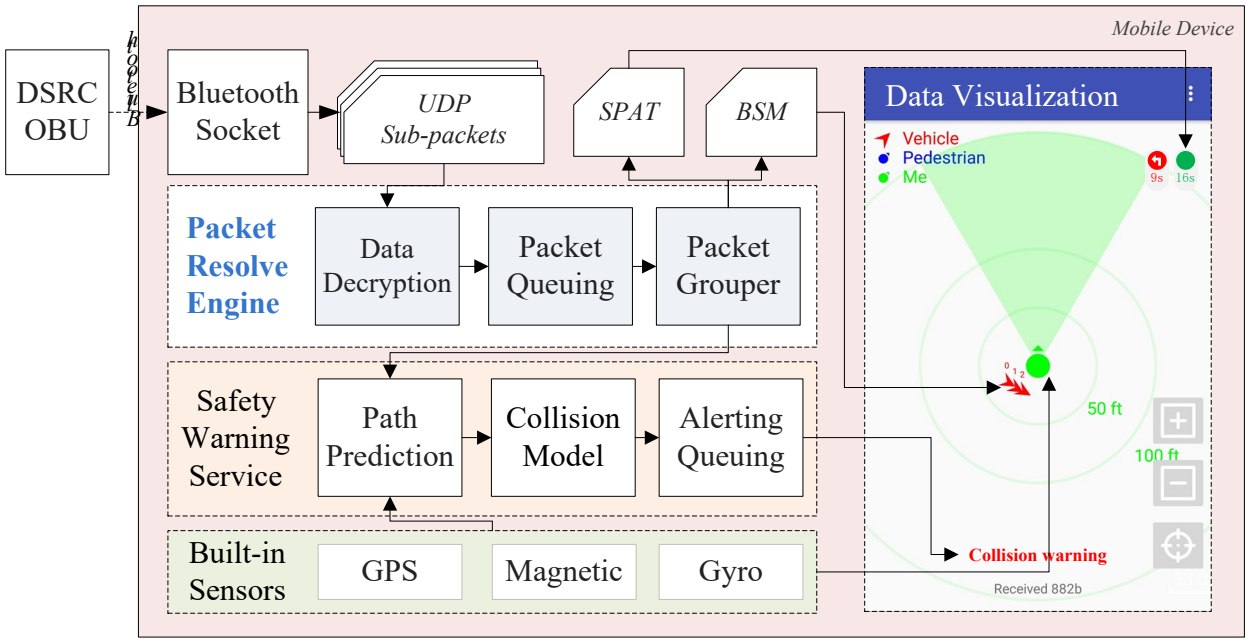

Figure 14-3. Modules of DBCMA-LS OBU framework

At the same time, the application also offers the safety alerting service to warn drivers with possible collision risks, which is a typical collision-avoidance application. It should be noted that connected-vehicle built-in sensors such as GPS/Magnetic/Gyro could be used by the application to help determine the position and direction of the connected vehicle.

Data visualization

Data visualization helps users understand the real-time traffic situation received from infrastructures and other road users. A map view is designed to display the user's vehicle and the vehicles and pedestrians surrounding. The user can see the general distance information from displayed distance circles. The zoom and move features of the interface make it possible to show traffic participants in the remote area (this function can be disabled to avoid the distraction of drivers). The real-time traffic signal timing status is displayed at the top-right corner of the screen as a countdown signal head.

Safety warning service

Presenting warning messages to the driver without causing distractions from a potentially hazardous situation is paramount to the success and safety of a CV system. The BSM messages, produced by both LiDAR sensors and other connected vehicles, are essential to traffic safety applications. In this module, the paths of surrounding vehicles can be predicted according to historical trajectories, speeds, and directions. Then the collision model will classify the collision risk and pop a warning message to drivers by displaying it at the bottom of the screen if any collision is predicted.

Implementation of the DBCMA-LS RSU framework at an intersection

A pilot DBCMA-LS system was built at a signalized intersection, 15th ST and N. Virginia ST, Reno, Nevada, to detect/track the vehicles and pedestrians and provide safety information at the intersection (Figure 14-4). Two LiDAR sensors are placed at the intersection to cover the four legs of the intersection. The parameters of the LiDAR sensor in the system are given (Table 14-1). The NUC computer was housed in the traffic signal controller cabinet. High-resolution roadside LiDAR data was first processed and then broadcasted via the DSRC RSU device at the intersection. It should be noted that multi-hop transmission in DSRC network is not allowed due to authentication. In this paper, the multi-hop transmission system means the hop between DSRC and Bluetooth network.

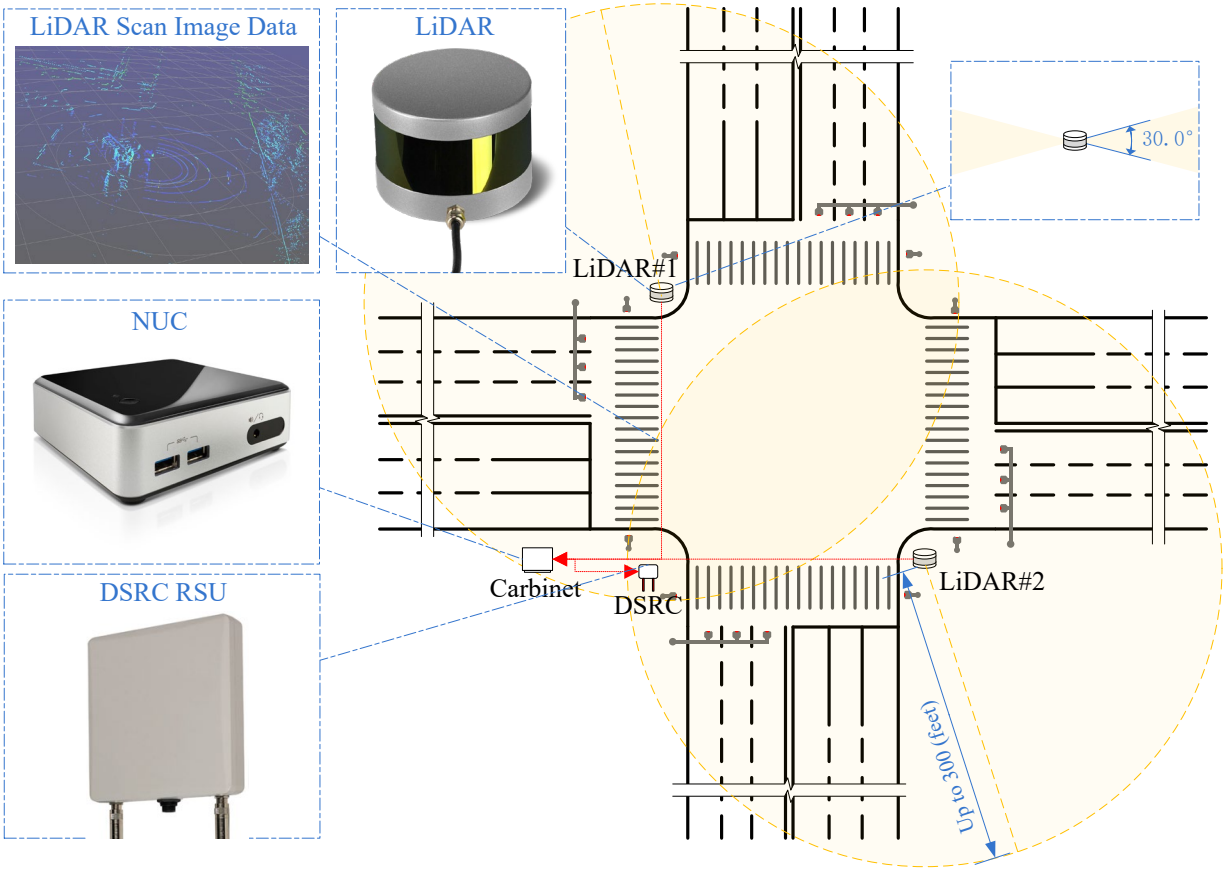

Figure 14-4. Implementation of the pilot DBCMA-LS RSU framework

Table 14-1. Basic Parameters of LiDAR Sensor for DBCMA-LS

Parameter	Performance
Measurement Range	Up to 300 (feet)
Field of View (Horizontal)	360 (°)
Field of View (Vertical)	+15.0(°) to -15.0(°) (30°)
Rotation Rate	20 (Hz)

The LiDAR data provide the comprehensive status of all road users at the intersection. A data dictionary presented in Table 14-2 describes the status information of each traffic participant, which is extracted from LiDAR data and broadcasted by the DSRC RSU devices. The data dictionary could be used as a starting point for NTCIP standardization.

Table 14-2. Data Dictionary from LiDAR

Data Name	Description	Format
ObjectID	Target ID for tracking an object	int32
ObjectType	Object type: Vehicle, Pedestrian, Bicycle, Wildlife, Obstacle, Other	enum (byte)
TimeStamp	Date and time stamp of the record	datetime
Object_Length	Object length, in Feet	float
Object_Width	Object width, in Feet	float
TrackPointType	Track point type: CP (center point), FR(front right corner), RR(rear right corner), FL(front left corner), RL(rear left corner)	enum (byte)
Coord_x	X value of local coordinate of track point, in Feet	float
Coord_y	Y value of local coordinate of track point, in Feet	float
Coord_z	Z value of local coordinate of track point, in Feet	float
Coord_dir	Direction of polar coordinate degrees (0-360) of track point	float
Coord_dis	Distance to the center of polar coordinate, in Feet	float
Longitude	Longitude of track point, in wgs84 system	float
Latitude	Latitude of track point, in wgs84 system	float
Elevation	Elevation of track point, in Feet	float
Direction	Direction of target movement, in degree 0-360	float
Speed	Speed of target movement, in MPH	float

Implementation of the DBCMA-LS OBU framework

The DBCMA-LS RSU framework pilot system was implemented including the DSRC OBU device and an Android device with an implemented application (Figure 14-5). The implemented onboard system received information of vehicles and pedestrians around this intersection; then, it displayed those road users on the map view of the Android application. The map is always centered at the location of the device so that user can monitor the surrounding traffic participants. Users can zoom in/out and pan the map to view the distant objects. On the top of the view, a countdown traffic signal head displays the real-time signal status of the next intersection in front of the user. The warning message can be displayed at the bottom of the screen.

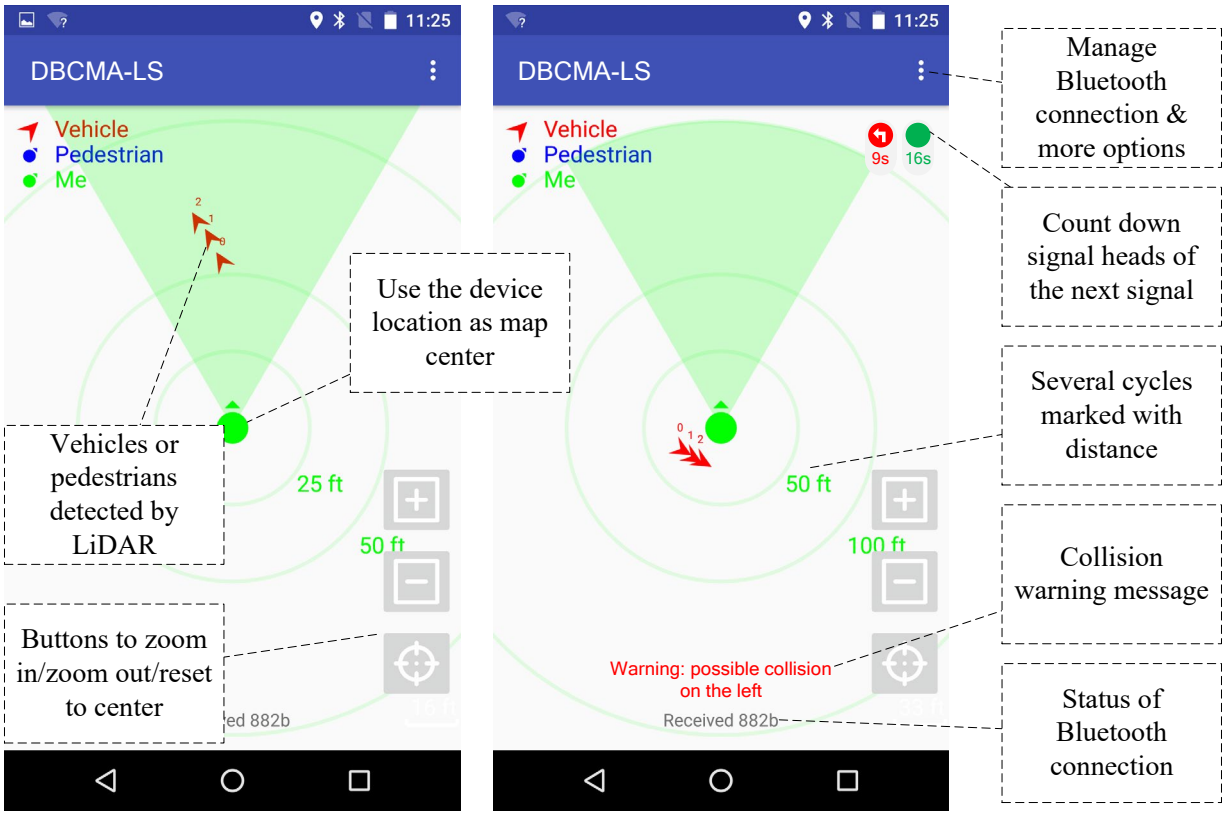

Figure 14-5. Implementation of the DBCMA-LS OBU framework on an Android device

Test results for platform performance

The end-to-end packet delay and the packet-dropping probability of the implemented DBCMA-LS system were tested in the field. In the test cases, packets of different sizes (L) were transferred. Different packet intervals (I) of sub-packets were used to seek the optimal communication performance of DBCMA-LS. The interval between two packets was long enough so that packages were not affected by each other. The end-to-end packet delay ($D_{e2e}(L,I)$) was counted by the time difference between the current GPS time on the Android device and GPS timestamp in the BSM message. The end-to-end packet-dropping probability ($p_{e2e}(L,I)$) was calculated by dividing the number of successfully resolved packages by the total number of packages.

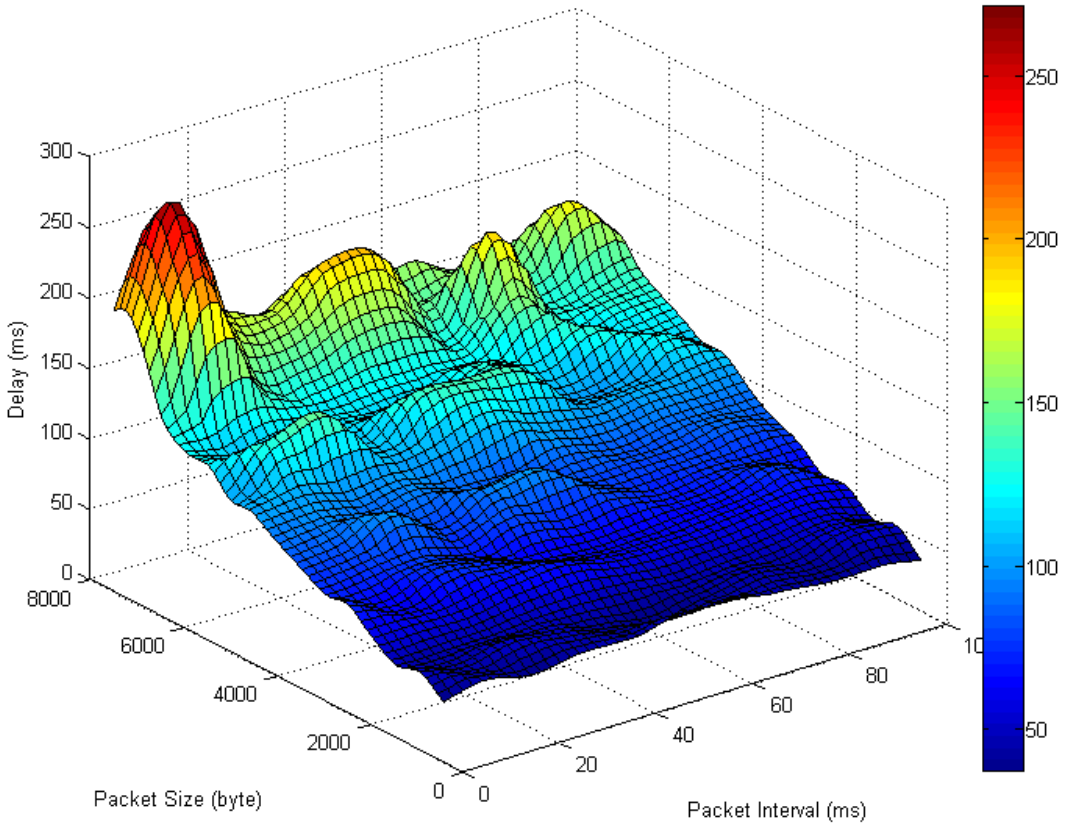

Figure 14-6. End-to-end packet delays of DBCMA-LS with different packet interval and size

As shown in Figure 14-6, end-to-end packet delay increased with the increase of packet size. The fluctuation of the 3D surface indicates that the delay is random in the DSRC/Bluetooth network. When the packet interval is less than 20 (ms), communication becomes congested with the larger packet size, which results in a rapid increase of delay.

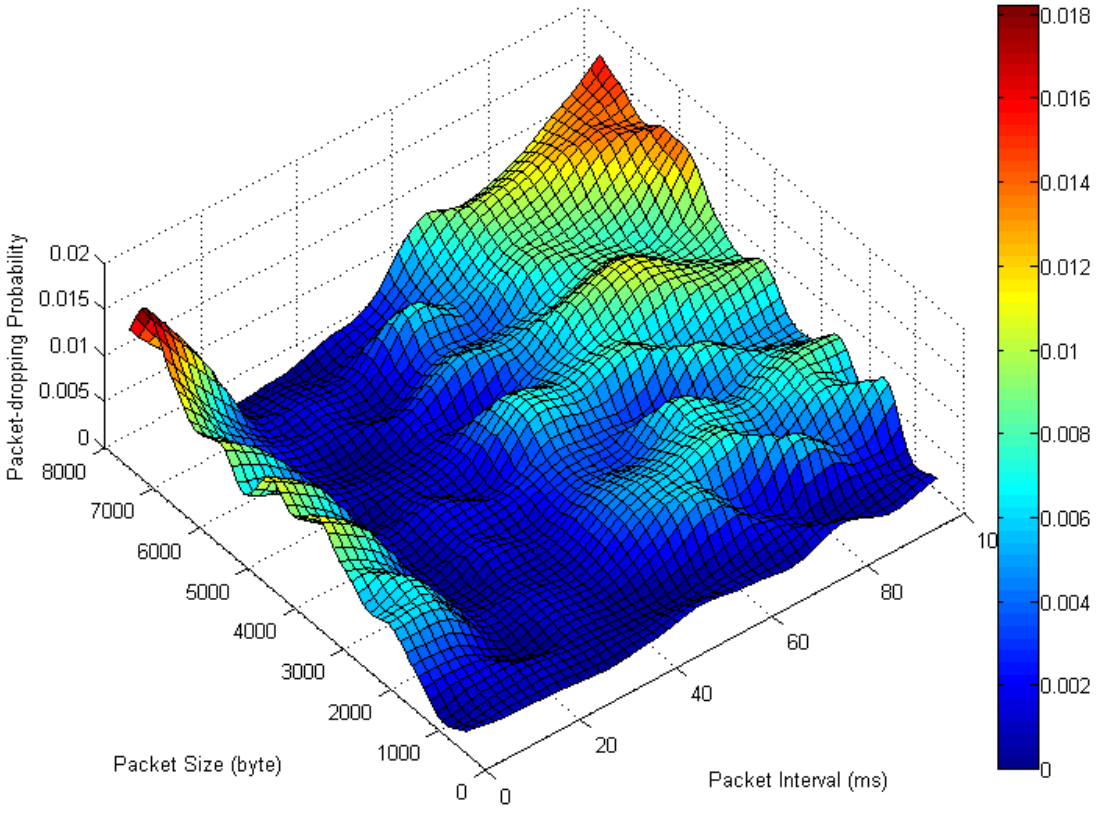

Figure 14-7. End-to-end packet-dropping probabilities with different packet interval and size

As shown in Figure 14-7, the packet-dropping probability was at a relatively low value (*16*), which means the overall communication stable. When the packet interval is less than 20 (ms), the packet-dropping probability increases, which means the reliability of the communication is degraded. On the other hand, with the rise of packet interval and packet size, the sub-packet may be affected by the next packet, which results in the rapid increase of packet-dropping probability.

The testing results show that the optimal communication performance of DBCMA-LS is reached when the packet interval is between 20 and 40 (ms); in fact, the best packet interval is chosen as $\hat{I} = 30$ (ms). As the result, the end-to-end equivalent packet delay ($\hat{D}_{nL}(L_S, \hat{I})\big|_{n=1, Ls=E[L]}$) is given in Figure 8.

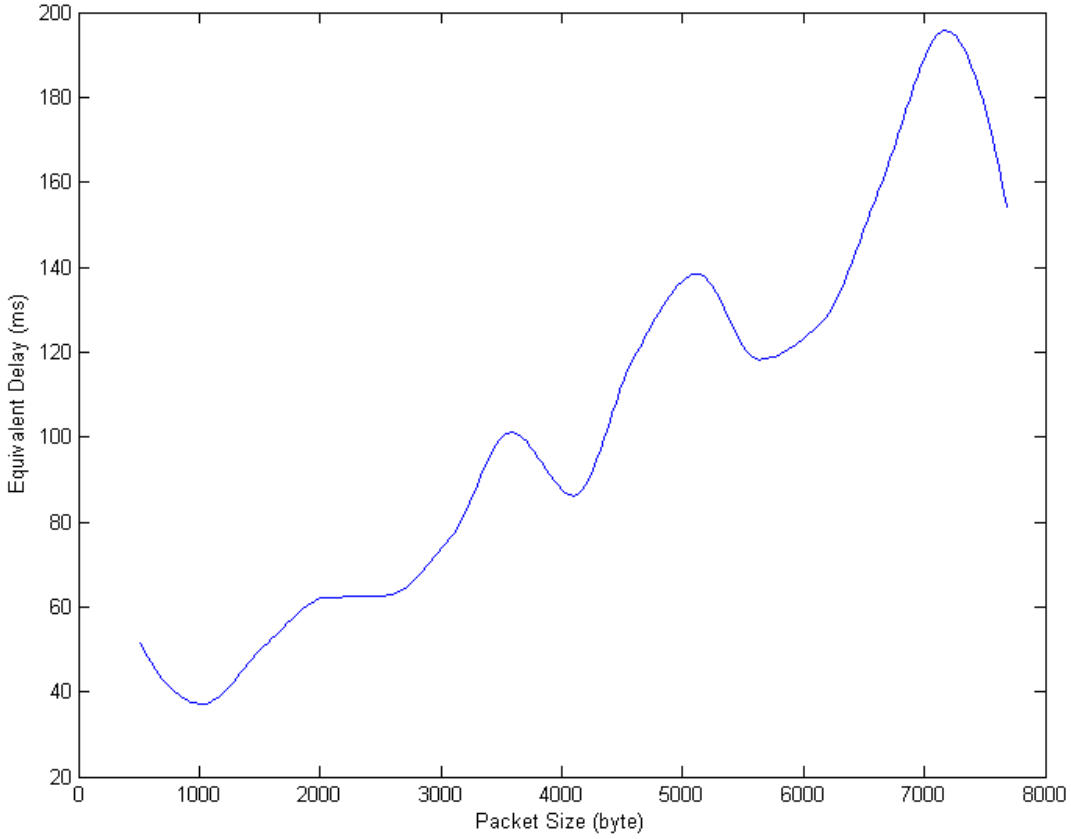

Figure 14-8. End-to-end optimal equivalent packet delays of DBCMA-LS

The maximum equivalent packet delay of DBCMA-LS sending a packet within 8 (MB) is less than 200 (ms) (Figure 8). Since the data size for a traffic participant from LiDAR can be estimated as 62 (byte) (Table 3), the delay is small enough for DBCMA-LS to provide collision-warning messages in the test case. In theory, at most 132 detected traffic participants can be transferred within the given delay.

5. CONCLUSION

In this paper, a CV system named DSRC/Bluetooth communication and mobile application with LiDAR sensor (DBCMA-LS) is proposed for collecting roadside LiDAR data, packaging and transferring messages to mobile devices. A smart device application was developed to receive and visualize data from other connected-vehicles and roadside LiDAR sensors. The communication performance of DBCMA-LS was analyzed by testing packet delay and packet-dropping probability. The core parameters of the system were determined for the optimal performance. Test results indicate that appropriate packet interval allows the DBCMA-LS to transmit high-resolution data extracted from roadside LiDAR and to serve connected-vehicle applications.

In this implemented system, the overall performance of DSRC-Bluetooth communication was tested, which recommended packet size and interval. This study also provides an example for evaluating V2X applications in a complex DSRC-Bluetooth multi-hop environment. This study approves the feasibility of using the roadside LiDAR data to serve connected-vehicle applications. One possible future work is to study the inter-influence between high-frequency packets in DSRC/Bluetooth network and bring out a better packet processing method to reduce this impact. Based on DBCMA-LS, more CV applications can be proposed to improve traffic safety and efficiency. It should be mentioned that the BSM content in this study was adjusted from the standard BSM, which was to transfer the comprehensive information from the roadside LiDAR sensors. However, the BSM has been patented, so that future work is to choose or design a more appropriate message format for the system.

test

15. CONCLUSION

Roadside LiDAR sensing technologies have been well developed and tested in the past few years. Hardware and software solutions are mature and market-ready. The roadside LiDAR components introduced in this report are not the only solution but demonstrate the key components, functions, and performance requirements to be considered. Installation influences the accuracy and reliability of LiDAR data, and it may also change the deployment costs by knowing an optimized installation can provide more extended effective detection ranges. The knowledge of installation height and angle's impact on sensing quality will support engineers and technicians in designing, installing, operating, and maintaining roadside LiDAR systems. Understanding how traffic flow rates or levels of service can change traffic occlusion rates, decision-makers and system designers can predict the roadside LiDAR system performance and provide the optimized sensor deployment design for the planned service periods.

LiDAR sensing is impacted by inclement weather, but it offers the same high-quality sensing data without the impact of light conditions, which is critical for both urban and rural traffic safety and smart traffic control. While weather's influence on LiDAR sensors is determined by physics, the data processing algorithms can address the impacts of different weather conditions and maximize sensors' capability. There is considerable published research on using customized algorithms or algorithm parameters for LiDAR sensors in different weathers. An automatic method of intelligently knowing the current weather condition through received LiDAR cloud points was developed in this project. It can be the controller for a smart system to automatically select the best algorithms and parameters based on environmental conditions.

To obtain all-road-user trajectory data, researchers and engineers mainly consider two sensor types – video and LiDAR. This project evaluated a video sensing solution on the market and the project team's LiDAR solution that can be a valuable reference for the audience considering the two technologies. The test details can help with evidence-based decisions.

While roadside LiDAR sensing has been exciting researchers, its real-world applications are interests of most agencies and industries. This project presented multiple roadside LiDAR applications, including data applications, smart-and-connected traffic signals, and connected-and-autonomous vehicles. While the real-time smart traffic signal system and connected-and-autonomous vehicle solutions are still pilot projects, roadside LiDAR is a ready-data solution to fill today's traffic plan, design, and engineering data requirements and gaps.

REFERENCE

[1]. Mukhtar, A., Xia, L., & Tang, T. B. (2015). Vehicle detection techniques for collision avoidance systems: A review. IEEE Transactions on Intelligent Transportation Systems, 16(5), 2318-2338.

[2]. Velodyne. (2016). VLP-16 Manual: User's Manual and Programming Guide. Velodyne LiDAR. Inc., Jose, CA, USA. Available at: https://usermanual.wiki/Pdf/VLP16Manual.1719942037.pdf

[3]. Ester, M., Kriegel, H. P., Sander, J., & Xu, X. (1996, August). A density-based algorithm for discovering clusters in large spatial databases with noise. In Kdd, 96(34), 226-231.

[4]. Rokach, L., & Maimon, O. Z. (2008). Data mining with decision trees: theory and applications (Vol. 69). World scientific.

[5]. Ho, T. K. (1995). Random decision forests. In Proceedings of 3rd international conference on document analysis and recognition, 1, 278-282.

[6]. Geurts, P., Ernst, D., & Wehenkel, L. (2006). Extremely randomized trees. Machine learning, 63(1), 3-42.

[7]. Velodyne. (2018). VLP-32C User Manual. Velodyne LiDAR. Inc., San Jose, CA, USA. Available at: https://icave2.cse.buffalo.edu/resources/sensor-modeling/VLP32CManual.pdf

[8]. Wu, J., Xu, H., Sun, Y., Zheng, J., & Yue, R. (2018). Automatic background filtering method for roadside LiDAR data. Transportation Research Record, 2672(45), 106-114.

[9]. Premebida, C., Ludwig, O., & Nunes, U. (2009). LIDAR and vision‐based pedestrian detection system. Journal of Field Robotics, 26(9), 696-711.

[10]. Premebida, C., Monteiro, G., Nunes, U., & Peixoto, P. (2007, September). A lidar and vision-based approach for pedestrian and vehicle detection and tracking. In 2007 IEEE intelligent transportation systems conference (pp. 1044-1049). IEEE.

[11]. Navarro-Serment, L. E., Mertz, C., & Hebert, M. (2010). Pedestrian detection and tracking using three-dimensional ladar data. *The International Journal of Robotics Research*, *29*(12), 1516-1528.

[12]. Kidono, K., Miyasaka, T., Watanabe, A., Naito, T., & Miura, J. (2011, June). Pedestrian recognition using high-definition LIDAR. In 2011 IEEE Intelligent Vehicles Symposium (IV) (pp. 405-410). IEEE.

Nevada Department of Transportation

Kristina L. Swallow, P.E. Director

Ken Chambers, Research Division Chief

(775) 888-7220

kchambers@dot.nv.gov

1263 South Stewart Street

Carson City, Nevada 89712